



**HAL**  
open science

# Rockfalls multi-methods detection and characterization

Gaëlle Le Roy

► **To cite this version:**

Gaëlle Le Roy. Rockfalls multi-methods detection and characterization. Applied geology. Université Grenoble Alpes [2020-..], 2020. English. NNT: 2020GRALU012 . tel-02921764

**HAL Id: tel-02921764**

**<https://theses.hal.science/tel-02921764v1>**

Submitted on 25 Aug 2020

**HAL** is a multi-disciplinary open access archive for the deposit and dissemination of scientific research documents, whether they are published or not. The documents may come from teaching and research institutions in France or abroad, or from public or private research centers.

L'archive ouverte pluridisciplinaire **HAL**, est destinée au dépôt et à la diffusion de documents scientifiques de niveau recherche, publiés ou non, émanant des établissements d'enseignement et de recherche français ou étrangers, des laboratoires publics ou privés.

## THÈSE

Pour obtenir le grade de

### DOCTEUR DE L'UNIVERSITÉ GRENOBLE ALPES

Spécialité : Terre Solide (CETSOL)

Arrêté ministériel : 25 mai 2016

Présentée par

**Gaëlle LE ROY**

Thèse dirigée par **David AMITRANO**, Université Grenoble Alpes  
et codirigée par **Agnès HELMSTETTER**, Université Grenoble  
Alpes

préparée au sein du **Laboratoire Institut des Sciences de la  
Terre**  
dans l'**École Doctorale Terre, Univers, Environnement**

### Détection et caractérisation multi-méthodes des éboulements rocheux

### Rockfalls multi-methods detection and characterization

Thèse soutenue publiquement le **10 janvier 2020**,  
devant le jury composé de :

**Monsieur DAVID AMITRANO**

MAITRE DE CONFERENCES HDR, UNIVERSITE GRENOBLE ALPES,  
Directeur de thèse

**Monsieur MICHEL JABOYEDOFF**

PROFESSEUR, UNIVERSITE DE LAUSANNE - SUISSE, Président

**Monsieur JEAN-ROBERT GRASSO**

PHYSICIEN, UNIVERSITE GRENOBLE ALPES, Examineur

**Monsieur THOMAS DEWEZ**

DOCTEUR-INGENIEUR, BRGM - ORLEANS, Examineur

**Monsieur JEAN-PHILIPPE MALET**

DIRECTEUR DE RECHERCHE HDR, CNRS DELEGATION ALSACE,  
Rapporteur

**Monsieur FABIAN WALTER**

PROFESSEUR ASSISTANT, ETH ZURICH - SUISSE, Rapporteur







# Abstract

Amongst mass wasting events, rockfalls remain the most unpredictable and the most frequent hazard in the alpine region. In a context of growing urbanization in mountainous regions, rockfalls represent an increasing risk for local communities and infrastructures. This thesis aims to develop an association of relevant methods for rockfall monitoring. One objective of this thesis is to associate topography measurement and seismological monitoring in order to improve significantly the understanding rockfall dynamics. This work was mainly carried out in the Chartreuse massif (Isère, French Alps), and in particular at two cliffs, Mount Saint-Eynard and Mount Granier. Using photogrammetry, we acquired diachronic Digital Elevation Models (DEMs) of the cliffs. Such monitoring enables us to carry out rockfall inventories and occurrence frequency analysis. It also provides us information on rockfall locations and their structural configurations. Combining DEMs and rockfall seismic monitoring allowed us to study relations between rockfall properties (location, volume, geometry, propagation, etc.) and the induced seismic signal. Characteristics of the seismic signal (duration and energy, frequency content, envelope shape) vary depending on the event propagation mode (mass-flow, free-fall, sliding, bouncing ...). Selecting events with the same propagation type provides a more accurate characterization of rockfall properties than when mixing different types of events. For free-falling rockfalls, we analyze the seismic signal of the detachment phases and first impacts. We found relations between seismic signal parameters and rockfall potential energy, free-fall heights, and volumes. For mass-flow type events, we found a scaling law between rockfall seismic energy and volumes. By coupling DEMs and seismic records, we can reconstruct rockfall sequence with accurate timing and correct volume estimates. Controlled block releases were realized in laboratory and on-site to widen our observations on rockfall events.



## Résumé

Parmi les mouvements de terrain, les éboulements rocheux restent le danger le plus imprévisible et le plus fréquent en région alpine. Dans un contexte d'urbanisation croissante des régions montagneuses, les éboulements représentent un risque croissant pour les communautés locales et les infrastructures. Cette thèse vise à développer une association pertinente de méthodes pour la surveillance des éboulements en couplant des mesures de relief à un suivi sismologique, afin d'améliorer la compréhension de la dynamique des éboulements. Ce travail a été principalement réalisé dans le massif de la Chartreuse (Isère, Alpes Françaises), et en particulier sur deux falaises, le mont Saint-Eynard et le mont Granier. Par photogrammétrie, nous avons obtenu des Modèles Numériques de Terrain (MNTs) des falaises. Ce suivi nous a permis de réaliser des inventaires de chutes de blocs et des analyses de fréquence d'occurrence. Cela nous a également fourni des informations sur les emplacements des éboulements ainsi que leurs configurations structurales. L'association des MNTs et du suivi sismique des éboulements nous a permis d'étudier les relations entre les propriétés des éboulements (emplacement, volume, géométrie, propagation, etc.) et le signal sismique induit par ceux-ci. Les caractéristiques des signaux sismiques (durée et énergie, contenu fréquentiel, forme de l'enveloppe) diffèrent selon le mode de propagation des événements (écoulement en masse, chute libre, glissement, rebondissement, ...). Une sélection d'évènements ayant le même type de propagation permet d'obtenir une caractérisation plus précise des propriétés des éboulements que si l'on mélange différents types d'évènements. Dans le cas d'éboulements subissant une chute libre, nous avons analysé le signal sismique des phases de détachement et du premier impact. Nous avons obtenu des relations entre certains paramètres des signaux sismiques et l'énergie potentielle des éboulements, leur hauteur de chute libre ou leur volume. Pour les événements de type écoulement en masse, nous avons observé une loi d'échelle entre l'énergie sismique d'un éboulement et son volume. En couplant les MNTs et les enregistrements sismiques, nous sommes ainsi en mesure de reconstruire le déroulement des éboulements avec une datation précise et une estimation de volume correcte. Des lâchers contrôlés de blocs ont été réalisés en laboratoire et in-situ pour élargir nos observations sur les éboulements de falaise.



# Remerciements

Il est difficile de prédire la trajectographie d'un compartiment rocheux dévalant une pente. Celle-ci dépend de nombreux paramètres tels que la nature du bloc (type de roche, fractures, etc.), de la topographie ou encore de la présence de végétation. Tel un bloc descendant la montagne j'aurais bien été incapable de prédire mon parcours jusqu'ici. Celui-ci a été influencé par de nombreuses personnes que je tiens à remercier ici.

Je ne me destinais pas à faire une thèse et je dois remercier mes professeurs d'école d'ingénieur Polytech Grenoble pour m'avoir fait découvrir la recherche. Merci également à Didier Hantz pour m'avoir mis en contact avec David Amitrano, mon futur maître de stage puis directeur de thèse, et pour s'être intéressé à mes travaux tout au long de ma thèse.

Pour poursuivre la métaphore, merci à David Amitrano qui a joué un rôle efficace de déviateur. Merci de m'avoir convaincue de faire cette thèse qui fut une très bonne expérience. Merci pour avoir toujours trouvé le temps pour discuter malgré un emploi du temps chargé et ce avec une bonne humeur invariable. Merci pour les nombreux projets, les idées encore plus nombreuses et les missions terrains (même au prix d'une belle entorse de la cheville).

Je tiens à remercier Agnès, ma co-directrice de thèse pour ses conseils toujours utiles, pour sa disponibilité à toute heure, et pour le nombre incalculable de relectures, corrections et suggestions. Merci infiniment pour ton aide, elle a été très précieuse.

Merci à Fabrice Guyoton, co-directeur de thèse, pour l'avoir rendue possible. J'ai eu la chance d'avoir tous les avantages d'une thèse Cifre : une collaboration et le point de vue d'un bureau d'étude tout en restant très libre sur mes travaux de recherche. Merci pour cette expérience, pour tes conseils et tes retours. Je souhaite également saluer Violaine Vignon et Romain Le Roux-Mallouf pour leurs encadrements successifs au sein de Géolithe.

Je voudrais également remercier tous mes collègues et stagiaires qui m'ont aidée lors des missions de terrain, les essais de lâchers de blocs et autres manips : Michaël Langlais, Benjamin Vial, Guillaume Clément, Théo Fernandez, Agathe Furet, Quentin Barbier, Etienne Rey, et tant d'autres.

Cette expérience n'aurait pas été la même sans les moments partagés et la convivialité toujours présente que ce soit à Géolithe ou à ISTerre. Merci à Anne-Marie pour m'avoir accueillie dans son bureau et pour toutes les attentions dont elle m'a entourée. Merci à

tous les pros du ski de fond, les fous de treks, les addicts du café, les assidus du gâteau du vendredi, les fans de chocolats, les musiciens et autres qui ont fait que ces trois années se sont passées si vite. Cyrielle, Noélie, Louise, Sylvie, Judith, Antoine, Sylvain, Benjamin, Agathe, Dorian, Elena, vous vous reconnaîtrez. Merci également à mes amis Mathieu, Basile, Clément, Estelle, Régis, Manon et Emilie pour avoir réussi à me faire sortir le nez de ma thèse.

Plus de 300 lâchers de blocs, plusieurs milliers de photographies de falaises, des litres de thé et de café plus tard, voilà cette thèse qui se termine. Je voudrais finir ces remerciements avec ceux qui comptent le plus. Merci à mes parents d'avoir tout fait pour que je puisse arriver jusqu'ici. Merci Anne et Edouard pour avoir supporté de bonne grâce mes discussions sur les cailloux. Merci à Mamily et son amour des montagnes. Finalement un immense merci à celui qui accompagne mon chemin dans tous ses tours et détours, à travers la distance, les carences de fer, et le stress d'une thèse. Merci Thomas pour ta bonne humeur constante, ton soutien indéfectible et tous les gestes du quotidien.

# Table of contents

Introduction .....	15
Structure and contents.....	17
Part I Rockfall hazard: processes and issues .....	21
<b>1 Slopes dynamics and weathering .....</b>	<b>23</b>
<b>1.1 Slope instability .....</b>	<b>23</b>
<b>1.2 Rockfalls .....</b>	<b>25</b>
1.2.1 Rockfall failure and triggers.....	25
1.2.2 Failure precursors .....	28
1.2.3 Rockfall propagation.....	29
<b>2 Rockfall hazard in the Alps.....</b>	<b>31</b>
2.1 Rockfall events in collective memory.....	31
2.2 Socio-economic impact of rockfall hazard.....	32
2.3 Risk management.....	34
<b>3 Rockfall monitoring techniques.....</b>	<b>37</b>
3.1 Field study and cartography.....	37
3.2 Displacement measurement methods.....	38
3.3 Geophysical methods .....	38
3.4 Remote sensing techniques .....	39
3.5 Limitations and challenges.....	41
3.5.1 Widespread hazard monitoring using remote sensing techniques .....	41
3.5.2 Seismic monitoring of rockfall occurrence.....	42
3.5.3 Need for multi-method monitoring .....	43



Part II	Rockfalls detection and characterization using DEMs .....	45
4	Methodological biases on rockfall inventories and empirical volume distributions .....	49
<hr/>		
4.1	Introduction.....	49
4.2	Study area.....	50
4.3	Distance measurement methods.....	51
4.3.1	2D DEMs .....	51
4.3.2	3D DEMs .....	52
4.3.3	2.5D DEMs .....	53
4.4	Rockfall inventories .....	54
4.4.1	Distance measurement .....	54
4.4.2	Erosion areas extraction.....	54
4.4.3	Volume measurement.....	55
4.5	Results .....	56
4.6	Discussion .....	59
4.7	Conclusion .....	61
5	Morpho-structural analysis of rockfalls .....	63
<hr/>		
5.1	Mount Saint-Eynard cliffs monitoring .....	63
5.2	Rockfalls distribution.....	63
5.3	Rockfall configurations.....	65
5.4	Structural analysis .....	68
5.5	Conclusions on rockfall monitoring using DEMs.....	71
Part III	Seismologic monitoring of rockfall .....	73
6	Seismic analysis of free-falling rockfalls.....	77
<hr/>		
6.1	Introduction.....	77
6.2	Study site.....	79
6.2.1	Chartreuse massif.....	79
6.2.2	Other sites.....	80
6.2.3	Instrumentation of the Chartreuse massif sites .....	81
6.2.3.1	Mount-Saint-Eynard.....	81
6.2.3.2	Mount Granier.....	82
6.3	Methods.....	82
6.3.1	Topographic data analysis .....	82

6.3.2	Detection and classification of seismic signals .....	84
6.3.3	Characterization of rockfalls from seismic signals.....	85
<b>6.4</b>	<b>Rockfall databases.....</b>	<b>87</b>
6.4.1	Rockfall catalogs obtained by topographic data.....	88
6.4.2	Rockfall catalogs obtained by seismic monitoring .....	88
6.4.2.1	Mount Saint-Eynard.....	88
6.4.2.2	Mount Granier.....	88
6.4.3	Association of topographic and seismic data .....	89
6.4.3.1	Mount Saint-Eynard rockfalls .....	89
6.4.3.2	Mount Granier rockfalls .....	89
6.4.4	Characteristics of selected rockfalls for Mount Saint Eynard and Mount Granier .....	91
6.4.5	Other datasets: controlled releases of blocks and Yosemite park rockfalls 91	
<b>6.5</b>	<b>Analysis of seismic signals.....</b>	<b>93</b>
6.5.1	Rockfall seismic signals typology .....	93
6.5.2	Detachment and free-fall.....	95
6.5.3	Impact.....	97
<b>6.6</b>	<b>Discussion .....</b>	<b>98</b>
6.6.1	Detachment phase.....	98
6.6.2	Relation between potential and seismic energy of the impact phase.....	99
6.6.3	Estimation of rockfall volume from the seismic energy of the impact phase .....	100
6.6.4	Real-time characterization of rockfalls.....	101
6.6.5	Comparison with other studies .....	101
<b>6.7</b>	<b>Conclusions .....</b>	<b>104</b>
<b>7</b>	<b>Controlled block release experiment of free fall type events .....</b>	<b>105</b>
<hr/>		
<b>7.1</b>	<b>Introduction.....</b>	<b>105</b>
<b>7.2</b>	<b>Datasets.....</b>	<b>106</b>
7.2.1	Large-scale block release experiment .....	106
7.2.2	Small-scale block release experiment .....	107
7.2.3	Other datasets.....	108
<b>7.3</b>	<b>Methods.....</b>	<b>108</b>
7.3.1	Impacts characteristics.....	108
7.3.2	Seismic characterization.....	109
<b>7.4</b>	<b>Results .....</b>	<b>110</b>

7.4.1 Detachment and free-fall.....	110
7.4.2 Impact.....	112
<b>7.5 Discussion .....</b>	<b>114</b>
<b>7.6 Conclusion .....</b>	<b>116</b>
<b>8 Seismic analysis of granular flow type rockfalls.....</b>	<b>117</b>
<hr/>	
<b>8.1 Introduction.....</b>	<b>117</b>
<b>8.2 Study sites .....</b>	<b>119</b>
<b>8.3 Instrumentation and methods.....</b>	<b>120</b>
8.3.1 Topographic data analysis .....	120
8.3.2 Seismic monitoring.....	122
8.3.3 Association of topographic and seismic data .....	122
8.3.4 Seismic data analysis .....	123
<b>8.4 Results .....</b>	<b>124</b>
8.4.1 Rockfall detection .....	124
8.4.1.1 Mount Granier.....	124
8.4.1.2 Mount Saint-Eynard.....	127
8.4.2 Characteristics of rockfall seismic signals .....	128
8.4.3 Volume estimation using rockfall seismic signals.....	129
8.4.3.1 Duration magnitude .....	130
8.4.3.2 Local magnitude .....	131
<b>8.5 Discussion .....</b>	<b>132</b>
<b>8.6 Conclusion .....</b>	<b>134</b>
<b>Part IV Outlook.....</b>	<b>137</b>
<b>9 Thermography of block impacts.....</b>	<b>141</b>
<hr/>	
<b>9.1 Thermographic monitoring of slope instabilities .....</b>	<b>141</b>
<b>9.2 Fundamentals of infrared Thermography.....</b>	<b>142</b>
<b>9.3 Thermography of impact prints.....</b>	<b>143</b>
9.3.1 Impacts characteristics.....	143
9.3.2 Results .....	144
<b>9.4 Trajectory benchmark .....</b>	<b>146</b>
9.4.1 Blocks dynamics and seismic monitoring.....	147
9.4.2 Thermography of blocks propagation .....	149
<b>9.5 Preliminary conclusions .....</b>	<b>151</b>

10	Development outlook .....	155
	Conclusions .....	157
	References .....	161
	Supplementary material.....	173
<hr/>		
	A.1 Equipment .....	175
	A.2 Survey design .....	175
	A.3 SfM processing.....	176
	A.4 Point clouds processing .....	176
	A.5 Split data tests .....	176
	B.1 Rockfalls catalogs .....	179
	B.2 Sensitivity analysis of parameters.....	180
	B.2.1 Distance error .....	180
	B.2.2 Seismic wave velocity error.....	182
	B.2.3 Frequency-dependence of the attenuation factor.....	182
	B.2.4 Body waves hypothesis .....	184



# Introduction

---

*Hox anno (563) mons validus Tauretunensis, in territorio Vallensi, ita subito ruit, ut castrum cui vicinus erat et vicos cum omnibus ibitem habitantibus oppressisset, et lacum [...], ita totum movit ut egressus utraqueripa, vicos antiquissimos cum hominibus et pecoribus vastasset ...*

In this year (563), the imposing mountain of Tauretunum, in the Valais territory, plunged so suddenly that it engulfed a fort that was close, as well as villages with all their inhabitants, and stirred so much the lake [...], which, emerged from both banks, it devastated very old villages with men and herds ... (Marius, Avenches Bishop, Marriaventicensis seu lausannensis episcopi Chronicon ... usque ad annum vulgaris aerae, 581)

*In ipsa nocte, circa partem primam noctis [...], mons quidam, durans in latum et longum per spatium leuce, translatus de loco suo [...], opprimens et atterens circa, villas et multas parrochias cum habitantibus ...*

The same night, before it was midnight [...] a mountain, which was no less than a league long and wide, moved and fell [...], burying and crushing about sixteen villages and a large number of parishes with their inhabitants ... (Etienne de Bourbon, Tractatus de diversis materiis predicabilibus, XIIIe century)

---

There is abundant historical testimony on dramatic mass wasting events such as landslide or rockfalls, and their consequences. Such events, characterized by volumes of several million cubic meters, remain exceptional. However, amongst mass wasting events, rockfalls remain the most unpredictable and the most frequent hazard in the alpine region. In some areas, such as Mount Saint-Eynard cliffs (Chartreuse Massif, French Alps), rockfalls  $> 1\text{m}^3$  occur every 6 days on average. Despite their limited size, rockfalls are extremely rapid and violent processes. They exhibit important damaging capability, which makes them the major cause of mass wasting event fatalities.

In a context of growing urbanization in mountainous regions, mass wasting events, such as landslide, rockfalls or debris flows, have an increasing impact on both human and material terms. It is not only urbanized areas that are at stake but also communication routes (roads, railways, etc.) with important socio-economic issues. In such context, mitigation measurements must be applied to reduce the hazard or the vulnerability of the elements at risk.

For risk management purposes, several crucial elements are to be assessed: what is the likelihood of an event of a given size? Where is it likely to go? With what energy? Uncertainties associated with the prediction of these elements make it difficult for

decision-makers to implement efficient stabilization and protection measures. To protect human lives or infrastructures without disrupting town development and economic activities, it is necessary to improve our knowledge about rock-fall processes and to compile exhaustive and unbiased rockfall catalogs.

In this work, we aim to develop methodologies to monitor and characterize diffuse rockfall events. This work was carried out in a main study area: Chartreuse massif (Isère, French Alps) and in particular two cliffs. Mount Saint-Eynard cliffs whose 7km long cliffs overlook a densely urbanized area (on average 300 inhabitants/km<sup>2</sup>) and Mount Granier cliffs renowned for their large rock avalanches of several thousand cubic meters (1248, 1953, 2016, 2017).

Rockfall detection is often carried out using remote sensing techniques such as terrestrial or airborne laser scanning. We used photogrammetry methods to acquire diachronic Digital Elevation Models (DEMs) of the cliffs. Such monitoring enables to carry out rockfall inventories and frequency estimation analysis. It also provides information on rockfall locations and failure configurations. However, due to significant time lags between surveys, these methods cannot constrain a precise time of occurrence. This limit prevents the retrieval of information on rockfall triggering mechanisms. Similarly, the dynamics of events (multiple failures from the same area or individual stages of an event, i.e., detachment, impact, propagation) cannot be determined.

The study of rockfall seismic signals provides a complementary solution to these shortcomings as it enables continuous monitoring of processes over a large area (several km<sup>2</sup>). Rockfalls seismology has been successfully used to detect and locate events. However, rockfall characterization using seismology is limited by the lack of knowledge on the relations between rockfall properties and the induced seismic signal. In this study, we have combined DEMs and seismic data at two cliffs, Mount Granier and Mount Saint-Eynard, in order to retrieve information on rockfall dynamics and characteristics. The interpretation of the seismic signals offers insights into event timing (whether the compartment collapsed in one piece or several, delays between failures) and rockfall properties (volume, free fall height, mass, blocks propagation ...).

Quantifying rockfall volume or energy from seismic energy remains however challenging. Many parameters may influence on the result (block volume, free-fall height, impacted slope, impacted materials...). Furthermore, characteristics of the seismic signal (duration and energy, frequency content, envelope shape) depend on the propagation mode (mass-flow, free-fall, sliding, bouncing...). In order to validate our observations on rockfall events, we carried out several controlled block releases. These experiments offered an opportunity to test how rockfall characteristics influence their induced seismic signal. It also allowed us to extrapolate results toward smaller scales.

This work has been carried out as part of a collaboration between the Institute of Earth Sciences (ISTerre) and the geotechnical engineering firm Geolithe.

# Structure and contents

This dissertation consists of four parts. The first part is devoted to the presentation of the state of knowledge in the field of mass wasting events and more precisely in the field of rockfall events. Loading and triggering mechanisms of rockfall events are briefly reviewed before presenting failure and propagation characteristics (Chapter 1). The concept of rockfall hazard is then defined along with several management measures for rockfall hazard (Chapter 2). Methods used to detect and monitor instabilities or rockfalls are discussed before presenting the motivation and relevance of this study (Chapter 3).

The second part introduces rockfall monitoring using photogrammetry. We first explore the implications of different methodologies (distance calculation methods, detection thresholds, etc.) for the creation of rockfall inventories (Chapter 4). We found that the number of events detected and their volumes show strong variations according to the adopted methodology, indicating a need for caution when interpreting rockfall inventories. Then, using diachronic photogrammetric monitoring of Mont Saint Eynard (Chartreuse, France), we studied the geometric properties of rockfall compartments and their failure configurations along with the structural analysis of the discontinuity families affecting the massif (Chapter 5).

The third part develops seismologic monitoring of rockfalls. We analyze rockfalls that occurred in limestone cliffs of the Chartreuse Massif (French Alps). These rockfalls were detected both by Terrestrial Laser Scanning or photogrammetry and by a local seismologic network. The combination of these methods allowed us to study relations between rockfall properties (location, volume, geometry, propagation) and the induced seismic signal. Characteristics of the seismic signal (duration and energy, frequency content, envelope shape) depend on the propagation mode (mass-flow, free-fall, sliding, bouncing...). Selecting events with the same propagation type provides a more accurate characterization of rockfall properties than when mixing different types of events. We first focus on events that experienced a free-fall after their detachment (Chapter 6). We analyze the first parts of the seismic signals corresponding to the detachment and first impact and found relations between seismic signal properties and rockfall potential energy, free-fall heights, and volumes. The relations identified for Mount Saint-Eynard rockfalls were then tested on different geological settings and for a larger range of volumes using Yosemite, Mount Granier rockfalls and with a dataset of controlled releases of blocks (Hibert et al., 2017). In order to further analyze seismic characteristics of block



impacts, we carried out controlled block releases (Chapter 7). A first dataset was obtained by releasing blocks (1 to 4m<sup>3</sup>), from heights ranging between 1 and 30m, on several protection embankment facings (granular platform, reinforced earth, concrete blocks). A second dataset was obtained by releasing a small block (2.9 kg), from heights ranging from 0.5m to 2m, on a tilted concrete block. The scaling law between seismic energy and kinetic energy obtained with these experiments agrees well with the one determined for rockfall events in Chapter 6. We then focus on mass-flow type events (Chapter 8). We analyze a series of rockfalls that occurred in 2016 at Mount Granier. By coupling DEMs and seismic records, we reconstructed this rockfall sequence with accurate timing and correct volume estimates. This also allowed us to find a scaling law between seismic energy of a rockfall and its volume.

In the fourth part, we present several perspectives on rockfall monitoring. We introduce the use of a thermographic camera (also called an infrared camera) for rockfall monitoring (Chapter 9). Using ambient infrared radiation we were able to qualitatively characterize block propagation. Finally, we present in Chapter 10 some perspectives on how this work can be further developed for rockfall monitoring.





## Part I

# Rockfall hazard: processes and issues



# 1 Slopes dynamics and weathering

*The earth surface is constantly reshaped by the combined actions of tectonic deformation and erosion. Erosion processes are hard to observe due to their extreme slowness or on the contrary to their sudden nature. Gravity-driven failures occur over a wide range of topographical settings and are reflected by a wide range of phenomena such as rockfalls, deep slope failures, shallow debris flows, and avalanches. These events are affected by various loading and triggering mechanisms. This chapter presents mass wasting event problems along with their characteristics.*

## 1.1 Slope instability

Slope morphology is the result of the combination of many factors: slope lithology and structure, climate, or anthropogenic activities. Mass movements, also called mass wasting events, refer to a variety of processes by which large masses of materials are moved by gravity. These movements affect mostly coastal areas and mountainous regions but can also be found under the oceans, or in the plains following mining activities for example.

Several classification methods exist depending on the propagation mode, the material involved, the movement velocity or its combination with other agents (water, snow, etc.). The classification most commonly used is the classification proposed by Cruden and Varnes (1996). This classification is based on the type of movement (falls, topples, slides, spreads, and flows) and on the type of material (i.e. rock, debris, and earth). This classification is presented in Figure 1.1. The main points are presented below.

A fall starts with the detachment of soil or rock from a steep slope along a surface on which little or no shear displacement takes place. The material then descends mainly through the air by falling, bouncing, or rolling. This movement type is always extremely rapid. Falls affect steep slopes and are commonly found in mountainous regions.

Topple movements are defined as a forward rotation out of the slope of a mass of soil or rock about a point or axis below the center of gravity of the displaced mass. Gravity is the main driver of this movement even though water and ice within cracks can exert pressure leading to topple. This process may be extremely slow or extremely rapid.

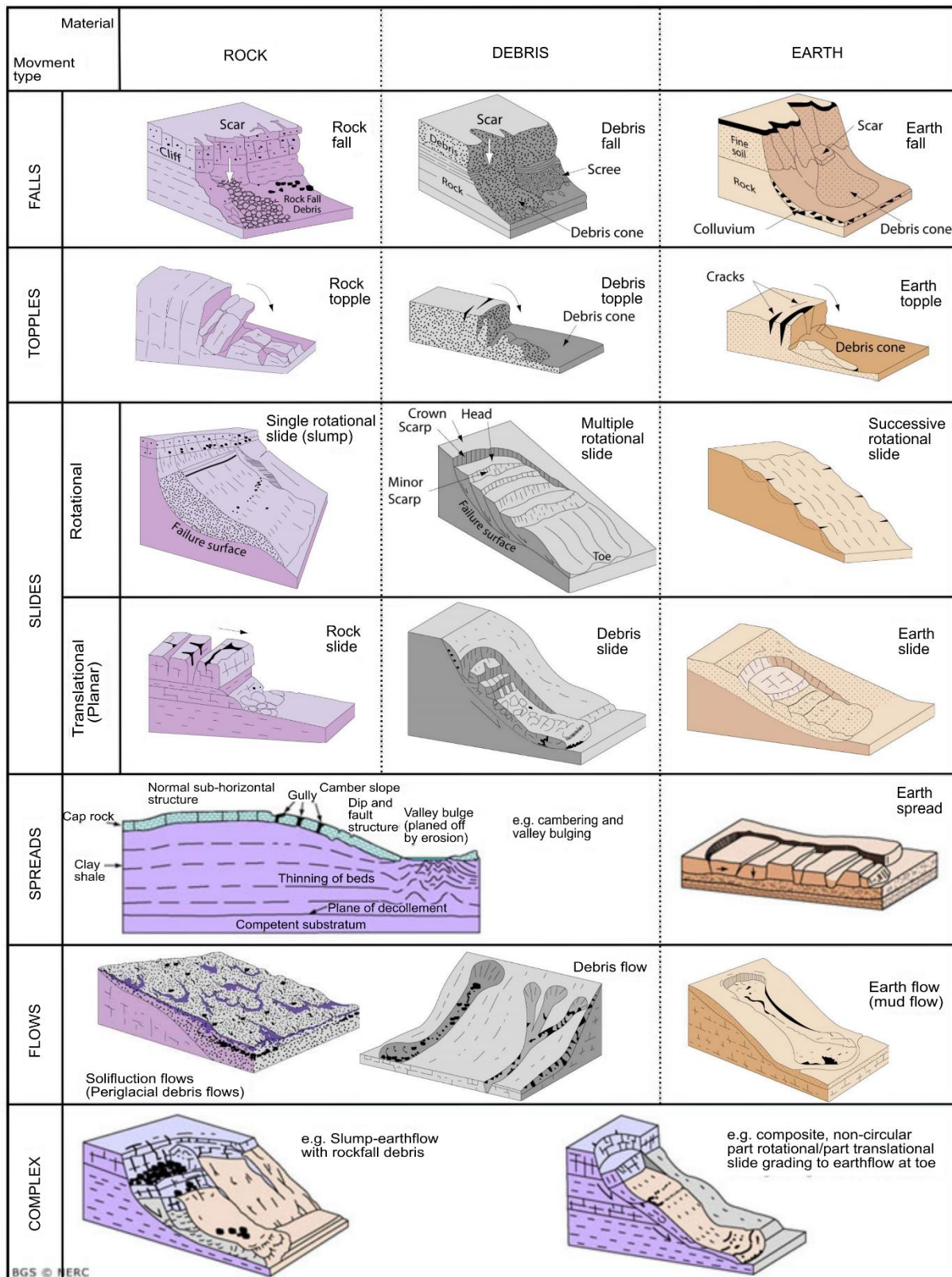


**Figure 1.1.** Landslide classification proposed by the British Geological Survey, based on the study of Cruden and Varnes (1996)

A slide is a downslope moving mass, occurring dominantly on surfaces of rupture or on relatively thin zones of intense shear strain. Several types of slides can be identified. Rotational slides are characterized by curved or concave rupture surface. Translational

slides are defined as mass displacements along a planar or undulating surface of rupture. This type of slide often occurs along a change of lithology or along a discontinuity. The velocity of movement is generally slow (a few cm to m per year) but it also may accelerate throughout the movement.

Spread is an extension of cohesive soil or rock mass combined with a general subsidence of the fractured mass of cohesive material into softer underlying material. These movements occur on gentle slopes and are rather slow with limited total displacement.

Flows are movements whose characteristics resemble those of a viscous liquid. Slides may evolve into flows depending on water content, mobility, and evolution of the slope.

The scale of mass movements is highly variable with events ranging from a few m<sup>3</sup> to events > 10<sup>6</sup> m<sup>3</sup> (Guzzetti et al., 2012). Movement velocity also ranges from a few mm per year to tens of m per second.

## 1.2 Rockfalls

Rockfalls represent only a small fraction of the mass wasting events. However, although they usually involve limited volumes, rockfalls are characterized by important mobility, high velocity and energy, making them a major cause of landslide fatalities (Guzzetti, 2000).

Rockfall is defined as a phenomenon during which a volume of rock detaches from a steep slope along discontinuities such as fractures, joints, and bedding planes, and moves down a steep slope by free-fall, bouncing, and rolling [paraphrased from Cruden and Varnes (1996)].

### 1.2.1 Rockfall failure and triggers

Slope stability is based on the ratio between movement resisting forces and driving forces. Resisting forces consist of shear strength, tensile strength, and compressive strength. These forces are related to rock properties and decline with time due to the influence of several physical processes such as physico-chemical alteration, subcritical crack, etc. Driving forces are principally controlled by gravity, even if other factors can accelerate or trigger the failure process. Failure occurs when either resisting forces decline until they are no longer superior to driving forces or when driving forces reach resisting forces (e.g. following an instability factor such as seismic waves, or freeze-thaw).

Cliff wear-off and rockfall occurrence can be triggered by many factors. These factors can be classified into two categories: intrinsic factors linked to the slope property and extrinsic factors favoring breakage through their degrading action.



Intrinsic factors include pre-existing discontinuity of fracturing whether at micrometric scale such as intercrystalline cracks or cleavage plane (Panet, 1976), or at a metric or kilometric scale: fault activity, fold hinges, change of lithography, etc. (Coe and Harp, 2007; Lim et al., 2010). Intrinsic factors are linked with the formation of the rock itself (Varnes, 1978). Physical properties of the rock material and all the subsequent events of crustal movement, erosion, and weathering, define the potential instability and its susceptibility to trigger influence.

Wieczorek (1996) defines a trigger as an external stimulus causing a near-immediate response by increasing the stress or by reducing the strength of slope materials. However, whereas some triggers indeed induce a nearly immediate response, others require a certain response time or minimum cumulative impact duration (Dietze et al., 2017b). Due to this response delay, and as trigger actions can overlap or have combined action, it is often difficult to associate rockfall occurrence with a specific trigger. Popescu (2002) differentiates triggers into two categories (**Erreur ! Source du renvoi introuvable.**).

- Preparatory factors, which make the slope susceptible to movement without actually initiating it. These factors affect the slope and set it into a marginally stable state.

- Triggering causal factors, which initiate movement. These factors shift the slope from a marginally stable to an actively unstable state.

Extrinsic factors are in number and variety. Earthquake and volcanic processes generate mechanical stress through inertial forces (Keefer, 1984; Yin et al., 2009). In some cases, magma rises and dome growth may lead to steeper and more unstable slope, leading to the generation of ash flows or rockfalls (Mueller et al., 2013).

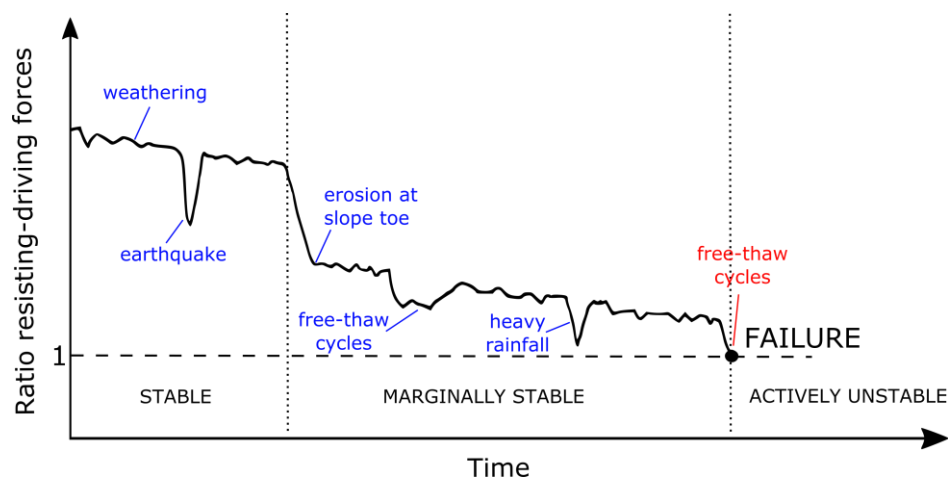


Figure 1.2. Variation of the ratio between resisting and driving forces through time (adapted from Popescu (2002)). In blue: preparatory factors, in red: triggering factor.

The influence of meteorological conditions has been highlighted in many studies. Precipitations affect slope stability in various ways. It can lead to erosion of cohesive fine material from cracks and dissolve rock compounds (Frayssines and Hantz, 2006; Stock

et al., 2013). It may also induce an increase of pore pressure and thus decrease cohesion (D'Amato et al., 2016; Dietze et al., 2017b; Matsuoka, 2019). Dietze et al. (2017), also observed a downward shift of rockfall activity likely driven by the lowering water table inside a limestone cliff.

Freeze-thaw transitions and permafrost have been increasingly linked to rockfall activities (Gruber and Haeberli, 2007; D'Amato et al., 2016; Dietze et al., 2017b; Matsuoka, 2019). Negative cooling induces rock contraction, which may result in crack propagation. However, with negative rock temperature, cracks may self-heal by freezing. During warming, a crack can propagate due to the expansion of ice. Moving water can progressively widen and deepen its passages in thawing rock (D'Amato et al., 2016; Gruber and Haeberli, 2007). Heat transition may also induce contraction and dilation of the rockfall mass leading to stress within the rock mass and crack propagation (Collins and Stock, 2016; Guerin et al., 2019).

Vegetation also undermines cliffs stability through the expansion of fractures by the root system. Dietze et al. (2017) note that vegetation may cause a local leverage effect through its interaction with the wind. They also suggest that wind may induce pressure fluctuations and thus cyclic stress. However, Matsuoka (2019) found that wind did not appear to be a key control for rockfall occurrence.

Rockfall can also be triggered by the traffic of animals or humans on loose rocks. Human activity can trigger rockfall occurrence through ground vibrations due to transport, construction or mining activities.

The 'detachment' (initial failure movement) can be considered as the moment from which the stability of a block is no longer assured, leading to the set in motion of this block.

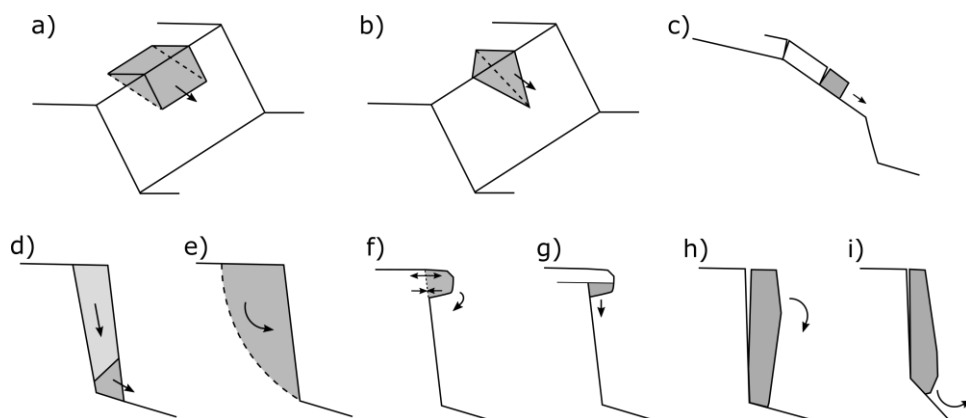


Figure 1.3. Rockfall failure mechanisms a) plane slide, b) wedge slide, c) slab failure, d) multiblock rotational slide, e) rotational slide, f) overhang topple, g) overhang failure, h) column topple, i) column foot failure. (adapted from Frayssines, 2005)

Rockfall failure may occur under several configurations (Figure 1.3). In most cases, the failure occurs by sliding or toppling, or by tensile, bending or buckling failure (Frayssines, 2005; Bourrier et al., 2013). Depending on the rock slope lithology and on

the fracture pattern within the rock mass, the detached compartment may remain in a single fragment, or in a less coherent block that may sooner or later disintegrate into several fragments (Cruden and Varnes, 1996; Bourrier et al., 2013).

### 1.2.2 Failure precursors

Rockfalls are often assumed as the sudden detachment of a rock mass from a cliff. However, several studies showed that progressive deformation of the slope could be detected before failure. Rockfall failure can be preceded by creep, progressive deformation, and extensive internal disruption of the slope (Terzaghi, 1950; Corominas et al., 2017).

In a brittle failure, three phases of time-dependent creep can be observed: transient creep for which strain rate is increasing (primary creep); steady-state for which strain rate remains constant (secondary); accelerating creep till failure (tertiary) (Varnes, 1978). Patterns of displacement evolution can be observed in the final stages (Varnes, 1978; Voight, 1989; Abellán et al., 2010; Royán et al., 2014).

Several studies detected occurrence of precursory phenomena, such as small rockfall increasing with time before a large failure event (Rosser et al., 2006; Suwa et al., 2008; Royán et al., 2014). The occurrence of such events demonstrates that strain accumulation is reflected not only through creep and displacement, but also through increased shedding of slope surface material via rockfall (Rosser et al., 2006). Rosser et al. (2007), Royán et al. (2014) or Kromer et al. (2015) observed that these events were essentially concentrated in the detachment zone and in the areas around the edges, particularly near the lower extent of the ultimate failure compartment.

Other precursors can be noted such as cracks opening or noises. In some cases, the detachment of a rockfall has been preceded by precursory seismic signals (Amitrano, 2005; Zeckra et al., 2015) or by a change in resonance frequency of prone-to-fall columns (Lévy et al., 2010; Valentin et al., 2017). These signals were interpreted as the result of rock bridge breakage and opening fractures.

Precursors are not observed for every rockfall. This lack of precursor can be interpreted in two ways. Either, no pre-failure deformation occurred, or it could not be detected due to limited sensitivity of the monitoring methods. The minimum detectable deformation may be higher than the pre-failure deformation, or the temporal duration of the deformation may be shorter than the monitoring sampling time (Abellán et al., 2010). Rockfall failure configurations might have an influence on the presence or absence of precursors. Overhang failure might be more sudden than column topple failure for which fracture openings can be more progressive.

### 1.2.3 Rockfall propagation

After its detachment, the blocks move down the slopes in different propagation modes (free-fall, bouncing, rolling or sliding). The propagation mode mainly depends on the slope gradient (Ritchie, 1963; Dorren, 2003) even if several other factors need to be considered to analyze rock trajectory (shape of the block, surface characteristics of the slope, broken slope features, etc.).

Free-fall propagation mode occurs on very steep slopes ( $>70\text{-}80^\circ$ , according to Ritchie (1963) and Dorren (2003)). If the slope gradient is lower than these angles, blocks will bounce along the cliff. Rebounds characteristics depend on material properties, such as energy restitution properties, angle between slopes and block trajectory, slope roughness (Hungr and Evans, 1988). After the free-fall impact or after the first bounces, blocks may break upon impact (Bozzolo and Pamini, 1986). On slopes below 45 degrees, bouncing blocks will tend to roll as the block gathers rotational momentum (Dorren, 2003). Rolling movements are characterized by very short bounces. A rolling rock is thus almost constantly in contact with the slope surface (Hungr and Evans, 1988). Sliding motion mainly occurs at small velocities and generally only occurs, when a block starts to move or comes to rest (Volkwein et al., 2011). Local steepening or slope breaks may induce a change of propagation mode of the blocks from sliding and rolling to free fall or bouncing (Hungr and Evans, 1988).

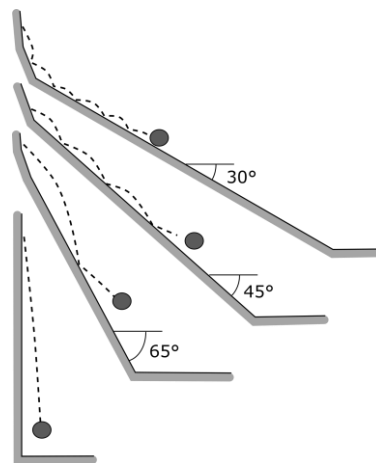


Figure 1.4. Propagation modes according to the slope gradient. Adapted from Ritchie (1963)

The word rockfall is usually used to describe small phenomena, (volume  $<100\text{ m}^3$ ). When dealing with higher volumes, the words rockslides ( $<10^6\text{ m}^3$ ) and rock avalanches ( $>10^6\text{ m}^3$ ) are often used (Dussauge-Peisser et al., 2002; Bourrier et al., 2013). Bourrier et al., (2013) proposed another classification based on the physical nature of the moving mass. They differentiate two distinct types of rockfall: fragmental rockfall and rock mass fall. Movement description aforementioned applies mainly to blocks independent of each other, and experiencing strong mechanical interaction only with the slope surface but not with each other. This type of event is defined as fragmental rockfall (Evans and Hungr,

1993; Bourrier et al., 2013). For some events, interaction between particles cannot be neglected. Such events are governed by the interaction between the moving fragments and become similar to a frictional fluid and are often highly mobile (Hungri et al., 2001; Bourrier et al., 2013). These events are defined as rock mass fall. This term is often used for very large rock failures (over  $10^6 \text{ m}^3$ ), this behavior can also concern smaller events. It is also possible for a fragmental rockfall to become a rock mass fall, as the block disintegrates along the path.

In this study, we will use the rockfall label without any volume distinction, or distinction in the failure mechanism.

## 2 Rockfall hazard in the Alps

*Rockfalls are one of the most common mass wasting event type in mountain areas. Despite usually involving limited size, rockfalls are extremely rapid processes that exhibit high kinetic energies and damaging capability. These characteristics make them a major cause of landslide fatalities. Even though they mostly take place in remote areas, they also threaten residential areas and transport corridors in many valleys of the Alps. Expansion of urbanized areas in hazardous regions have increased the impact of natural disasters in both human and material terms. To address this risk, mitigation measurements must be applied to reduce the hazard or the vulnerability of the elements at risk.*

### 2.1 Rockfall events in collective memory

Rockfalls are widespread phenomena in mountain ranges, coastal cliffs, volcanos, river banks, and slope cuts. The Alps are characterized by steep slopes and are strongly affected by rockfall hazard. Some events had a magnitude such that they became engraved in collective memory. Amongst such events is the Mount Granier landslide, one of the biggest landslides in Europe (500 million m<sup>3</sup>) (Goguel and Pachoud, 1972; Nicoud et al., 1999). In 1248, 25 million m<sup>3</sup> of limestone resting on marls slid into the valley,

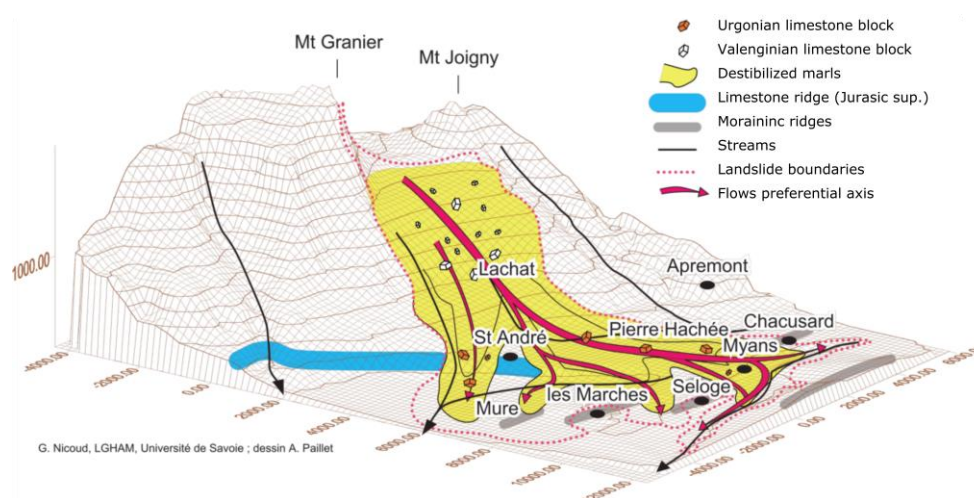


Figure 2.1. Reconstruction of the Mount Granier landslide deposit extent (Nicoud et al., 1999).

causing a massive landslide. The landslide consisted mostly of marl materials but also massive limestone blocks that were carried over several kilometers. The chronicles of a Benedictine monk described this event as a mud and stone flow, which covered the valley with a layer 10 to 40 meters thick, over a length of 9 kilometers (Figure 2.1). This event led to the death of several thousand people. Another significant event is the rockslide of Elm (Canton of Glarus, Switzerland) (Heim, 1932; Chowdhury et al., 2009). On September 11, 1881, 10 million m<sup>3</sup> of slate collapsed and traveled over 2 km. This event destroyed 90 hectares of land, killed 115 people and destroyed 83 buildings. Whereas Elm rockslide was partially caused by human activity (mining of slate), Mount Granier landslide was spontaneous and probably triggered by heavy rains.

Instability at Mont Granier remains high, with several large rockfalls observed during the 20<sup>th</sup> Century. In particular, a rockfall of approximately 500 000 m<sup>3</sup> occurred in 1953. More recently, a sequence of collapses occurred during the winter and spring 2016, with a large media impact (Hobléa et al., 2018). These events did not result in human or material damage. However, rockfall debris of spring 2016 were remobilized into debris flows that impaired the RD 285a county road during several weeks.

Such events remain rare. However, smaller rockfalls are a major and widespread hazard in mountainous terrain. Dussauge-Peisser et al. (2002) used a rockfall dataset from RTM Isère (1996) to estimate rockfall volume distribution over the Grenoble region (Isère, France). They found that a 100 m<sup>3</sup> event will likely happen every year. The Restauration des terrains en montagne (RTM) dataset is probably not exhaustive for rockfalls under 1000 m<sup>3</sup> and the return period of a 100 m<sup>3</sup> event is certainly shorter in the Grenoble region.

## 2.2 Socio-economic impact of rockfall hazard

It is difficult to assess the share of rockfall events in terms of socio-economic cost of mass-wasting events hazard. Most of the studies and datasets tend to gather all mass wasting events within a single category.

In 2009, slope movement susceptibility has been mapped over the metropolitan territory (Groupement d'intérêt scientifique sur les sols (France), 2011) (Figure 2.2a). Movement susceptibility is assessed using three factors: slope gradient and topology, lithology and land use. This map shows that the overall territory is affected to some extent to mass wasting hazard. Two areas are especially affected: Pyrenees and Alps regions. These areas are characterized by steep slopes favoring instabilities. In 2016, 2/3 of the Rhone-Alpes region municipalities were classified as exposed to a mass-wasting hazard and 20% of them were subject to PPR Mass Wasting events (Risk Prevention Plan based on French regulatory rule) (database GASPARE, Gestion Assistée des Procédures Administratives relatives aux Risques naturels et technologiques) (Figure 2.2b).



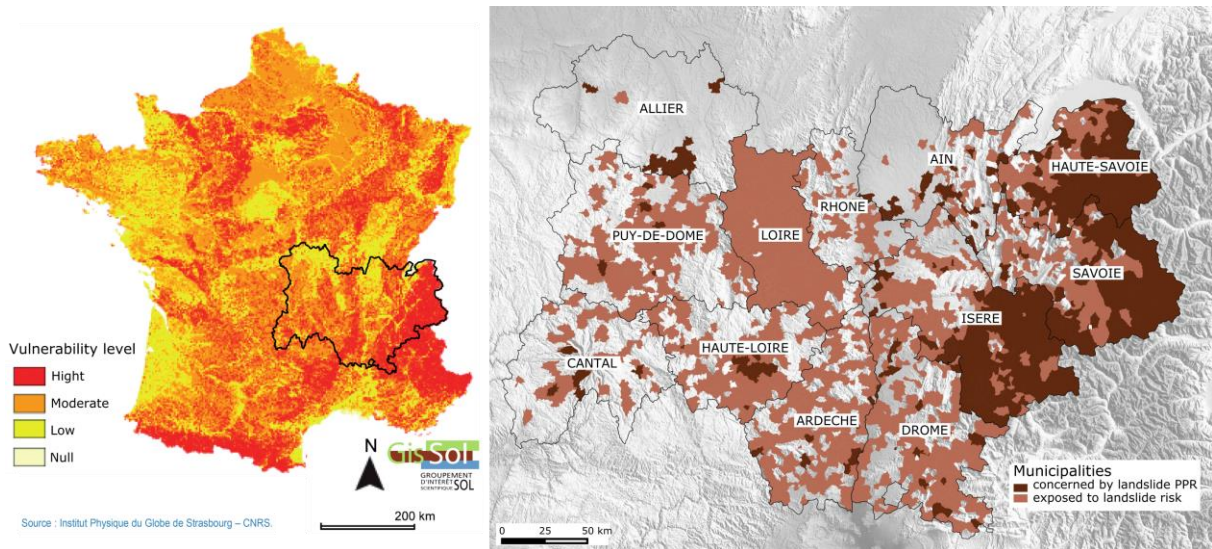


Figure 2.2. Slope movement susceptibility (Groupement d'intérêt scientifique sur les sols (France), 2011). b) Municipalities classified as exposed to a mass-wasting hazard and subject to PPR Mass Wasting events

Rockfalls constitute only a small fraction of landslides and do not represent the same level of economic risk as landslides. However, even having a limited size, rockfalls remain extremely rapid processes that exhibit high kinetic energies and damaging capability (Varnes, 1978; Corominas et al., 2017).

Even though they mostly take place in remote areas, they also threaten residential areas and transport corridors (Guzzetti, 2000; Corominas et al., 2005; Agliardi et al., 2009; Kromer et al., 2015). In some areas, rockfall events can be responsible for more than 80% of deaths and injuries related to mass wasting events (Guzzetti, 2000).

Rockfalls have high velocity and damaging capability. The kinetic energy of a block of  $1 \text{ m}^3$  falling from 10 m is equivalent of the energy of the car at 70 km/h,  $10 \text{ m}^3$  falling from 16 m is equivalent of the energy released by the explosion of 1 kg of dynamite (Ministère de l'écologie, du développement durable, et de l'énergie, 2014). When rockfalls impact infrastructures (buildings, communication routes, etc.), induced damage can range from partial damage to total destruction.

Economic impact induced by rockfalls can be split into two categories. Direct costs correspond to the repairs or maintenance of the buildings but also to the damages to facilities or properties impacted by the event. Indirect costs are difficult to quantify as they are related to the disruption of activities in the affected sector.

We can illustrate these costs with an example. In 2008, a rockfall of  $300 \text{ m}^3$  occurred in the Aspe valley (Pyrénées-Atlantiques). This rockfall blocked the road RN 134, in both directions, for 11 days (METL-MEDDE/DGPR, 2012). This road, linking France to Spain, had, at that time, a daily traffic slightly above 1000 vehicles, including 20% of heavy goods vehicles. Three villages and a ski-resort were isolated during this period. The cost of emergency work and safety work of the RN 134 amounted to 550 000 euros (direct cost). Several indirect costs can be listed. Personal of the ski resort of Somport



and a few employees of local industries were prevented from accessing to their working place. The ski resort and the villages were only accessible and supplied by Spain. The closure of two hotels and a drastic drop in town activity at Canfranc have been noted. About 40 college students were not able to access their school due to the interruption of school transport. Heavy goods vehicles coming from Spain had to make a detour of more than 200 km to arrive at Pau. This example illustrates well the panel of disruption that can be caused by a rockfall event.

Growing population and the expansion of settlements in hazardous areas have increased the impact of natural disasters in both human and material terms (CRED, 2019). Moreover, deforestation, change in land use, and climate change (precipitation rate and permafrost), will induce an increase in rockfall hazard.

## 2.3 Risk management

As settlements expand toward cliffs, inhabitants are increasingly exposed to rockfall hazard. As an example, over the last 50 years, the number of inhabitants of Lumbin (Isère, France) has increased from 400 to 2200 inhabitants (database EHESS/Cassini until 1999 then Insee) (Figure 2.3). Over the years, several protection embankments have been implemented. However, in 2002 a rockfall circumvented the protection embankments and impacted a house (Figure 2.3). Fortunately, none of the two inhabitants of the house were hurt. This example illustrates well the difficulty for authorities and decision-makers to assess correctly rockfall hazard and implement efficient mitigation measures. It also shows the necessity to improve our knowledge about rock-fall processes and overall to compile exhaustive and unbiased catalogs.

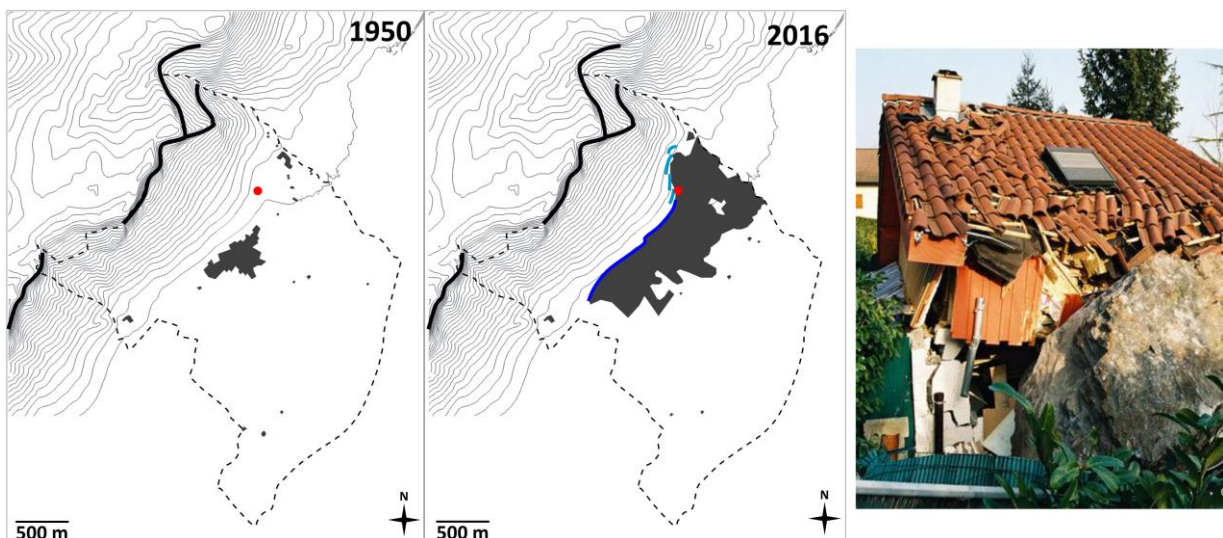


Figure 2.3. Evolution of the urban area of Lumbin (Isère, France) between a) 1950 and b) 2016 (according to aerial photographs). In black are represented cliffs likely releasing rockfalls. Red dot: 2002 rockfall event. Dark blue line: protection embankments prior to the rockfall., light blue line: embankments built following the 2002 rockfall occurrence. c) Photographs of the damage caused by the rockfall.

Rockfall hazard can be defined as probability that a specific location on a slope is reached by a rockfall of given intensity over a specified time interval (Volkwein et al., 2011).

$$H = P(H).P(S|H) \quad (2.1)$$

where  $P(H)$  is the annual probability of a rockfall event  $H$ . This probability is the product of two subsidiary probabilities: probability of detachment and probability of impact (linked to the block propagation).  $P(S|H)$  is the probability of spatial impact  $S$

Rockfall risk  $R$  (i.e. annual expected cost due to rockfall events) can be defined as (Dai et al., 2002; Agliardi et al., 2009):

$$R = P(H).P(S|H).V(P|S).Ve \quad (2.2)$$

$V(P|S)$  is the vulnerability of the element (proportion of property value lost  $P$ ),  $Ve$  is the value of the element at risk.

When rockfalls interact with people, buildings or infrastructures, mitigation measurements should be applied to reduce the hazard, elements at risk and/or vulnerability of the element at risk.

Authorities and decision-makers are increasingly reluctant to invest money in structural measures that can reduce natural risks (Guzzetti, 2000). To protect human lives and infrastructures without hampering town development and economic activities, several approaches have been developed. The main approach consists in the implementation of a risk prevention plan (Plan de Prévention des Risques Naturels, PPRN) and town planning (Plans Locaux d'Urbanisme, PLU) taking into account natural hazards.

PPRN legislation defines two area categories: areas exposed to hazard and areas not directly exposed to risks but for which measures can be planned to avoid aggravating the risk. Depending on the level of hazard, regulations distinguish three types:

- when the level of hazard is high the general rule is the prohibition to build,
- when the risk level is average, only projects, subject to prescriptions adapted to the type of stake, are allowed,
- when areas are not directly exposed to risks but where constructions, or agricultural, commercial or industrial exploitations could aggravate risks or provoke new ones.

When space is scarce, communities seek to exploit all available space, consequently, technical solutions must be searched to prevent or limit the consequence of an event (Corominas et al., 2005) (Figure 2.4). Several technical solutions exist and can be separated into two categories: active parades (stabilization through nailing, concrete wall, or net, etc.) and passive parades (protection embankments, passive nets, etc.). Warning systems can be implemented to enable the evacuation of an area or to block a transportation route.

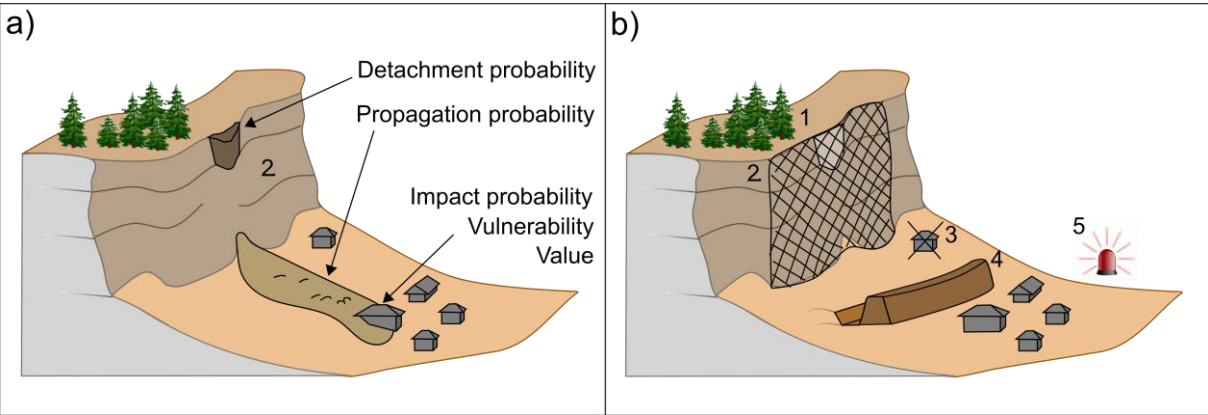


Figure 2.4. a) Schematic diagram of the risk analysis. b) Examples of mitigation measures: 1. blast of instables compartments, 2. protective net, 3. prohibition to build (PPRN, PLU), 4. protection embankments, 5. warning systems

## 3 Rockfall monitoring techniques

*Defining rockfall trajectories, return periods, and failure locations are of primary importance to support decision making and to enable appropriate remediation actions. Land-use planning and mitigation measures require an appropriate analysis of the rockfall hazard. Several approaches have been developed to detect and monitor instabilities or rockfalls. These techniques provide different characterization of the phenomenon: continuous or punctual monitoring, large area or reduced sections, surface or subsurface monitoring, etc. We present here the main techniques related to rockfall monitoring with a particular focus on the techniques used in this study. Limitations and the challenges of rockfall monitoring are discussed before presenting the goals of this study.*

### 3.1 Field study and cartography

Field studies allow an understanding of the rock slope and provides information on its morphology, petrography, and sedimentology. The main objective of such campaigns is to seek instability factors and to identify potentially unstable compartments.

Structural analysis can be carried out in order to retrieve information on the presence of faults, fractures, stratification orientation or other discontinuities. Presence of water, karstic galleries, leaking cracks are important indicators due to their ability to trigger rockfalls. Complementary information can be brought by map databases (BRGM, Bureau de Recherches Géologiques et Minières; IGN, Institut national de l'information géographique et forestière), such as geology, topography, hydrology, or hazard-prone areas (PPRN, Plan de Prévention des Risques Naturels).

Rockfall inventories can be retrieved from several databases (BD MVT from BRGM; georisques from the ONRN, Observatoire National des Risques Naturels). These inventories provide information on previous rockfalls, and occasionally their failure configuration or likely triggers.

Information brought by this kind of study enables the assessment of the slope sensitivity to rockfall occurrence and potential rockfall triggers. However, measures and collected data often exist in insufficient numbers and may rely on incomplete datasets. They are thus not adequate for statistical purposes or to reliably assess rockfall hazard.

Some projects such as the Multidisciplinary Observatory of Versant Instabilities (OMIV), of which Chartreuse cliffs observatory (Mount Saint-Eynard, Mount Granier) is part, aim to associate rockfall catalogs to cliff monitoring (DEMs, seismology, weather monitoring, etc.). The purpose of this project is to provide free open data sets close to real time in order to better understand mass wasting events dynamics.

### **3.2 Displacement measurement methods**

If a threatening compartment is identified, instruments can be installed for continuous monitoring of the compartment movements, e.g. extensometers, inclinometer. Data can be retrieved either manually or be transmitted to an alert center. These instruments record the movement rate of the unstable compartment. In case of rapid or unusual increase of movement, a hazard warning can be triggered (Wieczorek and Snyder, 2009; Walter et al., 2012; Bottelin et al., 2014).

One widely used method for landslide monitoring is GNSS displacement monitoring as it allows very accurate and high frequency temporal observations. For cliff monitoring, GNSS may be used to monitor an unstable compartment or be used as roving capture of cliff-top or cliff-base topography (Mills et al., 2005). Its main drawbacks for cliffs monitoring consist in the potential access difficulty, in the topographic occlusion which can affect signal quality and thus survey accuracy, and its elevated cost.

Displacement monitoring can also be carried out by total stations (Janeras et al., 2017). Measurement of distance is accomplished by the emission of a modulated infrared signal reflected on a prism reflector positioned on the monitored object. Similar results can be carried out using RFID (Radio Frequency Identification). By setting an RFID tag on an unstable compartment, the reader unit and RFID tag provide a displacement measurement through the emission and backscatter of a radio-frequency wave (Yan and Chai, 2017; Le Breton et al., 2019).

### **3.3 Geophysical methods**

Geophysics are based on the acquisition of physical measurements from which physical parameters of the subsurface can be deduced. These techniques are non-invasive. They provide information on the internal structure of the rock mass, and allow the investigation over a large volume. Several techniques exist according to the signal measured: seismology (seismic waves), electrical methods (resistivity and spontaneous-potential), Ground Penetrating Radar (electromagnetic radiation), gravimetry (gravitational field).

Two types of geophysical methods can be distinguished: active and passive. Active geophysical methods are used to determine physical properties of the materials or

lithological changes (layering, tectonic contact, fractures). They rely on an active signal injected into the ground. The reflected or refracted signals provide information from subsurface structures. Geophysical time-lapse surveys can be implemented in order to monitor the evolution of the slope property such as water content or fracture openings (Lebourg et al., 2005; Krautblatter and Hauck, 2007).

Passive geophysical methods measure naturally occurring fields or properties of the earth. For rockfall monitoring, seismology is mainly represented. Passive seismic monitoring splits into two fields. The first deals with the modification of wave propagation in the soil due to external environment processes, including hydro-meteorological phenomena, thermal evolution, and erosion processes (Larose et al., 2015). Recent studies showed that seismic noise properties (resonance frequencies, polarization, and spectral ratio amplitudes) allow the characterization of unstable rock masses (Lévy et al., 2010; Moore et al., 2011; Bottelin et al., 2013; Valentin et al., 2017). This field of application suits for monitoring unstable mass and ultimately its failure detection. It allows the monitoring of a small area (several tens of meters) and requires the prior identification of the instability.

The second field of passive seismic monitoring aims to analyze seismic signals induced by external phenomena such as wind, storms, icequakes, fluvial discharge, or mass wasting events (landslide, rockfall, etc.) (Deparis et al., 2008; Ebeling and Stein, 2011; Díaz et al., 2014; Allstadt and Malone, 2014). This field of application enables the detection of events occurrence and infrequently its precursors (Amitrano et al., 2005; Walter et al., 2012; Zeckra et al., 2015). Depending on the elastic energy emitted by the source, events can be monitored over large distances (tens of kilometers). In this study, we used seismic networks to detect and characterize rockfalls.

### 3.4 Remote sensing techniques

Remote sensing methods provide information about a phenomenon without making physical contact with this object. Among remote sensing techniques, Very High-Resolution satellite imagery (VHR) and Interferometric Synthetic Aperture Radar (InSAR) imagery represent very effective tools for landslide monitoring (Hooper et al., 2004; Riedel and Walther, 2008). However, these spaceborne tools do not match the spatial and temporal detail required for rockfall monitoring.

Ground-based temporal correlation imagery provides 2D displacement fields and pattern detection (e.g. rockfall occurrence, (Chanut et al., 2011)). However, the quality and accuracy of this technique depend on photograph quality. The size of the monitored area is directly dependent on the distance to the monitored object, the used camera lens, and on the required precision of measurement. A precise measure of displacement often requires to focus on a restricted area. Obviously, this monitoring method can only

function during day time and is strongly influenced by the weather (sun inducing strong shades, rain, fog, etc.).

Infrared Thermography (IRT) provides a surface temperature map of the investigated object. Temporal evolution and local radiant temperature differing from the temperature of surrounding areas enable the detection of thermal anomalies within the investigated object. Thermal anomalies can be induced by the presence of structural discontinuities (open fractures, exfoliation sheets, damaged rock), (Frodella et al., 2014; Mineo et al., 2015; Guerin et al., 2019) or moisture and seepage zones (Barla et al., 2016). Mueller et al. (2013) were able to detect rockfall occurrence due to the temperature anomaly left by blocks propagation in the slope.

Table 3.1. Rockfall monitoring methods

Dimension	Method	Physical principle	Range	Accuracy <sup>(a)</sup>	Sampling period <sup>(b)</sup>	Monitoring <sup>(c)</sup>	Reference
1D	Extensometer	Mechanical	<100m	1cm	<1s	Nucleation	Angeli et al., 2000
1D	Total stations	Optical	2km	0.5cm	10s	Nucleation	Janeras et al., 2017; Artese and Perrelli, 2018
1D	RFID	Radio	<100m	1cm	<1s	Nucleation	Le Breton et al., 2019
2D	Optical image correlation	Optical	500 m	1-5 cm	Hours	Events occurrence	Chanut et al., 2011; Travelletti et al., 2012
2D	IR	Optical	< 1km	0.01-1m	Hours	Nucleation	Mueller et al., 2013 ; Guerin et al., 2019
3D	GNSS	Radio	1 km	0.1-1 cm	<1s	Nucleation	Benoit et al 2015; Bellone et al. 2016
3D	GB-SAR	Radio	0.03-5 km	< 0.1cm	1 min	Nucleation	Frodella et al., 2016; Janeras et al., 2017; Carlà et al., 2019
3D	LiDAR	Optical	1 km	1 cm	10 min - year	Events occurrence	Williams et al., 2018
3D	Photogrammetry	Optical	500m	1-5cm	Daily	Events occurrence	Kromer et al., 2019
/	Active geophysics	Seismic waves	500m	/	Daily	Nucleation	Lebourg et al., 2005; Krautblatter and Hauck, 2007
/	Seismology monitoring	Seismic waves	1–100 km <sup>(d)</sup>	/	<1s	Events occurrence	Hibert et al., 2011; Dietze et al., 2017; Fuchs et al., 2018

(a) and (b) value commonly found in literature data

(c) Commonly monitored object using the listed methods

(d) Detection range depends on the event magnitude

Ground-Based Interferometric Synthetic Aperture Radar (GBInSAR) technique consists of a radar sensor emitting and receiving bursts of microwaves while moving along a rail track (Leva et al., 2003). Measures are based on Synthetic Aperture Radar (SAR) technique which provides the amplitude and phase of the received radar signal. By calculating the phase difference between two measurements, it is possible to compute the displacement of the SAR image pixels. Its high sensitivity to small deformations and long-range measurements makes GBInSAR well adapted to rockfall failure monitoring (Monserrat et al., 2014).

LiDAR (Light Detection and Ranging) provides high-resolution 3D models of the surveyed rock mass surfaces (Digital Elevation Models, DEM). It consists of a transmitter/receiver of infrared laser pulses. The laser beam is directly reflected on the land surface, distance measurement is based on the time-of-flight of the laser pulse. Its high accuracy makes LiDAR well adapted to rockfall detection even with limited volume ( $<1\text{m}^3$ ) (Abellán et al., 2010; Dewez et al., 2013; Kuhn and Prüfer, 2014). Similar results can be obtained using photogrammetry. Photogrammetry is a 3-dimensional coordinate measuring technique based on the analysis of photographs. By taking photographs at different locations, it is possible to calculate the position of the points of interest by triangulation (Firpo et al., 2011; Westoby et al., 2012; Kromer et al., 2019). Photogrammetric surveys are slightly less accurate than LiDAR surveys (Westoby et al., 2012; Kromer et al., 2019). Their accuracy mainly depends on the photograph quality and pixel resolution. The wider the survey coverage is, the less accurate the survey will be. In contrast, LiDAR accuracy remains rather constant independently of the size of the survey coverage. Nevertheless, photogrammetric surveys, present significant advantages in terms of mobility, cost and monitored area extent.

## **3.5 Limitations and challenges**

### **3.5.1 Widespread hazard monitoring using remote sensing techniques**

A rockfall hazard assessment should ideally predict where and when a slope failure is likely to occur (Guzzetti et al., 2004). Rockfall prediction requires detailed monitoring of the slope, which is often not possible due to the lack of scientific expertise and insufficient budgets (Wieczorek and Snyder, 2009). In addition, this kind of monitoring requires intensive examination and often involves a small area down to a single unstable block. Several methods serve well this purpose (in-situ methods, modification of wave propagation monitoring using passive seismology, GBInSAR). These techniques provide a real or near real-time hazard monitoring. However, most of these techniques enable the monitoring of only one or a few punctual points (in situ-methods) and may require installation interventions in remote and potentially dangerous locations. Large-zone monitoring techniques, such as GBInSAR, have a high station cost (50-100 k€), which



restricts their use in standard applications. Due to their short range, all these methods require prior identification of unstable compartments and allow the monitoring of a small area (up to several tens of meters). These techniques are thus not suitable to monitor widespread events which concern us in this study.

LiDAR and photogrammetric surveys are well adapted to monitor large areas (>1km) and enable to carry out rockfall inventories and frequency estimation analysis. These methods have limitations, as they often require manual data analysis, which makes them rather time-consuming methods. Surveys are thus often spaced by a few weeks or months. Time lags between surveys prevent the retrieval of information on rockfall triggering mechanisms or event dynamics. In order to reduce the time lapse between surveys, several studies implemented automated survey processes (Williams et al., 2018; Kromer et al., 2019). Such systems allow to study rockfall pre-failure deformation and magnitude frequency relationships. However, they require the immobilization of laser scanners or several cameras to provide photogrammetric monitoring. Since this monitoring depends on the view angle, irregular surface with sharp changes of orientation may generate occlusion patterns. Complex areas with presence of spurs and recesses necessitate the multiplication of viewpoints. Areas monitored by these systems require to be relatively planar in order to avoid occlusion patterns.

### **3.5.2 Seismic monitoring of rockfall occurrence**

The study of seismic signals emitted by rockfalls provides a complementary solution to these shortcomings as it enables continuous monitoring of the processes over a large area (several km<sup>2</sup>). However, this approach is predominantly limited by the lack of knowledge on the relations between rockfall properties and the induced seismic signal and by the difficulty related to even location.

One of the first detailed studies on landslide characterization using seismograms was reported by Kanamori and Given (1982). They interpreted the long-period seismic signal, recorded over a large seismic network, in terms of the  $2.5 \times 10^9$  m<sup>3</sup> landslide which occurred on the north slope of Mount St. Helens. Berrocal et al. (1978) and Weichert et al. (1994) also studied seismic signals induced by large failure events (Mantaro landslide,  $1.3 \times 10^9$  m<sup>3</sup>; Brenda Mine collapse,  $2 \times 10^6$  m<sup>3</sup>; Hope rockslides  $47 \times 10^6$  m<sup>3</sup>). These studies found that energy conversion, from potential to seismic energy, was rather low ( $10^{-6}$ - $10^{-4}$ ). Such events involve an important amount of dissipated energy. They were recorded by seismographs at distances up to several thousand kilometers. However, rockfall events generally involve smaller volumes and energy. With the densification of seismological networks, several studies have detected rockfall events of volumes ranging from  $10^3$  to  $10^6$  m<sup>3</sup> (Deparis et al., 2008; Dammeier et al., 2011; Manconi et al., 2016; Fuchs et al., 2018).

Several areas have been particularly monitored with local seismic networks. These networks, composed of several seismometers, spaced from a few hundred meters, enable the detection of events smaller than  $1 \text{ m}^3$  (Helmstetter and Garambois, 2010; Hibert et al., 2011; Lévy et al., 2015; Dietze et al., 2017), (Séchilienne rockslide, French Alps; Dolomieu crater, Réunion Island; Montserrat; Lauterbrunnen Valley, the Swiss Alps; etc.). Most of these studies aimed at monitoring or locating rockfall activity (Helmstetter and Garambois, 2010; Lévy et al., 2015; Dietze et al., 2017; Fuchs et al., 2018). Others strived to characterize rockfall events (volumes, velocity, energy, run out distance, etc.) (Deparis et al., 2008; Dammeier et al., 2011; Hibert et al., 2011; Manconi et al., 2016).

Deparis et al. (2008) found that signal duration was roughly correlated with the potential energy and the runout distance, while Manconi et al. (2016) proposed a relation between duration magnitude and rockfall volume. Dammeier et al. (2011) used multivariate linear regressions combining duration, peak envelope velocity, and envelope area and found a good correlation with rockfalls volume and potential energy. Finally, Fuchs et al. (2018) proposed relationships between rockfall or rockslide volumes, and local magnitude. In these studies, rockfall volumes are rather large (between  $10^3$  and  $10^7 \text{ m}^3$ ) and the signals recorded by regional networks are strongly affected and filtered by the distance between events and stations.

Rockfall characterization using seismology is often limited by the lack of validation using independent data. To fill this gap several controlled laboratory experiments or large scale controlled block releases have been carried out (Farin et al., 2015; Hibert et al., 2017; Saló et al., 2018; Bachelet et al., 2018, etc.). These experiments provide insights on the relations between rockfall properties and rockfall seismic signals.

Controlled releases of single blocks in a marl gully (Hibert et al., 2017) or in quarries (Saló et al., 2018) explored seismic amplitude and energy in relation to the kinematics of block impacts. Hibert et al. (2017) inferred single block mass and velocity from local seismic records. Farin et al. (2015) developed scaling laws relating characteristics of the seismic signal generated by an impact to the impactor mass and speed. These experiments were carried out under tightly controlled experimental conditions and do not entirely reflect the complexity of natural rockfall events.

### 3.5.3 Need for multi-method monitoring

In this study we aim to develop methods to improve rockfall detection and characterization. We used DEMs to detect rockfalls and retrieve their location, geometries and distributions. However, this method cannot provide temporal constraints.

Combining DEMs and seismic signal analysis provides essential and complementary information on rockfall dynamics and characteristics. Monitoring rockfalls using photographic time-lapse surveys and 3D reconstructions provides information such as

volume, geometry, location, detachment mode, etc. with relatively high accuracy. The interpretation of the seismic signals offers insights into event timing: whether the compartment collapsed in one piece or several, delays between failures, propagation duration. Signal amplitude and energy can provide information on the event volume or energy.

In this study we have coupled LiDAR or photogrammetric monitoring with a seismic monitoring at two cliffs, Mount Granier and Mount Saint-Eynard. This combined monitoring allowed us to yield numerous pieces of information on natural rockfalls onto complex topography. It allowed us to interpret rockfall seismic signals and to better understand the relations between block propagation and the induced seismic signal.

Characteristics of the seismic signal (duration and energy, frequency content, envelope shape) depend on the propagation mode (mass-flow, free-fall, sliding, bouncing...). Finding common relations between seismic signals and source properties for all types of rockfalls is therefore very challenging. In order to validate our observations, we carried out several controlled block releases.

## Part II

# Rockfalls detection and characterization using DEMs



---

*In recent years, rapid progress in geomatics technics, LiDAR and soft-copy photogrammetry have revolutionized geomorphological terrain analysis. The quality of Digital Elevation Models (DEMs) has been significantly enhanced, improving their spatial range, resolution, and accuracy. LiDAR and photogrammetry have been extensively used to monitor and quantify geological processes such as rockfalls, erosion processes or landslides. If some DEMs used in this study were acquired by Terrestrial Laser Scanning (DEMs before 2016, D'Amato et al. 2016), we mainly use photogrammetry to monitor cliff erosion.*

*In this part, we aim to analyze rockfall inventories obtained by diachronic comparison of DEMs. We first explore the implications of different methodologies (distance calculation methods, detection thresholds, etc.) for the creation of rockfall inventories (Chapter 4). Then, using diachronic photogrammetric monitoring of Mount Saint Eynard (Chartreuse, French Alps), we studied the geometric property of rockfalls compartments and their failure configurations along with the structural analysis of the discontinuities families affecting the massif (Chapter 5).*

---



## 4 Methodological biases on rockfall inventories and empirical volume distributions

*Rockfall hazard management requires the assessment of rockfall occurrence. Digital Elevation Models (DEM) are nowadays extensively used to monitor and quantify mass wasting processes. However, methodological and instrumental practices have a strong influence on the rockfall inventories. We examine the influence of the distance measurement methods and of the detection threshold for the creation of rockfall inventories. We compare several 2D, 2.5D and 3D methods of change detection using a DEM data set of the Mount Saint-Eynard cliffs (Chartreuse massif, French Alps). We also analyze the influence of the projection angle in case of 2D and 2.5D inventories. The number of detected events and their volumes show strong variations according to the adopted methodology. Discrepancies are found in both annual recession rate and rockfall volume distributions.*

### 4.1 Introduction

Rockfall hazard is significant in mountainous regions where steep rock slopes are found. This risk is especially high in some valleys of the Alps due to the high building density at cliff's foot. Knowledge of rockfall volumes frequency is needed for risk management and for the design of rockfall protections. Uncertainties associated with the prediction of the size and frequency of the potential events, make it difficult for decision-makers to implement efficient stabilization and protection measures. To protect human lives or infrastructures without disrupting town development and economic activities, it is necessary to better understand the cliffs erosion and to obtain reliable catalogs.

For risk management purposes, one of the most important questions to answer is what the likelihood of an event of a given size is. In several natural hazard fields, probability distribution functions have been proposed, based on the statistical analysis of historical events. For instance, earthquake energy distribution is usually described as a power law (Gutenberg and Richter, 1949). More recently, power-law distribution has been applied to landslides, to fit the distribution of landslide surfaces (e.g. Hovius et al., 1997; Stark and Hovius, 2001) or the volume distribution of rockfalls from limited homogeneous areas (Hungri et al., 1999; Dussauge-Peisser et al., 2002). The number  $N$  of



rockfalls larger than a volume  $V$  occurring in a given cliff during an investigation period is modeled by

$$N = aV^{-b} \quad (4.1)$$

where  $a$  and  $b$  are empirical constants. The parameter  $b$  controls the proportion between small and large events.

In recent years, due to rapid progress in geomatic technology, digital elevation modeling and geomorphological terrain analysis have been transformed. Airborne and more recently LiDAR and soft-copy photogrammetry, have revolutionized the quality of Digital Elevation Models (DEMs), improving their spatial range, resolution, and accuracy. In this context, DEMs' have been extensively used to monitor and quantify geological processes such as rockfalls (Abellán et al., 2010), erosion processes (Lim et al., 2010; Loye et al., 2012; Dewez et al., 2013), and landslides (Monserrat and Crosetto, 2008; Oppikofer et al., 2009). Thanks to these tools, the rockfall volume distribution has been studied over a large number of sites (Rosser et al., 2006; Dewez et al., 2013; Benjamin et al., 2016, amongst others). The empirical estimation of rockfall distribution provides the return period of rockfalls according to their size (Dewez et al., 2013; Rosser et al., 2006). It is thus often used for risk zoning and risk management (Guzzetti et al., 2003; Dewez et al., 2013; Farvacque et al., 2019).

However, so far few studies have investigated how methodological and instrumental practices influence the rockfall volume distribution (Benjamin et al., 2016). In this paper, we test the influence of the distance measurement methods and of the detection threshold on the volume distribution. This study focuses on the Mount Saint-Eynard, a 7 kilometers long limestone cliff in the Chartreuse massif (French Alps). The south of the cliff (3km) has been monitored by Structure from Motion (SfM) surveys since 2016. More than 1000 rockfalls have been detected in 3 years.

We first process a single DEM dataset using different distance measurement methods (2D, 2.5D and 3D) in order to compare the provided inventories. We also apply various detection thresholds and projection angles in order to analyze their influence on the rockfall inventories.

In this work, the term “rockfall” describes all events with a rock mass detaching and propagating on a steep slope, regardless of volume, dynamics or failure mode.

## 4.2 Study area

Our study area is located in the sedimentary cover of the External Crystalline Massifs of the French Western Alps (Belledonne, Mont Blanc, etc.) (Figure 4.1). These ranges are made of limestone and marls from the upper Jurassic and Cretaceous age. Valley walls consist of a succession of steep calcareous cliffs and marly slopes, between 200 m and 2000 m in elevation.

Mount Saint Eynard is located North East of Grenoble, Isère, French Alps. It is a long doubled cliff making up the western border of the Isère Valley and the oriental edge of the Chartreuse Massif. It peaks at 1308 m ASL. Its global morphology consists of two 7 km long subvertical cliffs dipping southeast (Figure 4.1). The lower cliff (240 m high) is separated from the 120 m high upper cliff by a forested ledge. The upper cliff consists of massive limestone of the Tithonian stage. The lower cliff consists of fractured thin-bedded limestone, of the Sequanian stage. The southern part of Mount Saint-Eynard cliffs has been monitored by photogrammetric surveys since 2015.

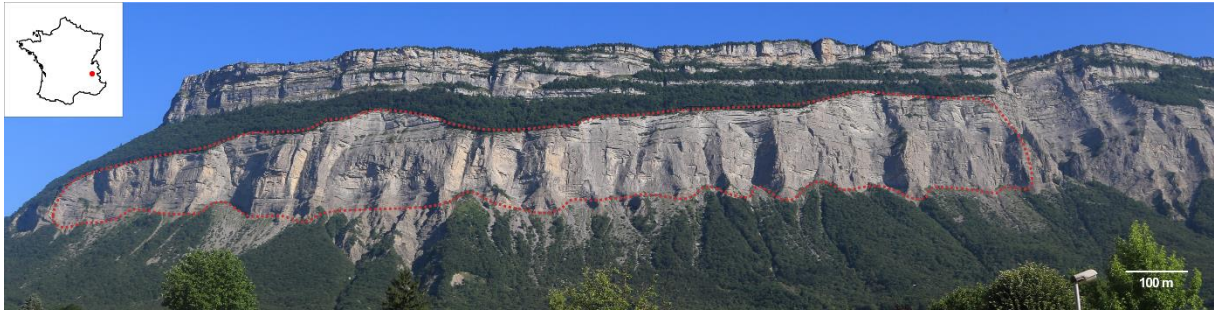


Figure 4.1. Photograph of the Mount Saint-Eynard cliffs. Red line: monitored area

### 4.3 Distance measurement methods

Rockfall volumes can be easily measured by computing the distance between DEMs obtained before and after a rockfall event (Abellán et al., 2010; Deline et al., 2011). Several methods have been developed to measure the distance between two DEMs, using either rasterized (2D) or 3D point clouds (see Figure 4.2).

#### 4.3.1 2D DEMs

The most straightforward method to quantify volumetric change between two DEMs can be achieved by differencing two rasterized point clouds as in Figure 4.2a (Adams and Chandler, 2002; Young, 2015; Benjamin et al., 2016). The mesh of the 2D grid, controlled by the density of the point clouds, imposes a limit on the level of detail that can be observed. Distance measurement uncertainties are related to point clouds registration, data quality and point cloud roughness (Wheaton et al., 2009; Schürch et al., 2001; Lague et al., 2013). This method is relatively simple, fast and can be easily automated. However, it implies a measure of topography changes in one dimension only. Since distance measurement depends on the view angle, irregular surfaces with sharp changes of orientation may generate occlusion patterns. This can significantly influence the distance measurement between two DEMs and be a source of error.

To avoid this kind of bias, it is possible to measure the distance between two 3D point clouds. Several methods have been developed to operate in a 3D coordinate system.

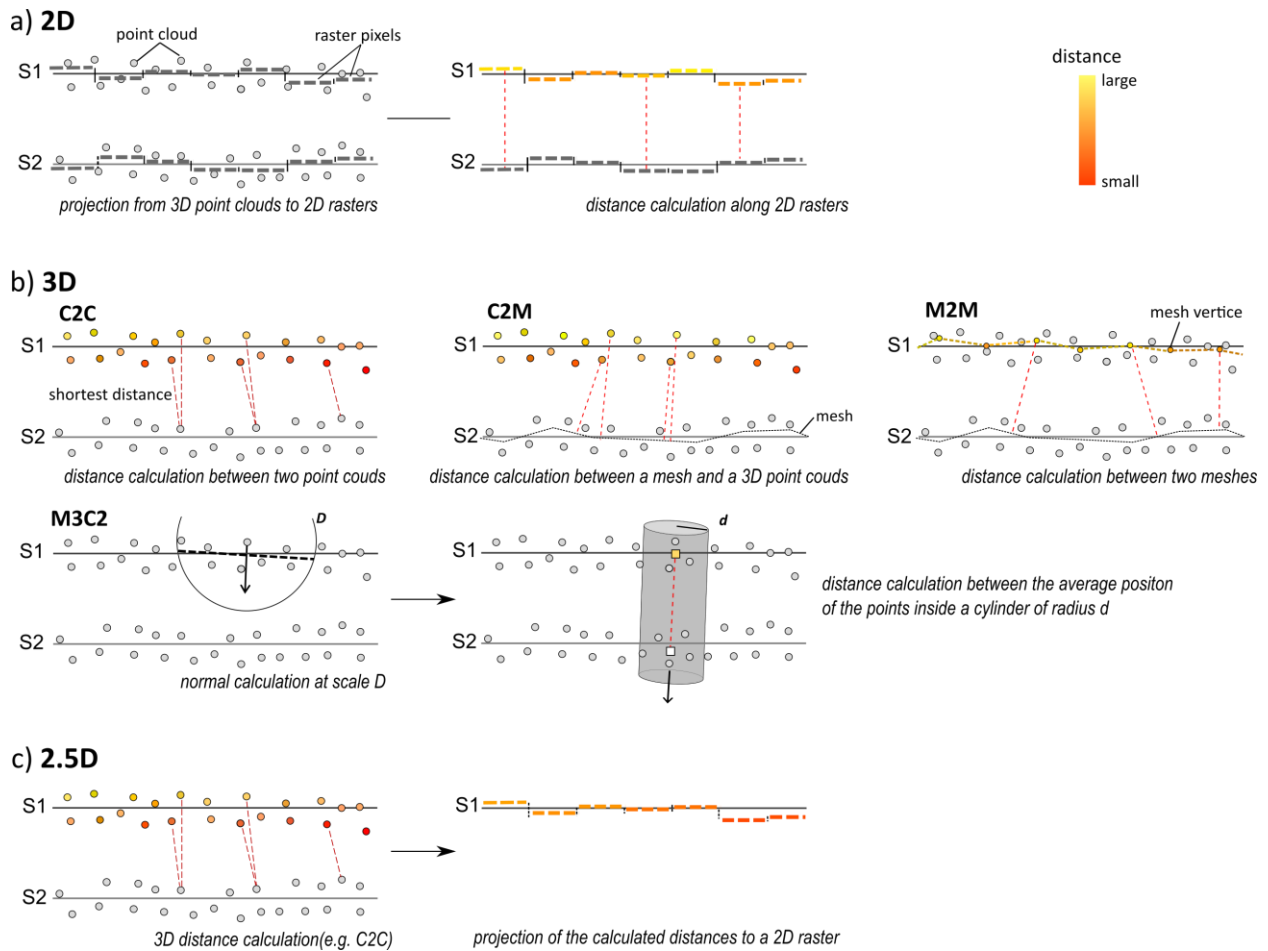


Figure 4.2. Distance calculation methods between two point clouds representing two surfaces S1 and S2. a) 2D distance calculation methods consisting of rasterizing S1 and S2. Distance is calculated along the projection direction between the two generated rasters. b) 3D distance calculation methods. These methods consist of measuring directly the distance between two 3D objects: point clouds or meshes. c) 2.5D distance calculation methods involving the calculation of the distance between S1 and S2 in 3D. Distances measured in the previous step are then rasterized.

### 4.3.2 3D DEMs

Clouds-to-Clouds (C2C) comparison method measures directly the distance between the points of the two compared point clouds (Figure 4.2b). This technique is the simplest and fastest 3D point clouds comparison method. The distances are measured using the Hausdorff metric. For each point of a point cloud, the nearest neighbor is searched on the point cloud of reference. The difference is measured as the absolute distance between the two points. It does not need any gridding or meshing of the data (Girardeau-Montaut et al., 2005; Oppikofer et al., 2009; Lague et al., 2013). However, the measured distance is sensitive to the roughness, outliers and point spacing of the studied clouds. This

measure can be improved by using a local model of the reference surface either by a least-square fit (C2C<sub>LSP</sub>), a quadratic fit (C2C<sub>Q</sub>) or a Delaunay triangulation (C2C<sub>2DT</sub>) of the closest point neighbors (Girardeau-Montaut et al., 2005). Distance computation using a local model based on a Delaunay triangulation allows the representation of sharp edges, while a quadratic height function is more appropriate for smooth surfaces. With the use of height functions, distance measurement is less sensitive to outliers or variations in surface roughness and allows a better estimation of the true distances.

The Cloud-to-Mesh (C2M) method compares a point cloud to a 3D mesh (Day et al., 2013; Lague et al., 2013; Royán et al., 2014). The accuracy of this technique depends on the quality of the mesh. Flat or regular surfaces are well suited for this method. However, rough surfaces with high topographic variability are often smoothed which affects surface change measurements. Interpolation of missing data, due to occlusion or point spacing, can also create difficulties requiring manual inspection. The difference sign is defined according to the normal orientation of the mesh.

Lague et al. (2013) have developed the Multiscale Model to Model Cloud Comparison (M3C2) algorithm, which directly compares two point clouds. This algorithm is composed of two steps. The first step consists in calculating the orientation of the surface normal in 3D at a scale consistent with the local surface roughness. Following this step, mean surface changes are measured along the normal direction with an explicit calculation of a local confidence interval. Local averaging around each point reduces the influence of the surface roughness.

Change detection analysis can also be conducted by measuring the distance between two meshes (R. Kromer et al., 2015; Lato et al., 2009). Distances between surfaces models are compared along the shortest distance vectors. For each vertice of a surface model, distance is measured to the corresponding nearest surface on the reference model. By doing so, the measured distance corresponds to the distance between the average locations of the two point-clouds. It is thus less sensitive to outliers and is not view-dependant. However, it is subject to the same limitations as the C2M method (smoothed surface, interpolation of missing data).

### 4.3.3 2.5D DEMs

An intermediate method between 2D and 3D consists of measuring topography changes in 3D and to interpolate them into 2.5D datasets (Rosser et al., 2006; Williams et al., 2018). This method (Figure 4.2c) has the advantage of computing distances in 3D, which minimizes the shortcomings of the 2D projection. This method may be suitable for regular and planar surfaces but would be rather inappropriate for surfaces with sharp changes of orientation as it may generate occlusion patterns.

## 4.4 Rockfall inventories

In this study, we detected rockfalls at Mount Saint Eynard using a diachronic comparison of point clouds acquired in November 2016 and July 2018 by terrestrial SfM photogrammetry. We used datasets of more than 500 photographs (resolution 5-9 cm/pixel, Canon EOS 7D Mark II) taken from 14 locations. SfM surveys' methodology is developed in the supplementary material A.

We use the same data set through this study with identical processes between models. This allows us to explore the influence of the methodology for the creation of rockfall inventories.

### 4.4.1 Distance measurement

We have calculated distance between two 2D models by differencing two rasterized point clouds with pixels size of 0.25x0.25 cm.

For C2C methods using a local model of the reference surface  $C2C_{LSP}$ ,  $C2C_Q$  or  $C2C_{2DT}$ , the surface local model was obtained by fitting a mathematical model (least-square fit, quadratic fit or Delaunay triangulation) on the nearest point and its neighbors within a distance of 0.5m of the nearest point. The distance from each point of the compared cloud is thus measured as the distance between the points to the local model of the reference surface.

For C2M method, we meshed the reference cloud according to a Delaunay-Voronoi triangulation (mean distance between points 0.15). For each point of the compared cloud, the distance is measured as the distance between the points and the nearest triangle in the reference mesh. For M2M method, the two clouds are meshed according to a Delaunay-Voronoi triangulation. Distances are measured as the distance between each vertice of a surface model to the nearest triangle in the reference mesh.

In the case of M3C2 method, for each point of the compared cloud, normals are computed using spherical neighborhood extracted around each point with diameters ranging from 0.5 to 1m with a step of 0.25. Distances are computed as the local distance between two point clouds along the normal surface direction defined previously. Local distance is determined as the average position of the neighbors points contained within a cylinder of diameter of 0.5m around a core point.

### 4.4.2 Erosion areas extraction

Once distances between two DEMs are measured, we try to extract areas corresponding to erosion from the rest of the DEMs. To do that, it is necessary to

determine a deviation threshold. In the case of 3D methods, points or mesh triangles corresponding to distances larger than the threshold are isolated. We apply different distance measurement methods or detection threshold (0.3, 0.35, 0.4, 0.45 and 0.5m) to this single data set. The minimal value of thresholds (0.3m) corresponds to a quantile of the distance distribution of about  $3\sigma$  (99.6%) (Figure 4.3). This allows us to consider only distances that are large enough to be unaffected by measurement noise. We then test how increasing the threshold affects the number of detected events and their volume estimation.

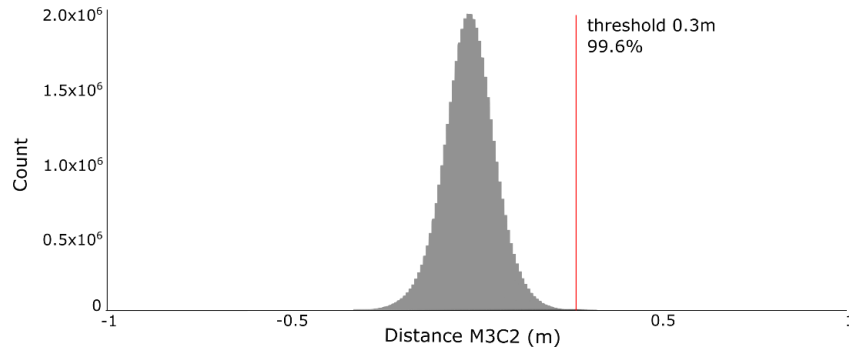


Figure 4.3. Distribution of the distance between DEMs. Only 0.4% of the points correspond to distance superior to 0.3m.

In the case of M2M method, meshes of less than 5 triangles are removed in order to limit noise influence and false erosion detection.

For 2.5D methods, points corresponding to distances larger than the threshold are isolated and then rasterized. In 2D, patches of pixels larger than the threshold are isolated. We then retrieve the connectivity of each pixel and assemble connected pixels above the threshold. Patches containing less than 4 pixels are removed, in order to limit noise influence and false erosion detections even if this procedure influence the detection of smallest areas.

To study the influence of the view angle during the DEM rasterization, 7 view angles, ranging from  $-30$  to  $+30^\circ$  around the average orientation of the cliff, were applied during the rasterization process. These projection angles were used to create inventories in 2D and 2.5D (M3C2).

#### 4.4.3 Volume measurement

In the case of 2D or 2.5D inventories, rockfall volumes are computed as the product of pixel area with the value of the pixel, i.e. distance between DEMs.

For 3D inventories, the bordure of the isolated meshes is projected on the reference DEMs. The reference DEMs are then cut along the projected bordures. Front and rear

faces of the compartments are then assembled. To compute a compartment volume, the closed mesh is decomposed into individual tetrahedrons and summed up.

## 4.5 Results

We have detected several hundred rockfalls, with volumes ranging from 0.1 to 300 m<sup>3</sup> (Figure 4.3a). Significant differences can be noticed between inventories depending on the chosen method and threshold. Rockfall surfaces and volumes are affected by distance calculation methods. Figure 4.4b presents distance maps used to calculate the volume of the biggest event in this study. Depending on the method adopted, distance maps differ significantly and the calculated volume can vary by up to 35%.

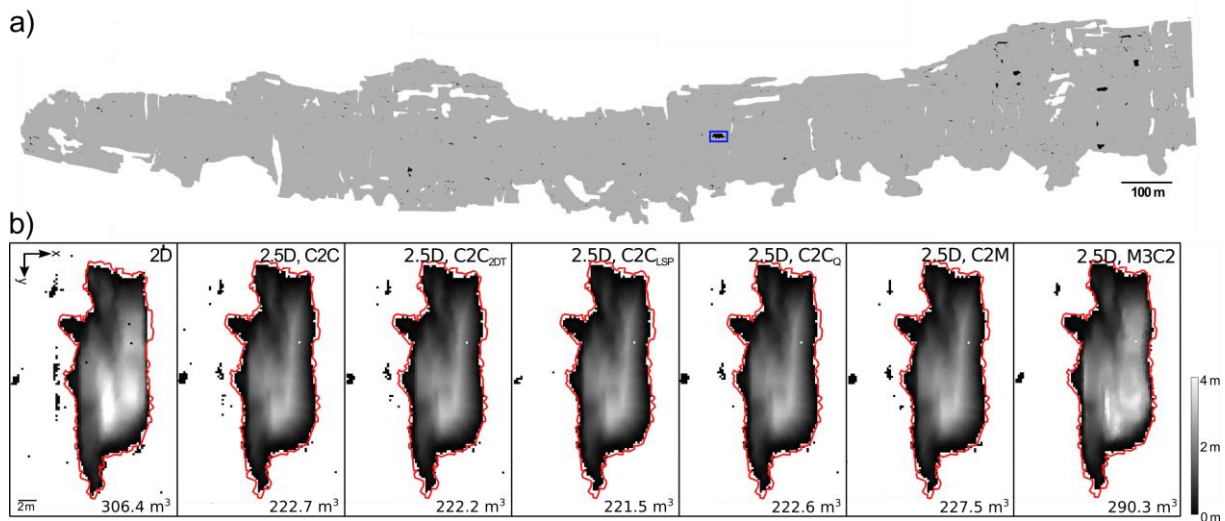
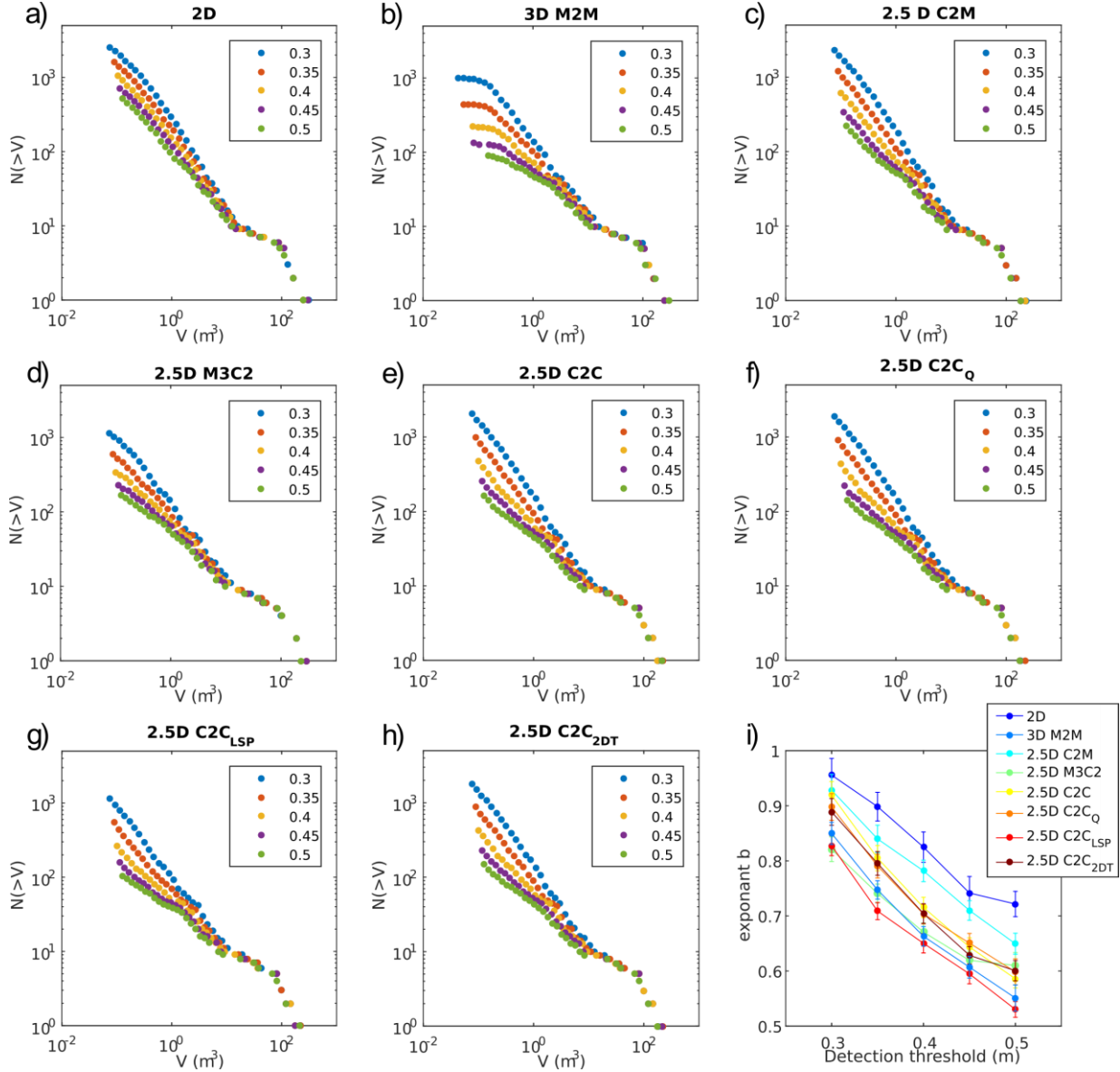


Figure 4.4. a) 2D representation of the rockfalls (in black) detected using the Cloud to Mesh (C2M) method. b) Influence of distance calculation methods on the magnitude of change detected. M2M method does not require rasterization. The outline of the rockfall compartment detected in 3D using M2M method (298.5 m<sup>3</sup>) is represented with a red line. The detection threshold adopted for this figure is 0.3m.

The difference between inventories also varies with rockfall volume. As shown in Figure 4.4b and Figure 4.5, the biggest event volume is similar amongst C2C methods (C2C, C2C<sub>Q</sub>, C2C<sub>LSP</sub>, C2C<sub>2DT</sub>). However, the number of detected events varies according to the method used (C2C: 2040 events, C2C<sub>LSP</sub>: 1150 events, for a detection threshold of 0.3 m). The volume distribution for these inventories can be fitted using a power-law distribution (equation 4.1). We used the methodology developed by Clauset et al. (2009) in order to estimate the parameters  $a$  and  $b$  of the power-law distribution (equation 4.1) This methodology combines a maximum-likelihood method with goodness-of-fit tests based on the Kolmogorov-Smirnov statistic and likelihood ratios. We compared these results with a linear regression on a doubly logarithmic plot and we found similar results with both methods.



As shown in Figure 4.5.i, the power-law exponent  $b$  varies between 0.82 (2.5D, M3C2) and 0.96 (2D) for a detection threshold of 0.3 m. Decreasing the detection threshold from 0.5 m to 0.3 produces a strong increase in the number of events, by a factor of 5 to 13 depending on the method used (Figure 4.5a to Figure 4.5h). This has an important impact on the distribution of rockfall volumes. For the C2M (2.5D) inventory, the power-law exponent  $b$  decreases from 0.92 to 0.65 as the threshold increases from 0.3 to 0.5 m.



**Figure 4.5.** Volume distribution of the rockfall inventories obtained using different methods for estimating distances. a) Using a 2D method, b) with the M2M 3D technic. 2.5D inventories were obtained using c) C2M, d) M3C2, e) C2C, f) C2C<sub>Q</sub>, g) C2C<sub>LSP</sub>, h) C2C<sub>2DT</sub> measuring methods in 3D. The distances measured in 3D were then rasterized in 2D. Several detection thresholds were used to generate these inventories: 0.3, 0.35, 0.4, 0.45 and 0.5. i) Power law exponent  $b$  obtained for the different inventories according to the 5 detection thresholds.

The variation of rasterization angle has a small impact on the creation of a 2.5D (M3C2) inventory (Figure 4.6b). The number of detected events ranges between 1106



and 1164 and the power-law exponent ranges from 0.81 to 0.86. The rasterization angle has, however, a strong impact on the creation of 2D inventories (Figure 4.6a). The number of detected events strongly varies with nearly twice as many events detected with an angle of  $-30^\circ$  as events obtained with an angle of  $0^\circ$ . The power-law exponent also strongly varies with  $b$  ranging from 0.95 to 1.1 (Figure 4.6c).

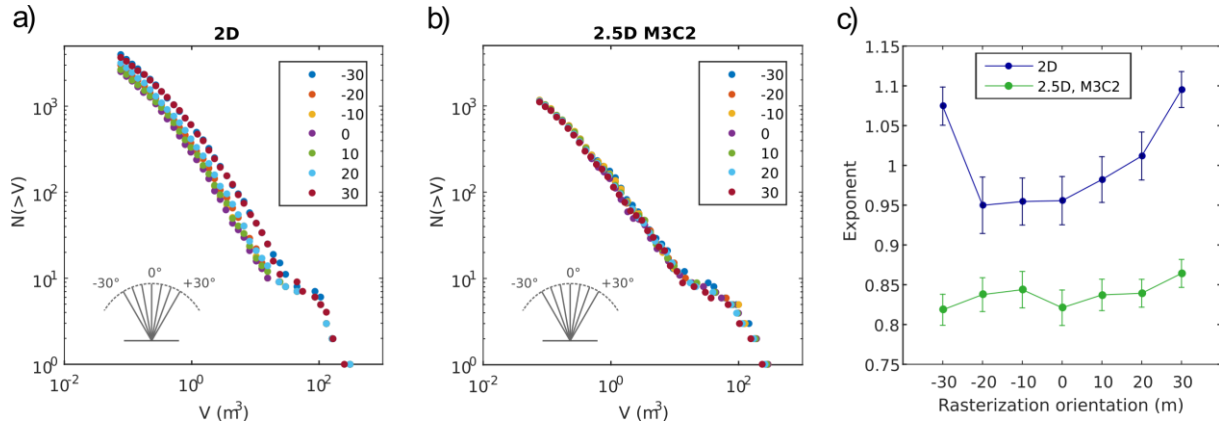


**Figure 4.6.** Influence of the view-angle during the rasterization process for the creation of a) 2D inventories and b) 2.5 (M3C2) inventories. c) Power law exponent  $b$  obtained for each inventory.

Another parameter used to characterize cliff erosion is the annual recession rate  $R$  (Dewez et al., 2013; Marques, 2006; Matasci et al., 2015). It is estimated by summing all volumes in a rockfall inventory

$$R = \frac{\sum V}{S \cdot d} \quad (4.2)$$

with  $V$  is rockfall volume,  $S$  the cliff surface area and  $d$  the monitoring duration.

As shown in Figure 4.7, this parameter is also strongly dependent on the method used to estimate distances and on the value of the detection threshold. The annual recession rate presents a similar behavior as the exponent  $b$ .

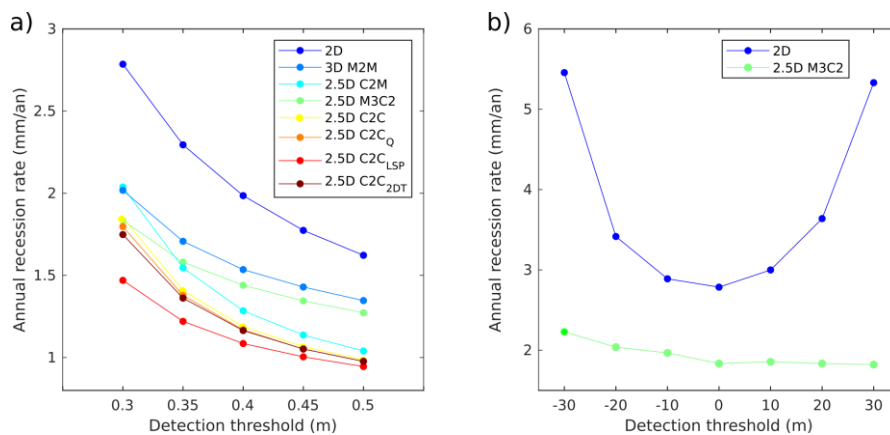


**Figure 4.7.** Annual recession rate according to a) the method and detection threshold used or b) according to the view-angle of the rasterization process.

The R factor is higher with the 2D method than for 2.5D and 3D methods and decreases if the detection threshold increases. It remains rather constant for the different view angles for the 2.5D (M3C2) method but strongly varies for the 2D method (Figure 4.7b).

## 4.6 Discussion

These systematic tests clearly show that the distance measurement methods have a strong influence on both the number of detected events and on their volumes. Depending on point density, surface roughness, normal direction or the overall geometry of the rockfall compartments, distance calculation methods described above can be more or less adequate. As shown in Figure 4b and as discussed by Benjamin et al. (2016), the estimated rockfall volumes can be significantly under- or over-estimated depending on the method used. This bias affects particularly small rockfalls. When considering small depth changes on the edge of a rockfall, volumetric differences introduced by these edge effects represent a greater fraction of the overall rockfall volume for small events than for larger rockfalls. This has a direct impact on the  $b$  parameter of the power-law fit, as this parameter reveals the proportion between small and large events. Inadequate use of a distance measurement method can lead to an underestimation of the rockfall number or, on the contrary, an overestimation of the rockfall number with false rockfall detections. Inventories carried out in 3D are less sensitive to these biases. However, these methods are time-consuming and difficult to automate. 2.5D inventories using M3C2 and C2C<sub>LSP</sub> provide similar results than 3D inventories. These methods appear to be a good alternative to 3D inventories. However, the normal scale and projection scale can be difficult to define and have a strong influence on the results. Moreover, this method require larger computing time than other methods (C2C, C2M, 2D). This may be disincentive for large point clouds.

Erosion is defined as areas corresponding to a distance between point clouds larger than a specific threshold. The choice of this threshold is critical to correctly separate erosion from noise. If the selected threshold is too low, erosion will be poorly isolated from the noise, which will induce false detections. If this threshold is too high, shallow events may not be detected. Once again, while the biggest events ( $> 5\text{m}^3$ ) are less sensitive to the detection threshold, smaller and shallower events are strongly impacted. The power-law may thus be strongly affected as it describes the relation between small and large event frequency. Most studies define their threshold using the distance distribution between DEMs (quantile of the distance distribution  $< 1\%$ ). This criterion allows considering only distances that are significantly high to be unaffected by measurement noise.

Rough surfaces generate occlusion patterns that are view-dependent. Moreover, sharp changes in topography are often smoothed if rasterized. We found that the view-angle

has a strong influence on the estimation of rockfall volumes using 2D and 2.5D methods. For instance, the volume of the biggest event in this study is underestimated by 30% when rasterized using a view-angle of  $30^\circ$  from the orientation normal. This bias has an even stronger impact on 2D methods compared with 2.5D methods, with twice the number of events detected with a difference of view angle of  $30^\circ$ . When cliffs have a non-planar aspect, an alternative consists of creating separate sections in order to maintain a normal viewing angle for each section.

These aforementioned points lead to an important discrepancy in the estimated value of the annual recession rate. It highlights the difficulty to accurately quantify the erosional fluxes associated with rockfalls. The total erosion estimated using a 2D method ( $2408 \text{ m}^3$ ) is twice as much as obtained with a 2.5D, C2C<sub>LSP</sub> method. A similar result was found by Benjamin et al. (2016) with an erosion volume estimated using a 2D method exceeding the one obtained by volumetric meshing by over 25%. These results suggest that inventories conducted in 2D overestimate rockfall volumes.

Other factors can influence the quality of a rockfall inventory. Barlow et al. (2012) and Williams et al. (2018) studied the impact of the temporal resolution on the distribution of rockfall volumes. They showed that the selection of an arbitrary time window has a strong effect on the number of detected events as well as on their volumes. Rockfalls from the same source area occurring a few hours or days apart are often listed as the same event, overestimating their volumes. In the case of the superimposition of rockfalls, frequent monitoring allows the detection of a higher fraction of small rockfalls, whereas sporadic monitoring only allows for the detection of the cumulated rockfalls. An arbitrary time window also impacts the frequency estimates of extreme events, as it may over-estimate the probability of large events (Barlow et al., 2012). Tanyaş et al. (2019) share this conclusion for the distribution of landslide surfaces. They also pointed out the influence of quality and resolution of the imagery or DEMs leading to strong discrepancy between inventories. Clean and high-resolution datasets allow the detection of a greater number of events, especially smaller ones. Lower resolutions or noisier datasets often lead to the amalgamation of several events. An opposite effect can be observed with high thresholds as it may lead to the non-detection of shallow parts and the fragmentation of a compartment into several parts.

Rockfall volume distribution is often used to determine the return period of rockfalls as a function of their size. This estimation is of prime importance for risk mitigation or for the design of protective structures. Several authors hypothesized that the parameters  $a$  and  $b$  of the volume distribution (equation 1) can be linked to characteristics of the source area, such as geological, geomechanical and morphological settings of the rock mass, climatic conditions, etc. (Dussauge-Peisser et al., 2002; Hantz, 2011). Other studies found that both  $a$  and  $b$  were independent of these characteristics (Brunetti et al., 2009). Power-law distributions are also used to extrapolate the observed distribution for smaller or larger volumes (Dussauge-Peisser et al., 2002; Hantz, 2011; Straub and Schubert, 2008).

In this study, we found that the differences between inventories induce a strong variation of the parameters  $a$  and  $b$  of the rockfall volume distribution. The power-law exponent  $b$  ranges from 0.5 to 0.95. The erosion of limestone cliffs surrounding Grenoble has been the subject of several previous studies. Dussauge-Peisser et al. (2002) and Hantz et al. (2003) studied the volume distribution of 120 km of limestone cliffs around Grenoble including the Mount Saint-Eynard cliffs. They found a power-law exponent  $b$  of respectively 0.41 and 0.55 using a data set of about 100 events ranging from 10 m<sup>3</sup> and 1 000 000 m<sup>3</sup>. These datasets were compiled by a forest service (RTM, 1996), listing rockfalls based on field evidence and historical documents. The volumes of these events were mostly estimated according to the dimension of the rockfall scar left on the cliffs. Guerin et al. (2013) and D'Amato (2015) also analyzed rockfall datasets from Mount Saint-Eynard and found a power-law exponent  $b$  of respectively 0.65 (100 events ranging from 0.1 to 100 m<sup>3</sup>, detection threshold 0.2m) and 0.80 for (800 events, 0.1 to 1000 m<sup>3</sup>, detection threshold 0.1m). These two datasets covered the same area and used terrestrial Laser Scan (TLS) to detect rockfalls. Rockfall volumes were then processed using a 3D, M2M method. These studies illustrate well the fluctuations of the power-law distribution obtained for the same area.

In light of these observations, questions arise about the pertinence of the statistical analysis of rockfall volumes and on the use of power-law distributions to extrapolate the rate up to very large volumes. This also questions the relevance of comparing power-law parameters or recession rates obtained for different studies using distinct methodologies. Such studies need to be conducted in other geological contexts in order to assess if the methodological influence on rockfall distribution applies the same way in other sites. It would also be interesting to analyze if the cliff roughness amplitude has an influence on these biases by applying the methodology developed in this paper to other sites with larger roughness.

## 4.7 Conclusion

We have processed a single DEM dataset using different distance calculation methods (2D, 2.5D and 3D methods), different detection thresholds and projection angles. We explored the implications of different methodologies for the creation of rockfall inventories.

Rockfall numbers and volumes can be significantly under- or over-estimated depending on the methodology adopted. The annual recession rate and the rockfall volume distribution show strong variations between rockfall inventories. This affects particularly small rockfalls for which small depth changes on the edge of a rockfall are not negligible. 2D and 2.5D inventories are also strongly influenced by the view-angle with large discrepancies on rockfall numbers and volumes.



## 5 Morpho-structural analysis of rockfalls

*We have carried out diachronic photogrammetric monitoring of Mount Saint Eynard (Chartreuse, France) using DEMs acquired between 2016 and 2019. The objective of this study is to provide a detailed rockfall inventory. This inventory allows us to analyze the morpho-structural influence of Mount Saint-Eynard cliffs on the rockfall distribution. We have studied the geometric properties of rockfall compartments and their failure configurations along the structural analysis of the discontinuity families affecting the massif. This work was carried out as part of the graduate internship of Guillaume Clément, supervised by David Amitrano and myself.*

### 5.1 Mount Saint-Eynard cliffs monitoring

In this study, we monitored rockfalls that occurred at Mount Saint Eynard between November 2016 and March 2019. We used diachronic comparison of point clouds acquired in November 2016, July 2018, and March 2019. Point clouds were created by photogrammetry using datasets of more than 500 photographs (resolution 5-9 cm/pixel, Canon EOS 7D Mark II) taken from 12 locations (supplementary A).

Point clouds were cleaned and georeferenced (see Chapter 4). Erosion detection was carried out by measuring distance between two meshes (Lato et al., 2009; R. Kromer et al., 2015). Fallen compartments were defined using a threshold of 0.3 m. Rockfall volumes are measured in 3D in order to ensure a good depiction of the rockfall compartment geometry. In order to validate the detection of rockfalls, each rockfall was checked using photographs. This prevents the false detection of rockfall but might also prevent the detection of the smallest rockfalls. We detected 257 rockfalls, with volumes ranging from 0.1 to 1000 m<sup>3</sup>.

### 5.2 Rockfalls distribution

Rockfalls are not evenly distributed along the cliffs. Of the 257 detected rockfalls, only 10 events are located on the upper cliff. This difference is probably linked to the geological differences between the two cliffs. The upper cliff consists of massive limestone

of the Tithonian stage. The lower cliff consists of fractured thin-bedded limestone, of the Sequanian stage. The marly content of the lower cliff is higher which may induce a higher sensibility to weathering.

The distribution of rockfall volumes is presented in Figure 5.1. The number  $N$  of rockfalls larger than a volume  $V$  occurring in a given cliff during an investigation period is modeled by

$$N = aV^{-b} \quad (5.1)$$

where  $a$  and  $b$  are empirical constants. Parameter  $b$  controls the proportion between small and large events. Power-law distribution parameters (i.e  $a$  and  $b$ ) are estimated as in Chapter 4. The volume distribution of all Mount-Saint-Eynard rockfall events is characterized by an exponent  $b=0.71\pm 0.02$  (Figure 5.1). The distribution evolves along the cliffs. The southern end of the cliffs appears more affected by smaller rockfalls than the northern end.

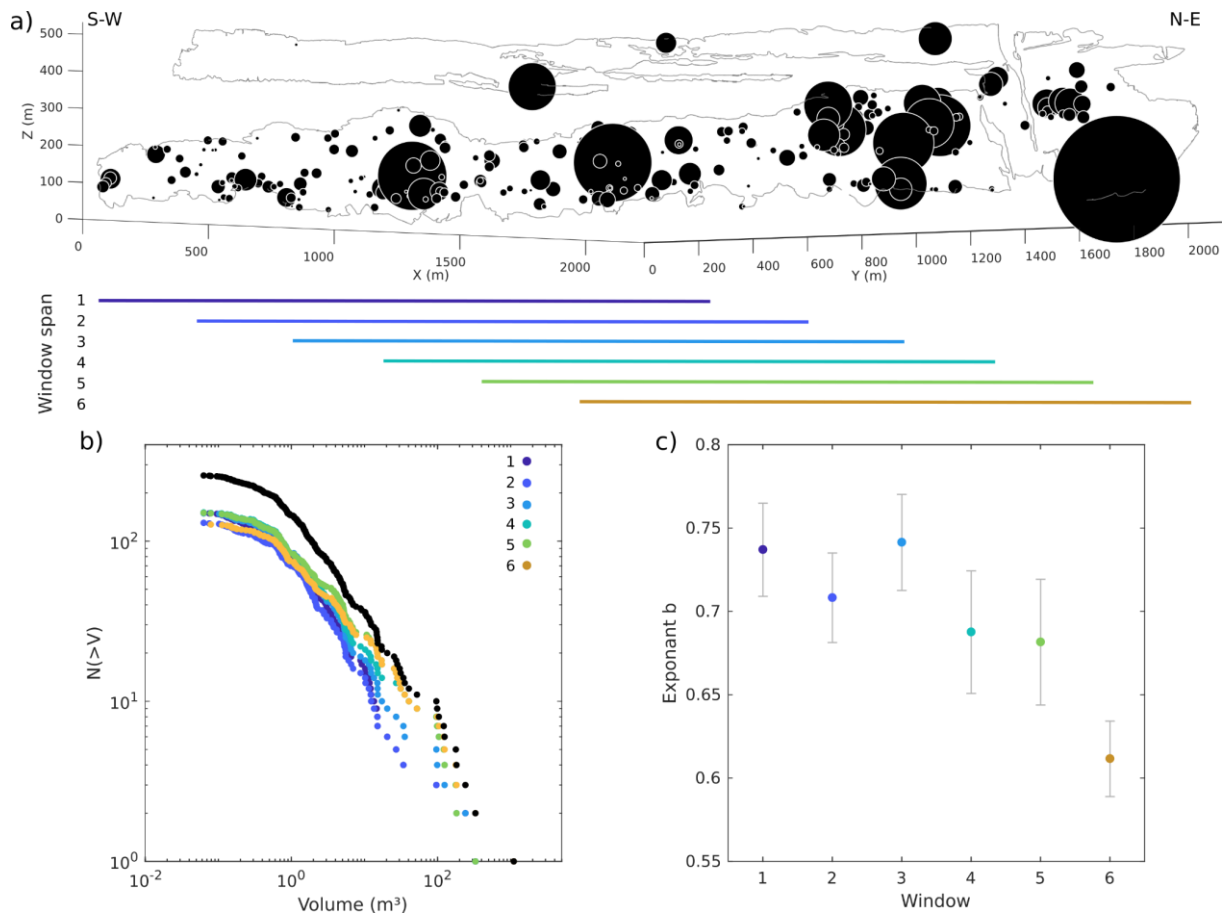


Figure 5.1. a) Rockfall spatial distribution. Circle sizes indicate rockfall volumes. b) Volume distribution of the rockfall inventory. In black: total inventory, in color inventories corresponding to the sliding windows shown in (a). For clarity reasons power fits were not represented. The lower bound of the power-law fit varies depending on the window (from 1 to 6: 1.4, 4.2, 3.0, 0.6, 0.5, 0.5 m<sup>3</sup>). c) Exponents  $b$  of the power-law distributions according to the sliding window number (exponents  $b$  of the total inventory: 0.71, lower bound of the power-law: 1.40 m<sup>3</sup>).

In order to characterize this evolution, we analyzed the variation of volume distribution along the cliff. We defined a sliding window of 1500m long with a sliding shift of 250 m. The volume distribution of the rockfalls within each sliding window is presented in Figure 5.1b). The exponent  $b$  of the power-law distributions decreases as the sliding window shifts toward the northern end of the cliffs (Figure 5.1c). This indicates an increasing proportion of bigger volumes over the overall rockfall distribution in the northern part of Mount Saint-Eynard.

### 5.3 Rockfall configurations

The 3D reconstruction of rockfall compartment provides information on the shape of the fallen compartments. We measured the width, height, depth of rockfall compartments, with width defined as parallel to the local cliff plane and depth perpendicular to it. In order to investigate typical rockfall failure configurations we defined 6 compartment types according to their relative width, height and depth (Figure 5.2a):

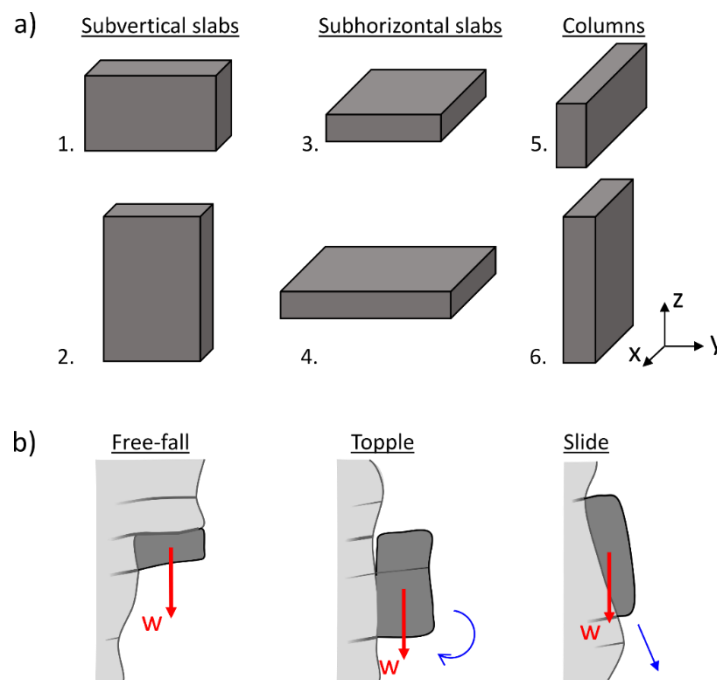


Figure 5.2. Illustration of a) the compartment types b) the failure mechanisms. Red arrow: weight vector, blue arrow: movement direction.

1. width > height > depth
2. height > width > depth
3. depth > width > height
4. width > depth > height
5. height > depth > width



6. depth > height > width

These 6 compartment types can be gathered into 3 categories (Figure 5.2, Figure 5.3):

1 and 2: subvertical slab

3 and 4: subhorizontal slab

5 and 6: column

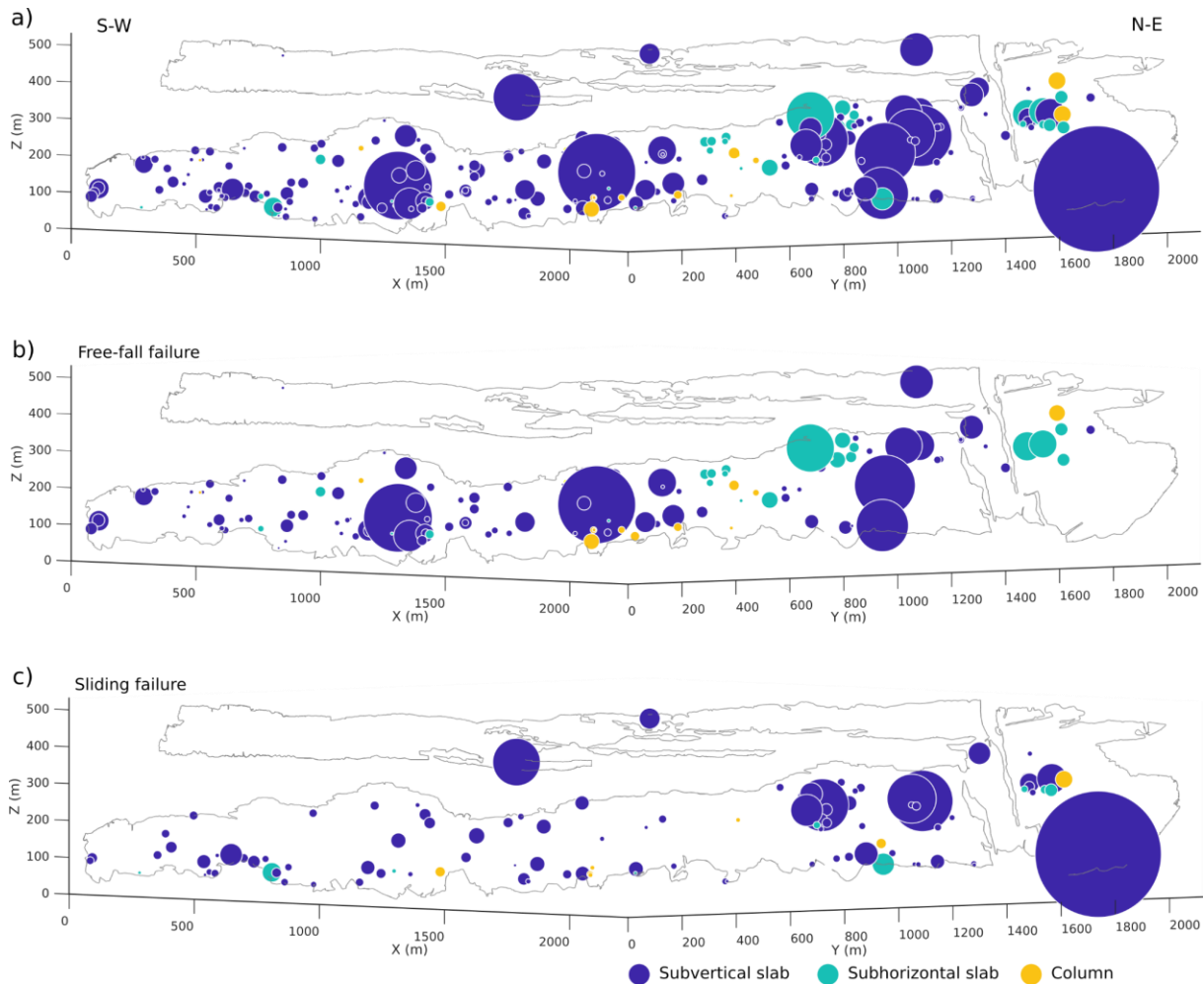


Figure 5.3. a) Representation of all rockfall events. Rockfall events according to their failure mode: b) free-fall and c) sliding. Colors represent compartment type, dark blue: subvertical slab, light blue: subhorizontal slab, yellow: column. Circle sizes are function of rockfall volumes.

The compartments are always defined by two bedding planes. They often correspond to a single limestone bed but may also occur on several limestone beds.

By considering that the main force, involved in the failure process, is gravity, we can determine failure mechanisms. Three types of failure were considered: slide, free-fall or topple. When the weight vector intersects a rock joint, the mechanism is a slide (Figure 5.3b). When it intersects a free face, the failure type is a free-fall or topple. As presented in Chapter 1, topple involves a forward rotation out of the slope of the compartment

about an axis below the center of gravity of the compartment (Cruden and Varnes, 1996). This kind of failure is likely to occur if the lower part of the compartment is intact whereas fractures are present in its upper part. For topple or free-fall detachment, no, or little, shear displacement takes place, contrary to slide failure. Topple and free-fall could not be distinguished in this study due to the lack of information on the repartition of fractures before failure. We thus use the term “free-fall” to designate both free-fall and topple mechanisms in the following.

A subvertical slab represents the majority of rockfalls (79%, Table 5.1). A subhorizontal slab and column rockfall type represents only 21% of the rockfall and defines smaller rockfall volumes. Amongst the 34 events with volume larger than 10m<sup>3</sup>, 31 are subvertical slabs, 3 are subhorizontal slabs and none are columns. Free-fall failure is slightly prevailing with respect to sliding failure (56%). This prevalence is even more pronounced in the case of subhorizontal slabs and with a lesser degree for columns.

D’Amato (2015) studied Mount Saint-Eynard rockfall occurrence between 2013 and 2015. She carried out a TLS monitoring of the cliff over a 600m long area, located at the southern end of the cliffs. The criteria used to define the compartment type slightly differ between these study and the study carried out by D’Amato (2015). They are however overall rather similar. She determined the following failure ratio: free-fall 80%, sliding 20% and compartment type proportion: subhorizontal slabs 30%, subvertical slabs 30%, columns 10%, undefined 30%. The gap between these results and those presented in this study might be related to the different monitored areas. It might also be related to the size of the monitored events. D’Amato (2015) was able to study smaller events than in this study (75% of the rockfall volumes were smaller than 1m<sup>3</sup>). The larger proportion of free-falling events, determined by D’Amato (2015), is probably linked to the detected event size. The bigger the event is, the less likely an overhang exists (for a same bench thickness).

Table 5.1. Repartition of compartment type and failure mode

Compartment type	Free-fall	Sliding	(%)
Subvertical slab	108	96	79
Subhorizontal slab	22	9	12
Column	14	8	9
(%)	56	44	100

Sliding failure occurs predominantly in areas characterized by smoother slopes, whereas free-fall failure affects mainly steeper areas. Free-fall and sliding failures are evenly distributed from S-W to N-E (Figure 5.3b, Figure 5.3c).

Subvertical slabs also appear to be rather evenly distributed from S-W to N-E. However, subhorizontal slabs and columns seem to be more frequent in the northern part of the cliffs (Figure 5.3).

## 5.4 Structural analysis

The orientation of the main discontinuity sets of the rock mass can be extracted from point clouds. Based on azimuth and dip of the point normal vectors, the software CloudCompare defines the dip and dip direction at each point.

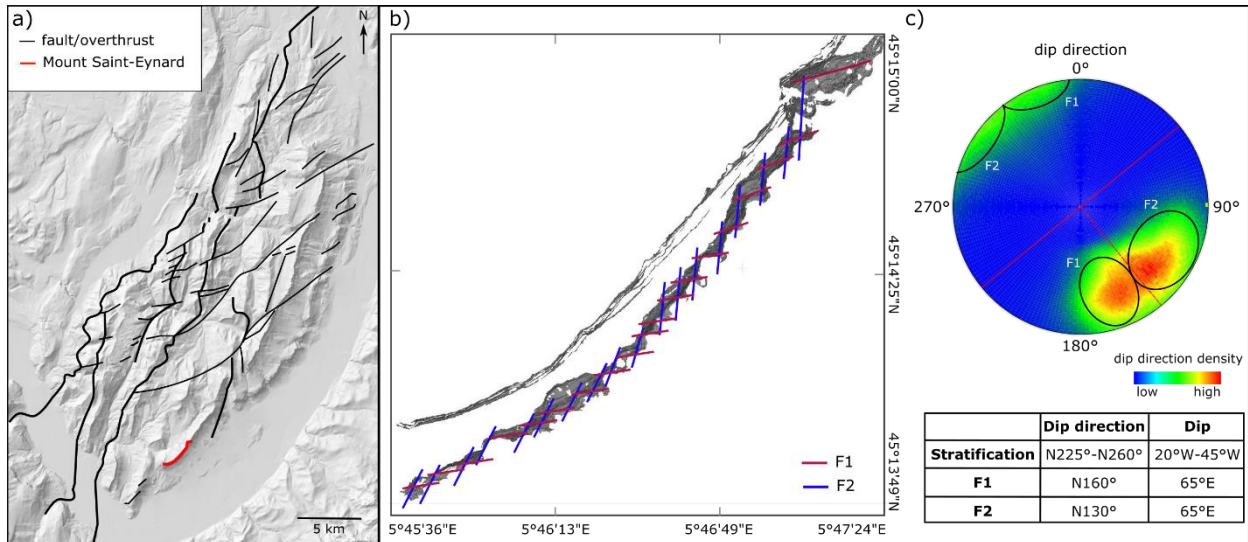


Figure 5.4. a) Structural diagram of the Chartreuse massif (adapted from Gidon, 1990). b) Main discontinuity sets present on the lower cliff. c) Stereographic representation of the main discontinuity sets. The color ramp represents the density of point normal vectors falling into each bin of dip and dip direction.

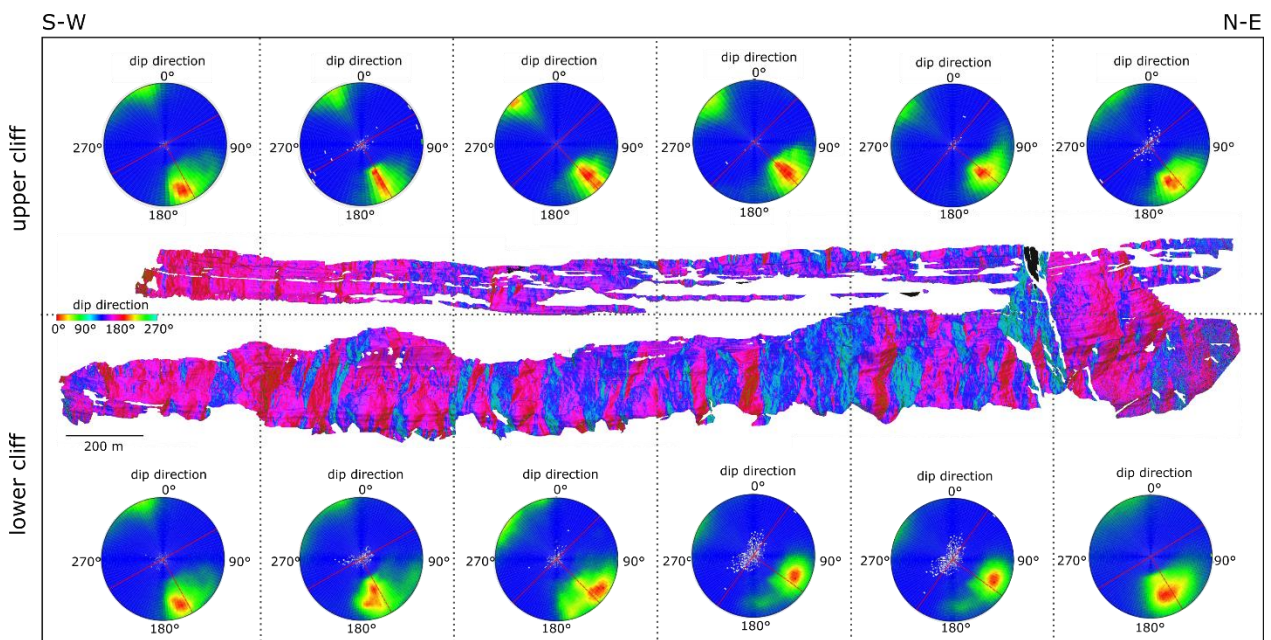


Figure 5.5. Stereographic representation of the discontinuity sets of the upper and lower cliffs and variation of the main discontinuity sets along the cliff. Windows size: in average 500m. Dip directions are shown according to a color code. Pink: F1 discontinuity set, blue: F2 discontinuity set.

We were able to characterize two main discontinuity sets: a first discontinuity set F1 with a global orientation N70° and a second discontinuity set F2 with a global

orientation  $N40^\circ$  corresponding to the direction of the main faults of the Chartreuse Massif (GIDON, 1990). These two main discontinuity sets form the horizontal spurs and recesses carving Mount Saint-Eynard cliffs at large scale. Stratification orientation is difficult to determine and evolves around the axis of the syncline constituting Mount Saint-Eynard.

The prevailing discontinuity set slightly evolves from S-W to N-E. Whereas at the southern end of the Mount Saint-Eynard the F1 discontinuity set is mainly present, at the northern end, the F2 discontinuity becomes predominant (Figure 5.5). We investigated whether this variation could have an influence on the rockfall distribution (Figure 5.6, Figure 5.7). In order to illustrate this influence, we determined which discontinuity set was predominant for each rockfall scar.

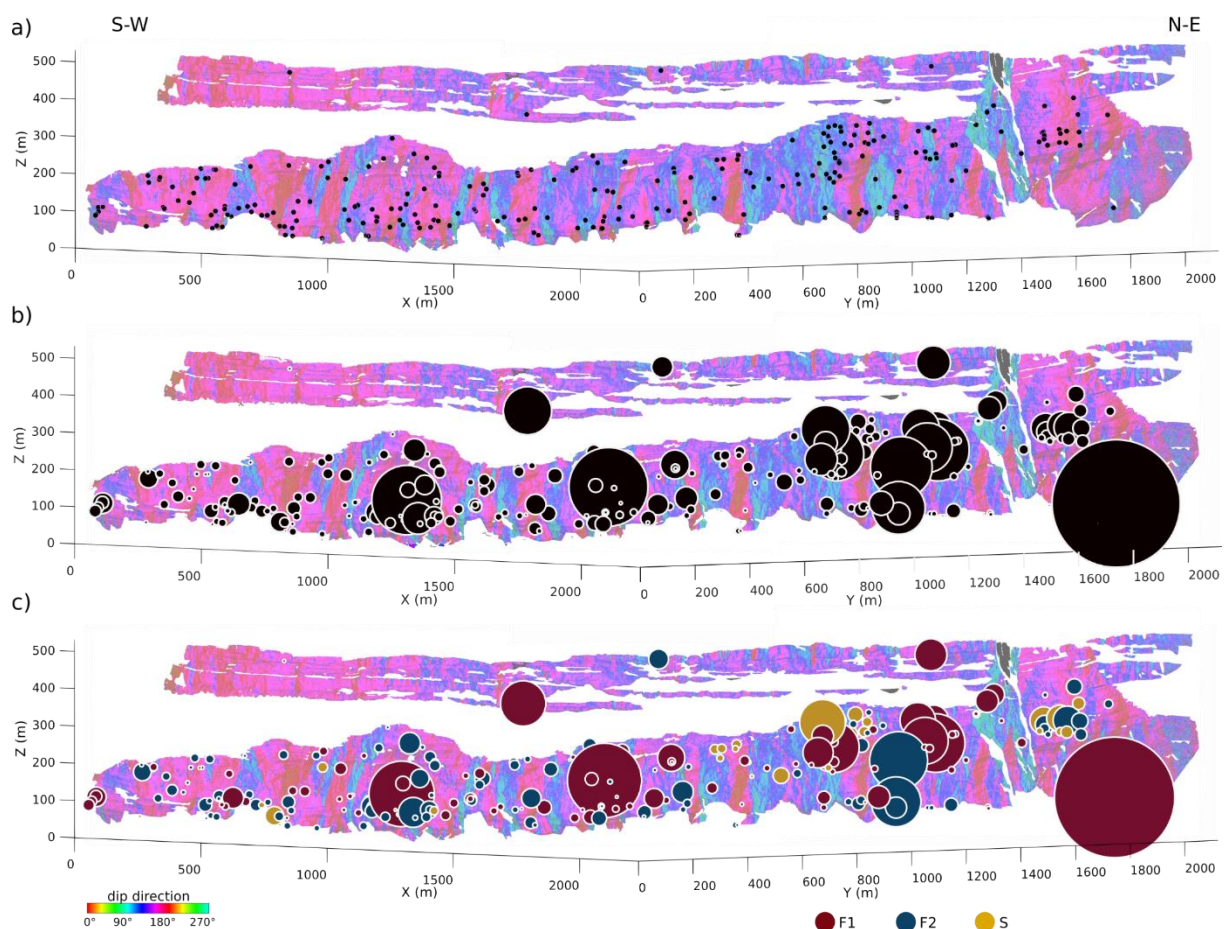


Figure 5.6. a) Rockfall distribution along the dip directions of the cliffs discontinuities. Dip directions are shown according to a color code. b) Circle sizes represent rockfall volumes. c) Distribution of rockfall events  $>10 \text{ m}^3$ . Color represents the main discontinuity set of the rockfall scar: F1, F2 and S.

In Figure 5.7, we distinguish the rockfalls according to the prevailing discontinuity set of their scar (set corresponding to the largest faces of the compartments). The prevailing discontinuity set of the subhorizontal slab is as expected the stratification set. However, we could not associate rockfall failure type or the compartment type to either the F1 or F2 discontinuity sets.



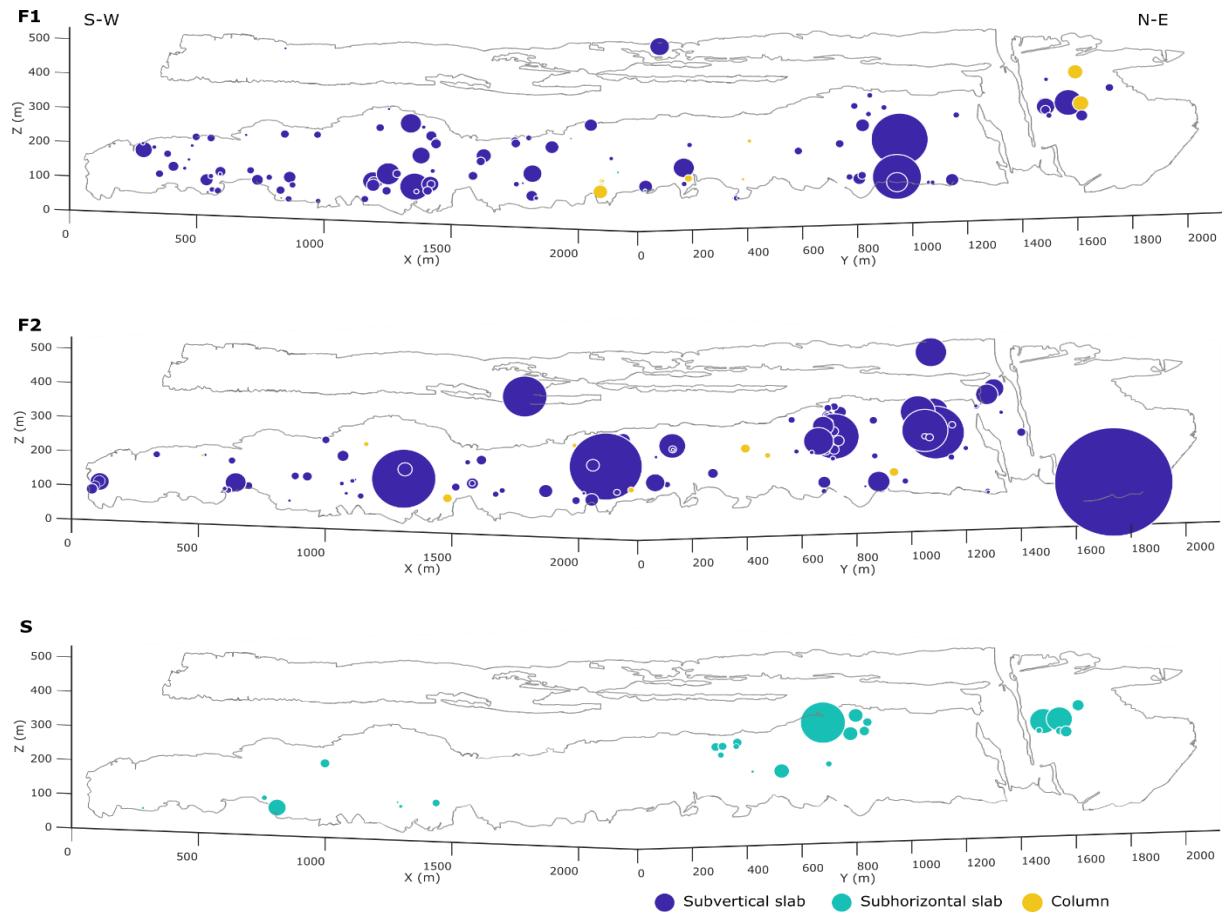


Figure 5.7. Rockfall distribution according to their prevailing discontinuity set a) F1, b) F2, c) stratification S. Circle sizes are function of rockfall volumes. Colors represent the compartment type, dark blue: subvertical slab, light blue: subhorizontal slab, yellow: column

Rockfall distribution varies with the change of predominant discontinuity set (Figure 5.6, Figure 5.8). In Figure 5.8, we present the volume distribution of Mount-Saint-Eynard rockfalls according to their prevailing discontinuity set F1 or F2. The volume distribution of rockfalls associated with F2 prevailing is characterized by a power law of exponent  $b=0.57\pm 0.02$ , lower bound of the power-law:  $0.7 \text{ m}^3$ . However, for a prevalence of F1, the rockfall distribution cannot be characterized by a power-law. This may be due to the reduced number of events. Nevertheless, it appears that for rockfalls volume  $10 < V < 50 \text{ m}^3$ , F1 is the predominant discontinuity sets. However, for  $V > 50 \text{ m}^3$ , F2 is the predominant discontinuity sets. This variation of distribution might be linked to the fracture density of the discontinuity sets limiting the apparition of volumes  $> 50 \text{ m}^3$  in the case of F1 discontinuity sets.

In this study, we bring to light the complex erosion behavior of Mount Saint-Eynard cliffs. Despite their geological consistency, the cliffs present variations in rockfall distributions. An increasing number of events  $> 50 \text{ m}^3$  occur closer to the Northern part of the cliffs. This variation appears to be associated with the evolution of the prevailing discontinuity set of the cliff. While rockfall volume distribution is affected, discontinuity sets do not seem to influence failure type or compartment types.

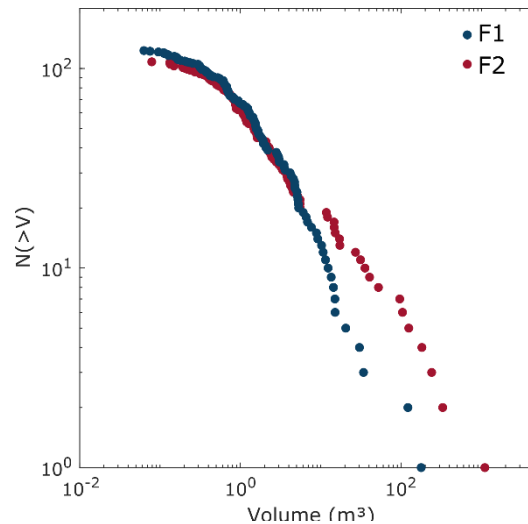


Figure 5.8. Volume distribution of the rockfall inventory. In blue: rockfalls characterized by prevailing discontinuity set F1 and in red F2. Rockfalls characterized by prevailing discontinuity set S where not represented due to their limited number.

## 5.5 Conclusions on rockfall monitoring using DEMs

Rockfall hazard is defined by the magnitude (volume, energy), recurrence time and location of rockfall occurrence. We saw that these elements could be determined using DEMs (rockfall volume distribution, location, frequency of occurrence, etc.). However, rockfall numbers and volumes can be significantly under- or over-estimated depending on the adopted methodology (2D/3D change detection methods, detection threshold, etc.). When using rockfall inventories to assess rockfall hazard, it is necessary to check whether the inventories are not skewed and that they are representative (proper monitored area and proper monitored time lapse).

In this study, we bring to light the complex erosion behavior of Mount Saint-Eynard cliffs. Despite their geological consistency, the cliffs present variations in rockfall distributions. An increasing number of events  $> 50\text{m}^3$  occur closer to the Northern part of the cliffs. This variation appears to be associated with the evolution of the prevailing discontinuity set of the cliff. While rockfall volume distribution is affected, discontinuity sets do not seem to influence failure type or compartment types.

---

## Part III

# Seismologic monitoring of rockfall





---

*Seismic monitoring of rockfalls offers numerous insights into event characteristics (timing, dynamics, location, etc.). We analyze rockfalls that occurred in limestone cliffs of the Chartreuse Massif (French Alps). These rockfalls were detected both by Terrestrial Laser Scanning or photogrammetry and by a local seismological network.*

*Rockfalls analyzed in this study occurred on complex topography. Characteristics of the seismic signal vary depending on the propagation mode of rockfalls (mass-flow, free-fall, sliding, bouncing...). Finding common relations between seismic signals and source properties for all types of rockfalls was therefore very challenging. In order to better characterize rockfall events using their seismic signals, we chose to select only events with the same propagation type instead of mixing different types of events. We aimed to develop individual methodologies to characterize each type of rockfall event: free-fall, mass-flow, rebounds.*

*We first focus on events that experienced a free-fall after their detachment (Chapter 6). The relations identified for Mount Saint-Eynard rockfalls were then tested on different geological settings and for a larger range of volumes using Yosemite, Mount Granier rockfalls and with a dataset of controlled releases of blocks (Hibert et al., 2017). In order to further analyze seismic characteristics of block impacts, we carried out controlled block releases (Chapter 7). A first dataset was obtained by releasing blocks (1 to 4 m<sup>3</sup>), on several protection embankment facings. A second dataset was obtained by releasing a small block (2.9 kg) on a tilted concrete block. We then focus on mass-flow type events (Chapter 8) and analyze a series of rockfalls that occurred in 2016 at Mount Granier.*

*The chapters of this part correspond to articles either accepted (Chapter 6), in review (Chapter 8) or in preparation (Chapter 7). Repetitions are thus present in these chapters, especially in the context presentation and methods.*

---



## 6 Seismic analysis of free-falling rockfalls

*We analyzed 21 rockfalls that occurred in limestone cliffs of the Chartreuse Massif (French Alps). These rockfalls were detected both by Terrestrial Laser Scanning or photogrammetry and by a local seismological network. The combination of these methods allowed us to study relations between rockfall properties (location of detachment and impacts areas, volume, geometry, propagation) and the induced seismic signal. We observed events with different propagation modes (sliding, mass flow, free-fall) that could be determined from Digital Elevation Models. We focused on events that experienced a free-fall after their detachment. We analyzed the first parts of the seismic signals corresponding to the detachment phase and to the first impact. The detachment phase has a smaller amplitude than the impact phase, and its amplitude and duration increases with rockfall volume. By measuring the time delay between the detachment phase and first impact, we can estimate the free-fall height. We found a relation between the potential energy of a rockfall and the seismic energy generated during an impact. We can thus estimate both the potential energy of a block and its free-fall height from the induced seismic signals. By combining these results, we obtain an accurate estimate of the rockfall volume. The relation between potential and seismic energy was tested on different geological settings and for larger range of volumes using Yosemite, Mount Granier rockfalls and with a dataset of controlled releases of blocks (Hibert et al., 2017).*

*This chapter has been published in the Journal of Geophysical Research: Earth Surface: Le Roy, G., Helmstetter, A., Amitrano, D., Guyoton, F., & Le Roux-Mallouf, R. (2019). Seismic analysis of the detachment and impact phases of a rockfall and application for estimating rockfall volume and free-fall height. Journal of Geophysical Research: Earth Surface, 124. <https://doi.org/10.1029/2019JF004999>*

### 6.1 Introduction

Characterizing rockfall properties such as location, occurrence time, volume and propagation path, is a key point to improve the mitigation of the associated hazards and to better prevent them. Several approaches can be used to detect rockfalls and to assess erosion activity such as satellite imagery or terrestrial and airborne laser scanning. These methods can deliver accurate information on detachment and impact zones, and on

released volumes. It thus provide volume-frequency relationships. However, temporal information is often limited as they rely on the survey lapse times (respectively 2.5, 0.5 and 1 year interval for Dewez et al., 2013; Kuhn and Prüfer, 2014; D'Amato et al., 2016). Hence, with these approaches, it is impossible to resolve the gradual collapse of blocks released from the same location or to determine the relation between rockfalls occurrence and external triggers. This presents significant drawbacks for the knowledge of site activity (number and size of individual events, occurrence time, triggering factor, etc.). In addition, monitoring using DEMs is yet difficult to apply automatically and cannot be used for real-time detection and warning system of rockfalls.

Continuous seismic monitoring provides a solution for this shortcoming as rockfalls can be automatically detected and located from the seismic signal they generate (Battaglia and Aki, 2003; Lacroix and Helmstetter, 2011; Burtin et al., 2013; Lévy et al., 2015; Dietze et al., 2017a). According to the definition given by Varnes (1978), a rockfall is a slope process that involves rock fragment detachment proceeding down the slope by free falling, bouncing, rolling, and sliding until their deposition. All these processes can be identified on rockfalls induced seismic signals. However, as gravitational mass wasting events are complex and composed of several processes occurring simultaneously, it is often difficult to determine the link between block dynamics and the seismic signals generated.

Seismic signals of rockfalls detachment have been identified in several studies (Rousseau, 1999; Deparis et al., 2008; Hibert et al., 2011; Dietze et al., 2017b). However, the origin of these signals was linked to different processes: elastic rebound of the cliff (Rousseau, 1999; Deparis et al., 2008; Hibert et al., 2011), fractures opening, and friction between the detached compartment and the cliff (Dietze et al., 2017b). In some cases, the detachment of a rockfall has been preceded by precursory signals. For instance, the 15 000 m<sup>3</sup> Illgraben rock avalanche (Rhône Valley, Switzerland) was preceded by seismic pulses lasting for a few seconds (Zeckra et al., 2015).

Controlled experiments allow an accurate estimation of rockfall properties, and thus a better understanding of the processes generating the seismic signal. Vilajosana et al. (2008) and Bottelin et al. (2014) studied artificially triggered rockfall events. These studies allowed relating the most energetic seismic phases to boulder impacts after a free-fall and showed that impacts were characterized by waves packets with frequency contents over the range 1-50 Hz. Controlled releases of single blocks in a marl gully (Hibert et al., 2017) or in quarries (Saló et al., 2018b) explored seismic amplitude and energy in relation to the kinetics of block impacts. Hibert et al. (2017) inferred single block mass and velocity from local seismic records with a fair accuracy (median ratio between calculated and measured velocity of 0.2). In contrast, Saló et al. (2018) did not find a correlation between kinetic parameters of the blocks and the measured seismic energies. All these studies highlight the large uncertainties on rockfall properties (volume, velocity, location, etc.) estimated from the associated seismic signal.

In the present study, we analyze Terrestrial Laser Scanning (TLS), photogrammetric and seismic data of natural rockfalls in order to investigate the relations between blocks dynamics and the associated seismic signal. The monitoring of two limestone cliffs, Mount Saint-Eynard and Mount Granier (Chartreuse massif, French Alps), allowed us to obtain numerous data on the characteristics of rockfalls (location, occurrence time, volume, failure mode, etc.).

We select 16 rockfalls from Mount Saint Eynard and Mount Granier that experienced a free fall phase and that were detected both by DEMs and seismic monitoring. We focus on the first part of the seismic signals (detachment and first impact), to better understand the link between seismic signals and rockfalls kinetics. This dataset allows us to establish scaling laws between seismic parameters (free-fall duration, frequency, seismic energy) and rockfall characteristics (volume, potential energy, free fall height).

A first data set of Mount Saint-Eynard rockfalls is used as a training data set to determine relations between rockfall properties and the characteristics of the seismic signals. These relations are then applied to a second data set of the Mount Granier rockfalls. Finally, we compare our results with two other sites, to test whether our relation could be applied to both smaller and larger rockfall volumes and for different geological settings. In the Yosemite area, we analyze the Happy Isle and Ahwiyah Point rockfalls to investigate volumes larger than 10 000 m<sup>3</sup>. The controlled releases of block of Hibert et al. (2017) extend the range of volumes down to 0.03 m<sup>3</sup>.

## 6.2 Study site

### 6.2.1 Chartreuse massif

Our main study area is located in the sedimentary cover of the External Crystalline Massifs of the French Western Alps (Figure 6.1). The Chartreuse massif is mainly composed of limestone and marls forming a succession of synclines and anticlines. The eastern edge of this massif is characterized by long linear limestone cliffs overtopping marly talus slopes. Two major rock formations make up these cliffs: Tithonian stage limestone and Urgonian stage limestone, with near-horizontal beddings. This study area is interesting due to its frequent rockfall activity covering a large range of volumes, from less than 1 m<sup>3</sup> up to a few thousand cubic meters. Typical failure configurations and triggering factors of rockfalls have been studied in previous studies (Frayssines and Hantz, 2006; D'Amato et al., 2016). These studies inferred that rainfall and freeze-thaw cycles had triggered about half of the rockfall during the studied period (2013-2015).

Mount Saint Eynard is located North East of Grenoble, Isère, French Alps (Figure 6.1a). It is a long doubled cliff making up the western border of the Isère Valley and the eastern edge of the Chartreuse Massif. It peaks at 1308 m above sea level. Its general morphology consists of two 7 km long subvertical cliffs dipping southeast (Figure 6.1c).

The lower cliff (240 m high) is separated from the 120 m high upper cliff by a forested ledge. The upper cliff consists of massive limestone of the Tithonian stage. The lower cliff consists of fractured thin-bedded limestone, of the Sequanian stage.

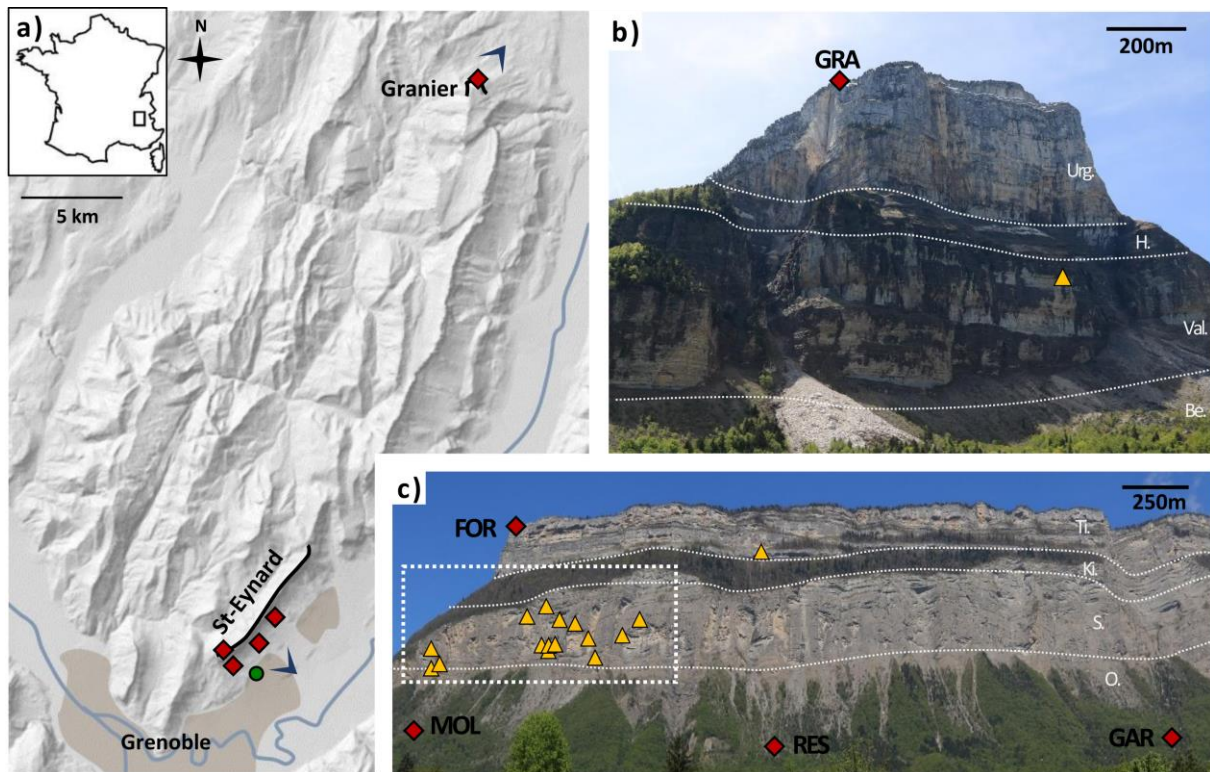


Figure 6.1. a) DEM of the Chartreuse massif (France), with the location of the photographs shown as blue triangles. b) photograph of the north face of Mount Granier. c): photograph of Mount Saint-Eynard. Red diamonds indicate the location of seismic stations, green dot is the camera enabling a time lapse monitoring of the cliff. Dashed rectangle: area monitored by TLS survey and by a photographic time lapse survey. Yellow triangles: location of origin of rockfall detachment areas. Stage formations: Urg. Urganian limestone, H. Hauterivian marls, Val. Valanginian limestone, Be. Berriasian marls, Ti. Tithonian limestone, Ki. Kimmeridgian marls, S. Sequanian limestone, O. Oxfordian marls.

Mount Granier (1933 m ASL), located north of the Chartreuse massif (Figure 6.1b), is an iconic mountain affected, in 1248, by one of the biggest landslides in Europe (500 million m<sup>3</sup>, Nicoud et al., 1999). Its north face, a 800 m high rock wall that appeared after the landslide, forms a natural geological cross section in Urganian limestone, Hauterivian marls, Valanginian limestone and Berriasian marls. Formed by perched syncline oriented to the east, the Mount Granier presents numerous fractures and karst network.

## 6.2.2 Other sites

In order to validate our method, we considered data from two other sites where seismic waves induced by rockfalls have been recorded. Yosemite Valley is a deep, glacier-carved valley bounded by steep granite cliffs. These steep cliffs produce numerous

rockfalls and rockslides, which range from small boulders to massive events of several million cubic meters. In this study, we focus on three events exceptional due to their size and induced damages. The Happy Isles rockfalls occurred on July 10, 1996 (Morrissey et al., 1999; Wieczorek et al., 2000). Two rockfalls of combined volume estimated between 23 000 and 38 000 m<sup>3</sup> broke loose from cliffs adjacent to the Happy Isles Nature Center. The impact of these blocks generated pressure waves that downed over 1000 trees, destroyed a bridge and caused one fatality and several injuries. We also study the unusually large rockfall (25 400 m<sup>3</sup>, which dislodged en route 21 300 m<sup>3</sup>) that occurred in 2009 near Ahwiyah Point (Zimmer et al., 2012).

In order to study smaller rockfalls, we analyzed data from controlled releases of single blocks carried out by Hibert et al. (2017). 28 blocks, with masses ranging from 76 kg to 472 kg, were released within a soft-rock gully of the Rioux Bourdoux torrent (Barcelonnette, French Alps). Rioux Bourdoux slopes consist mainly of Callovo-Oxfordian black-marls. Due to the high erosion susceptibility of this facies, this site presents numerous steep gullies.

### 6.2.3 Instrumentation of the Chartreuse massif sites

#### 6.2.3.1 Mount-Saint-Eynard

Mount Saint-Eynard has been monitored since 2013 by several methods. The south of the Mount Saint-Eynard has been yearly surveyed by TLS since 2009, using an Optech Iris-LR laser scanner, along a 750 m zone of interest (D'Amato et al., 2016). In this study, we focus on rockfalls detected at the Mount Saint-Eynard cliffs between November 2013 and December 2015. In order to monitor a larger area, located between the seismic stations MOL and GAR (Figure 6.1c), and to reduce the delay between TLS surveys (once a year), we have carried out sporadic photogrammetric surveys over a larger area. These surveys were carried out using data sets of more than 500 photographs (camera Canon EOS 7D, resolution 5-9 cm/pixel, focal length ranging from 24 mm to 200 mm) taken from 12 locations at the base of Mount Saint-Eynard. The cliffs are also monitored using an autonomously operating camera Canon EOS Rebel T3 1100D (Figure 6.1c) taking photographs every 10 min.

In 2013, four broad band 3-components seismometers (Guralp CMG40T, with a corner frequency of 0.1 Hz and a sampling frequency of 100 Hz) have been installed a few hundred meters apart, to detect rockfall activity. Stations MOL, RES and GAR are located at the cliff foot on top of scree, while station FOR is located on the cliff head, on top of rock (Figure 6.1c).



### 6.2.3.2 Mount Granier

There were no TLS or photogrammetric time lapse surveys at Mount Granier. Therefore, we used sporadic photogrammetry surveys to reconstruct DEMs. Three Mount Granier photogrammetric surveys were carried out between January and February 2017, providing each a dataset of 100 photographs taken from eight locations (resolution < 8 cm/pixel). The first photograph dataset gathers photographs taken in January and April 2016. The second and third dataset consist of photographs taken a few days after the occurrence of events A and B.

In 2016, a series of rockfalls occurred at Mount Granier with volumes up to 75 000 m<sup>3</sup> (Hobléa et al., 2018). In order to monitor the Mount Granier rockfall activity following these rockfalls, station GRA, was installed on the cliff head of Mount Granier (Figure 6.1) in June 2016. The seismometer was a 3-component velocimeter with a corner frequency of 2 Hz. The signal was sampled at 250 Hz. When events were seismologically detected, complementary photogrammetric surveys were carried out within the next week.

## 6.3 Methods

### 6.3.1 Topographic data analysis

Repeated topographic surveys allow identifying missing rock mass volumes, which can be interpreted as result of rockfalls and provide information on its detachment area, impact area, volume, free-fall height and failure mechanism. Point clouds were constructed using Structure from motion (SfM) technics with Agisoft Photoscan software. Raw point clouds were cleaned, in order to remove vegetation noise and keep only the rock surface. Mount Saint Eynard point clouds were georeferenced using a georeferenced point cloud of the site obtained by airborne laser scanning in 2011. Mount Granier point clouds were georeferenced using a georeferenced 1 m spacing DEM of the site (from the IGN, French National Institute of Geography). The co-registration (or alignment) of the 3D point clouds is achieved first by a manual alignment, which consists in identifying common points in the different point clouds. Following this rough matching, we then apply an automated iterative procedure with a point-to-surface Iterative Closest Point (ICP) algorithm (Besl and McKay, 1992; Teza et al., 2007), in order to minimize the co-registration errors. The quality of photogrammetric surveys is slightly coarser than TLS surveys (mean points distance for photogrammetric surveys: 15 cm, TLS surveys: 10 cm). Once raw point clouds are georeferenced and meshed, deviation between DEMs are measured. We considered negative deviations larger than a threshold (TLS: 10 cm; photogrammetry: 30 cm, corresponding to a 99.5% quantile of the distribution of the distance between the two point clouds), as rockfalls.

3D reconstructions provide constraints on the morphology of the fallen compartments. For each event, volume, surface and geometry (length, width, depth, and gravity center) can be determined. For Mount-Saint Eynard area, this work was primarily carried out by D'Amato et al. (2016). They determined the volume and geometry of the detected events. We reprocessed these TLS point clouds to retrieve complementary information (volume uncertainty, free-fall height, cliff profile).

Based on these characteristics and by considering that the main force involved in the process is gravity, we can determine failure mechanisms. Depending on the weight vector characteristics (built from the gravity center, Figure 6.2a, b), two main types of failure were considered, (i) slide and (ii) free-fall or topple. When the weight vector intersects the cliff, the mechanism is a slide (Figure 6.2a). When it intersects a free face, the failure type is free-fall (Figure 6.2b) or topple. Topple involves a forward rotation out of the slope of the compartment about an axis below the center of gravity of the compartment (Cruden and Varnes, 1996). This kind of failure is likely to occur if the lower part of the compartment is intact whereas fractures are present in its upper part. For topple or free-fall detachment, no, or little, shear displacement takes place, contrary to slide failure. Topple and free-fall could not be distinguished in this study due to the lack of information on the repartition of fractures before failure. We thus use the term “free-fall” to designate both free-fall and topple mechanisms in the following.

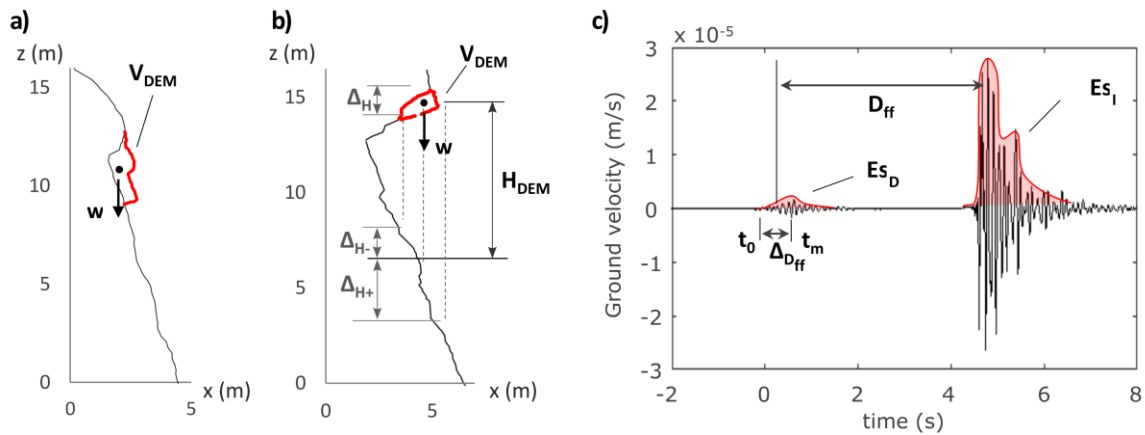


Figure 6.2. Definition of the metrics used in this study using a), b) DEM of the cliff and c) rockfalls seismic signals of the 01.18.2015 event. a) Cliff profile of the 02.02.2015 event presenting a sliding failure mechanism, b) cliff profile of the 15.08.2014 event presenting a free-falling failure mechanism. The black arrow represents the weight vector  $w$  built from the gravity center.

Some rockfalls experienced a free-fall after their detachment. In this case, the free-fall heights are obtained by measuring the distance  $H_{DEM}$  between the gravity center of the compartments and their vertical projections on the cliff face. As illustrated in Figure 6.2b,  $\Delta_H$  the uncertainty on  $H_{DEM}$  depends on the size of the compartment and on the angle of the slope, e.g., a steeper slope induces a larger uncertainty. The 25.11.2015 event underwent a 2 m slide after its detachment. In this case, the impact location and free-

fall height were constrained by clear impact marks observed on the field. Using the DEMs, we can also calculate the potential energy of a rockfall  $E_{pDEM}$  before its impact.

$$E_{pDEM} = \rho V_{DEM} g H_{DEM} \quad (6.1)$$

where  $V_{DEM}$  is the volume,  $\rho$  is the density and  $g=9.81 \text{ m.s}^{-2}$  is the gravity constant.

### 6.3.2 Detection and classification of seismic signals

A rockfall event is characterized by a series of pulses of ground velocity with frequency contents between 5 and 50 Hz and duration between several seconds and about one minute (Dietze et al., 2017a; Provost et al., 2018). This characteristic pattern makes rockfalls distinct from other sources, such as earthquakes and anthropogenic noise.

We have used the method of Helmstetter and Garambois (2010) in order to detect seismic events. The detection is performed by analyzing the seismic energy between 2 and 20 Hz averaged over all stations. An event is detected when the amplitude exceeds the long-term average by a factor of 3 or more. Events that are also detected by the regional seismic network Sismalp are automatically classified as earthquakes. We check all events in order to classify them based on the properties of rockfall seismic signals described in previous studies (Helmstetter and Garambois, 2010; Provost et al., 2018). The configuration of the network, with large distances between stations, does not allow us to use the apparent velocity or the inter-trace correlation as classifying parameters. Earthquakes are characterized by distinct P and S waves, and have similar waveforms on all stations (amplitude, frequency content and shape of envelope). Rockfalls usually display a more complex envelope, with a succession of peaks corresponding to successive block rebounds. Events that are only visible at one station are likely noise (e.g., road traffic). Wind, rainfall and storms also generate seismic signals, which can be recognized by their relatively high-frequency content (mostly above 20 Hz) and by a large variability of signal properties between stations. For signals with ambiguous waveforms, we checked the seismic signal at nearby seismic stations from the regional network Sismalp to help distinguishing earthquakes from rockfalls.

The small number of sensors and the large distance between sensors do not allow an accurate source location. Signals are emergent, therefore manual picking is difficult, and uncertainty can be as large as 1 second, leading to large location errors. The large distances (several hundred meters) between sensors make inter-sensor correlation very weak and does not allow the use of beam-forming methods (Lacroix and Helmstetter, 2011; Dietze et al., 2017a). Nonetheless, we can obtain information about the source location from manual picks of the seismic signals and from amplitude ratios (corrected from site effects). The rockfall is likely located closest to the station with the strongest amplitude. This information is only used to select rockfalls that are likely located within the study area.

### 6.3.3 Characterization of rockfalls from seismic signals

In order to compare characteristics of the seismic signals and rockfalls dynamics, we use six metrics extracted from either the seismograms or the DEMs: seismic energy of the detachment phase  $E_{sD}$ , seismic energy of the impact phase  $E_{sI}$ , detachment phase duration  $D_{urD}$ , free-fall duration  $D_{ff}$ , rockfall volume measured  $V_{DEM}$  and free-fall height  $H_{DEM}$  measured on the DEMs. Figure 6.2 presents an overview of the different metrics.

To calculate the seismic energy  $E_s$ , we assume a point-source (Kanamori and Given, 1982; Eissler and Kanamori, 1987) and we consider the medium as isotropic and homogeneous. We also consider that surface waves dominate the seismic signal (Dammeier et al., 2011; Lévy et al., 2015; Lévy et al., 2018). Signals were band-pass filtered between 2 and 50 Hz for the entire analysis.

The following relations were used:

$$E_s = 2\pi r p h c \int_{t_0}^{t_1} u_{env}(t)^2 e^{\alpha r} \varepsilon dt \quad (6.2)$$

$$u_{env}(t) = \sqrt{u(t)^2 + H(u(t)^2)} \quad (6.3)$$

$$u(t) = \sqrt{u_E^2(t) + u_N^2(t) + u_Z^2(t)} \quad (6.4)$$

where  $t_0$  and  $t_1$  are the manually picked onset and end times of the seismic signal,  $r$  is the distance between the event and the recording station,  $h$  is the thickness of the layer through which surface waves propagate,  $p$  is the ground density,  $c$  is the phase velocity of the seismic waves,  $u_{env}(t)$  is the envelope of the ground velocity  $u(t)$  obtained using the Hilbert transform ( $H$ ),  $\alpha$  is a damping factor that accounts for inelastic attenuation of the waves (Aki and Richards, 1980) and  $\varepsilon$  a coefficient accounting for site effects. Uncertainties on the distance, frequency, ground density, attenuation factor and wave velocity are taken into account in the calculation of seismic energy.

The distance between the detachment zone and the stations is well constrained by DEM data. For free-fall events, the distance between the impact area and each station is determined as the distance between the station and the intersection of the vertical projection of the compartment gravity center and the cliff face. We considered that this distance was prone to a maximal error of 20 m for Mount Saint-Eynard and 30 m for Mount Granier, due to the size of the block and to the slope angle in the impact zone (see Figure 6.2b and 3c).

We have estimated the seismic wave velocity from the location of rockfalls estimated from the TLS surveys and from the manual picking of the first impact for all stations and all rockfalls detected at Mount Saint Eynard. We search for the velocity  $V$  that minimizes the residuals on the differential travel times. For each rockfall and each couple of stations  $i, j$ , we estimate the difference in arrival times  $t_j - t_i$ . The theoretical travel time

delay is  $(r_i - r_j)/V$ . Minimizing the differences between the observed and theoretical time delays allows us to estimate  $V = 1810 \pm 100 \text{ m.s}^{-1}$  (Figure 6.3a).

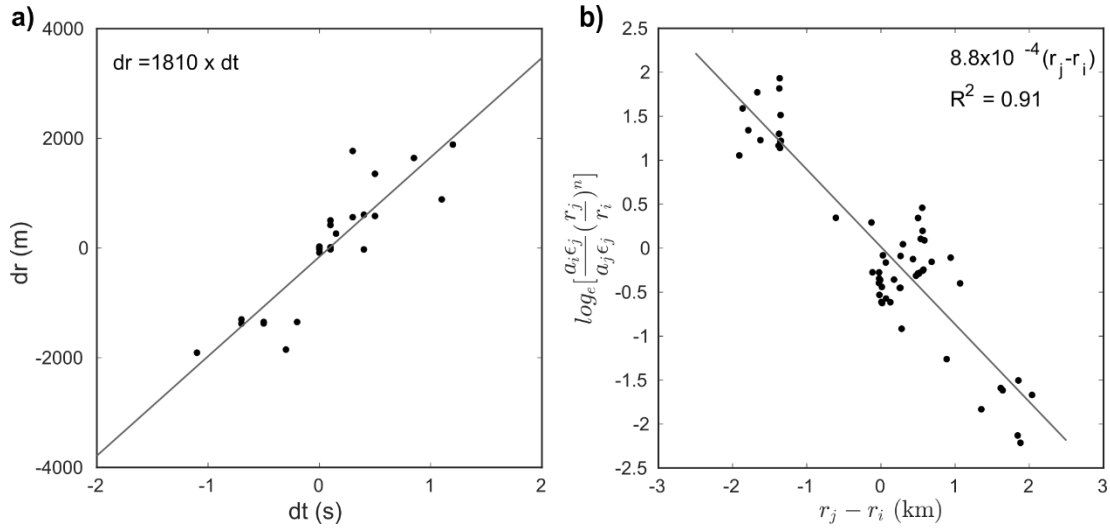


Figure 6.3. a) Estimation of the seismic wave velocity. For each rockfall detected at Mount Saint Eynard and each couple of stations, we plot the difference in source-station distance  $dr$  as a function of the time delay between the impact time detected on each seismogram. b) Estimation of the attenuation factor  $\alpha$  using equation (6.6) with  $n=0.5$ .

We assume a density of  $2500 \pm 100 \text{ kg.m}^{-3}$ . The frequency centroid of the impact seismic signals averages at  $10 \pm 2 \text{ Hz}$ . Therefore the thickness was taken as one wavelength of Rayleigh waves,  $h = 181 \pm 20 \text{ m}$  for a frequency of  $10 \text{ Hz}$ . We have estimated the site effect coefficient  $\varepsilon$  using a catalog of 200 earthquakes recorded by the Mount Saint-Eynard network and located by the regional seismic network Sismalp. We have computed the ratio of amplitude at stations MOL, GAR and RES over the reference station FOR located at the cliff head. This way we were able to correct the amplification at each station (Borcherdt, 1970). Site effect of Mount Granier was computed using 4 earthquakes recorded by the reference station FOR and by station GRA.

In order to estimate the attenuation factor, we used the relationship derived by Kanai et al. (1984):

$$\left[ \frac{a_i}{a_j} \left( \frac{r_i}{r_j} \right)^n \right] = \left( \frac{\varepsilon_i}{\varepsilon_j} \right) - \alpha(r_j - r_i) \quad (6.5)$$

with  $a_i$  and  $a_j$  the maximum amplitudes at two stations filtered around the frequency centroid, between  $9$  and  $11 \text{ Hz}$ ,  $n = 0.5$  for surface waves,  $r_i$  and  $r_j$  the corresponding epicentral distances, and  $\varepsilon_i$  and  $\varepsilon_j$  constants depending on the ground and installation conditions of each sensor. This method has also been used in previous studies of rockfalls (Lévy et al., 2015; Hibert et al., 2017).

Since we have estimated the site effects term  $\varepsilon$  for each station, we can normalize each signal by this factor and rewrite (6.5) as

$$\left[ \frac{a_i \varepsilon_j}{\varepsilon_i a_j} \left( \frac{r_i}{r_j} \right)^n \right] = -\alpha(r_j - r_i) \quad (6.6)$$

We can thus estimate  $\alpha$  from a linear regression using Equation (6.6). We have selected seismic records of the rockfalls detected at Mount Saint Eynard (listed in Table 6.1) at all stations. Using the location derived from the topographic analysis, we have estimated  $\alpha=8.8 \times 10^{-4} \text{ m}^{-1}$  (Figure 6.3) with a regression uncertainty of  $\pm 0.9 \times 10^{-4}$  (confidence interval 68%). This factor is sensitive to the choice of the frequency band. Thus, as the centroid frequency of the impact phase has been determined as  $10 \pm 2 \text{ Hz}$ , the lower bound of  $\alpha$  has been set to  $6.9 \times 10^{-4} \text{ m}^{-1}$  (frequency 8 Hz) and the upper bound to  $10.3 \times 10^{-4} \text{ m}^{-1}$  (frequency 12 Hz).

There is only one station at Mount Granier, therefore we cannot estimate seismic wave velocity or the damping factor. We thus assume that material parameters ( $V$ ,  $h$ ,  $p$ ,  $c$  and  $\alpha$ ) are the same as for Mount Saint-Eynard, since the geological context is similar in both cases.

Seismic energy can also be derived from the Gutenberg-Richter magnitude-energy relation with  $M$  the magnitude (Kanamori and Anderson, 1975).

$$\text{Log}E_s = 1.5M + 4.8 \quad (6.7)$$

This relation was used for the Yosemite rockfalls.

When the fallen compartment undergoes a free-fall immediately after its detachment, the seismic signal of the detachment phase can be isolated from the blocks propagation. In our dataset, when the seismic signal of the detachment and first impact are not overlapping, it is possible to calculate the free-fall height  $H_s$  by measuring the free-fall duration  $D_{ff}$ :

$$H_s = \frac{D_{ff}^2 \cdot g}{2} \quad (6.8)$$

where  $g$  is the gravity constant ( $9.81 \text{ m/s}^2$ ). The impact time is determined on the seismograms at the maximum amplitude of the impact phase. In order to determine the detachment time, we average the initial time of the detachment phase  $t_0$  and the time of maximum amplitude  $t_m$  (see Figure 6.2c).

## 6.4 Rockfall databases

We have constructed a database of rockfalls at Mount Saint Eynard and Mount Granier by coupling topographic surveys and seismic monitoring. We tried to associate each rockfall detected using DEMs with a rockfall seismic signal. Complementary information on the rockfall databases can be found in the supplementary material B.

As described in paragraph 6.2.2, we also analyze two other datasets, Yosemite rockfalls and controlled releases of blocks, in order to extend the range of rockfall volumes.

### **6.4.1 Rockfall catalogs obtained by topographic data**

The south of the Mount Saint-Eynard has been yearly surveyed by TLS along a 750 m zone of interest (D'Amato et al., 2016). We use the database obtained by D'Amato et al. (2016), who detected 508 events by TLS comparison between November 2013 and April 2015 with volumes as small as 0.01 m<sup>3</sup>. The majority of these events have volumes < 0.5 m<sup>3</sup>. Only 51 events volumes were > 0.5 m<sup>3</sup> and 15 events > 2m<sup>3</sup> (see supplementary B).

There was no regular monitoring of Mount Granier using TLS or photogrammetric surveys. Rockfalls were first detected by the seismic station GRA. After these events, we reconstructed DEMs of the cliff based on existing photographs taken before the rockfalls and we performed photographic surveys after the rockfalls.

### **6.4.2 Rockfall catalogs obtained by seismic monitoring**

#### **6.4.2.1 Mount Saint-Eynard**

At Mount Saint-Eynard, we have detected several thousand events between November 2013 and December 2015. Most of these events have been classified as noise (electronic noise, road traffic, helicopters, storms...). Most of the remaining events (740) are likely seismic signals. Most of these events have also been detected by the regional seismic network Sismalp. We found only 87 events that could be identified as rockfalls. Among these events, 46 events were ruled out because the seismic signal had a stronger amplitude at station RES and GAR compared to station MOL, indicating that they were likely located outside of the area monitored by the photographic time lapse survey. This spatial distribution of event (about 50% of events located between stations MOL and RES) is consistent with the data provided by photogrammetric surveys, which cover the area located between stations MOL and GAR (40% of the events detected by photogrammetry occurred between stations MOL and RES.). We also discarded all events detected by only one seismic station (7 events).

#### **6.4.2.2 Mount Granier**

At Mount Granier, thousands of events were also detected between June 2016 and June 2017. Most of these events likely originate from the cliff just under station GRA, where a large rockfall occurred on May 2016 (Hobléa et al., 2018). Most events were indeed very short and high frequency. On the night of January 17<sup>th</sup>-18<sup>th</sup> 2017, we detected two events with amplitudes and duration much larger than all preceding events. Between these two large events, we also detected two smaller events, with similar waveforms but

smaller amplitudes. Another seismic signal with similar properties was detected on February 1<sup>st</sup> 2017.

### 6.4.3 Association of topographic and seismic data

#### 6.4.3.1 Mount Saint-Eynard rockfalls

In order to associate events detected by TLS to those seismologically detected, we used the dating periods determined with the time-lapse photographic survey. This information allows us to associate events detected by TLS to those seismologically detected. In several cases, especially during winter when nights are longer and weather conditions unfavorable, several events can be distinguished within a pair of photographs. In this case, it is impossible to associate unambiguously events detected by TLS and by the seismic network. In order to avoid any mismatch, if several events can be distinguished within a pair of photographs, these events were ruled out.

One event detected by photogrammetry at the Mount-Saint-Eynard was added to this catalog (25.11.2015-03:54:39). This event, located outside of the area monitored by the photographic time-lapse survey, could not be accurately dated making the association with seismically detected events ambiguous. During the time interval between two photogrammetric surveys (27 days), three rockfalls have been detected by the seismic network. Among these events, two events likely occurred near station MOL, as the amplitude at station MOL was much larger than at station GAR. The last event had similar amplitudes at stations MOL and GAR, in agreement with the rockfall location determined by photographic survey in between MOL and GAR. This allowed us to associate the event detected by photogrammetry to its seismic signal.

#### 6.4.3.2 Mount Granier rockfalls

Field observations on January 20, 2017 revealed the occurrence of a recent rockfall on the north face of Mount Granier. It was clearly visible as the rock deposits were not covered by snow. Since the last snow fall occurred on January 14, it provides a strong constraint on the date of occurrence, and allows us to associate this rockfall with the seismic signals recorded at station GRA on January 17<sup>th</sup>-18<sup>th</sup> 2017 (events A<sub>1</sub>, A<sub>2</sub>, A<sub>3</sub>, A<sub>4</sub>, in Table 6.1). Another seismic signal with similar properties was detected on February 1<sup>st</sup> (event B). It can be associated with another rockfall that occurred at the same location and that can be dated from photographs taken the 2<sup>nd</sup> of February 2017. By constructing DEMs using photogrammetry, we could locate and measure the volume of the event of February the 1<sup>st</sup>. However, due to the quick succession of the first sequence of rockfalls, we were only able to build a 3D model corresponding to the cumulated volume of the A<sub>1-4</sub> sequence (Figure 6.4, Table 6.1).



Table 6.1. Rockfall characteristics.

Site	Event	Dating interval <sup>(a)</sup>	Failure mechanism <sup>(b)</sup>	Volume V <sub>DEM</sub> (m <sup>3</sup> )	Volume V <sub>ESD</sub> <sup>(c)</sup> (m <sup>3</sup> )	Volume V <sub>ESl</sub> (m <sup>3</sup> )	Free-fall height DEM (m)	Free fall height (m)
Saint-Eynard	04.11.2013 – 19:35:36	1 day	topple	1.4 ± 0.1	2.2 - 2.6	0.5 - 0.9	37 - 67	31 - 44
	16.11.2013 – 22:11:37	1 day	topple	13.6 ± 0.1	3.8 - 5.0	3.0 - 14.8	6 - 11	12 - 19
	25.11.2013 – 06:44:54	10 min	topple	3.2 ± 0.1	3.9 - 9.6	1.3 - 6.4	12 - 38	21 - 37
	06.12.2013 – 04:25:05	2 days	topple	6.1 ± 0.1	3.2 - 4.9	4.5 - 19.2	19 - 28	24 - 28
	30.12.2013 – 23:27:19	1 day	topple	5.1 ± 0.1	2.9 - 3.9	2.2 - 9.0	12 - 38	36 - 48
	07.02.2014 – 22:00:40	2 days	topple	1.9 ± 0.1	-	-	0 - 1	-
	08.02.2014 – 19:48:44	10 min	sliding	1546.5 ± 5	-	-	0	-
	15.08.2014 – 01:08:33	1 day	topple	5.3 ± 0.2	3.1 - 3.9	2.4 - 10.1	6 - 17	16 - 24
	07.01.2015 – 08:45:12	1 day	topple	1.2 ± 0.1	-	-	0 - 1	-
	18.01.2015 – 08:20:13	1 day	topple	100.4 ± 0.2	61.4 - 140.6	40.4 - 182.4	79 - 82	65 - 88
	22.01.2015 – 21:01:31	1 day	topple	1.9 ± 0.1	3.8 - 4.3	1.1 - 7.2	5 - 8	3 - 10
	02.02.2015 – 17:44:10	1 day	sliding	14.7 ± 0.1	-	-	0	-
	15.02.2015 – 20:54:28	1 day	topple	8.0 ± 0.1	14.9 - 26.3	3.1 - 13.8	98 - 105	90 - 119
	05.03.2015 – 19:36:19	1 day	topple	20.7 ± 0.1	-	-	0 - 1	-
	18.04.2015 – 01:13:11	1 day	sliding	2.0 ± 0.1	-	-	0	-
25.11.2015 – 03:54:39	27 days	sliding	94.0 ± 5	38.1 - 79.4	35.6 - 216.5	20 - 36	23 - 44	
Granier	17.01.2017- 21:38:12 (A <sub>1</sub> )		-		71.1 - 164.9	108.5 - 632.5		125-189
	17.01.2017 – 23:20:29 (A <sub>2</sub> )		-		18.2 - 31.6	0.8 - 2.6		127-140
	18.01.2017 – 01:10:18 (A <sub>3</sub> )	6 days	-	4600 ± 50	10.7 - 18.1	2.7 - 9.3	100-160	97-107
	18.01.2017 – 01:12:30 (A <sub>4a</sub> )		-		256.5 - 828.2			78-104
	18.01.2017 – 01:12:32 (A <sub>4b</sub> )		-		534.5 - 1950.8	570.7 - 3533.1		73-89
	01.02.2017 – 12:14:38 (B)	13 days	sliding	11.5 ± 0.5	20.2 - 41.0	3.8 - 18.8	110-175	141-183

(a) Dating interval is based on photographic surveys and field evidences.

(b) Failure mechanism is described in section 6.3.1.

(c) The detachment phase is not visible for 6 Mount Saint-Eynard rockfalls (empty cells).

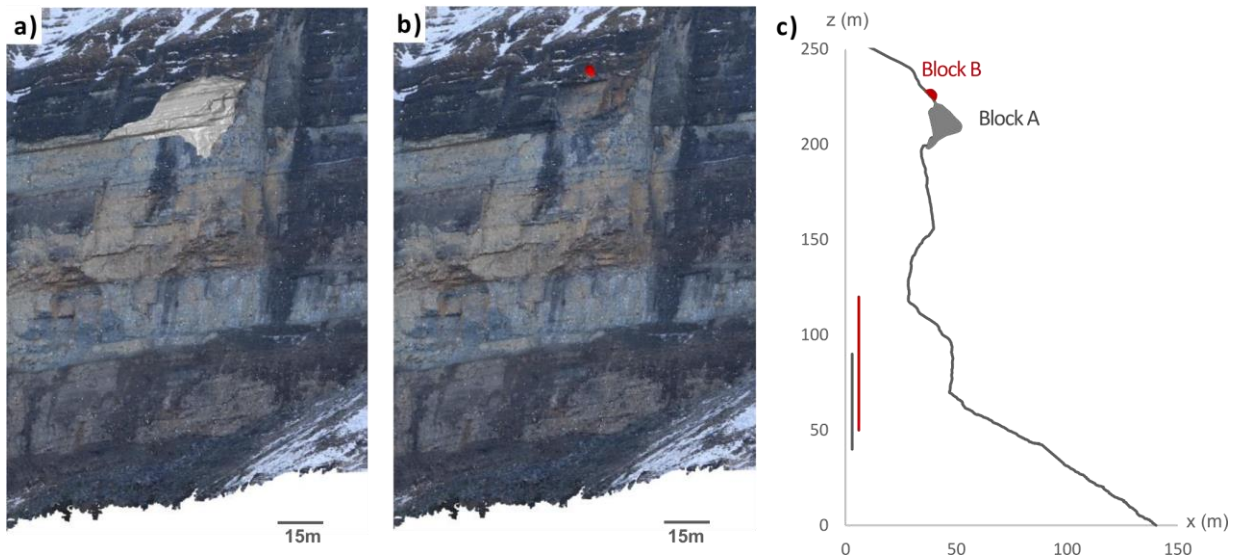


Figure 6.4. a) Illustration of the set of events A1-4 (January 17th-18th 2017), photographs taken January 19th, in grey: rockfall compartment, b) DEM of the event B (February 1st 2017), photographs taken February the 2nd, in red: rockfall compartment, c) cliff profile with the event location in red. Colored lines: calculated impact areas of events A and B obtained from the DEM.

#### 6.4.4 Characteristics of selected rockfalls for Mount Saint Eynard and Mount Granier

By coupling DEM and seismic monitoring, we have compiled a catalog of 16 rockfalls that occurred at Mount Saint-Eynard between November 2013 and December 2015 with an accurate time, location, geometry and volume (Table 6.1). The volume of these events ranges from  $1.4 \text{ m}^3$  to  $1550 \text{ m}^3$ . Among these 16 events, it is possible to distinguish the detachment phase for 10 events. This catalog is completed by five rockfalls that occurred at Mount Granier.

Mount Saint Eynard is better instrumented than Mount Granier (regular TLS and time-lapse photographic surveys, more seismometers). Therefore, rockfall parameters (volume, free fall height, seismic energy...) are better constrained. We thus use this site as a training dataset to build scaling laws between rockfalls properties (volume, free-fall height, potential energy) and seismic parameters (seismic energy, free-fall duration). Mount Granier has a similar geological setting than Mount Saint Eynard and allows us to extend the range of investigated volumes and free-fall heights.

#### 6.4.5 Other datasets: controlled releases of blocks and Yosemite park rockfalls

We analyze three very large rockfalls that occurred in Yosemite valley, with well constrained parameters, to test how seismic energy scales with rockfall volume. The

rockfalls were detected by regional seismic sensors located several tens of kilometers away. The first two events, Happy Isles rockfalls, occurred on July the 10<sup>th</sup> 1996 (Morrissey et al., 1999; Wieczorek et al., 2000; Stock et al., 2013). Rockfall characteristics were reconstructed by Morrissey et al. (1999) and Wieczorek et al. (2000) from eyewitness accounts, seismic records and field evidences. Four separate events occurred within a short time interval. The first two events, which mobilized between 23000 and 38000 m<sup>3</sup> of granite, experienced a 550 m free fall. The impact at the base of the cliff generated seismic waves with magnitudes of 1.55 for the first block (block A) and 2.12 for the second block B (Morrissey et al., 1999). Seismic energies ( $1.33 \times 10^7$  J and  $9.5 \times 10^7$  J, respectively for block A and B) were inferred from the magnitude using Equation (6.7). (Stock et al., 2013) estimated that the volume of block A represented about 15 to 20% of the total volume. In this study, we thus assume a volume of 3450-7600 m<sup>3</sup> for block A and 15450-34500 m<sup>3</sup> for block B. These two blocks slid down a steeply inclined ramp or shelf. They then fell on a ballistic trajectory about 500 m before hitting the northern part of a talus slope at the base of a cliff. In order to estimate the potential energy of these events, we use two extreme free fall heights: 665 m, which represents the total height from the point of origin of the blocks to the base of the cliff, and 500 m, which represents only the height for which the block fell with a ballistic trajectory. This way we estimate that the potential energy ranges between  $4.5 \times 10^{10}$  and  $1.3 \times 10^{11}$  J for block A and between  $2.0$  and  $5.9 \times 10^{11}$  J for block B.

The third event occurred in 2009 near the summit of Ahwiyah Point. The rockfall involved a block of volume  $27\,400 \pm 1370$  m<sup>3</sup> that slid off a ramp after its detachment and fell approximately 350 m down the northwest face of Ahwiyah Point. It then impacted a prominent ledge, which induced the dislodging of additional material. The combined debris then tumbled down the cliff over an additional 300 m. The rockfall volume was estimated from airborne LiDAR surveys collected in 2006 and 2010 (Zimmer et al., 2012). This event was detected on seismic networks as far away as 350 km and was measured as a magnitude 2.4 (seismic energy  $2.5 \times 10^8$  J). Zimmer et al. (2012) studied this event, its dynamics and trajectography. They determined that the primary seismic signal was induced by the impact, at a high velocity of the falling block ( $73 \pm 5$  m/s), on a prominent ledge 300 m below the bottom of the source area. This way, the kinetic energy of the falling block before impact was estimated to  $4.0 \pm 0.75 \times 10^{11}$  J.

Finally, we compare our results with the controlled releases of single blocks performed by Hibert et al. (2017). 28 blocks with mass ranging from 76 to 472 kg were manually launched within one gully. Block propagation was monitored using short-period and broadband seismic stations allowing to record the seismic signal generated at each impact. Block trajectories and impact dynamics were reconstructed with video cameras (Sony alpha7 - 25 frames per seconds). Block travel paths of length of approximately 200 m, is characterized by slope angles ranging from 20 to 45 degrees. Kinetic energy of block impacts ranges between  $10^3$  and  $10^5$  J.

## 6.5 Analysis of seismic signals

### 6.5.1 Rockfall seismic signals typology

Figure 6.5 presents three examples of rockfall seismic signals along with their runout topography and volume. The first example (a) corresponds to a rockfall experiencing a succession of rebounds before rolling on the scree. It may have fragmented during its impacts and have mobilized loose blocks in the debris slopes while other blocks may have stopped along the slope. The second example (b) is typical of rockfalls that experienced a long free-fall after their detachment. After impacting the cliff foot, the fallen compartment underwent an important fragmentation, leading to a mass flow type propagation of the blocks. The third example (c) is a more complex event. Due to the irregular topography of the cliff, the blocks experienced different propagation modes: free-fall, rebounds, and mass flow.

The analysis of seismic signals highlights the complexity and variability of rockfalls. It is possible to identify the block propagation mode through the analysis of seismic signals. Combined movement of several particles leads to a smooth seismic signal as rebound wave packets overlap. In the case of mass flow propagation, the simultaneous arrivals of the waves produced by a combined movement of numerous particles lead to a rather smooth envelope with frequency concentrating around 5-20 Hz. In contrast, seismograms of events having suffered little or no fragmentation present irregular envelopes showing several energetic pulses. These pulses can be linked to rebounds of blocks along the cliff. As also observed by Vilajosana et al. (2008) and Bottelin et al. (2014) the most energetic phases are produced by impacts after a free-fall. These impacts generate impulsive signals with frequency contents up to 50 Hz, whereas successive block rebounds are less energetic with more emergent waveforms and frequencies up to 30 Hz.

Our goal is to link rockfall properties (failure mechanism, propagation mode, free-fall height, volume, propagation velocity, extension) with characteristics of the seismic signal (signal duration and energy, frequency content, envelope properties). The studied events display a wide variability of volume and propagation mode. Some events went through free-fall phases whereas others only rolled and tumbled down the slope. This variability of rockfall sources leads to very different rockfalls signals. Finding common relations between source properties and seismic signals is therefore very challenging. In this study, we select only rockfalls with a free-fall phase and with a detachment seismic signal that can be isolated from the propagation phase. To remove the influence of the propagation mode, we focus on the first parts of the seismic signals, the detachment phase and the first impact. We assume that the rockfall compartment detached in one piece and that the associated seismic signal corresponds to the entire compartment detected by TLS or photogrammetry.

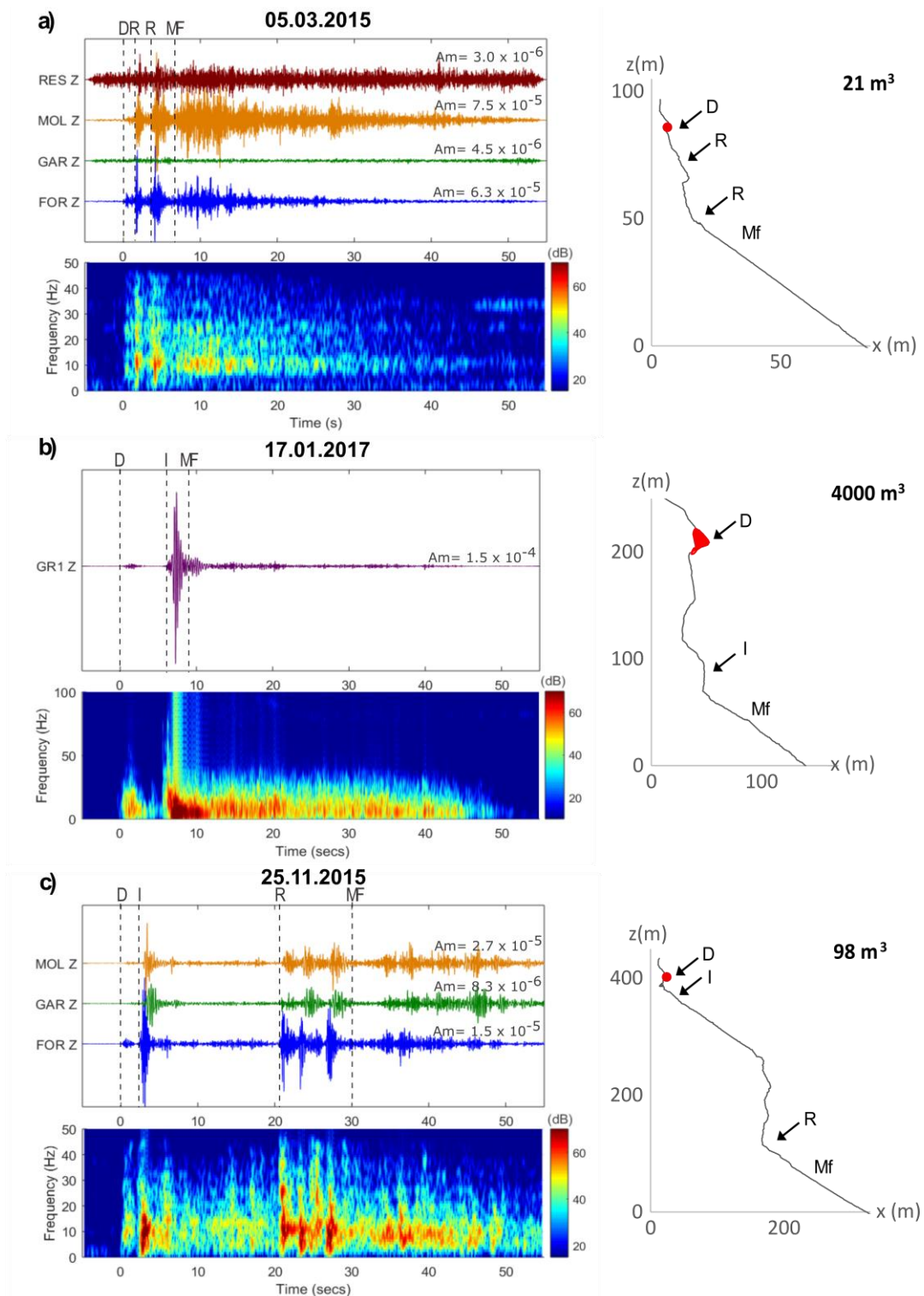


Figure 6.5. Left: seismic signal (vertical ground velocity, filtered between 2 and 50 Hz) and corresponding spectrogram. The peak amplitude of each trace,  $A_m$  is indicated in m/s. The spectrograms are computed using a simple fast Fourier transform, using a hanning taper, with a window of 128 points and an overlap between successive windows of 64 points. Right: Cliff profile for each event, the red dot indicates the starting point of the rockfall. a) 05.03.2015 Mount Saint Eynard event, b) 17.01.2017 (A1) Mount Granier event, c) Mount Saint Eynard 25.11.2015 event. Some propagation phases are identified on the seismic signal, on the spectrogram and on the cliff profile: D. rockfall detachment, R. rebound of blocks, I. impact of blocks after a free-fall, Mf. simultaneous propagation of fragmented blocks leading to mass flow.

## 6.5.2 Detachment and free-fall

The detachment phase has a smaller amplitude than the impact phase. For Mount Saint-Eynard rockfalls, the detachment phase was visible for all free-fall type events at station FOR, located on rock at the top of the cliff face. However, the detachment phase was visible only for events larger than 6 m<sup>3</sup> at the other stations located on the scree slope. Although most events were not located closer to station FOR than to the other stations, the detachment phase is more visible at station FOR. This station has a better signal to noise ratio because it is located on rock and because it is farther away from the anthropogenic noise generated in the valley.

For the Mount Granier rockfalls, the detachment phase was clearly visible on all five rockfalls detected at station GRA, located 650 m away. Event A<sub>4</sub> was more complex, suggesting that the compartment fragmented during its detachment (A<sub>4a</sub> and A<sub>4b</sub>, Figure 6.6b). Two pulses separated by 2 seconds can be distinguished on the detachment phase. Event A<sub>4a</sub>, is very small in comparison to event A<sub>4b</sub> as the seismic energy of event A<sub>4b</sub> is about ten times higher than A<sub>4a</sub>. This separation is difficult to establish for the impact phase as the two events overlap.

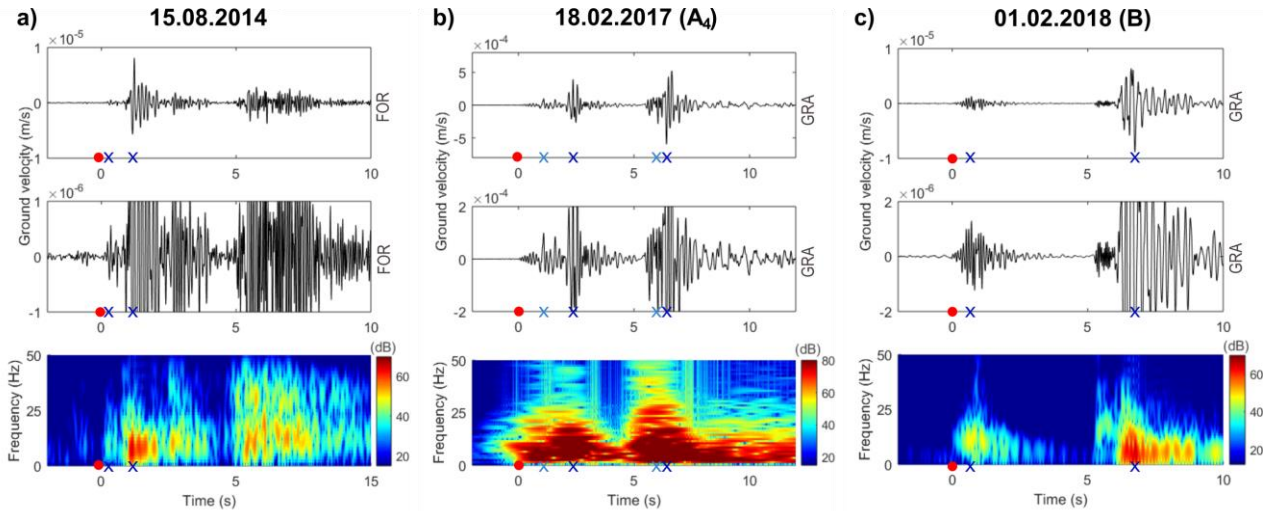


Figure 6.6. Detachment seismic signal, enlargement of the seismic signal and corresponding spectrogram of the a) 15/08/2014, b) 18/02/2017 (A<sub>4</sub>) event and of the c) 01/02/2017 (B) event recorded at station GRA located at the top of Mount Granier. Red dot: initial time of the detachment phase, blue cross: maximal amplitude of the detachment and impact phases.

The detachment phase is characterized by frequency contents around 20 Hz but in some cases up to 40 Hz (Figure 6.6). The duration of this phase varies between 0.5 second and 4 seconds (Figure 6.7a). The waveforms generally show a slowly rising and falling seismic signal.

We investigated how properties of the detachment phase (duration and energy) scale with the rockfall volume determined by TLS  $V_{DEM}$ . We first consider Mount Saint Eynard rockfalls as a training dataset. In a second step, we test our results using Mount Granier rockfalls.



We estimated the duration of the detachment phase  $Dur_D$  recorded at station FOR. We picked manually the initial and final times of the detachment phase, because the seismic signal of the detachment phase is slowly rising and falling and because in some cases the detachment phase is not well separated from the impact phase. The duration increases slowly with rockfall volume (Figure 6.7a) and can be fitted by:

$$Dur_D = aV_{DEM}^b \quad (6.9)$$

with  $a = 0.6 \pm 0.05$  and  $b = 0.2 \pm 0.03$  (regression uncertainty for a confidence interval 68%) and with a correlation coefficient  $R^2$  of 0.76.

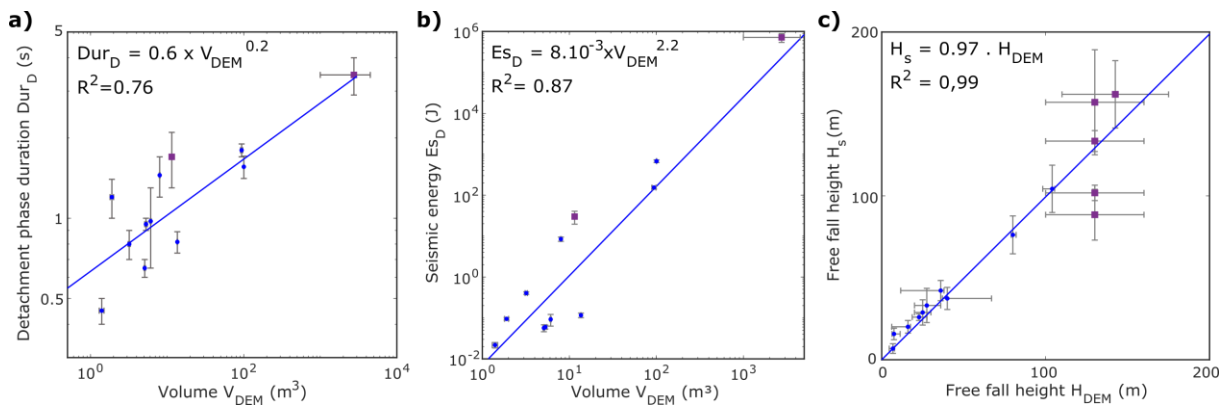


Figure 6.7. a) Duration of detachment phase and b) seismic energy of the detachment phase as a function of rockfall volume determined with DEMs. In a) and b), we consider only events A<sub>4b</sub> and B for Mount Granier and assume a volume  $V_{DEM} = 2850 \pm 1800 \text{ m}^3$  for event A<sub>4b</sub> c) Free fall height calculated from the seismic signals as a function of the free fall height measured on the DEMs, Blue dots: Mount Saint-Eynard rockfalls; violet squares Mount Granier rockfalls. Straight lines are power-law fits obtained using only Mount Saint-Eynard rockfalls.

The seismic energy of the detachment phase  $E_{sD}$  recorded at station FOR is better correlated with the rockfall volume  $V$  ( $R^2 = 0.87$ , Figure 6.7b) and increases much faster with volume than the duration. A power-law fit

$$E_{sD} = aV_{DEM}^b \quad (6.10)$$

yields  $a = 8 \pm 3 \times 10^{-3}$  and  $b = 2.2 \pm 0.2$ .

We calculated Mount Granier rockfall volumes  $V_{EsD}$  using Equation (6.10). The total volume of the set of events A<sub>1-4</sub> is estimated to  $891\text{--}2994 \text{ m}^3$ . This represents about half of the global volume  $4600 \pm 50 \text{ m}^3$  determined using the DEMs. The calculated volume of event B is, for its part, higher than the one obtained by the DEMs:  $V_{DEM} = 11\text{--}12 \text{ m}^3$  versus  $V_{EsD} = 20\text{--}41 \text{ m}^3$ .

Some detachment signals are preceded by a low amplitude and low frequency (<30 Hz) phase. We interpret these signals as precursory rupture nucleation leading to the failure and detachment of the compartment. This part of the seismic signal can be isolated from the detachment signal itself by a change in amplitude and frequency content (Figure 6.8).

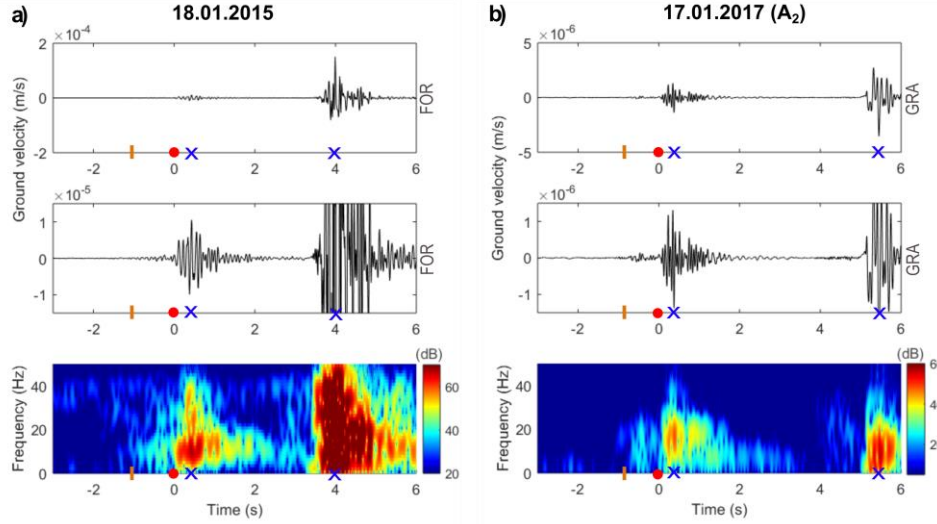


Figure 6.8. Seismic signal for free-fall type rockfalls a) the 18/01/2015 event recorded at station FOR station located at the top of Mount Saint-Eynard. b) 17/01/2017 ( $A_2$ ) events recorded at station GRA located at the top of Mount Granier. Top: seismic signal of the detachment phase, middle: enlargement of the amplitude scale, bottom: corresponding spectrogram. Red dot: beginning of the detachment phase, orange line: beginning of a precursory phase, blue cross: maximal amplitude of the detachment and impact phases.

We compare the free fall height  $H_s$  estimated from the seismic signal using equation (6.8) with the value  $H_{DEM}$  determined on the DEMs (Figure 6.7c). In some cases, there is a large uncertainty on the free-fall height due to the geometry of the event (Figure 6.2b, Figure 6.4c). For Mount Granier events, it can be observed by the marks left on the cliff, that the rockfalls have impacted two different areas: a cliff ledge or the scree slope at the base of the cliff (Figure 6.4c).

Uncertainties on the calculated free-fall height  $H_s$  are due to the spreading of the detachment seismic signals. However, we can see that the calculated free-fall heights are consistent with the ones measured on the DEMs with a value of  $R^2$  of 0.99.

This result first validates our identification and interpretation of the different phases of the seismic signal: detachment phase, sometimes preceded by a precursory signal, and first impact.

### 6.5.3 Impact

The seismic energy of the impact phase is strongly correlated with the potential energy. Our data for Mount Saint Eynard suggest the following relation:

$$E_{SI} = aE_p^b \quad (6.11)$$

We used only Mount Saint Eynard rockfalls in order to fit a power law relation between  $E_{SI}$  and  $E_p$  (Figure 6.9a). The estimated parameters are  $a=1\pm 0.5 \times 10^{-8}$  and  $b=1.55\pm 0.05$  (confidence interval 68%) and the correlation coefficient is  $R^2=0.98$ . This fit correctly explains Mount Granier data, although these events were not used in the fit.



This fit is also consistent with the controlled release block data. Hibert et al. (2017) determined a relation  $E_s = a E_p^b$  with  $a=4.6 \times 10^{-8}$ ,  $b=1.38$ , in good agreement with our results. However, relation (6.11) overestimates the seismic energy for Yosemite rockfalls. The seismic energy estimated using this law is larger than the measured value by 1000 to 10000 %.

The volume of the blocks  $V_{ESI}$  can be calculated using the following relation:

$$V_{ESI} = \frac{E p_s}{g p H_s} = \frac{E_{SI}^{1/b}}{a g p H_s} \quad (6.12)$$

The computed volumes  $V_{ESI}$  for Mount Saint-Eynard rockfalls are in good agreement with those determined from the DEMs (Figure 6.9b) with a value of  $R^2$  of 0.99. Uncertainties on the calculated volumes  $V_{ESI}$  are related to the uncertainties on the parameters used to determine  $E_{SI}$  ( $V$ ,  $\alpha$ ,  $r$ ,  $p$ ,  $c$ ,  $f$ , see supplementary B) and  $H_s$ . This relation established for Mount Saint Eynard rockfalls has been tested with Mount Granier events. The calculated volume of event B is in agreement with the measured one ( $V_{ESI}$ : 4-19  $m^3$ ,  $V_{DEM}$ : 11-12  $m^3$ ). However, the total volume of the set of events A<sub>1-4</sub> is slightly underestimated with a calculated volume of  $V_{ESI}=683-4178$   $m^3$  for a measured volume of  $V_{DEM}=4550-4650$   $m^3$ .

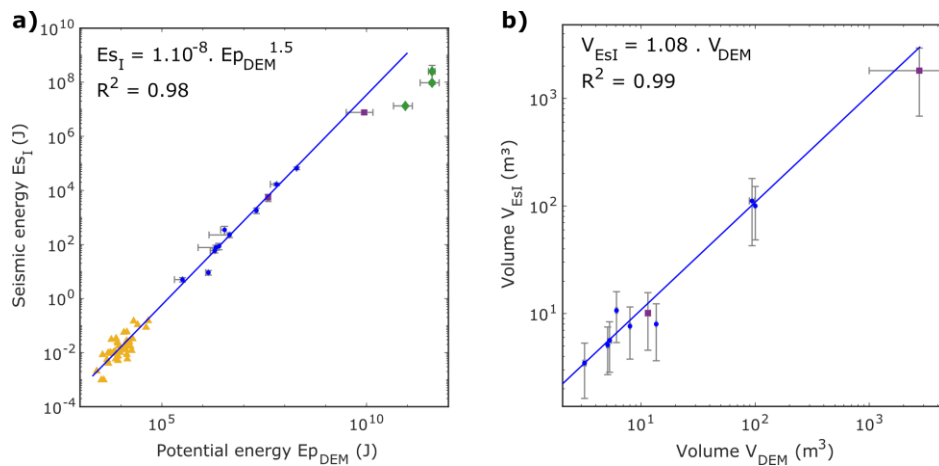


Figure 6.9. a) seismic energy of the impact phase as a function of potential energy calculated with DEM metrics, b) rockfall volume calculated using seismic metrics as a function of rockfall volume measured on the DEMs. Blue dots: Mount Saint-Eynard rockfalls; violet squares: Mount Granier rockfalls: A<sub>4</sub> and B; green diamond Yosemite rockfall (Morrissey et al., 1999; Wiczorek et al. 2000; Stock et al., 2013); yellow triangles controlled release block data of Hibert et al. (2017). Lines are linear fits using only the Mount Saint-Eynard rockfalls.

## 6.6 Discussion

### 6.6.1 Detachment phase

We found that both the duration and the seismic energy of the detachment phase increase with rockfall volume. However, this relation is not well constrained. The scatter of these data might be due to the complexity of the detachment phase and to its variety

of processes. Several factors may influence the detachment seismic signal, such as the surface of the rupture area, the detachment mode (slide, free-fall or topple), its duration, the fragmentation of the compartment during the detachment, etc. However, due to the limited number of studied events and due to the lack of information on the detachment mode of these events, the influence of these factors could not be studied.

In order to distinguish the detachment phase from the impact phase, the free-fall duration must be longer than the duration of the detachment phase. By combining Equations (6.8) and (6.10), we can estimate the minimal free-fall height detectable as a function of rockfall volume. For instance, for a 1 m<sup>3</sup> event the minimal free-fall height detectable is about 2 m, whereas for a 100 m<sup>3</sup> event the minimal free-fall height is about 11 m. This drawback prevents us from studying all free-fall or topple events (3 events over 16 in the Mount Saint-Eynard data set).

### 6.6.2 Relation between potential and seismic energy of the impact phase

The relation (6.11) between potential energy and seismic energy is difficult to interpret physically. The fact that the exponent  $b$  is larger than 1 implies that the process is not scale invariant, the ratio of seismic to potential energy increases with rockfall size. This relation cannot be extrapolated to very large energies. Indeed, this relation predicts that the seismic energy  $E_p$  would exceed the potential energy  $E_p$  for  $E_p > 3 \times 10^{12}$  J, which is of course impossible. This suggests that the relation between potential energy and seismic energy presents a change of slope for potential energies larger than  $10^{10}$  J.

The ratio between seismic energy and potential energy  $R_{s/p} = E_{sI}/E_{pDE}$  of our data ranges from  $10^{-6}$  to  $10^{-4}$ . This ratio  $R_{s/p}$  is in good agreement with values found by previous studies. Deparis et al. (2008) estimated a ratio  $R_{s/p}$  ranging from  $10^{-5}$  to  $10^{-4}$  for rockfalls with volumes ranging from  $10^3$  to  $10^6$  m<sup>3</sup>, Hibert et al. (2011) found  $10^{-5} < R_{s/p} < 10^{-3}$  for granular flows at the Piton de la Fournaise volcano with  $1 < V < 10^3$  m<sup>3</sup>, Lévy et al. (2015) estimated  $R_{s/p} = 10^{-5}$  for volumes  $10^3 < V < 10^6$  m<sup>3</sup> and Saló et al. (2018)  $10^{-6} < R_{s/p} < 10^{-4}$  for volumes  $0.5 < V < 5$  m<sup>3</sup>. Farin et al. (2015) and Bachelet et al. (2018) observed through laboratories experiments that variations of  $R_{s/p}$  could be associated with the size of the impactor and with properties of the impacted medium (e.g., roughness and bed thickness). Farin et al. (2015) estimated larger values of  $R$  between 0.001 and 1 in laboratory experiments with impactors masses ranging from 0.001 to 100 g. For smooth impacted plates, this ratio increases toward 1 as the mass of the impactor increases, in agreement with their theory, assuming that impact energy is dissipated as elastic energy and viscous deformation. However, for impacts on rough surfaces and for natural rockfalls, Farin et al. (2015) suggest that viscous deformation becomes negligible, and that most energy is dissipated through other processes such as plastic deformation, adhesion, or rotational modes of the impactor owing to surface roughness. Thus the value

of  $R_{s/p}$  can be influenced by site properties, and may be scale-dependant as we observe in our dataset.

In our study, the parameters used for the calculation of the seismic energy slightly influence the  $R_{s/p}$  ratio. The exponent of the power law between  $E_p$  and  $E_s$  decreases with the frequency from 1.56 for a frequency of 20 Hz to 1.50 for a frequency of 5 Hz. For lower frequencies (e.g. 5 Hz), this change in exponent provides a better agreement with Mount Granier and Yosemite's events (supplementary B, Figure B.3.b). The exponent of the power law between  $E_p$  and  $E_s$  varies very little with the change of seismic wave velocity. Changing the velocity mainly affects the  $R_{s/p}$  ratio.

### 6.6.3 Estimation of rockfall volume from the seismic energy of the impact phase

We have shown in this study how potential energy and free fall height can be estimated from seismic signals, allowing the estimation of rockfall volumes. However, this methodology only allows for the characterization of rockfalls experiencing a free fall immediately after their detachment. This represents 60% of the Mount Saint-Eynard rockfalls. This limitation is balanced by the improved accuracy of the results. In order to characterize all event types, it may be appropriate to calibrate a different relation between rockfall volume and seismic energy for each rockfall type.

The free-fall duration is estimated by manual picking of the detachment and of the impact phase. This is a delicate task and leads to uncertainties on both the free fall duration and on the seismic energy. In some cases, the time of maximum amplitude of the impact phase can be significantly off the first onset of this phase. This delay might be related to several points. In a few cases, the fallen compartment may have scraped a ledge before impacting the slope (e.g. 01.02.2017 Mount Granier rockfall, Figure 6.6). In this case, the impact signal is preceded by a small amplitude and high-frequency wave packet. This part of the seismic signal was not taken into account in the seismic energy calculation. This delay can also be interpreted as the delay between the first contact between the slope and the compartment and the time for which the maximum energy was transferred to the slope. This explanation was assumed for most cases (e.g. 18.01.2015 Mount Saint-Eynard rockfall or 17.01.2017 Mount Granier rockfall, see Figure 6.8). In this case, this delay might vary depending on the volume of the compartment, on the impacted material (loose scree or cliff face) and on the slope angle. However, no clear relations appeared in our data.

The relation between seismic and potential energy has been derived for Mount Saint-Eynard dataset and then tested on the Mount Granier rockfalls. The underestimation of the Mount Granier rockfall volume ( $V_{ESI}=683-4178 \text{ m}^3$ ,  $V_{DEM}=4550-4650 \text{ m}^3$ ) may be due to the parameters used to calculate seismic energy of the impact phase. They might need to be adjusted for the Mount Granier setting to account for

differences in the wave propagation medium. Another explanation can be the overestimation of the free fall height due to high uncertainties on  $H_s$  ( $\pm 30$  m) for events  $A_1$  and  $A_4$ , leading to smaller volumes. The seismic energies determined for the Yosemite Park events are smaller than expected from the relation (6.11) obtained for the Mount Saint-Eynard rockfalls. This discrepancy may be due to the method used to estimate seismic energy from the local magnitude of the signals recorded at large distances (several tens of kilometers). This method (developed for earthquakes and assuming body waves) may produce different values from the estimation of seismic energy using Equation (6.2), using nearby stations (less than 2 km) and assuming surface waves. The Mount Saint-Eynard relations were determined using rockfall volumes ranging from 1 to 100 m<sup>3</sup>. As the Mount Granier events included volumes larger than 1000 m<sup>3</sup>, the relation (6.11) between  $E_p$  and  $E_s$  might need to be adjusted in order to better fit bigger volumes.

#### 6.6.4 Real-time characterization of rockfalls

Real time characterization of rockfalls from seismic signals would be useful for rockfall hazard mitigation. However, developing a fully automated method is very challenging. Automatic location of rockfalls from seismic monitoring has been studied in previous works (Lacroix and Helmstetter, 2011; Hibert et al., 2014; Manconi et al., 2016; Fuchs et al., 2018). However, in the case of Mount-Saint Eynard, the number of sensors is too small to obtain accurate locations, therefore we used rockfall locations determined from 3D point clouds. We have also manually checked all events detected by the seismic network to select rockfall signals, and manually picked the detachment and first impact phases. A fully automatic procedure may be possible using artificial intelligence methods (Hibert et al., 2014; Provost et al., 2018). Most automatic methods (artificial neural networks, random forest, hidden Markov models, support vector machines) require a training set. By coupling different methods of detection (TLS, photogrammetry, seismology), we are confident that all events in our dataset have been correctly classified and located. Therefore, our dataset could be useful to develop or to test such automatic method for rockfall detection, location and characterization. There are very few studies that were able to distinguish the detachment phase of rockfalls, therefore our database would provide a useful dataset in order to develop an automatic classification method.

#### 6.6.5 Comparison with other studies

Previous studies, such as Deparis et al. (2008), Dammeier et al. (2011), Manconi et al. (2016) or Fuchs et al. (2018), studied scaling relations between rockfall parameters and seismic signals properties using regional seismic networks. In these studies, the distance between rockfalls and stations is much larger than in our study, of the order of tens of kilometers for regional networks, compared with several hundred meters up to 2

km in our study. The rockfall volumes are also much larger (between  $10^3$  and  $10^7$  m<sup>3</sup>) than in our study. The seismic signals are thus very different. The signals recorded by regional networks are strongly affected and transformed by the distance between events and stations. The propagation phases (i.e. detachment, impacts, mass-flow) can hardly be identified in these records. Thus, in these studies, seismic parameters (seismic energy, duration, peak ground velocity, etc.) were defined over the entire seismic signal. Deparis et al. (2008) found no clear relation between rock-fall parameters (fall height, runout distance, volume, potential energy) and rockfall seismic magnitudes. However, they found that signal duration was roughly correlated with the potential energy and the runout distance. Dammeier et al. (2011) used multivariate linear regressions combining duration, peak envelope velocity, and envelope area. They found a good correlation with rockfalls volume and potential energy. Finally, Manconi et al. (2016) and Fuchs et al. (2018) proposed relationships between rockfall or rockslide volumes, and respectively duration and local magnitude. Hibert et al. (2017) carried out controlled releases of single blocks in a marl gully. They analyzed the relation between rockfall properties and the induced seismic signals. They found that seismic energy was well correlated with the blocks kinetic energy ( $R^2=0.64$ ) and poorly correlated with the blocks mass ( $R^2=0.39$ ).

We have compared the scaling laws between magnitude and rockfall volume obtained in these previous studies with our results. We used Equation (6.7) in order to estimate magnitude from the seismic energy estimated by Hibert et al. (2017) and in our study. For the Mount Saint Eynard and Mount Granier database, we tested two methods for estimating seismic energy. We first selected the 18 rockfalls listed in Table 6.1 with a known volume  $V_{DEM}$  (excluding events A<sub>1-3</sub>) and used the whole signal to estimate seismic energy (blue dots in Figure 6.10). Secondly, we selected only free-fall events and computed the seismic energy using the impact seismic signals (red dots in Figure 6.10). Results are shown in Figure 6.10 and Table 6.2.

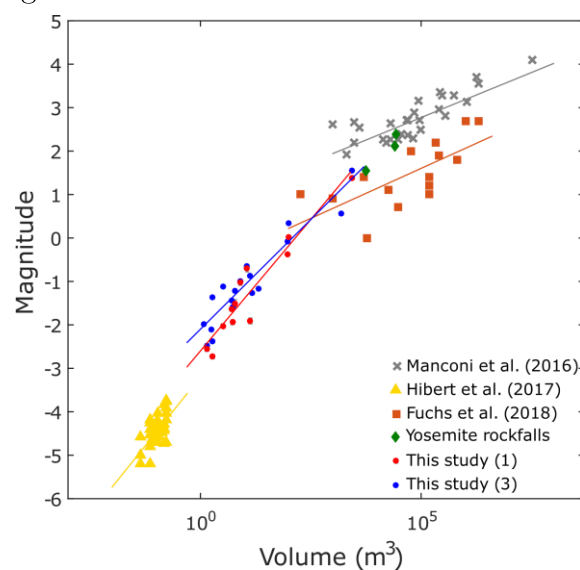


Figure 6.10. Magnitude of the events versus their volume. Straight lines are linear relations between magnitude and logarithm of volume. This study (1): whole dataset of Mount Saint Eynard rockfalls, magnitude calculated over the entire seismic signal. This study (3): free-fall events, magnitude calculated over the impact seismic signal

Table 6.2. Scaling laws between rockfall seismic magnitude

Study	Scaling law <sup>(a)</sup>	Nb events	Volume (m <sup>3</sup> )	R <sup>2</sup>	Median relative error on V
Fuchs et al. (2018)	$M_L = -0.6 + 0.44 \log(V)$	16	10 <sup>2</sup> -10 <sup>6</sup>	0.60	99%
Hibert et al. (2017)	$M_L = -3.13 + 1.3 \log(V)$	37	0.03-0.2	0.39	29%
Hibert et al. (2017)	$M_L = -1.69 + 0.92 \log(E_k)$	37	0.03-0.2	0.60	28%
Manconi et al. (2016)	$M_D = 1.4 + 0.23 \log(V)$	33	10 <sup>3</sup> -10 <sup>8</sup>	0.71	71%
This study <sup>(1)</sup>	$M_L = -2.1 + 1.01 \log(V)$	18	1-10 <sup>3</sup>	0.89	56%
This study <sup>(2)</sup>	$M_L = -2.2 + 1.17 \log(V)$	12	1-10 <sup>3</sup>	0.92	41%
This study <sup>(3)</sup>	$M_L = -2.6 + 1.21 \log(V)$	12	1-10 <sup>4</sup>	0.91	33%
This study <sup>(4)</sup>	$M_L = -2.13 + 1.38 \log(E_p)$	12	1-10 <sup>5</sup>	0.98	18%

<sup>(a)</sup>  $M$  ( $M_L$ : local magnitude,  $M_D$ : duration magnitude), volume  $V$ , kinetic energy  $E_k$  (Hibert et al., 2017) and (last model) free-fall height  $H$ .

<sup>(1)</sup> whole dataset of Mount Saint Eynard rockfalls, magnitude calculated over the entire seismic signal

<sup>(2)</sup> free-fall events, magnitude calculated over the entire seismic signal

<sup>(3)</sup> free-fall events, magnitude calculated over the impact seismic signal

<sup>(4)</sup> free-fall events, relation between potential energy and impact seismic energy

Manconi et al. (2016) and Fuchs et al. (2018) mix different types of propagation (free-fall, sliding, rebounds), different geological settings and slope angles. This leads to a large scatter between the observed and modelled volumes. In our study, we obtain a smaller error between observed and modelled rockfall volumes, even when using all events, probably because all events come from the same site, and also because our volumes are more accurate. Selecting only free-fall events further decreases the error. This highlights the importance of selecting rockfalls from their propagation mode. In order to remove the influence of the propagation mode, we focus on the first impact. Once again, this greatly improves the accuracy of the estimated volume. Our relation (3) in Table 6.2 between rockfall volume and magnitude is in good agreement with the results obtained by Hibert et al. (2017) for much smaller rockfall volumes. However, Figure 6.10 suggests that the relation between magnitude and rockfall volume changes for volumes larger than 1000 m<sup>3</sup>. This could explain why our relation derived for Mount Saint Eynard rockfalls with  $V < 100$  m<sup>3</sup> underestimates the volumes for Mount Granier and Yosemite rockfalls with  $V > 1000$  m<sup>3</sup>.

Finally, we use the scaling relation between seismic and potential energy (6.11) in order to account for variations of free-fall height. This produces the strongest improvement on the estimated rockfall volume (relation (4) in Table 6.2). Similar results are obtained for the dataset of Hibert et al. (2017). The seismic energy is better correlated with kinetic energy than with volume.

## 6.7 Conclusions

Monitoring rockfalls using photographic time-lapse surveys and 3D reconstructions provides information such as volume, geometry, location, detachment mode, etc. The use of seismology adds information on the time of occurrence and on the propagation mode and duration of individual stages of an event. Coupling these methods at Mount Granier and Mount Saint-Eynard yields numerous information on natural rockfalls onto complex topography.

Analysis of seismic signals allows identifying several phases: detachment, free fall followed by an impact, rebounds, and granular flow. As the propagation mode strongly differs among rockfalls in our dataset, we were not able to find seismic signal features allowing a satisfying estimation of rockfall dynamics (energy, volume, etc.) for our whole data set. We therefore chose to focus on free-fall type of rockfalls and we considered only the beginning of the seismic signal: the detachment and the first impact. At Mount Saint-Eynard and Mount Granier, we have detected 15 detachment seismic signals corresponding to rockfalls of volume ranging from 1 to more than 1000 m<sup>3</sup>.

We found a significant correlation between the seismic energy of the detachment phase and the rockfall volume. By measuring the time delay between the detachment phase and the impact phase we were able to infer the free fall heights, which are in good agreement with values estimated from the DEMs. This result supports our interpretation of the different phases of the seismic signals. We also found that the seismic energy of an impact was well correlated with the potential energy of the rockfall. Rockfall volumes can thus be calculated by using the estimated potential energy and free fall height.

The relations developed with the Mount Saint-Eynard rockfalls were then tested using the Mount Granier and Yosemite rockfalls. We found that the results were in good agreement with the measurements for the smallest Mount Granier rockfall, but slightly underestimate the largest Mount Granier rockfall (volume estimated from seismic energy is 15-89% of the volume determined using DEMs). Our results are also in good agreement with controlled block release experiments of Hibert et al. (2017), which involved much smaller volume (0.03-0.2 m<sup>3</sup>) than in our study. For Yosemite rockfalls, the seismic energy recorded is significantly smaller than the seismic energy predicted by our relation for all three events (1000 to 10000 %). This might be due to a site effect or to the range of volumes of Mount Granier and Yosemite rockfalls.

By segregating rockfalls experiencing a free-fall from those with sliding or bouncing transport modes, and by focusing on a specific part of the rockfall seismic signal, i.e., the detachment and first impact, we were able to obtain more accurate volume prediction than other studies considering mixed propagation modes (Deparis et al., 2008; Dammeier et al., 2011, Manconi et al., 2016, Fuchs et al., 2018).

# 7 Controlled block release experiment of free fall type events

*To further analyze seismic characteristics of block impacts, we carried out two controlled block releases. A first data set consists of a large-scale block release experiment. Blocks (1 to 4m<sup>3</sup>) were released from heights ranging between 1 and 30m, on several protection embankment facings (granular platform, reinforced earth, concrete blocks). A second data set was obtained by releasing a small block (2.9 kg), from heights ranging from 0.5m to 2m, on a tilted concrete block. These experiments allowed us to further explore the influence of blocks impacts properties on the induced seismic signal.*

## 7.1 Introduction

Seismic data analysis proved to be a powerful tool to detect, locate, and monitor mass wasting events (Battaglia and Aki, 2003; Lacroix and Helmstetter, 2011; Burtin et al., 2013; Dietze et al., 2017a). Moreover, some characteristics of rockfall seismic signal (duration, magnitude or energy, frequency content, etc.) have been linked to rockfall properties such as fall height, volume, propagation mode, etc. (Deparis et al., 2008; Hibert et al., 2011; Dietze et al., 2017b).

Seismic signals of rockfall detachment have been detected in several studies (Rousseau, 1999; Deparis et al., 2008; Hibert et al., 2011; Dietze et al., 2017b). We found a correlation between the seismic energy of the detachment phase and the rockfall volume Chapter 6. We also showed that we were able to estimate both the potential energy of a block and its free-fall height from rockfall seismic signals (Chapter 6). By combining these results, we obtained an accurate estimate of Mount Saint-Eynard rockfall volume.

We found that these results were in fair agreement with events of different size and geological settings. The volume of the smallest Mount Granier rockfall was correctly inferred but it was slightly underestimated for the largest Mount Granier rockfall. These results were also in good agreement with controlled block release experiments of Hibert et al. (2017), which involved much smaller volume (0.03-0.2 m<sup>3</sup>).

However, quantifying rockfall volume from seismic energy remains challenging. Many parameters may have an influence on the result (block volume, free-fall height, impacted slope, impacted materials...). Experiments offer an opportunity to control these



parameters and to test how they influence the seismic signal. They also allow to test the feasibility of extrapolating results toward smaller scales.

In this study, we analyze seismic signals produced by rockfall impacts using two datasets at different scales. Our goal is to investigate the relations between impacts properties (kinetic energy, impacted material, angle of the impacted surface) and the associated seismic signal features. The first dataset was obtained with a large-scale experiment consisting of dropping boulders from heights ranging between 1 and 30m. The second dataset consists of a small-scale experiment. A small block (2.9kg) is dropped on a tilted concrete block embedded in a gravel tank. We then compare our results with other studies, in order to test whether our conclusions could be applied to larger rockfall volumes and for different settings. We use a dataset of controlled block release experiments (Hibert et al., 2017) and a dataset of rockfalls having experienced in a free-fall after their detachment (Chapter 6).

## 7.2 Datasets

### 7.2.1 Large-scale block release experiment

A first dataset consists of a large-scale experiment carried out at the Montagnole rockfall testing station (Chambery, France). It is located at a limestone quarry exploiting a massive limestone layer of the Tithonian stage. This rockfall testing station consists of a jib located at the top of a vertical 90-meter high cliff. The jib enables a free-fall drop of blocks up to 20 tons from height up to 70m (Figure 7.1).

In October 2017, experiments of controlled block releases were carried out within the framework of the research project C2ROP (Chutes de blocs, Risques Rocheux et Ouvrages de Protection (Rockfalls, rock hazard and protection measures)). The aim of this campaign was to characterize the dynamic response of several protection embankment facings, to an impact. We carried out 12 drops using ETAG27-type reinforced concrete projectiles (2580 to 12 490 kg), from heights ranging between 1 and 30 m. Three protection embankment facings were tested.

Table 7.1. Overview of the large-scale experiment initial conditions.

Impacted surface	Granular platform			Reinforced earth facing				Concrete block facing				
Block volume (m <sup>3</sup> )	4.8	4.8	4.8	1.0	1.0	2.9	2.9	2.9	2.9	1.0	4.8	4.8
Free-fall height (m)	1.6	1.6	2.5	7.7	19.2	13.8	27.5	6.9	6.9	7.7	16.5	16.5

Three impacts were carried out on a 2 m thick granular platform. This platform was constituted of rolled gravel (grain size 20-40 mm). This material was chosen for its mechanical characteristics allowing deformations, while being weakly sensitive to

compaction. The granular platform was then overlaid with two different facings. Four block releases were carried out on a reinforced earth structure laid on the support platform. Five drops were then made on a facing composed of concrete blocks (0.8-m thick) linked with metallic frames (Bloc Armé® patent). Block volumes and free-fall heights varied over the experiment. Unfortunately, block releases were not systematically repeated. It is thus impossible to evaluate the variability of the impacts conditions. The granular platform compaction probably increased within the experiment. For the analysis of these data, the sequence order is thus taken into account.

Two high-speed cameras (500 frames per second) were installed at impact height, along two perpendicular axes. Seismic signals generated by these impacts were recorded by a seismic array composed of 13 geophones (GS-11D, corner frequency 4.5 Hz, sampling rate 2000 Hz) located at distances up to 100m.

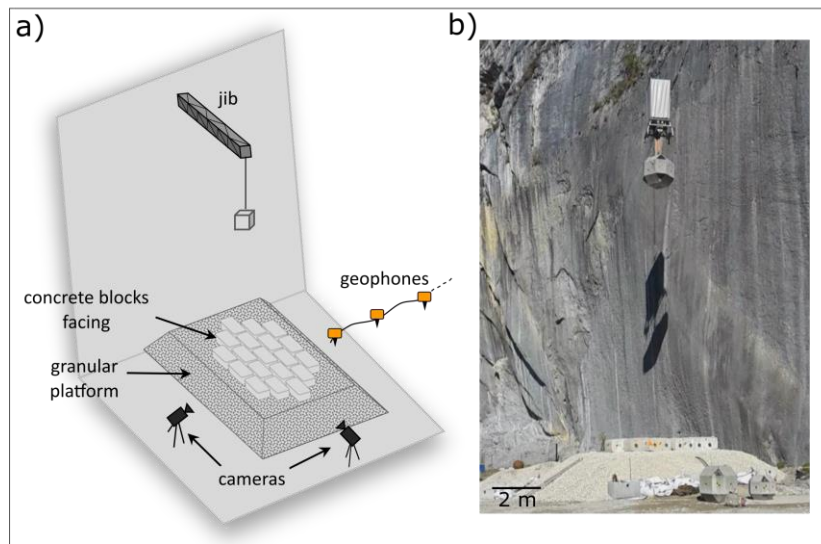


Figure 7.1. a) Sketch and b) photograph of the large-scale block release experiment.

### 7.2.2 Small-scale block release experiment

A second dataset was obtained by dropping a small block (2,9kg) on a concrete block (40x40x20cm) embedded in a gravel tank. The block was lifted using a pulley and released using a quick release shackle. This equipment allowed us to release the block without friction and with a good repeatability of the release initial conditions. 104 release experiments were carried out using the same limestone block. Free-fall heights were varied between: 0.5, 1.0, 1.5, and 2.0 m. The angle of the impacted surface was changed throughout the experiment: 20°, 30°, 40°, 50°, 60°. We repeated each drop at least 4 times.

Two cameras (optical camera Canon EOS 7D, InfrRed camera Optris PI640, both at 30 frames per second) were used to record blocks impacts. Impacts seismic signals were recorded by a seismic array composed of 8 geophones located at distances ranging from 2m to 20m (Figure 7.2).

In this chapter we focus on the analysis of the impact seismic signals. Analysis of the thermographic print of the blocks impacts can be found in Chapter 9.

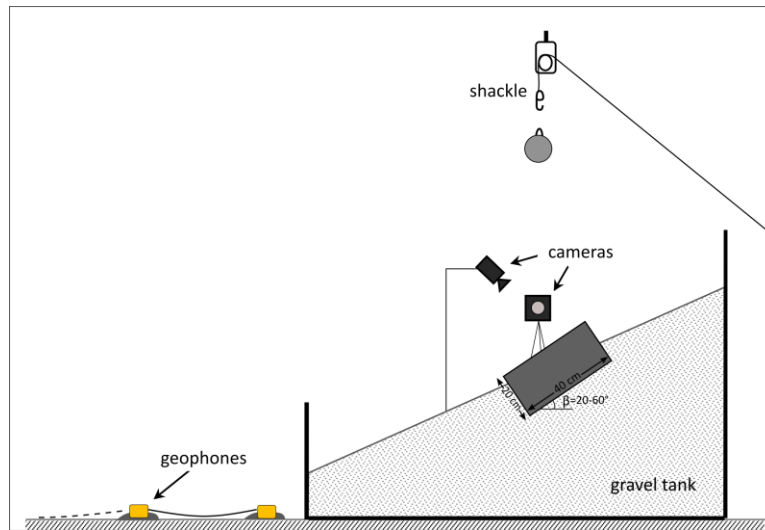


Figure 7.2. Sketch of the small-scale block release experiment

### 7.2.3 Other datasets

In order to validate our results, we consider two previous studies. We analyze 16 rockfalls from Chartreuse cliffs (French Alps) that experienced a free-fall phase, to test whether our observations can be applied to larger rockfall volumes. These rockfalls were characterized by DEMs and seismic monitoring (Chapter 6). We determined the free-fall duration, the frequency content and the seismic energy from the seismic signals. Rockfall characteristics (volume, potential energy, free-fall height) were also determined from the DEMs.

In order to study smaller rockfalls, we analyze controlled block releases carried out by Hibert et al. (2017). 28 blocks, with masses ranging from 76 kg to 472 kg, were released within a soft-rock gully of the Rioux-Bourdoux torrent (Barcelonnette, French Alps). Block impacts of this study are not truly free-fall impacts. However, block rebounds are well separated and impacts occur after a flight period.

## 7.3 Methods

### 7.3.1 Impacts characteristics

In order to characterize rockfall dynamics, we use two metrics: block volume  $V_B$ , free-fall height  $H_{ff}$ . The velocity of the block  $v$  before impact can be inferred from its free-fall height  $H_{ff}$  and the gravity: constant  $g=9.81 \text{ m.s}^{-2}$ .

$$v = \sqrt{2gH_{ff}} \quad (7.1)$$

Kinetic energy can be derived from the block velocity  $v$ , blocks volumes  $V_B$  and ground density  $\rho=2500\pm 100$  kg.m<sup>-3</sup>.

$$Ek = \frac{1}{2}\rho V_B v^2 \quad (7.2)$$

For free-fall impacts, kinetic energy is equal to the potential energy. If the impacted surface is tilted, we decompose the impact velocity into its normal  $v_N$  and tangential  $v_T$  components as a function of the tilt angle  $\beta$ .

$$v_N = v \cos \beta \quad (7.3)$$

$$v_T = v \sin \beta \quad (7.4)$$

The tilt angle can be accurately measured for controlled block release experiments, but for natural rockfalls, there is some uncertainty on the slope of the impacted surface. The impacted area is estimated from the DEMS as presented in Chapter 6. The angle of the slope is averaged over the impacted area. In some cases, strong variations of slope angle are present within the impacted area. We use extreme values to account for uncertainties on the slope angle.

Block trajectory following the impact is measured using two cameras (large-scale experiment: two Optronis CR600 at 500 fps; small-scale experiment: Canon EOS 7D, Optris PI640, both at 30 fps). Two 2D trajectories are obtained on each camera and then combined to provide the 3D trajectory. Translational velocity  $v_t$  and rotational velocity  $v_r$  can be inferred allowing us to deduce kinetic energy following the impact  $Ek_R$ .

$$Ek_R = Ek_{Rt} + Ek_{Rr} \quad (7.5)$$

with  $Ek_{Rt}$  translational kinetic energy computed using equation (7.2) and  $v_t$ , and  $Ek_{Rr}$  rotational kinetic energy computed as following with  $R$  block radius and  $m$  block mass

$$Ek_{Rr} = \frac{1}{2}Iv_r^2 \quad (7.6)$$

$$I = \frac{2}{5}mR^2 \quad (7.7)$$

We calculate the dissipated kinetic energy during the impact  $dEk$  as:

$$dEk = Ek - Ek_R \quad (7.8)$$

For the large-scale experiment, we consider that the block kinetic energy following the impact is null.

### 7.3.2 Seismic characterization

We define three metrics to characterize the block seismic signals: free-fall duration  $D_{ff}$ , seismic energy of the detachment phase  $E_{sD}$ , and seismic energy of the impact phase  $E_{sI}$ .

By measuring the free-fall duration  $D_{ff}$  it is possible to calculate the free-fall height  $H_s$ :

$$H_s = \frac{D_{ff}^2 \cdot g}{2} \quad (7.9)$$

To estimate the seismic energy we assume a point-source (Kanamori and Given, 1982; Eissler and Kanamori, 1987) and an isotropic and homogeneous medium.

The seismic energy of surface waves is computed as:

$$E_s = 2\pi r p h c \int_{t_0}^{t_1} u_{env}(t)^2 e^{\alpha r} dt \quad (7.10)$$

For volume waves, it is calculated as:

$$E_s = 4\pi r^2 p c \int_{t_0}^{t_1} u_{env}(t)^2 e^{\alpha r} dt \quad (7.11)$$

where  $t_0$  and  $t_1$  are the onset and end times of the seismic signal,  $r$  is the distance between the event and the recording device,  $p$  is the ground density,  $h$  is the thickness of the layer through which surface waves propagate,  $u_{env}(t)$  is the envelope of the ground velocity. We have estimated the seismic wave velocity  $c$  by measuring the delay of arrival time of the impact seismic signal over the array.  $\alpha$  is a damping factor that accounts for anelastic attenuation of the waves (Aki and Richards, 1980). In order to estimate the attenuation factor, we used the relationship derived by Kanai et al. (1984). The methodology used to determine  $c$  and  $\alpha$  is developed in Chapter 6.

For the large-scale release block experiment, the pattern of wave attenuation shows the presence of volume waves. We used equation (7.11) to calculate seismic energy with  $p=2500\pm 100 \text{ kg.m}^{-3}$ ,  $c=2700\pm 100 \text{ m.s}^{-1}$ ,  $\alpha=10^{-4}$ .

For the small-scale release block experiment, seismic waves were propagating through a concrete slab. We used equation (7.10) to calculate seismic energy  $p = 2500 \pm 100 \text{ kg.m}^{-3}$ ,  $c = 1035 \pm 50 \text{ m.s}^{-1}$ ,  $\alpha = 0.12 \pm 0.01$ ,  $h=1\text{m}$ . The thickness  $h$  was taken as the thickness of the concrete slab on which the waves were recorded.

## 7.4 Results

### 7.4.1 Detachment and free-fall

Detachment seismic signals were recorded in the case of the large-scale experiment. These signals are characterized by lower amplitudes than impacts seismic signals and by lower frequencies (0 - 100 Hz). The waveforms generally show a slowly rising and falling seismic signal (Figure 7.3b). These properties are similar to seismic signals of natural rockfalls analyzed in Chapter 6. By measuring the delay between the detachment and impact seismic signals, we calculate the drop height  $H_s$ . Calculated values are in agreement with the measured ones  $H_m$  (Figure 7.3a).

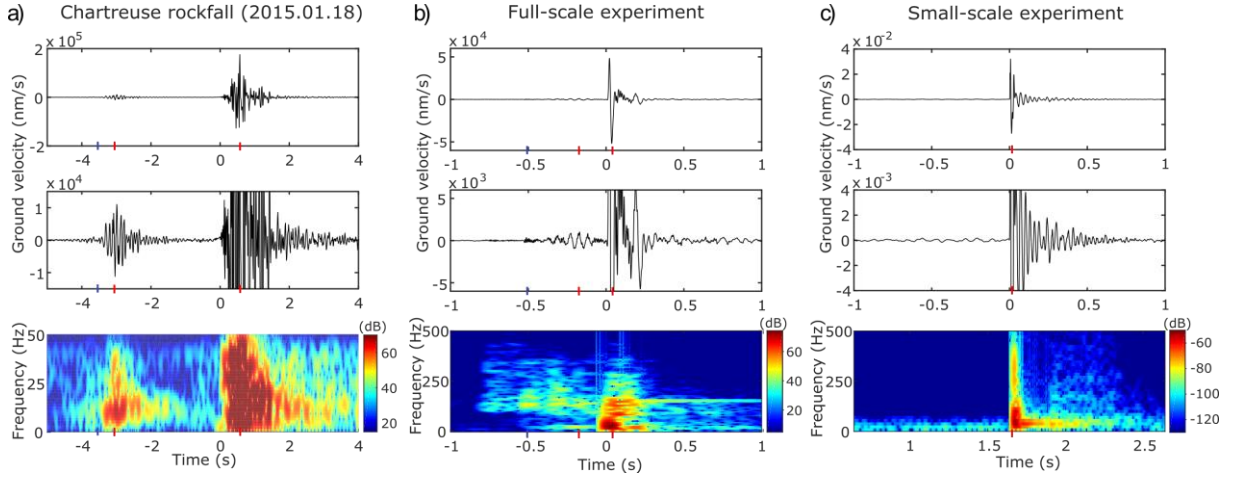


Figure 7.3. Seismic signal, enlargement of the seismic signal and corresponding spectrogram of a) a rockfall of 100 m<sup>3</sup>, distance source-station 750m (Mount Saint-Eynard, 2015.01.18 (Chapter 6)), b) a large-scale block release filtered between 0 and 300 Hz (4.8 m<sup>3</sup> dropped of 1.6 m on the granular platform, distance source-station 20 m) and c) small-scale block release (2.9kg, drop height 1.5 m, tilt angle 30°, distance source-station 5m). Blue lines: initial time of the detachment phases, red lines: maximal amplitude of the detachment and impact phases. In the case of the large-scale experiment, the release system involves an electrohydraulic system clearing up the mechanical deformation energy. This system produces a high-frequency noise (150-1000Hz). Seismic signal of Figure 3.b was band-pass filtered between 1 and 300 Hz in order to reduce this noise.

We found that the seismic energy of the detachment phase for the large-scale experiment is well correlated with block volume  $V_B$  (Figure 7.4). Moreover, it is consistent with values obtained for Chartreuse rockfalls (Chapter 6). We found that a power law fit well these datasets (Figure 7.4):

$$EsD = aV_B^b \tag{7.12}$$

With  $a = 5 \pm 1 \times 10^{-3}$  and  $b = 2.3 \pm 0.1$

We did not detect detachment seismic signals for the small-scale experiment. The amplitude of the detachment seismic signal is probably very low and lost in the noise.

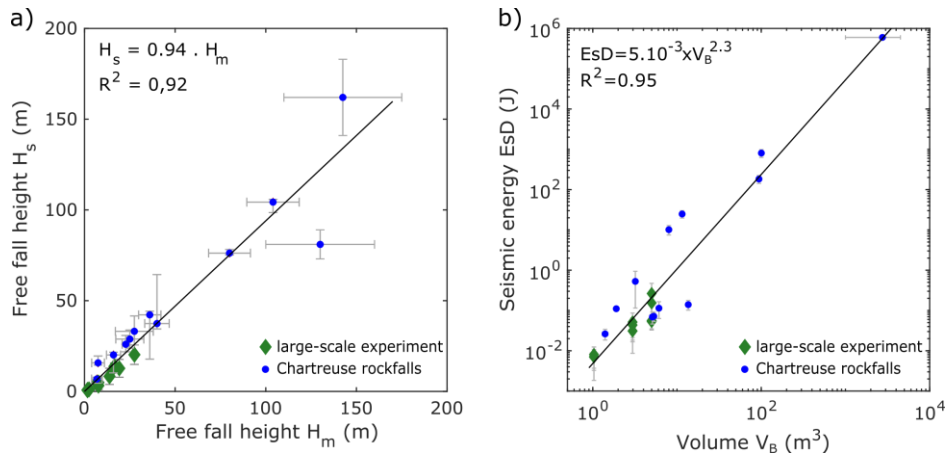


Figure 7.4. a) free-fall height  $H_s$  calculated from the seismic signals as a function of the measured free fall height  $H_m$ . b) Seismic energy of the detachment phase  $EsD$  as a function of rockfall volume  $V_B$ . Green diamonds: large-scale experiment, blue dots: Chartreuse rockfalls (Chapter 6). Straight lines are fits obtained using both data sets.

## 7.4.2 Impact

Seismic signatures of block impacts of both large-scale and small-scale experiments are rather similar (Figure 7.3.b, c) Seismic signal are rising and falling quickly with frequencies stretching up to 500 Hz. Seismic energy for both experiments increases with the block kinetic energy (Figure 7.5a, b).

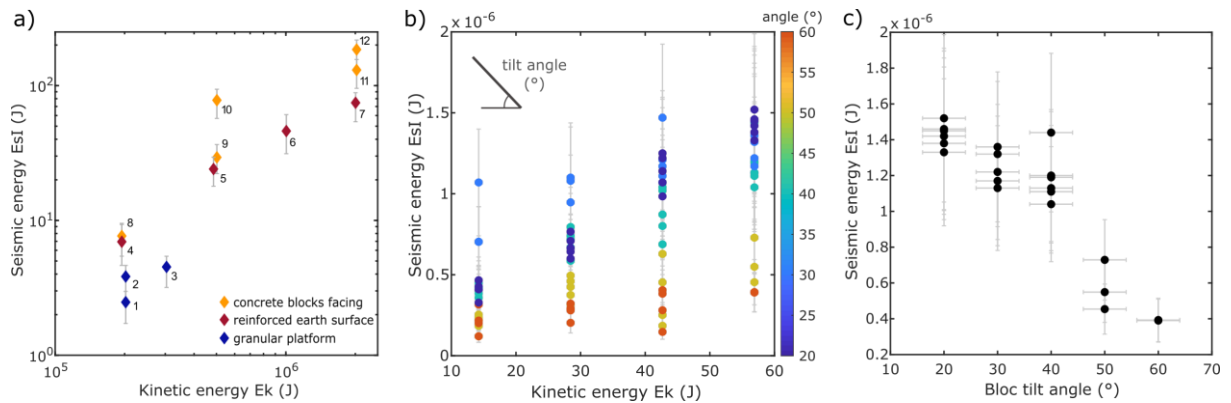


Figure 7.5. a) Seismic energy of the impact phase as a function of kinetic energy for the large-scale experiment according to the impacted surface. The release sequence is indicated on the side of each symbol. b) Seismic energy of the impact phase as a function of kinetic energy for small-scale experiment (color scale represents the tilt angle of the impacted surface). c) Impact seismic energy as a function of the tilt angle of the impacted surface (drop height 1.5m).

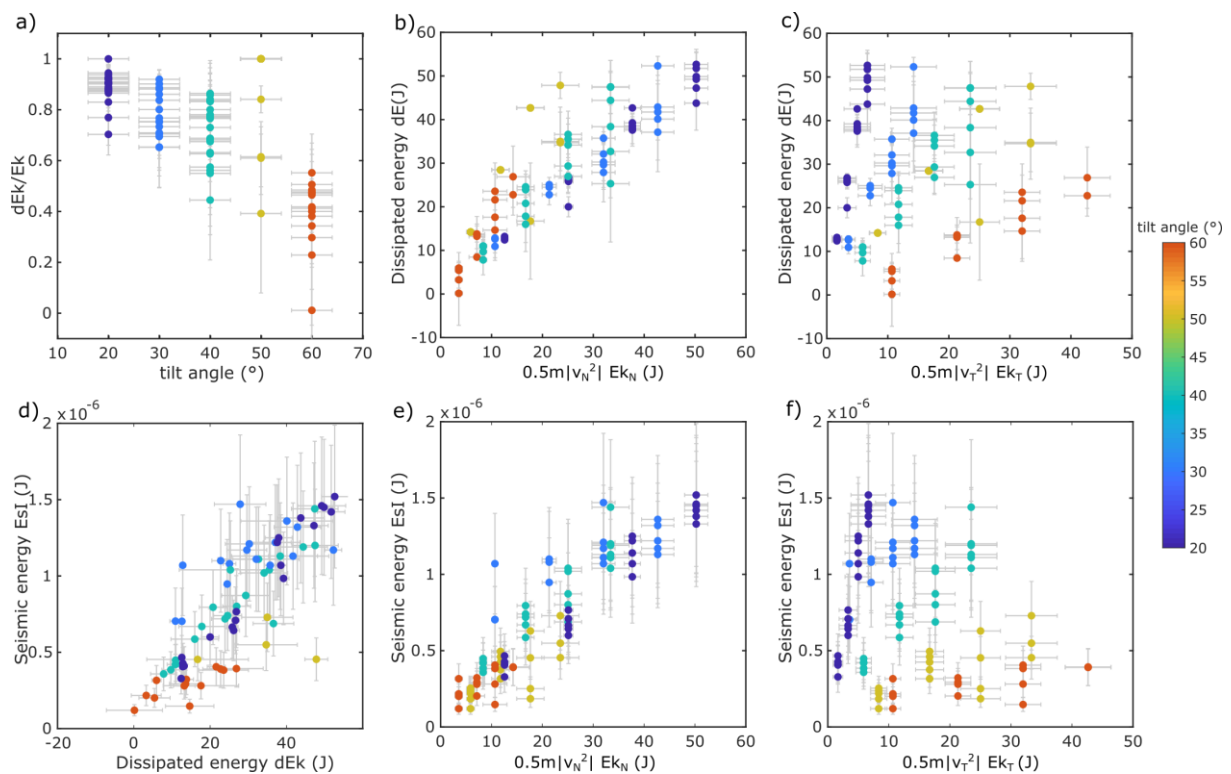


Figure 7.6. a) Ratio between dissipated kinetic energy and kinetic energy as a function of the tilt angle of the impacted surface. b) Dissipated kinetic energy as a function of the normal component of the kinetic energy and c) d) the tangential component of the kinetic energy. Seismic energy of the impact as function of d) kinetic energy dissipated during the impact, e) the normal component of the kinetic energy, f) the tangential component of the kinetic energy. The color scale represents the tilt angle of the impacted surface.

For the small-scale block experiment, seismic energy of the impact also depends on the tilt angle of the impacted block (Figure 7.5c). In Figure 7.6b, we can see that a variation of tilt angle seems to shift the ratio  $E_s/E_p$ . Using equations (7.3) and (7.4), we have decomposed the block initial velocity into its normal and tangential component.

Table 7.2. Power-law fit between seismic energy and kinetic energy  $E_k$ , dissipated kinetic energy  $dE_k$ , normal component of the kinetic energy  $E_{kN}$  and the tangential component of the kinetic energy  $E_{kT}$

Angle	$E_k$	$dE_k$	$E_{kN}$	$E_{kT}$
20	$E_{sl} = 3.10^{-8} \times E_k^{0.93}$	$E_{sl} = 6.10^{-8} \times E_{kN}^{0.77}$	$E_{sl} = 6.10^{-8} \times E_{kN}^{0.82}$	$E_{sl} = 2.10^{-7} \times E_k^{0.92}$
30	$E_{sl} = 2.10^{-7} \times E_k^{0.41}$			$E_{sl} = 4.10^{-7} \times E_k^{0.39}$
40	$E_{sl} = 5.10^{-8} \times E_k^{0.75}$			$E_{sl} = 1.10^{-7} \times E_k^{0.75}$
50	$E_{sl} = 4.10^{-8} \times E_k^{0.66}$			$E_{sl} = 5.10^{-8} \times E_k^{0.66}$
60	$E_{sl} = 5.10^{-8} \times E_k^{0.48}$			$E_{sl} = 8.10^{-8} \times E_k^{0.40}$

If the tilt angle  $\alpha$  is inferior the friction angle  $\phi$ , the impact force is balanced by the reaction force. However when  $\alpha > \phi$ , the impact force is unbalanced and a sliding motion appears.

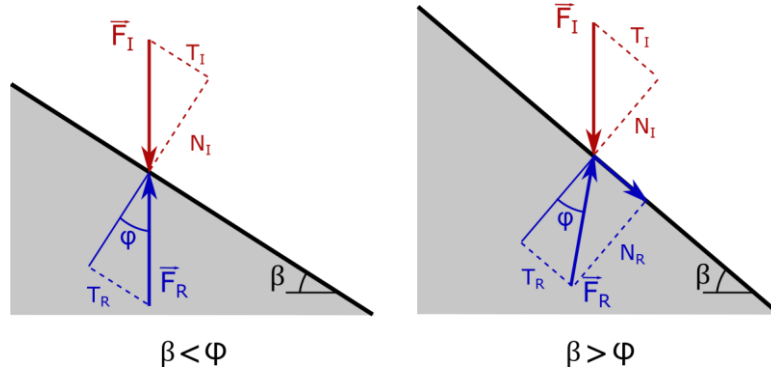


Figure 7.7. Diagram of the force balance during an impact.  $\vec{F}_I$  impact force,  $\vec{F}_R$  reaction force, T and N tangential and normal components of the force,  $\alpha$  tilt angle,  $\phi$  friction angle.

As presented in Figure 7.6a., the coefficient of restitution between initial and residual kinetic energy (equation 7.8) varies according to the tilt angle of the impacted surface. The coefficient of restitution decreases with the augmentation of the tilt angle (Chau et al., 2002; Asteriou et al., 2012).

The dissipation of kinetic energy seems to be controlled by the normal component and almost independent of the tangential component. Seismic energy appears to be correlated with the dissipated kinetic energy and thus to the normal component of the kinetic energy (Figure 7.6d., Table 7.2). It then might be related to a surface deformation by Hertz contact.



## 7.5 Discussion

For natural free-fall rockfalls in Chartreuse, we found a relation between the seismic energy of the detachment phase and the rockfall volume (Chapter 6). We detect similar seismic signals with the large-scale experiment. This part of the seismic signal might be affected by the jib. However, it is difficult to determine the influence of the jib in the detected seismic signal. Nonetheless, we found a similar relation between seismic energy and block volume as for natural rockfalls. We also calculated the drop height by measuring the time delay between the detachment and impact seismic signals. We found that drop heights are underestimated (Figure 7.4). This is likely due to a delay of arrival of the detachment seismic waves propagating through the cliff and jib.

For the impact phase, we found that the seismic energy increases with the block kinetic energy for both experiments. However, seismic energy also depends of other parameters, including the impacted material and the slope of the impacted surface. For the large-scale experiment, impact seismic energy is larger for concrete block facings than for reinforced earth structures (Figure 7.5a). Reinforced earth structure shows strong deformations during the impacts. Impact energy is more dissipated with earth structure facings than with concrete block facings. Less seismic energy is thus recorded. Some drops were repeated with the same initial conditions. Variations in the recorded seismic energy may be due to a variation of the state of the impacted surface. The granular platform compaction may have changed within the experiment. Twice drops were repeated on the concrete blocks facing. The second drop was realized on a damaged facing. The seismic energy of these repeated drops is higher than for the first drop (Figure 7.5a). This is probably due to a compaction of granular platform combined with facing damage, leading to a lower dissipation of the initial kinetic energy.

Previous studies showed that seismic energy increases with the kinetic energy of the blocks (Hibert et al., 2017; Chapter 6). These controlled block release datasets allowed us to expand the range of kinetic energy studied. Figure 7.9 presents the two experiment datasets of this study along with the Chartreuse rockfall dataset (Chapter 6) and a controlled block release dataset (Hibert et al., 2017). These four datasets are in good agreement and are fitted by a power-law relation (equation 7.9), with  $a=2\pm 0.1 \times 10^{-9}$  and  $b=1.69\pm 0.01$

Changing the tilt angle of the impacted surface leads to variations in the induced seismic energy. The rebound energy after impact increases with the tilt angle. This means that for steep angles, less kinetic energy is dissipated during the impact, leading to a lower induced seismic energy.

We have decomposed the block initial velocity into its normal and tangential component for the Chartreuse rockfalls. Contrary to the small-scale experiment, seismic energy better matches the tangential component of the kinetic energy (Figure 7.8).

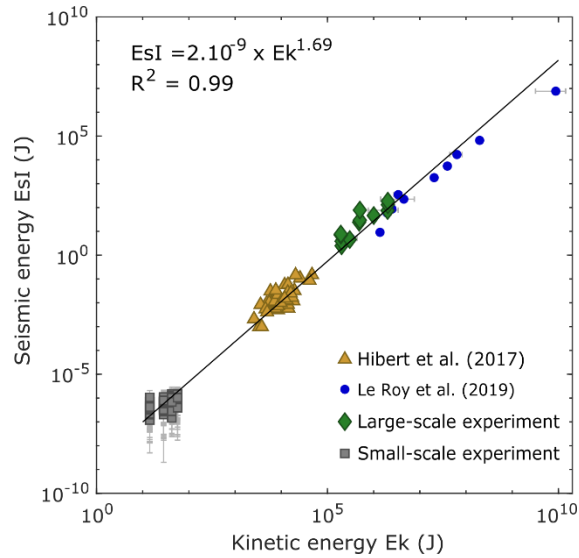


Figure 7.9. Seismic energy of the impact phase as a function of the kinetic energy.

In the case of Chartreuse rockfalls, slope angles are steeper ( $35\text{--}80^\circ$ ) than for the small-scale experiment. Large slope angles may induce a change of behavior. With such angles, the normal component of the kinetic energy is much smaller than the tangential component. This suggests that energy loss at larger impact angles is almost exclusively caused by the tangential forces (Hussainova et al., 2006; Garland and Rogers, 2009). For such angles friction coefficients are not negligible.

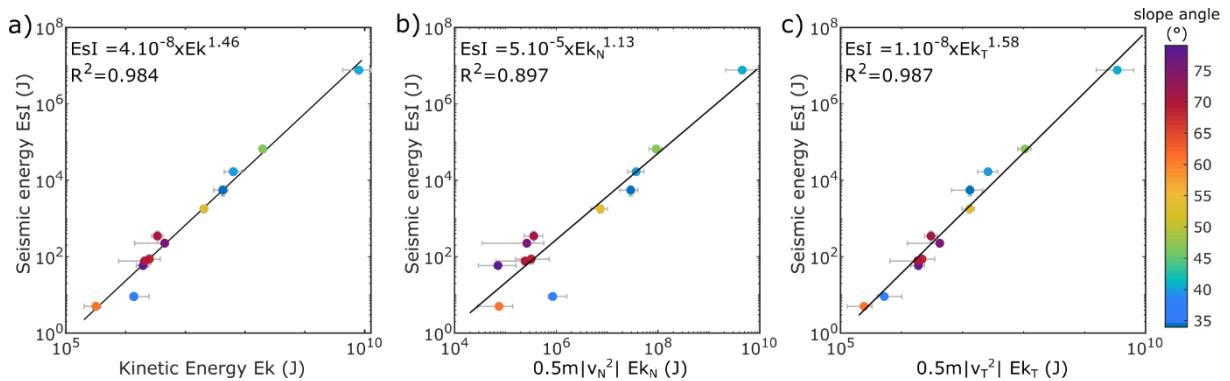


Figure 7.8. Seismic energy of the impact phase of Chartreuse rockfalls (Chapter 6) as a function of a) kinetic energy, b) the normal component of the kinetic energy, c) the tangential component of the kinetic energy. The color scale represents the slope angle.

For smooth impacted plates, Farin et al. (2015) assume that impact energy is dissipated as elastic energy and viscous deformation. However, for impacts on rough surfaces and for natural rockfalls, they suggest that viscous deformation becomes negligible and that most energy is dissipated through other processes such as plastic deformation, adhesion, or rotational modes of the impactor owing to surface roughness. This is certainly what we observe in our data

## 7.6 Conclusion

We carried out controlled block releases in order to analyze seismic characteristics of block impacts. A first dataset was obtained by releasing blocks (1 to 4m<sup>3</sup>) from heights ranging between 1 and 30m. Blocks were dropped on several protection embankment facings (granular platform, reinforced earth, concrete blocks). A second dataset was obtained by releasing a small block (2.9 kg) from heights ranging from 0.5m to 2m. The angle of the impacted surface was changed through this experiment. The results of these experiments were compared to another dataset of controlled blocks release experiments (Hibert et al., 2017) and to a dataset of rockfalls having experienced a free-fall after their detachment (Chapter 6).

We detected the seismic signal of the detachment phase only for the first large-scale experiment, with results similar to the dataset of natural rockfalls. By measuring the time delay between the detachment phase and the first impact, we estimated the free-fall height.

We found that the impact seismic energy of both experiments is correlated with the block kinetic energy. The scaling law between seismic energy and kinetic energy agrees well with the experiment of Hibert et al. (2017) and with the natural rockfalls analyzed in Chapter 6. We found that seismic energy also depends on the angle of the impacted surface and on the impacted materials. These results can explain the scatter of results for natural rockfalls that often mix different types of impacted materials and different slope surfaces. However, we found that the slope angle has a different impact on the seismic energy for natural rockfalls than for the small-scale experiment. This discrepancy may be related to the cliff roughness which may not be negligible for smaller rockfall events.

## 8 Seismic analysis of granular flow type rockfalls

*Rockfalls are extremely rapid processes that exhibit high kinetic energies and damaging capability. However, their unpredictable nature makes them hard to monitor. In January 2016, a rockslide of 65 000 m<sup>3</sup> detached from the NW pillar of Mount Granier (Chartreuse Massif, French Alps). A few months later, in April and May 2016, a series of rockfalls occurred on its NE pillar with cumulated volumes, estimated by Digital Elevation Models (DEMs), of about 60 000 m<sup>3</sup>. The timings of these rockfalls and their characteristics (geometry, volume, location, etc.) were poorly known because this cliff was not instrumented. Rockfalls were, however, detected by a local seismic network located 30 km away.*

*In this work, we show how seismic monitoring can be used to obtain more information on this sequence of rockfalls. We used a template-matching filter technic to detect all events of this sequence. We found relations between duration magnitude or seismic energy and rockfall volume in order to calculate the volume of Mount Granier rockfalls. These relations were also tested on another dataset composed of smaller rockfalls (<1500 m<sup>3</sup>) to investigate their accuracy on a wider scale. A relation between duration magnitude and rockfall volume provides a good volume estimation of Mount Granier rockfall volumes but did not provide good results for the second dataset (events <1500 m<sup>3</sup>). We found a relation between local magnitude and rockfall volume over a large range of rockfall volumes (1 -106 m<sup>3</sup>). We show that using different relations according to the propagation type provides more accurate volume estimates than when mixing all events.*

### 8.1 Introduction

Rock slopes are constantly shaped by gravitational mass wasting, whose volumes range from small blocks (<1 m<sup>3</sup>) to catastrophic failures (>10<sup>4</sup> m<sup>3</sup>). They present significant hazards due to their unpredictable nature, high-velocity propagation, and energy. To understand the underlying mechanisms of rockfalls and to mitigate associated hazards, it is crucial to be able to characterize rockfall properties such as location, timing, volume, and dynamics. Rockfalls detection is often carried out using remote sensing

techniques such as satellite imagery or terrestrial and airborne laser scanning. These methods deliver accurate information on detachment zones and released volumes. However, due to significant time lags between surveys, these methods cannot constrain triggering mechanisms. Similarly, the dynamics of events (multiple failures from the same area or individual stages of an event, i.e., detachment, impact, propagation) cannot be determined.

In this study, we analyze a series of rockfalls that occurred at Mount Granier in 2016. Mont Granier is known for its catastrophic failure of 1248, one of the biggest landslides in Europe (500 million m<sup>3</sup>). More recently, several large rockfalls were observed during the 20<sup>th</sup> Century. A rockfall of approximately 500 000 m<sup>3</sup> occurred in 1953 and a sequence of collapses occurred during the winter and spring 2016, with a large media impact (Hobléa et al., 2018). If these events did not result in human or material damage, some rockfall debris were remobilized into debris flows that impaired the RD 285a county road during several weeks. Due to inadequate remote sensing monitoring of the cliff, the rockfall sequence timing and characteristics (geometry, volume, location, etc.) were poorly known. De facto, using only DEMs it was neither possible to determine the number of events that occurred between two surveys nor their chronology and triggers.

Seismology is an efficient tool to detect and locate earth's surface processes such as landslides, debris flows, or rockfalls (Hibert et al., 2011; Provost et al., 2018); Coviello et al., 2019). The interpretation of the seismic signals offers insights into events timing (whether the compartment collapsed in one piece or several, delays between failures) and on other rockfall properties (volume, free fall height, mass, propagation velocity...).

Here we show how seismic monitoring can be useful to detect and characterize a sequence of rockfalls. Using DEM analysis, we could only measure the cumulated volume of all events that occurred between two surveys. To retrieve a thorough catalog of Mont Granier rockfalls along with accurate timing, we analyzed seismic data recorded by Mount Saint-Eynard array, 29km away. To detect the rockfalls, we used a template-matching filter technic (Gibbons and Ringdal, 2006). We also tried to estimate rockfall volume from properties of the seismic signals (seismic energy and duration). We compare these results with small rockfalls (<1500 m<sup>3</sup>) detected at Mount-Saint-Eynard for which volume and location are known by DEM analysis (Le Roy et al., 2019). We also consider other datasets from previous studies (Wieczorek et al., 2000; Deparis et al., 2008; Dammeier et al., 2011; Manconi et al., 2016; Fuchs et al., 2018) to test our relations on a wider scale.

To ease the readability of this study, the term 'rockfall' will be used for all the events of this study, whether they involve blocks of a few cubic meters or events of several thousand cubic meters.

## 8.2 Study sites

Chartreuse massif is located in the sedimentary cover of the External Crystalline Massifs of the French Western Alps. It is mainly composed of limestones and marls forming a succession of synclines and anticlines forming long ridges oriented NNE-SSW.

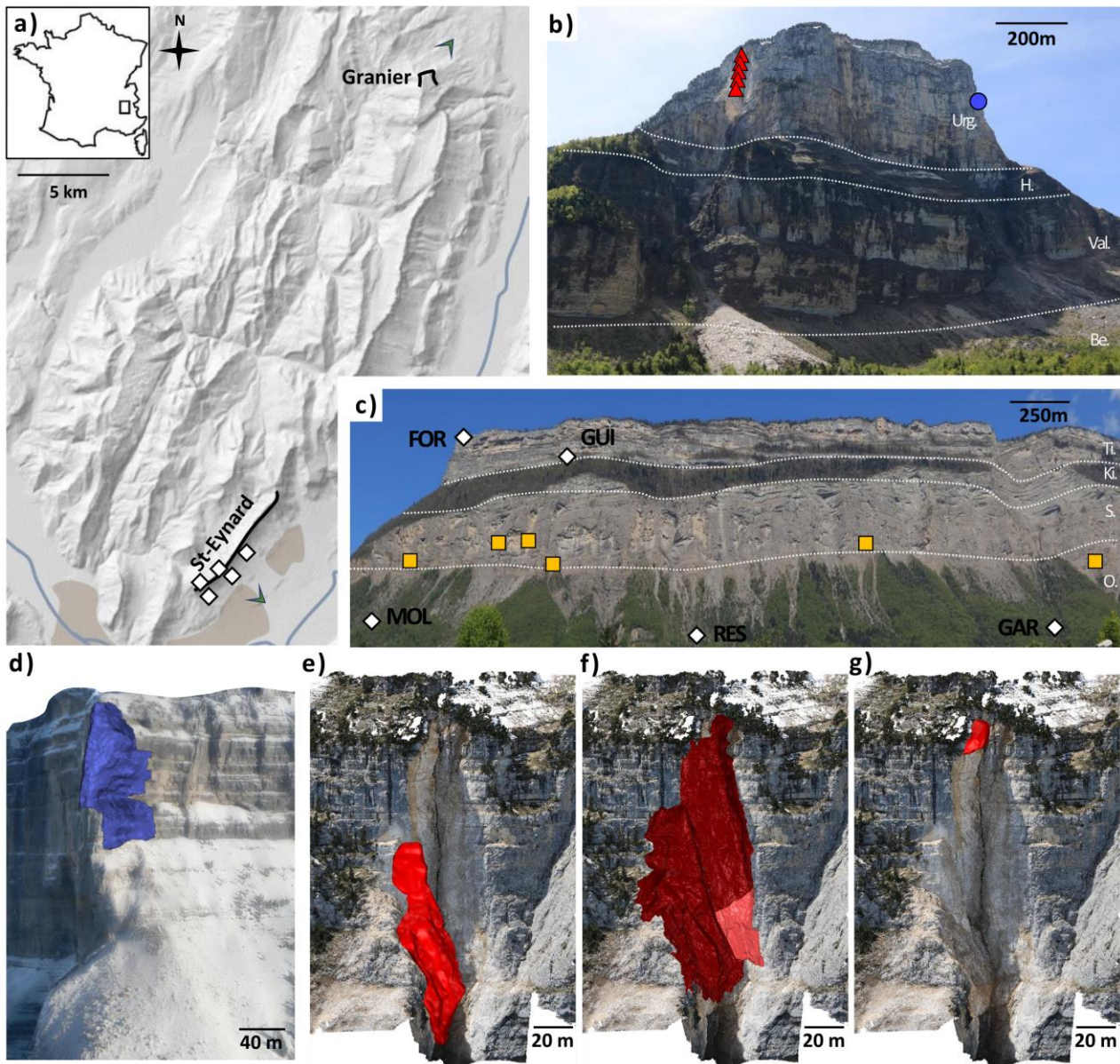


Figure 8.1. a) DEM of the Chartreuse massif (France), with the location of the photographs b) and c) shown as green triangles. Photograph of the b) north face of Mount Granier and c) Mount Saint-Eynard. White diamonds indicate the location of seismic stations. Triangles: location of origin of rockfalls, in yellow: Mount Saint-Eynard rockfalls, in blue: 2016/01/09 Mount Granier rockfall, in red: Mount Granier rockfall series of April/May 2016. Stage formations: Urg. Urgonian limestone, H. Hauterivian marls, Val. Valanginian limestone, Be. Berriasian marls, Ti. Tithonian limestone, Ki. Kimmeridgian marls, S. Sequanian limestone, O. Oxfordian marls. Illustration of the Mount Granier rockfall sequence, rockfall compartments are represented in blue for d) 2016/01/09 event ( $65000 \pm 10000 \text{ m}^3$ ) and in red for e) 2016/04/28 to 2016/05/01 ( $9000 \pm 3000 \text{ m}^3$ ), f) 2016/05/07 ( $2000 \pm 250 \text{ m}^3$  and  $50500 \pm 1000 \text{ m}^3$ ) and g) 2016/05/17 events ( $500 \pm 100 \text{ m}^3$ ).



Two cliffs of the Chartreuse massif are particularly monitored (Figure 8.1). The Mount Granier (1933 m above sea level), located North of the Chartreuse massif, was affected in 1248 by one of the biggest landslides in Europe (500 million m<sup>3</sup>). This landslide revealed a vertical limestone cliff of nearly 900 meters formed by Urgonian limestone, Hauterivian marls, Valanginian limestone, and Berriasian marls. Mount Granier forms a perched half-syncline and presents numerous fractures and a large karst network with a cave system of 90 km under a surface of less than 3 km<sup>2</sup> (D'Amato et al., 2016; Le Roy et al., 2019) (Hobléa, 2011).

On 2016/1/9, a first rockfall occurred on the NW pillar of Mount Granier (Figure 8.1). The pillar collapsed throughout its height (180 m) over a width of 85 m (Ravanel et al., 2016). Its volume was estimated by DEMs to  $65000 \pm 10000$  m<sup>3</sup>. Blocks spread over 700 m on the western slope before stopping in the forest.

A few months later, on 2016/04/29, another rockfall was observed and was detected by the Mount Saint Eynard seismic network located 29 km away. Field observations showed that this event was located on the NE pillar of Mount Granier (Figure 8.1b, 8.1e). Testimonies reported that this event was preceded and followed by several others in the following days from the same area. These events originated from the NE pillar and propagated through a narrow gully before reaching the foot of the cliff. On 2016/5/3, while taking photographs of the cliffs, we witnessed an event. We were able to characterize this event using DEMs ( $350 \pm 50$  m<sup>3</sup>). On 2016/5/7, two rockfalls occurred within two minutes. These events were detected by the seismic network and were also observed visually and filmed by inhabitants of the valley. Using the video images of the second largest event, we can distinguish the first event from the second on the DEMs.

In order to expand Mount Granier data set, we also analyze rockfalls that occurred at Mount Saint-Eynard. Mount Saint-Eynard (1308 m above sea level) is a long doubled cliff making up the eastern edge of the south of the Chartreuse Massif. Its two 7 km long subvertical cliffs form a marly-limestone alternation. The upper cliff (120 m high), consisting of massive limestone of the Tithonian stage, is separated from the lower cliff by a marl forested ledge. The lower cliff (240 m high) consists of fractured thin-bedded limestone, of the Sequanian stage. These cliffs experience a frequent rockfall activity with volumes ranging from less than 1 m<sup>3</sup> up to a few thousand cubic meters (D'Amato et al., 2016; Le Roy et al., 2019).

## 8.3 Instrumentation and methods

### 8.3.1 Topographic data analysis

Mount Saint-Eynard and Mount Granier cliffs have been monitored over the years by several methods. We carried out a diachronic comparison of DEMs to identify and characterize rockfalls that occurred between two DEMs. Several methods were used to

acquire DEM: TLS (Terrestrial Laser Scan) and photogrammetry. Between 2013 and 2015, D'Amato et al., (2016) yearly surveyed a 750 m zone of interest of the Mount Saint-Eynard using TLS (Optech Iiris-LR laser scanner). They determined the volume and geometry of the detected events. To better constrain rockfall occurrence times, D'Amato et al., (2016) installed an autonomously operating camera (Canon EOS Rebel T3 1100D) taking photographs of Mount Saint-Eynard every 10 min.

In order to monitor a larger area of the Mount Saint-Eynard cliffs and on a more frequent basis, we also performed terrestrial Structure from Motion (SfM) photogrammetric surveys. Such surveys have been carried at Mount Saint-Eynard cliffs every two months since November 2015. Photographs panoramas (camera Canon EOS 7D) were taken from 12 locations along Mont Saint-Eynard cliffs, with a 60% overlap between consecutive images. This way, data sets of 400-500 photographs were obtained. Two lines of panoramas acquisition locations were adopted. The first line of photographs acquisition presents distance to the cliff ranging from 0.6 and 1.2 km. Shorter distances to the cliffs were limited by the cliff's topography and vegetation. Due to the presence of spur and recesses in the cliff, 9 panoramas acquisitions were adopted with distances between acquisitions on average 450 m over a total distance of 3500 m. The second line of photographs acquisition (5 locations) was adopted to provide better viewpoints of the overall cliff (distance to the cliff ranging from 1.7 and 2.2 km). Panoramas obtained this way presents overlaps of at least 60%. Photographs were taken in either sunny or fairly hazy sky condition with even illumination conditions over the cliff and over the entire photographs dataset. Software Agisoft Photoscan Pro version 1.2.6 was used to process the data. Images were aligned with 'Very High' accuracy; the MVS reconstruction was set to 'High' quality and 'Mild' depth filtering. This way, we obtained clouds characterized by densities ranging from 50 to 70 points/m<sup>2</sup>, depending on the area, and mean point spacing of 0.12cm. SfM surveys' methodology is further developed in supplementary material A.

Although the North cliff of Mount Granier was already monitored by LiDAR before 2016, the Eastern and Western cliffs had never been monitored and no DEM of these areas existed before the 2016 rockfall series. In that case, public calls were made to collect photographic archives of the cliffs before the rockfalls. Using the collected photographs, we obtained models of the cliffs using SfM photogrammetry. The models obtained this way are less accurate but allow a gross evaluation of the events volumes. In the first half of May 2016, we carried out three photogrammetric surveys using data sets of 100 photographs taken from 7 locations distance to the cliff ranging from 1 and 2,5 km (resolution < 8 cm/pixel). Mount Granier surveys' were carried out as described before.

Once photogrammetry point clouds were obtained, we cleaned them from vegetation or noise and georeferenced them. We then measure the distance between two DEM point clouds. Deviations higher than a specific threshold (Mount Saint-Eynard rockfalls: 30 cm, Mount Granier: 50 cm) are considered as rockfalls. Point clouds defining a fallen compartment are meshed, making it possible to calculate the volume of the compartment



and to get its location and geometry. This procedure is further described in the supplementary A.

### 8.3.2 Seismic monitoring

In 2013, four seismometers (Guralp CMG40T, 3-components, with a corner frequency of 0.1 Hz and a sampling frequency of 100 Hz) were installed around Mount Saint-Eynard cliffs (Figure 8.1c). Stations MOL, RES, and GAR are located a few hundred meters apart, at the cliff foot, on top of scree. Station FOR is located on the cliff head, on top of rock. On May 11<sup>th</sup> 2016, a new station GUI was installed at the base of the upper cliff on top of rock, and stations FOR and MOL were removed on June 16<sup>th</sup>. To detect seismic events, we used the method developed by Helmstetter and Garambois (2010). Seismic events are detected automatically using a spectrogram analysis. We average the spectrogram over all channels and detect an event when the energy in a 1-s long window for frequencies between 2 and 20 Hz exceed the long-term average by a factor 2. All events are then checked by eye to identify rockfall signals (long duration, multiple peaks, no clear P and S arrivals, not present in the regional earthquake catalog). More details on the classification of seismic signals are given in Le Roy et al. (2019).

This network allowed us to monitor Mount Saint-Eynard rockfall activity but also rockfalls occurring outside of the network. In January and May 2016, several rockfalls occurred at Mount Granier with volumes, measured using DEMs, up to several thousands of cubic meters. In order to retrieve smaller Mont Granier rockfalls that were not identified within the seismic recordings, we used a template-matching filter (Gibbons and Ringdal, 2006). This method consists in scanning continuous data to search for signals with waveforms similar to template signals. Using known rockfall events as template, we search for similar waveforms by correlating this template signal with continuous data. If seismic events have similar waveforms, it implies that they have similar source locations and source mechanism. We use the three stations from Mount Saint-Eynard network (FOR, MOL ad RES) and the three components of the signal. Signals are band-pass filtered between 2 and 10 Hz. We use a time window of 25 s starting one second before the beginning of the signal. We set the minimum correlation threshold to 0.2. This value is much larger than the standard deviation of the correlation between continuous and template signals ( $\sigma=0.05$ ) in order to avoid false detections. The template-matching filter method has the advantage of being fully automatic. However, it can only detect events that occurred close to previous events and were detected by the same stations.

### 8.3.3 Association of topographic and seismic data

To associate rockfalls detected with DEMs to those detected using seismic sensors, we used information on the dating periods between two DEMs (D'Amato et al., 2016; Le

Roy et al., 2019), information on rockfall location and type of propagation (free-fall, sliding, etc.).

Several events may occur between two DEM surveys. In such cases, only the cumulated volumes of rockfall compartments can be measured. In the case of Mount Granier rockfalls, visual testimonies helped us to constrain the association of events.

Mount Saint-Eynard array is composed of a small number of sensors (< 4 sensors) separated by several hundred meters. Manual picking of rockfall seismic signals is difficult as their signals are emergent. Uncertainties can be as large as 1 second, leading to large location errors. The large distances between sensors make inter-sensor correlation very weak and do not allow the use of beam-forming methods (Lacroix and Helmstetter, 2011; Dietze et al., 2017a). Therefore, this network does not allow an accurate source location. Nonetheless, for rockfalls occurring near the array, manual picks of the seismic signals and amplitude ratios (corrected from site effects) provide us information about the source location. The rockfall is likely located closest to the station with the strongest amplitude. This information is only used to select rockfalls that are likely located within the study area.

Rockfall seismic signals are very different according to their propagation mode. In the case of flow propagating events, the combined movement of several particles leads to a smooth seismic signal as rebounds wave packets overlap and envelope frequency concentrating around 5-20 Hz. Seismograms of events having suffered little or no fragmentation present irregular envelopes showing several energetic pulses which can be linked to rebounds of blocks along the cliff. The most energetic phases are often produced by impacts after a free-fall (Vilajosana et al., 2008; Bottelin et al., 2014; Le Roy et al., 2019). It is thus possible to distinguish a mass-flow type event from an event experiencing a free-fall or rebounds along the cliff (Le Roy et al., 2019). If several events may occur between two DEMs surveys, the propagation mode help us to constrain the association of events.

### 8.3.4 Seismic data analysis

We estimated the seismic energy of each event in order to analyze the relation between seismic energy and rockfall properties. We assume a point-source (Kanamori and Given, 1982; Eissler and Kanamori, 1987) and consider the medium as isotropic and homogeneous. We also consider that surface waves dominate the seismic signal (Deparis et al., 2008; Dammeier et al., 2011; Lévy et al., 2018). Signals were band-pass filtered between 2 and 50 Hz. We use the following relation to estimate the seismic energy  $E_s$

$$E_s = 2\pi r p h c \int_{t_0}^{t_1} u_{\text{env}}(t)^2 e^{\alpha r} \varepsilon_i dt \quad (8.1)$$

where  $t_0$  and  $t_1$  are the manually picked onset and end times of the seismic signal,  $r$  is the distance between the event and the recording station,  $h$  is the thickness of the

layer through which surface waves propagate,  $p$  is the ground density,  $c$  is the phase velocity of Rayleigh waves,  $u_{env}(t)$  is the envelope of the ground velocity  $u(t)$  obtained using the Hilbert transform. The damping factor  $\alpha$  accounts for anelastic attenuation of seismic waves (Aki and Richards, 1980). This factor has been estimated for Mount Saint-Eynard rockfalls at  $\alpha = 8.8 \times 10^{-4} \text{ m}^{-1}$  with a frequency centroid of 10 Hz (Le Roy et al., 2019). To estimate the damping factor of Mount Granier rockfalls, we used the events presented in this study and found  $\alpha = 1.4 \times 10^{-4} \text{ m}^{-1}$  using a frequency centroid of 5 Hz. The coefficient  $\epsilon_i$  accounts for site effects. It was estimated for each station by Le Roy et al., (2019) using a catalog of 200 earthquakes located by the regional seismic network Sismalp. This coefficient is estimated as the average ratio of peak amplitude at stations MOL, GAR, RES, and GUI over the reference station FOR, located at the cliff head. We assume a density of  $2500 \pm 100 \text{ kg.m}^{-3}$ . Seismic wave velocity ( $1810 \pm 100 \text{ m.s}^{-1}$ ) was estimated from the arrival times of seismic signals for rockfalls that occurred at Mount Saint Eynard (Le Roy et al., 2019). The location of the rockfalls is estimated from the TLS surveys. The thickness was taken as one wavelength of Rayleigh waves,  $h = 181 \pm 20 \text{ m}$  for a frequency centroid of 10 Hz.

Rockfall seismic signals can also be characterized by their equivalent magnitude, using the same relations as for earthquakes. Different types of magnitude have been used, either local magnitude ( $M_L$ ) or duration magnitude ( $M_D$ ). Local magnitude is estimated using the Gutenberg-Richter magnitude-energy relation (Kanamori and Anderson, 1975).

$$\text{Log } E_s = 1.5M_L + 4.8 \quad (8.2)$$

Duration magnitude is calculated as a function of the signal duration  $\tau$  (in s) and of the distance  $r$  (in km) between events and stations (Real and Teng, 1973; Manconi et al., 2016).

$$M_D = 2 \log(\tau + 0.082r) - 0.87 \quad (8.3)$$

In order to estimate the signal duration we used the following criteria:

$$\frac{(A_S - A_N)}{A_N} < 0.1 \quad (8.4)$$

with  $A_N$  the mean noise amplitude and  $A_S$  the average amplitude of the seismic signal envelope.  $A_S$  is evaluated at each time step using a sliding window of 0.5 second.

## 8.4 Results

### 8.4.1 Rockfall detection

#### 8.4.1.1 Mount Granier

On 2016/1/9, a first rockfall occurred on the NW pillar of Mount Granier (**Erreur ! Source du renvoi introuvable.**). This event was detected by the regional seismic array

over several tens of kilometers, including the Mount Saint-Eynard array. We used a template matching filter using this event as template, to detect small rockfalls preceding or following this event. We found no other event with similar waveform during the time interval between 2016.01.01 and 2016.06.16.

A few months later, on 2016/04/29, we detected another rockfall using the Mount Saint Eynard network and the standard detection method. This event was preceded and followed by several others in the following days originated from the same area and underwent similar run-out propagations through a narrow gully before reaching the foot of the cliff. These elements: same-origin area, large sensor-source distance (29 km), same mode of propagation, made it possible for us to use the template matching technic. Using the 2016/04/29 event as template, we identified 8 other events between 2016/04/28 and

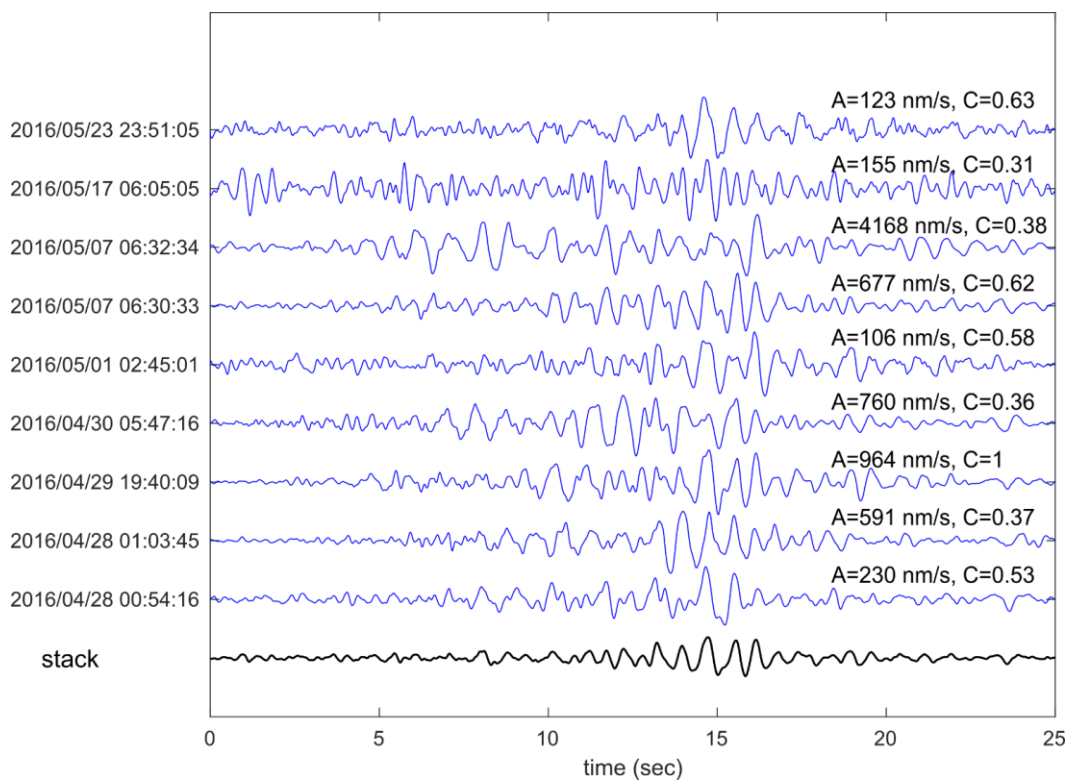


Figure 8.2. Seismic signals of the Mount Granier rockfalls recorded by station FOR (North component of ground velocity) between April and May 2016. Each signal is band-pass filtered between 2 and 10 Hz and normalized by peak amplitude A. The correlation C is computed between each event and the reference event (2016/04/29) for the North component of station FOR.

2016/05/23. These events are shown in (Figure 8.2).

The monitoring of the NE pillar of the Mount Granier using DEM started on 2016/5/3 a few days after the beginning of the rockfall series. Using DEMs, we thus can only measure the cumulated volume of events that occurred before the 2016/5/3 to  $9000 \pm 3000 \text{ m}^3$ . In contrast, using seismology we detected five rockfalls between 2016/4/28 and 2016/5/1.

Table 8.1 : Rockfall characteristics.

Site	Event	Method used for the DEM <sup>(1)</sup>		Propagation mode	Volume VDEM (m <sup>3</sup> )	Volume V <sub>MD</sub> <sup>(2)</sup> (m <sup>3</sup> )	Volume V <sub>ML</sub> <sup>(2)</sup> (m <sup>3</sup> )	Volume V <sub>MLff</sub> <sup>(2)</sup> (m <sup>3</sup> )			
		T1	T2								
Granier	2016/01/09 – 03.57.17	Ph Ar 1 <sup>(3)</sup>	Ph 2016/01/15	Flow	65000 ± 10000	51744 ± 36544	21667.7 ± 10240.7	141366.1 ± 78796.1			
	2016/04/28 – 00.54.00			Flow					2098 ± 735	23.9 ± 7.1	63.7 ± 27.7
	2016/04/28 – 01.03.47			Flow					354 ± 137	189.8 ± 67.8	665.1 ± 316.1
	2016/04/29 – 19.40.08	Ph Ar 2	Ph 2016/05/03_1	Flow	9000 ± 3000	1549 ± 552	548.2 ± 211.2	2208.3 ± 1092.9			
	2016/04/30 – 05.47.16			Flow					718 ± 267	333.2 ± 124.1	1257.4 ± 610.9
	2016/05/01 – 02.45.02			Flow					1027 ± 374	31.3 ± 9.6	86.5 ± 38.1
	2016/05/03 – 02.45.02	Ph 2016/05/03_1 <sup>(4)</sup>	Ph 2016/05/03_2	Free-fall/Flow	350 ± 50	/	/	/			
	2016/05/07 – 07.10.57	Ph 2016/05/03_2	Ph 2016/05/07	Flow	2000 ± 250	4139 ± 1397	576.5 ± 222.9	2337.5 ± 1159			
	2016/05/07 – 08.32.27			Flow	50500 ± 1000	20005 ± 6195	15982.2 ± 7446.1	100192.7 ± 55359.1			
	2016/05/17 – 06.05.05	Ph 2016/05/17	Ph 2016/05/20	Flow	600 ± 100	2424 ± 843	35.4 ± 11	99.7 ± 44.1			
2016/05/23 – 23.51.06	-	-	Flow	-	283 ± 111	20,3 ± 14,3	53,2 ± 30,2				
Saint-Eynard	2013/11/04 – 19:35:36	Li 2012/11/16	Li 2013/11/26	Free-fall	1.4 ± 0.1	44.8 ± 26.2	0.1 ± 0				
	2013/11/16 – 22:11:37	Li 2012/11/16	Li 2013/11/26	Free-fall	13.6 ± 0.1	97718.4 ± 72894.4	24 ± 7.2				
	2013/11/25 – 06:44:54	Li 2012/11/16	Li 2013/11/26	Free-fall	3.2 ± 0.1	7822.8 ± 5488.0	10.6 ± 2.9				
	2013/12/06 – 04:25:05	Li 2013/11/26	Li 2014/07/15	Free-fall	6.1 ± 0.1	14240.9 ± 10149.9	7.8 ± 2.1				
	2013/12/30 – 23:27:19	Li 2013/11/26	Li 2014/07/15	Free-fall	5.1 ± 0.1	66603.8 ± 49265.0	3.8 ± 0.9				
	2014/02/07 – 22:00:40	Li 2013/11/26	Li 2014/07/15	Flow	2 ± 1	12830.9 ± 9120.4	0.4 ± 0.1	0.6 ± 0.2			
	2014/08/02 – 19:48:44	Li 2013/11/26	Li 2014/07/15	Flow	1546.5 ± 5	148010.5 ± 111393.9	1714.4 ± 709.5	8019.5 ± 4131.5			
	2014/08/15 – 01:08:33	Li 2014/07/15	Li 2015/04/22	Free-fall	5.3 ± 0.2	64192.2 ± 47441.7	2.2 ± 0.5				
	2015/01/07 – 08:45:12	Li 2014/07/15	Li 2015/04/22	Free-fall	1.2 ± 0.1	17393.4 ± 12460.2	0.6 ± 0.1				
	2015/01/18 – 08:20:13	Li 2014/07/15	Li 2015/04/22	Free-fall	100.4 ± 0.2	15009.0 ± 10711.8	1394.7 ± 570.1				
	2015/01/22 – 21:01:31	Li 2014/07/15	Li 2015/04/22	Free-fall	1.9 ± 0.1	6154.5 ± 4289.3	0.2 ± 0				
	2015/02/02 – 17:44:10	Li 2014/07/15	Li 2015/04/22	Flow	14.7 ± 0.1	6320.7 ± 4408.4	6.8 ± 1.8	15.3 ± 6.3			
	2015/02/15 – 20:54:28	Li 2014/07/15	Li 2015/04/22	Free-fall	8.0 ± 0.1	61935.3 ± 45736.8	16.8 ± 4.9				
	2015/03/05 – 19:36:19	Li 2014/07/15	Li 2015/04/22	Free-fall	20.7 ± 0.1	85324.5 ± 63460.5	8.8 ± 2.4				
	2015/04/18 – 01:13:11	Li 2014/07/15	Li 2015/04/22	Flow	2.0 ± 0.1	49287.9 ± 36207.9	3.4 ± 0.8	7 ± 2.7			
	2015/11/25 – 03:54:39	Ph 2015/11/05	Ph 2015/12/02	Free-fall	94.0 ± 5	139320.2 ± 104720.1	345 ± 128.8				
	2017/12/30 – 13.28.48	Ph 2017/11/21	Ph 2018/01/11	Flow	105 ± 5	111503.2 ± 83414.9	12.8 ± 3.6	31.4 ± 13.3			
2018/10/28 – 01.35.42	Ph 2018/10/10	Ph 2018/12/05	Flow	1075 ± 25	55362.4 ± 40778.9	104.1 ± 35.5	337.1 ± 156.4				

<sup>(1)</sup> Method used for the DEM before (T1) and after (T2) the event. DEMs obtained by photogrammetry: 'Ph', obtained using LiDAR: 'Li'. Acquisition date is given for each model.

<sup>(2)</sup> Volume estimated from equations (8.6), (8.7), (8.8).

<sup>(3)</sup> We used a set of photographs obtained at various dates; these models are indicated as 'Ar'.

<sup>(4)</sup> Two photogrammetric data sets were acquired on 2016/5/3. Ph 2016/05/03\_1 was acquired between 6 and 7 am, shortly before the 2016/5/3 rockfall and Ph 2016/05/03\_2 was acquired after the rockfall, between 7 and 8 am.

On 2016/5/3, a rockfall estimated to  $350 \pm 50 \text{ m}^3$  was observed. However, even knowing the exact occurrence time, we did not find a corresponding seismic signal. Similarly, on

2016/5/23, we detected a rockfall using the template-matching method. However, we could not identify this event on the photographs or DEMs.

Overall, we have detected ten Mount Granier rockfalls using the Mount Saint-Eynard seismic network, of which only four could be individually characterized using DEMs (Figure 8.3, Table 8.1).

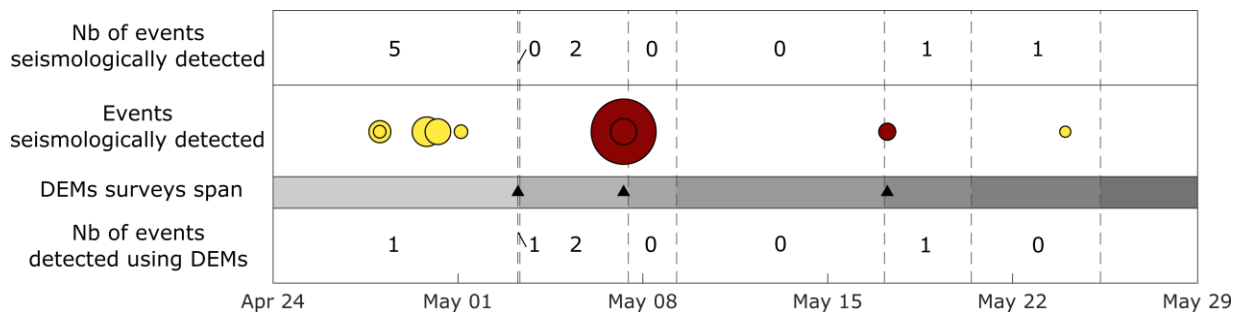


Figure 8.3. Timeline of the Mount Granier rockfall series of April-May 2016. Yellow dots: events seismologically detected, red dots: events seismologically detected and characterized using DEMs. The size of the dots is proportional to the seismic energy of the event. Black triangles: video or photographs witnessing the occurrence of a rockfall.

#### 8.4.1.2 Mount Saint-Eynard

By coupling DEM and seismic monitoring, we have compiled a catalog of 16 rockfalls that occurred at Mount Saint-Eynard between November 2013 and December 2015 with accurate time, location, geometry, and volume (Table 8.1 : Rockfall characteristics. Table 8.1). The volume of these events ranges from  $1.4 \text{ m}^3$  to  $1550 \text{ m}^3$ . An extensive presentation of this dataset can be found in a previous study (Le Roy et al., 2019).

We added to this dataset two rockfalls detected by photogrammetry that occurred outside of the area covered by the photographic surveys and that could not be precisely dated. These events have volumes of  $105$  and  $1075 \text{ m}^3$ , and are much larger than the volumes of other events detected in this area (less than  $14 \text{ m}^3$ ). These events either occurred at the base of the cliff or on a subvertical cliff where no free-fall phase can occur. A dating interval is given by the time between two consecutive DEMs: 2017/11/21-2018/1/11 for the first event and 2018/10/10-2018/12/5 for the second one. In these time intervals, we detected several rockfall seismic signals.

Using the peak amplitude recorded at each station, corrected from site effects, we can estimate which station is closest to the source. This way, we determined that most events seismically detected in these time intervals occurred between station MOL and RES. In contrast, the two events detected by TLS occurred near station GAR.

Due to the cliff configuration, mass-flow type events are quite rare. For the first period (2017/11/21-2018/1/11), we detected 4 seismic signals corresponding to a mass-flow type propagation and with the strongest amplitude at station GAR. Amongst these signals, three were characterized by rather low amplitude and short durations ( $<50$  s), and one with a particularly strong amplitude (at least 10 times larger than the others) and a larger duration ( $>60$  s). The first three signals were likely induced by events of volumes ranging from several cubic meters to a few tens of cubic meters. We thus associated the fourth seismic signal (2017/12/30 – 13.28.48) to the event of volume  $1075\text{ m}^3$  detected by DEMs between 2017/11/21 and 2018/1/11.

For the period 2018/10/10-2018/12/05, two mass-flow seismic signals were detected near station GAR. One characterized by rather low amplitude and short duration ( $<50$  s) and the other characterized by amplitude about ten times larger than the first and longer duration ( $>60$  s). Once again, if the first event was likely induced by an event of volume ranging from a few cubic meters to a few tens of cubic meters, it cannot correspond to a rockfall of  $1075\text{ m}^3$ . The largest seismic event (2018/10/28 – 01.35.42) was thus associated with the event detected by DEM between 2018/10/10 and 2018/12/5.

#### **8.4.2 Characteristics of rockfall seismic signals**

The seismograms of the Mount Granier events are similar to each other. This is due to several factors. Overall the events had similar dynamics and close location of origin but overall it is mostly due to the common wave's propagation path (from Mount-Granier to the stations at Mount Saint Eynard) for all events. Because of the distance from the source (about 30 km), there is very little energy above 20 Hz.

The seismograms of the Mount Saint-Eynard rockfalls are more complex and often present irregular envelopes with several energetic pulses. These pulses can be linked to rebounds of blocks along the cliff with the most energetic phases produced by impacts after a free-fall (Vilajosana et al., 2008; Bottelin et al., 2014; Le Roy et al., 2019). Mount Saint-Eynard rockfalls experiencing free-falls have been extensively analyzed in Le Roy et al. (2019). We focus here on events experiencing slides or flow like propagations.

For such events, two phases can be identified in the seismograms. The first one ( $t=0$ -10 s in Figure 8.4) is characterized by an irregular envelope, with several peaks. This phase can be interpreted as the detachment of the rockfall compartment and propagation of the blocks along the cliff. This phase is concluded by a high amplitude peak, which may be related to the impact of the blocks on scree, at the foot of the cliff, where the slope becomes less steep. During the second phase ( $t=10$  s to end in Figure 8.4), the envelope is smoother and slowly decaying. This phase can be associated with the propagation of the blocks on the scree until their deposit.

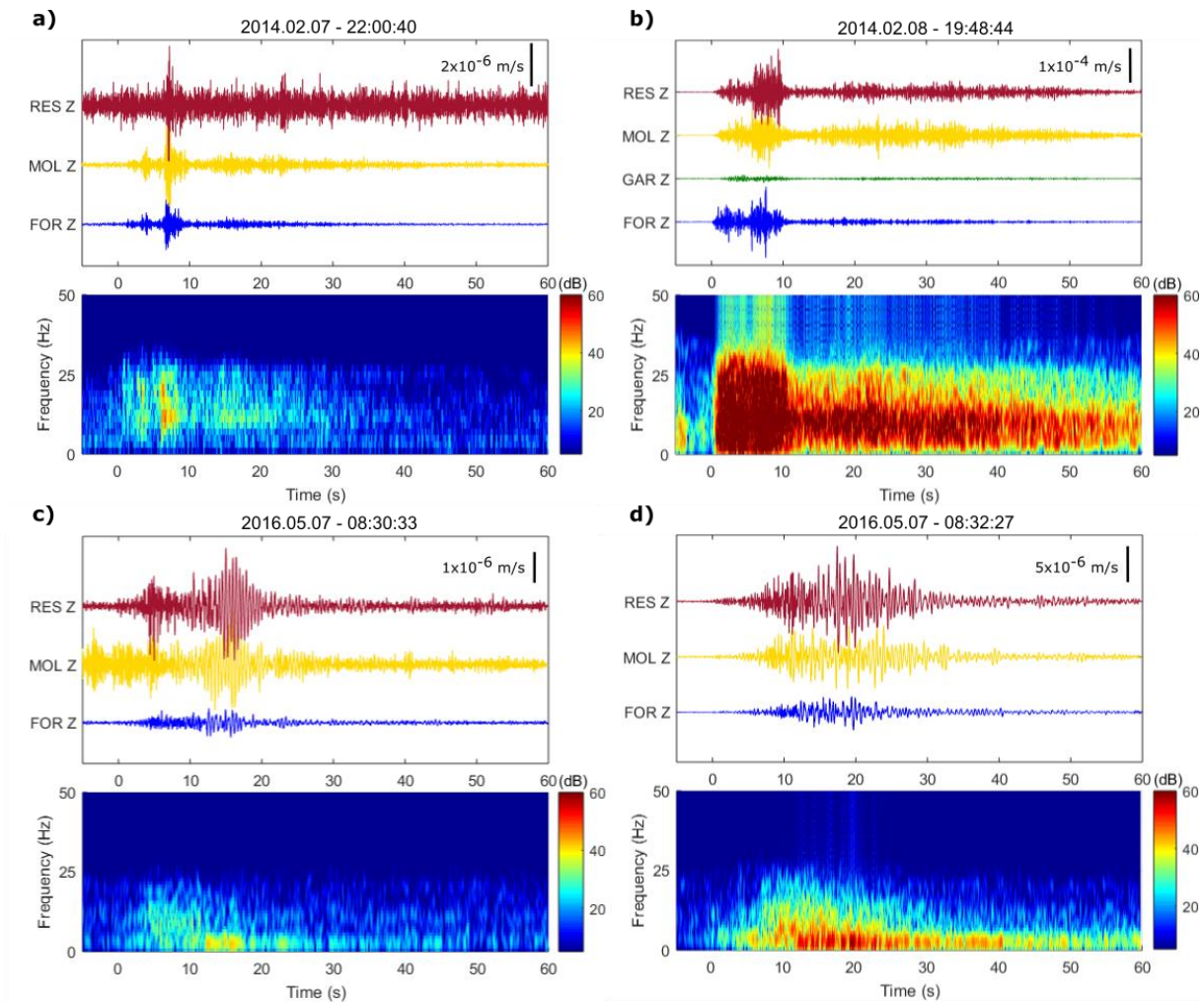


Figure 8.4. Seismic signal (vertical ground velocity, band-pass filtered between 2 and 50 Hz) and corresponding spectrogram of the a) 2014/02/07, and b) 2014/02/08 Mount Saint-Eynard rockfalls and c) and d) 2016/05/07 Mount-Granier rockfalls.

These events present common characteristics with Mount Granier rockfalls. Frequency contents stretch up to 30 Hz but lower frequencies (2-10 Hz) are mainly dominant. The envelopes of these signals present a triangular shape with a peak of amplitude a few seconds after the beginning, followed by a slow decay. The frequency content also varies with time, with high frequencies mainly observed during the first 10 s of the signals.

### 8.4.3 Volume estimation using rockfall seismic signals

We estimated the local and duration magnitudes from the seismic signals using Equations (8.2) and (8.3). To compare our results with other sites over a wider range of volumes, we present in Figure 8.5.a and 8.5.b our data along with data from previous studies (Wieczorek et al., 2000; Deparis et al., 2008; Dammeier et al., 2011; Manconi et al., 2016 Fuchs et al., 2018). To observe the influence of the propagation mode of the events, we have color-coded (Figure 8.5.c and 8.5.d) our datasets according to the



propagation mode: events that experienced free-falls (>5 m) during their propagation or events sliding along the cliff or experiencing slides or flow like propagation.

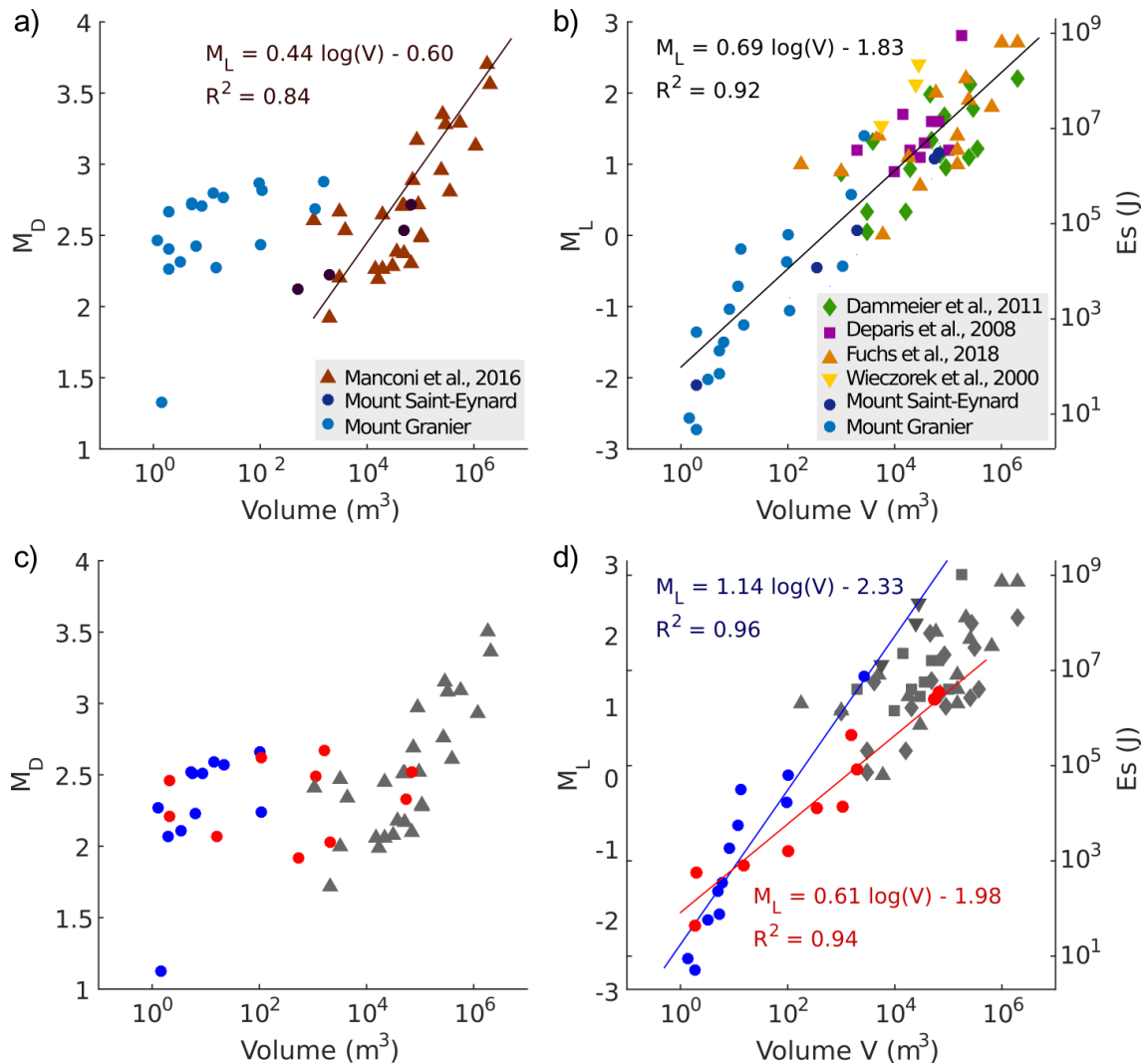


Figure 8.5. Equivalent magnitude as a function of rockfall volume for duration magnitude (a, c) or local magnitude (b, d). Graphs (c) and (d) presents the same data as respectively (a) and (b) with events color-coded according to their propagation type: in blue, events that experienced free-falls during their propagation; in red, events sliding along the cliff or experiencing a flow like propagation; in grey, undefined. Lines are linear relations between magnitude and logarithm of volume using (a) the dataset of Manconi et al., (2016), (b) all datasets, (d) in blue rockfalls having experienced a free-fall (>5 m) during their propagation and in red events sliding or having experienced a flow like propagation.

### 8.4.3.1 Duration magnitude

In their paper, Manconi et al., 2016, proposed a relation between duration magnitude  $M_D$  and rockfall volume  $V_{MD}$  for rockslide phenomena located in the European Alps detected by broadband seismic arrays.

$$M_D = a \log(V_{MD}) - b \quad (8.5)$$

with  $a = 0.44 \pm 0.03$  and  $b = 0.60 \pm 0.13$  (confidence interval 68%).

The relation between duration magnitude and rockfall volume for of Mount Granier is consistent with Manconi's dataset. Using this relation, we calculated the volume of Mount Granier rockfalls that were only detected using the seismic network (Table 8.1). We obtained a cumulated volume of  $5750 \pm 3430 \text{ m}^3$  for a volume estimated by DEMs  $9000 \pm 3000 \text{ m}^3$ . Overall, Mount Granier rockfall volumes are well estimated (Table 8.1) with a mean relative error  $e = \langle \log(V_{\text{DEM}}) - \log(V_{\text{M}}) \rangle = 0.32$ .

On the contrary, the duration magnitudes of Mount Saint-Eynard dataset are scattered and do not follow the trend of Manconi's dataset.

### 8.4.3.2 Local magnitude

As shown in Figure 6.b, the relation between local magnitude and rockfall volume for Mount Granier and Mount Saint-Eynard datasets is in good agreement with previous studies. Using all datasets (Wieczorek et al., 2000; Deparis et al., 2008; Dammeier et al., 2011; Fuchs et al., 2018; Mount Granier and Mount Saint-Eynard), we found a relation between magnitude  $M_L$  and rockfall volume  $V_{ML}$ .

$$M_L = a \log(V_{ML}) - b \quad (8.6)$$

with  $a = 0.69 \pm 0.02$  and  $b = 1.83 \pm 0.07$ .

Using this relation, we calculated the volume of Mount Granier rockfalls that were only detected using the seismic network (Table 8.1). We obtained a cumulated volume of  $1126 \pm 419 \text{ m}^3$  ( $V_{\text{DEM}} = 9000 \pm 3000 \text{ m}^3$ ). Overall, Mount Granier rockfall volumes are underestimated by on average 25%. Mount Saint-Eynard rockfalls are better estimated (Table 8.1;  $mE=1.54$ ) than with duration magnitude with  $e = 0.53$ .

As shown in Figure 8.6d, the relation between local magnitude and rockfall volume of free-falling events  $V_{ML_{ff}}$  does not follow the same trend as other events.

$$M_L = a \log(V_{ML_{ff}}) - b \quad (8.7)$$

with  $a = 1.14 \pm 0.05$  and  $b = 2.33 \pm 0.07$ .

As found by Le Roy et al. (2019), selecting events with the same propagation type provides a more accurate characterization of rockfalls properties than when mixing different types of events. We thus defined a relation between local magnitude  $M_L$  and the rockfall volume of mass-flow events  $V_{ML_{mf}}$  at Mount Saint Eynard and Mount Granier

$$M_L = a \log(V_{ML_{mf}}) - b \quad (8.8)$$

with  $a = 0.61 \pm 0.03$  and  $b = 1.98 \pm 0.12$ . And the equivalent relation between seismic energy  $E_s$  and the rockfall volume of mass-flow events  $V_{ML_{mf}}$ .

$$E_s = a V_{ML_{mf}}^b \quad (8.9)$$

With  $a = 66.7 \pm 19.3$  and  $b = 0.89 \pm 0.5$  (confidence interval 68%).

Mount Granier rockfalls only detected using the seismic network have a cumulated volume estimated to  $4281 \pm 3712 \text{ m}^3$  ( $V_{\text{DEM}} = 9000 \pm 3000 \text{ m}^3$ ). Both Mount Granier and Mount Saint-Eynard rockfall volumes are well estimated (Table 8.1) with respectively  $e = 0.36$  and  $e = 0.54$ .

Table 8.2 Relation between the magnitude of the rockfall seismic signal (MI or MD) and the observed volume V for different datasets using a linear relation between magnitude and  $\log(V)$ .

Eq.	Dataset	Number of events	Volume range <sup>(1)</sup>	Variable	Average error <sup>(2)</sup>	R <sup>2</sup> <sup>(3)</sup>	P <sup>(3)</sup>
5	Manconi (2016)	29	$10^3 - 10^7$	M <sub>D</sub>	0.55	0.84	$3.2 \times 10^{-8}$
5	Granier	11	$10^2 - 10^4$	M <sub>D</sub>	0.32	/	/
5	Saint Eynard	18	$1 - 10^3$	M <sub>D</sub>	3.24	/	/
6	All datasets <sup>(4)</sup>	70	$1 - 10^6$	M <sub>L</sub>	0.62	0.92	$2.0 \times 10^{-25}$
6	Granier	11	$10^2 - 10^4$	M <sub>L</sub>	0.73	/	/
6	Saint Eynard	18	$1 - 10^3$	M <sub>L</sub>	0.53	/	/
8	Mass flow events, St-Eynard/Granier	10	$1 - 10^4$	M <sub>Lmf</sub>	0.51	0.94	$1.1 \times 10^{-5}$
8	Granier	4	$10^2 - 10^4$	M <sub>Lmf</sub>	0.36	/	/
8	Saint Eynard	6	$1 - 10^3$	M <sub>Lmf</sub>	0.64	/	/

<sup>(1)</sup> Minimum and maximum rockfall volumes in each dataset.

<sup>(2)</sup> Average error on  $\log(V) = \log(V_{\text{DEM}}) - \log(V_M)$

<sup>(3)</sup> R and p are the values of the correlation coefficient between M and  $\log(V)$  and the associated probability p of observing a larger correlation by chance.

<sup>(4)</sup> Datasets: Wieczorek et al., 2000; Deparis et al., 2008; Dammeier et al., 2011; Fuchs et al., 2018, Mount Granier and Mount Saint-Eynard).

## 8.5 Discussion

This study highlights the benefits of combining seismology and topographic data for rockfall monitoring. DEMs provide accurate information on rockfalls geometry, volume, and location. Seismology provides accurate occurrence times and information on rockfalls dynamics (type and duration of propagation, etc). Rockfall volume can also be inferred from properties of the seismic signal, either seismic energy or signal duration.

The relation between rockfall volume and duration magnitude of Mount Granier events is consistent with the dataset of Manconi et al. (2016). This agreement is probably due to the common characteristics between datasets: similar volume range and similar distances between events and seismic stations (average station-event distance of 30 km). The relationship between duration magnitude and rockfall volumes defined by Manconi et al. (2016) allowed a good estimation of the volume of the rockfall sequence (average error on  $\log(V)$   $e = 0.32$ ). However, this relation does not allow a good characterization of another dataset composed of smaller events (Mount Saint-Eynard dataset,  $V < 1500 \text{ m}^3$ ), which duration magnitudes are strongly scattered (**Erreur ! Source du renvoi introuvable.**). Small rockfalls are prone to erratic behavior; they may rest upon landing, roll or slide along the slope, or trigger subsequent scree slope activity by their

impact. In the Mount Saint-Eynard dataset, the duration of the propagation phase is strongly influenced by the topography, the slope, and the forest cover, etc. For such processes, propagation duration may not be correlated with rockfall volume. This discrepancy might also be due to the difference in source-station distance. The end of the propagation phase has a smaller amplitude than the first part of the seismic signals and may not be visible above the noise level at large distances. In our study, the source-station distance ranges from less than 1 km up to 30 km, while the distance is larger (average station-event distance 30 km) in the dataset of Manconi et al. (2016).

In contrast, using the local magnitude, we obtain consistent volume estimates for all datasets (Mount Granier and Mount saint-Eynard datasets; Wiczorek et al., 2000; Deparis et al., 2008; Dammeier et al., 2011; Fuchs et al., 2018). The relation between local magnitude and rockfall volumes defined using all datasets allowed a fair estimation of the volume of Mount Saint-Eynard and Mount Granier rockfall volumes (Table 8.1 : Rockfall characteristics.) with average errors on  $\log(V)$  of respectively 0.53 and 0.73. This relation thus provides a much more accurate characterization of Mount St-Eynard volumes than with the duration magnitudes. Nevertheless, this relation underestimates the volumes of Mount Granier rockfalls by on average 25%. This suggests that this relation obtained using all datasets may need to be calibrated for each site to improve the accuracy.

In a previous study Le Roy et al. (2019) showed that by segregating rockfalls experiencing a free-fall from those with sliding or bouncing transport modes, they obtained more accurate volumes than other studies considering mixed propagation modes (Deparis et al., 2008; Dammeier et al., 2011, Manconi et al., 2016, Fuchs et al., 2018). By selecting rockfalls experiencing a flow like propagation for Mount Saint-Eynard and Mount Granier events, we defined a relation between the local magnitude  $M_L$  and the rockfall volume of mass-flow events  $V_{ML_{mf}}$ . This relationship allowed a better estimation of the volume of Mount Granier rockfalls ( $e = 0.36$  than when mixing all type of events ( $e = 0.73$ , equation 8.6). The volume of Mount Saint-Eynard rockfalls calculated using this method may, however, vary from those measured using DEMs (Table 8.1) and present a slightly larger mean relative error  $e = 0.64$  than when using equation 8.6 ( $e = 0.53$ ). This hypothesis needs thus to be further explored with a larger dataset.

Several studies showed that rockfall seismic energy is better correlated to the potential energy of granular flows and rockfall events (Hibert et al., 2011; Hibert et al., 2015) and similar results were found for impacts for free-falling rockfalls (Le Roy et al., 2019) than with rockfall volumes. The difficulty of this method is to calculate the potential energy of the propagation of an event. This requires an in-depth knowledge of the dynamics of the event (location of departure and arrival, duration of propagation, knowledge of the topography, etc.) and this information is often difficult to determine precisely.

The relations (8.6) and (8.9) provided us with an estimate of the volume for rockfalls of the 2016 Mount Granier sequence that were only detected using the seismic network. Only the total volumes could be determined by DEMs for the five rockfalls that occurred between 2016/4/28 and 2016/05/1. We obtained a cumulated volume of  $5750 \pm 3430 \text{ m}^3$  using the relation (8.6) (mixing all datasets) and  $4281 \pm 3712 \text{ m}^3$  with the relation (8.9) (selecting mass-flow events). These values are lower than the total volume of  $9000 \pm 3000 \text{ m}^3$  determined by DEMs but the difference is within error bars. The volume of this compartment measured using DEMs may be overestimated. The photo dataset used to construct the DEM “Ph Ar 2” prior to the rockfall sequence did not provide extensive coverage of the area as the following DEM, as it was not originally meant to be used for a photogrammetric purpose.

The scar area is complex with grey areas on the photographs and DEMs. Events occurring in these areas might not have been detected using DEMs. This might be the case for the 2016/05/23 event, which was detected by seismology but not on the DEMs. On the contrary, we witnessed an event on 2016/5/3 and we could characterize this event using DEMs. However, we did not detect the associated seismic signal, either using the template-matching method or looking at the continuous seismic signal at the time of this event. This is the smallest event detected by DEM ( $350 \text{ m}^3$ ), so it may be too small to be detected by template-matching method, especially since the seismic noise level was quite high at this time (twice as high as the mean level of seismic noise of the other events, and larger than the maximum amplitude of the smallest event detected using template-matching on 2016/5/23).

## 8.6 Conclusion

We monitored two cliffs, Mount Saint-Eynard and Mount Granier using DEMs and seismology. In this study, we used seismic monitoring to detect and characterize a rapid succession of rockfalls. In 2016, we detected 10 Mount Granier rockfalls with a seismic network using the template-matching filter method. Only four of these events could be individually characterized using DEMs.

We have derived several relations between rockfall volume and properties of the seismic signal (duration and seismic energy). We first used a relation between duration magnitude and rockfall volume defined by Manconi et al. (2016). We found a good agreement for Mount Granier rockfalls. This relation, however, is not consistent with a dataset composed of smaller rockfalls detected at Mount Saint-Eynard ( $2 - 1500 \text{ m}^3$ ). We then tested a relation between local magnitude and rockfall volume obtained using different datasets of rockfalls with volume between 1 and  $10^6 \text{ m}^3$ . This relation provides fair results but underestimate Mount Granier rockfall volumes (Table 8.1). Using a specific relation derived using only mass-flow type of propagation for Mount Saint-

Eynard and Mount-Granier rockfalls, we obtained more accurate volume estimates than when mixing all events.

By coupling DEMs and seismic records, we have reconstructed this rockfall sequence with accurate timing and correct volume estimations, providing us a good understanding and a precise chronology of this rockfall sequence. This information can be used to analyze the triggering factors. However, in the case of Mount Granier, we found no obvious triggering factor. The meteorological conditions (temperature and precipitations) at the time of each rockfall were not unusual.

Mount Granier rockfall hazard is still high in the area. The rock-mass located at the left of the failure zone is cut by the same vertical fracture plane that was delimiting the 7<sup>th</sup> of May event, forming an important flake about 100 m high, 30 m wide and 20 m thick. This 50 000 m<sup>3</sup> flake is separated from the cliff by a 30 m long tension crack with an opening of up to 2 m. Rockfall detection using template matching could play a decisive role in detecting future rockfall events at Mount Granier. The relations between magnitude and volume defined in this study can provide a quick estimation of rockfall volumes whether at Mount Granier or for other cliffs. DEMs remains necessary for a better calibration and a better knowledge of the compartment's geometry (location, volume, dimension, etc.). Nonetheless, through this study we showed that seismology may be a valuable tool for near real-time hazard management.



Part IV

Outlook





---

*In this part, we present several perspectives on rockfall monitoring. We introduce the use of a thermographic camera (also called an infrared camera) for rockfall monitoring (Chapter 9). Using ambient infrared radiation we were able to qualitatively characterize blocks propagation. We present observations obtained from two experiments: a small scale block release experiment presented in Chapter 7 and an experiment of controlled releases of single blocks in a limestone quarry. The latter allowed us to characterize rockfall impacts combining several methods: broadband seismic stations, video cameras, and an infrared camera. These datasets have not yet been fully processed. Preliminary results are presented in Chapter 9.*

*Finally, we present in Chapter 10 some perspectives on how this work could be further developed for rockfall monitoring.*

---



## 9 Thermography of block impacts

*Infrared Thermography (IRT) provides a surface temperature map of the investigated object. Temporal evolution and local radiant temperature differing from the temperature of the surrounding areas enable the detection of thermal anomalies within the investigated object (structural discontinuities, open fractures, exfoliation sheets, etc.). We used an infrared camera to detect changes in surface temperature of the slope during blocks propagation. We present in this chapter a short presentation of the fundamentals of IRT and a rapid review of its application for slope instability monitoring. We then present our work on IRT of block impacts. We present the observations obtained from two experiments: the small scale block release experiment described in Chapter 7 and a field experiment of controlled releases of single blocks carried out in a limestone quarry (Authume, France). This experiment allowed us to characterize rockfall impacts combining several methods: seismic stations, video cameras. We also used an infrared camera to detect changes in surface temperature during the block propagation. These datasets are currently being processed. We present here the context of these experiments, preliminary results and long-term goals.*

### 9.1 Thermographic monitoring of slope instabilities

IRT technique is used in several areas, such as construction, car manufacturing, industries, or medicine. In recent years, IRT has been more and more used in Earth sciences, particularly in volcanology (Spampinato et al., 2011; Mueller et al., 2013).

Infrared Thermography (IRT) provides a surface temperature map of the investigated object. Temporal evolution and local radiant temperature differing from the temperature of surrounding areas enable the detection of thermal anomalies within the investigated object.

Compact and sound rocks have greater thermal inertia (Moore et al., 2011; Baroň et al., 2014) than fractured rocks which experience faster temperature variations (Pappalardo et al., 2016). The repetition of IRT surveys during cooling or heating periods enabled the detection of thermal anomalies induced by the presence of structural discontinuities: open fractures, weathered rock, etc. (Frodella et al., 2014; Teza et al., 2015). Fractured rocks favor air circulation and present a poor thermal conductivity.

This way, loose rock sections of slopes or mine roofs have been successfully detected using IRT (Wu et al., 2005; Vogt et al., 2010; Prendes-Gero et al., 2013). Guerin et al. (2019) were also able to remotely characterize the stability of granitic exfoliation sheets on El Capitan cliffs (Yosemite Valley, USA). They used IR thermal imaging to detect the intact rock bridges of these exfoliation sheets prior to failure. Moisture and seepage zones have also been identified by Spampinato et al. (2011) and Barla et al. (2016).

Mueller et al. (2013) have detected rockfall occurrence due to the temperature anomaly left by blocks propagation on an active volcano slope. They also found that rockfall volumes were correlated with the maximum temperature of the freshly exposed dome surface. To our knowledge, this study is the first study characterizing rockfall occurrence using an IR camera. Unfortunately, this method cannot be widely applied, as it requires a hot slope surface.

## 9.2 Fundamentals of infrared Thermography

Each body (with a temperature larger than absolute zero) emits electromagnetic radiations proportional to its intrinsic temperature. A fraction of this radiation consists in IR radiation. Infrared radiations are characterized by wavelengths longer than those of visible light (wavelengths range from about 0.7  $\mu\text{m}$  1000  $\mu\text{m}$ ). Infrared temperature measurements commonly use wavelengths ranging from 0.7 to 14  $\mu\text{m}$ . Above these wavelengths, the energy level is so low that detectors are not sensitive enough to detect them. In simplified terms, an infrared (IR) camera consists of a lens focusing radiation beams on a detector element. This detector generates an electrical signal with an output signal proportional to the object temperature.

However, when measuring IR radiation  $W_{\text{tot}}$ , the camera not only receives radiations emitted from the object  $\epsilon \cdot \tau \cdot W_{\text{obj}}$ . Most bodies (grey bodies) have a reflectivity greater than zero (Usamentiaga et al., 2014) which means that they reflect infrared radiations emitted by the surroundings  $(1-\epsilon) \cdot \tau \cdot W_{\text{ref}}$ . Another emission of infrared radiations comes from the atmosphere  $(1-\tau) \cdot W_{\text{atm}}$  (Figure 9.1).

$$W_{\text{tot}} = \epsilon \cdot \tau \cdot W_{\text{obj}} + (1 - \epsilon)W_{\text{ref}} + (1 - \tau)W_{\text{atm}} \quad (9.1)$$

$$W_i = \sigma T_i^4 \quad (9.2)$$

with  $\epsilon$  the emissivity of the object material,  $\tau$  the transmittance of the atmosphere and  $\sigma$  the Stefan-Boltzmann constant ( $5.67 \cdot 10^{-8} \text{ W} \cdot \text{m}^{-2} \cdot \text{K}^{-4}$ ).

Object emissivity depends on several parameters such as its material, surface roughness, temperature, wavelength or measuring angles. Atmospheric transmittance depends mainly on the distance between the target object and the camera, the relative humidity, and the atmospheric temperature. However, when the distance target/camera is small (a few meters), the atmospheric transmission is close to 1.0 (Minkina and Klecha, 2016).

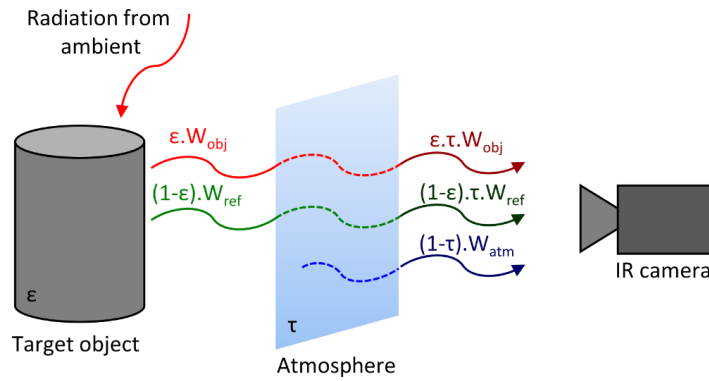


Figure 9.1. Principle of infrared radiation received by an IR camera.

### 9.3 Thermography of impact prints

A question that arises is the capacity to characterize impacts' properties (blocks' volume, kinetic energy) using thermography. Wu et al. (2005) and Shi et al. (2007) found relations between the kinetic energy of a steel bead bouncing on rock blocks and the thermic print left by the impact.

We carried out an experiment to develop these observations for block impacts. As presented in Chapter 7, a small-scale block release experiment was realized. We dropped a small block (2.9kg) on a concrete block (40x40x20 cm) embedded in a gravel tank. The block was lifted using a pulley and released using a quick release shackle. This equipment allowed us to release the block without friction and with a good repeatability of the release initial conditions. 104 release experiments were carried out using the same limestone block. Free-fall heights were variable: 0.5, 1.0, 1.5, 2.0 m. The angle of the impacted surface was changed through the experiment: 20°, 30°, 40°, 50°, 60°. We repeated each drop at least 3 times.

One camera (Canon EOS 7D, 30 frames per second (fps)) was placed on one side of the gravel tank and used to record blocks impacts. An infrared camera (Optris PI640, 30 fps) was placed perpendicular to the slope with a constant distance (1 m) and angle (45°) with the impacted concrete block. Using this camera we could monitor the boulder impact on the concrete block.

#### 9.3.1 Impacts characteristics

As presented in Chapter 7, the velocity of the block  $v$  before impact can be inferred from its free-fall height  $H_{ff}$  (equation 7.1) allowing us to determine the boulder kinetic energy before impact (equation 7.2). As the impacted surface is tilted, it is possible to decompose the impact velocity into its normal  $v_N$  and tangential  $v_T$  components as a function of the tilt angle  $\beta$  (equation 7.3 and 7.4). Block trajectory following the impact

is measured using the two cameras. This way, translational velocity  $v_t$  and rotational velocity  $v_r$  could be inferred allowing us to deduce kinetic energy of the blocks following the impact  $E k_R$  (equation 7.6) and the dissipated kinetic energy  $dEk$  (equation 7.9).

In order to characterize the thermal footprint created by the boulder impact we defined three parameters: maximal temperature  $T_{max}$ , mean temperature  $T_a$  and the integral of temperature change of impacted area over its surface  $\int_S \Delta T$ .

To characterize the increase of temperature  $\Delta T_{impact}$ , we subtract for each pixel its temperature value just before impact  $T_{ini}$  to the measured temperature after impact  $T_{meas}$ . After impact, the boulder stays within the field of view during several frames and may prevent a clear vision of the impacted area. The impact temperature  $T_{meas}$  was thus taken 0.3 s after impact in order to insure a consistency between drops.

$$\Delta T_{impact} = T_{meas} - T_{ini} \quad (9.3)$$

$$T_{max} = \max(\Delta T_{impact}) \quad (9.4)$$

$$T_a = \text{mean}(\Delta T_{impact}) \quad (9.5)$$

Thermal energy  $Q$  depends on the mass of the body  $m_T$ , its heat capacity  $c$  and the change in temperature between the initial and final body temperature  $\Delta T$ . In our case, only a fragment  $\Delta V$  of the body volume is affected by the temperature change.

$$m_T = \Delta V \cdot \rho \quad (9.6)$$

$$Q = \Delta V \cdot \rho \cdot c \cdot \Delta T \quad (9.7)$$

IR camera can only provide a temperature measurement of the surface of the object. To retrieve the sub-surface temperature it would be necessary to make assumptions about the temperature distribution at any depth. 6 thermistor elements were cast in the concrete block to measure the temperature changes between 2 and 4 cm below the surface. Temperature changes were recorded by the thermistors. However, they were not recorded in a systematic way or in a sufficiently dense manner to correctly characterize the sub-surface temperature variations. We thus only present the variation of temperature at the surface:

$$\int_S \Delta T = \sum a_{pix} \cdot T_{impact} \quad (9.8)$$

with  $a_{pix}$  the pixel area.

### 9.3.2 Results

The thermography of the impacts shows an increase of temperature on the impacted area up to 200°C (Figure 9.2, Figure 9.3).

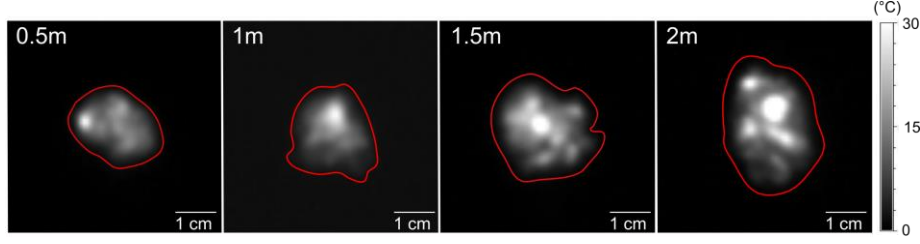


Figure 9.3. Impacts thermography of impact print for various free-fall height: 0.5 m, 1 m, 1.5 m, 2 m.

$T_a$ ,  $T_{max}$  and  $\int_S \Delta T$  increase as a function of kinetic energy (Figure 9.2). Alike seismic energy (Chapter 7), these parameters also depend on the tilt angle of the impacted block (Figure 9.4).

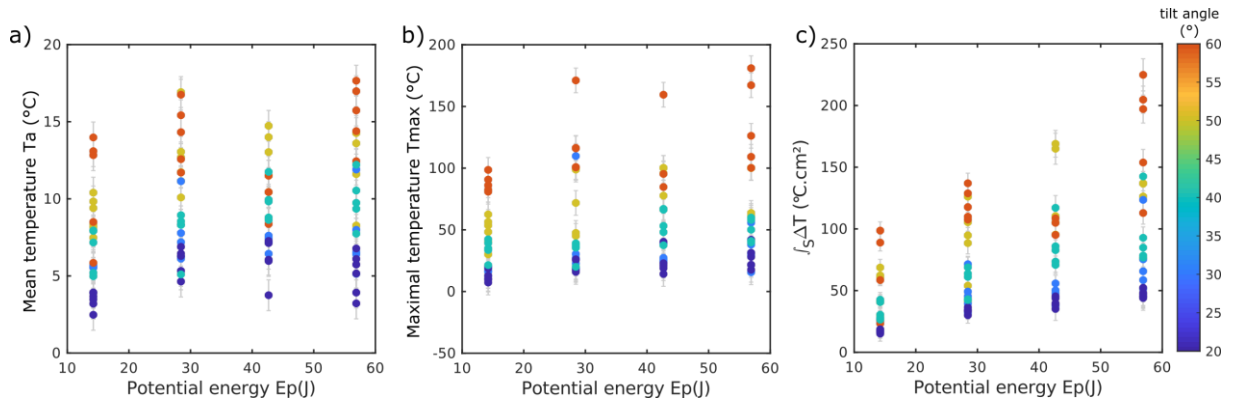


Figure 9.2. a) Mean temperature, b) maximal temperature and c) integral of temperature change over the impacted area as a function of kinetic energy. Color scale represents the tilt angle of the impacted surface.

Seismic energy and heat generation seem to have a complementary behavior. While seismic energy is correlated to the dissipated kinetic energy and normal component of the kinetic energy (Figure 7.5, Table 7.2), thermic parameters  $T_{max}$ ,  $T_a$  and  $\int_S \Delta T$  are correlated with the tangential component of the kinetic energy. Normal component of the energy produces a surface deformation by hertz contact, inducing a seismic signal. The tangential component can be connected to a sliding movement. This suggests that heat generation might be related to friction during the impact. These relations remain however unclear and should be further investigated.

As mentioned before, to calculate thermic energy, it is necessary to retrieve the variation of temperature at any depth. To reach this goal it would be necessary to associate measured sub-surface temperature changes and numerical simulations.

Computing thermal energy  $E_{th}$  could also help us to complete an energy balance assessment with the initial kinetic energy  $Ek_i$ , the residual kinetic energy  $Ek_r$ , seismic energy  $Es$  and other  $E_o$ :

$$Ek_i = Ek_r + Es + Ek_{th} + E_o \quad (9.9)$$



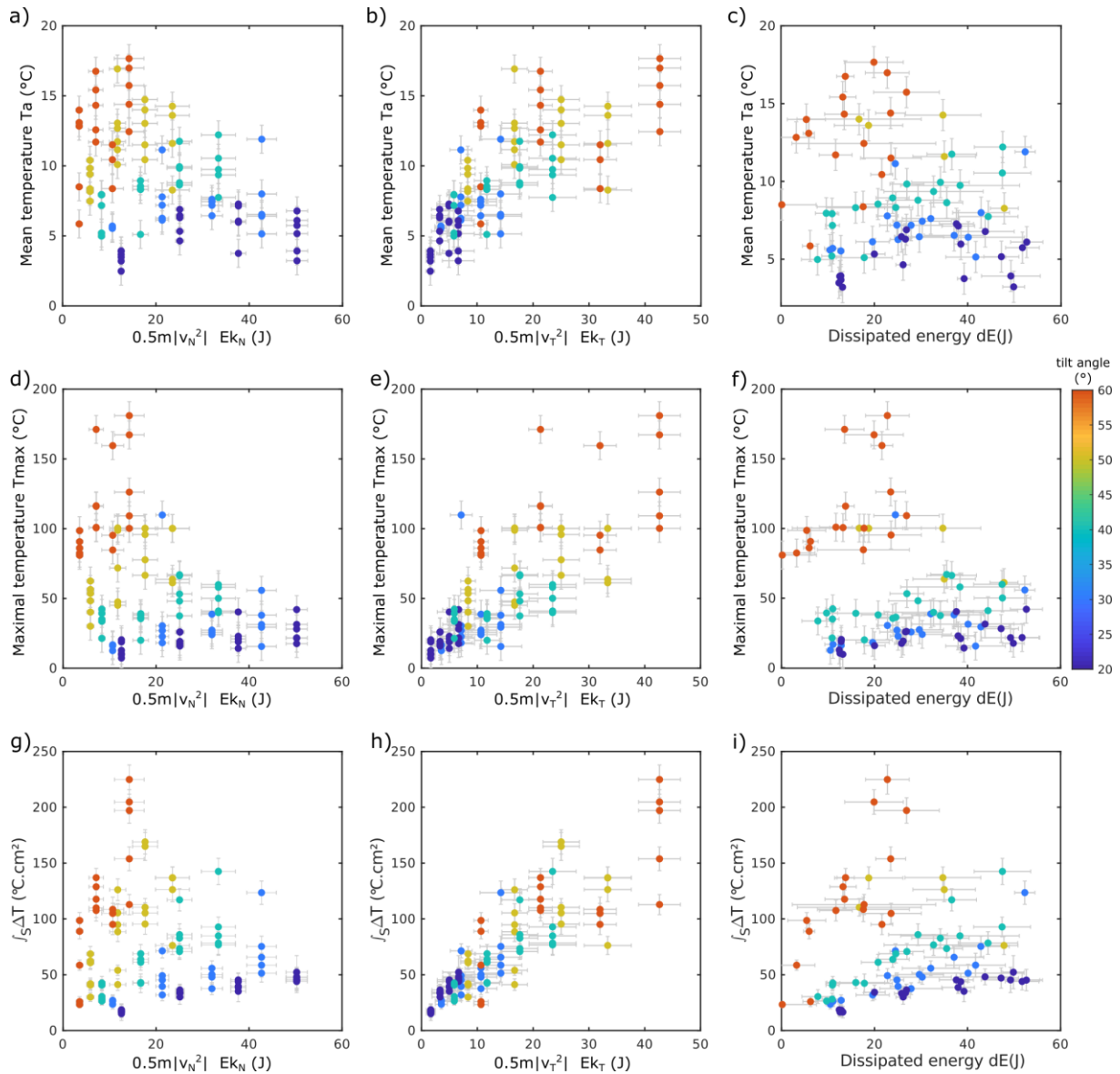


Figure 9.4. Respectively mean temperature, maximal temperature and integral of temperature change of the impacted area as a function of a, d, g) the normal component of the velocity  $0.5m |v_N^2|$ , b, e, h) the tangential component of the velocity  $0.5m |v_T^2|$  and c, f, i) the kinetic energy dissipated during the impact  $dE$ . Color scale represents the tilt angle of the impacted surface.

$E_o$  denotes other types of energy, such as the dissipation energy through surface energy or radiation energy within other wavebands. Surface energy related to the creation and propagation of cracks within the concrete block is difficult to estimate. It could be obtained through the analysis of a thin section of the impacted block. This work is complex and is beyond the scope of this study.

## 9.4 Trajectory benchmark

A benchmark of trajectory analysis methodologies was held in October 2017 (Authume, France). The objective of this benchmark was to provide recommendations

for improving numerical rockfall simulations and assessing their accuracy (Consortium of task A3, C2ROP project, 2018). This experiment was carried out in a limestone quarry (Callovian stage). Two propagation paths were adopted. The first propagation path P1 consists of slopes of 30-40° overhanging two successive rock walls (10 and 15m high) separated by a flat track (Figure 9.5). The second path P2 is characterized by slopes of 30-40° overhanging two successive slightly sloping tracks ( $\approx 10^\circ$ ).

50 blocks, ranging from 180 to 1750 kg, were released on each propagation path. The blocks themselves were extracted by blasting from the same limestone of the quarry. Each block was dropped using a bulldozer from a fixed release height (Figure 9.5).

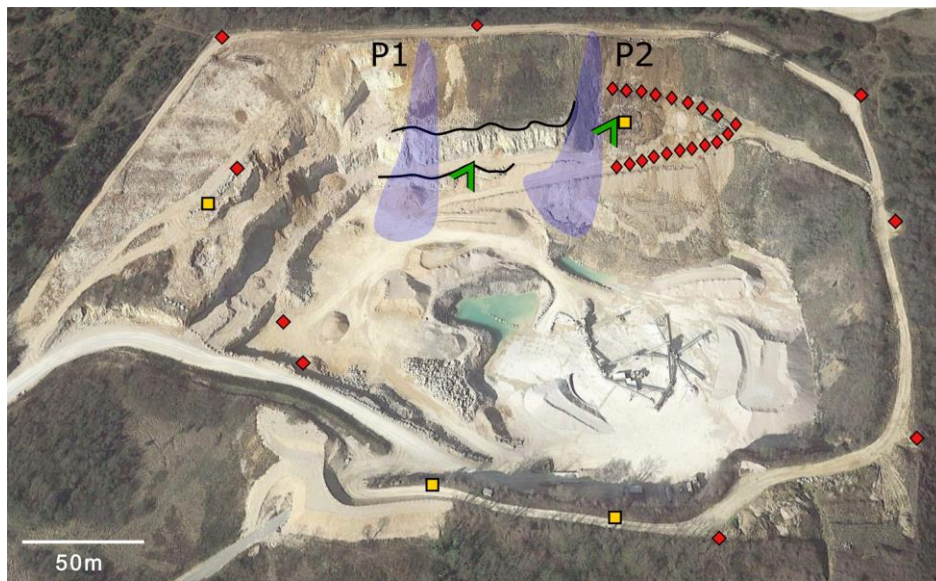


Figure 9.5. Aerial view of the test site. Blue areas: propagation paths, yellow square: video cameras locations, red diamonds: seismometers and geophones location, green triangles: infrared camera.

#### 9.4.1 Blocks dynamics and seismic monitoring

Blocks trajectories were filmed by two video cameras to provide information on block dynamics. The tri-dimensional positions of the blocks were determined by projecting the digital footage onto a DEM of the quarry (resolution: 2m). Translational velocities were calculated from block impact locations and block travel times between consecutive impacts, assuming a parabolic trajectory of the block.

To investigate relations between impacts' properties and the associated seismic signal features, we deployed several broadband seismic stations and a seismic array composed of 24 geophones (GS-11D, corner frequency 4.5 Hz, sampling rate 1000 Hz) (Figure 9.5).

This seismic monitoring has two purposes. The first purpose is to develop a rockfall location methodology based on the identification of Rayleigh waves on the seismic signals. This work is primarily carried out by Clara Lévy. In a previous work, Lévy et al. (2018) showed that the signal processing method proposed by Meza-Fajardo et al. (2015) allowed isolating Rayleigh waves from seismic signals of rockfalls. For all signals, it was

always possible to reconstruct, at least partially, a signal corresponding to Rayleigh waves. The reconstructed signals are simplified (as only Rayleigh waves trains are extracted) and have a better signal-to-noise ratio than the original signals. The simplified seismic signals were used for the location of Mount Saint-Eynard rockfalls. However, the geometry of the Mount Saint-Eynard network does not ensure an azimuthal constraint for location by a triangulation procedure and may be too large for detailed rockfall locations. Overall events were located with an error between 50 m and 300 m.

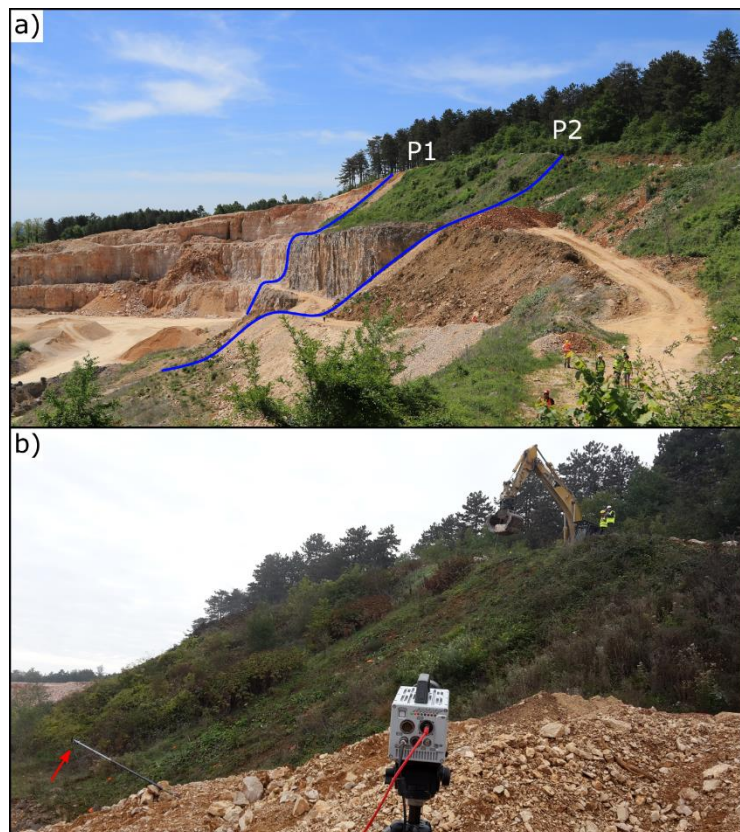


Figure 9.6. a) Photograph of the test site. The propagation paths are represented by the blue lines. b) Photographs of a block release. A video camera can be seen at the forefront and the infrared camera is indicated by the red arrow.

This method may be more efficient with a more confined network of seismometers (mesh of a few hundred meters). For this experiment, distances between the seismometers and sources are consequently smaller than for Mount Saint-Eynard rockfalls. Moreover, the geometry of this seismic network will allow a better azimuthal constraint to locate block impacts. This experiment will thus allow us to analyze the potential benefits of this method for rockfall location.

The second purpose of the seismic monitoring of this experiment is to investigate relations between impacts properties and their induced seismic signals. In Chapters 6 and 7, we presented our work on free-falling rockfall. In Chapter 8, we focused on mass-flow type events. This experiment involves two different propagation paths inducing various propagation modes of the blocks. For P1, blocks often began their propagation



by rolling down the slope before going into a free-fall when passing the rock walls. P2 allows us to analyze another type of propagation: single blocks bouncing along the slope.

Slope composition varies according to the propagation path. P2 and the upper part of P1 consists of poorly consolidated materials. The lower part of P1 and two tracks present at P2 consists in either rock or well-compacted soil. This might induce variations of the impacts' seismic signals. Angle slope also differs from flat or slightly tilted ( $\approx 10^\circ$ ) at the tracks or quarry floor, to angles of  $30\text{-}40^\circ$  at the slopes. This might also affect the impacts seismic signals.

This experiment will thus allow us to validate the previous observations and to further develop our knowledge on the relations between dynamic parameters of single-block rockfalls and their seismic signals. These datasets are currently being processed.

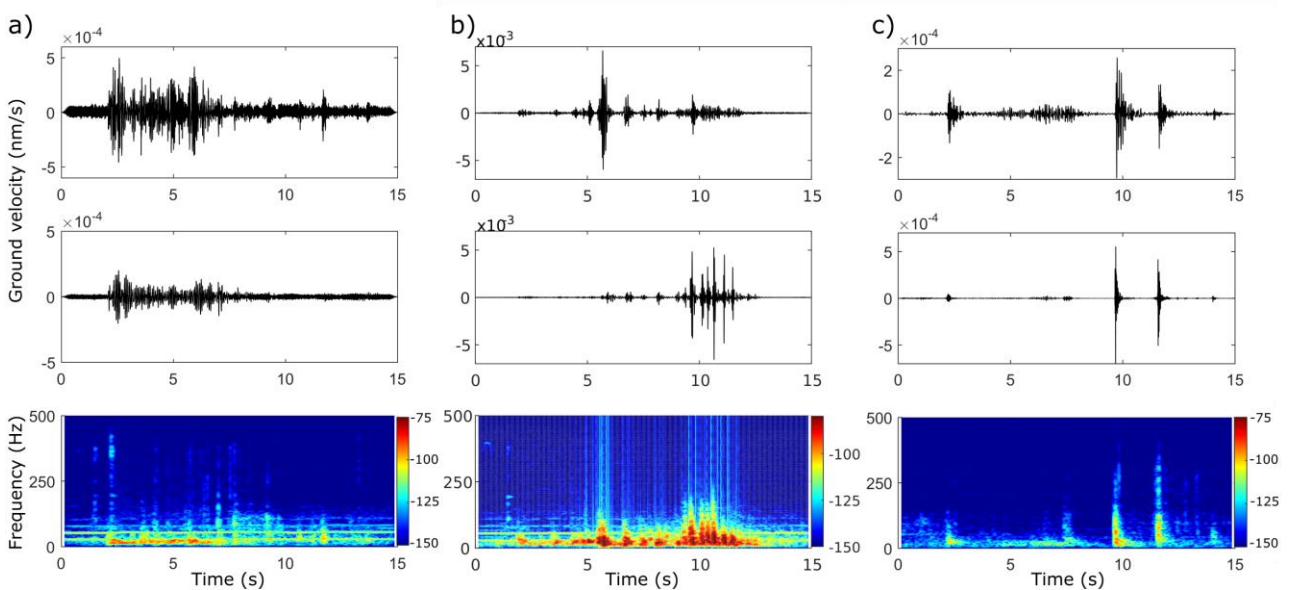


Figure 9.7. Seismic signals recorded by two geophones located on the upper part of the slope and of the lower part of the slope, and corresponding spectrogram of a) an event rolling/sliding (P1), b) an event rolling/sliding before free-falling when passing the rock walls (P1), c) an event bouncing along the slope (P2).

### 9.4.2 Thermography of blocks propagation

In this study, an IR camera was deployed to record the movements of the blocks. This camera was used to detect changes in temperature during the propagation of the blocks.

To detect rockfall events, we can apply the same motion detection techniques realized using digital cameras (McHugh, 2004; Fantini et al., 2017). These techniques are based on color change detection on time-lapse images. The advantage of the use of an IR camera, instead of optical ones, relies in its ability to detect movements day and night. In addition to the detection of the movement of the boulders, it is also possible to detect their interactions with the slope for each impact. Impacts produce small environment

deformations, which can be observed through the change of the environment temperature. Two types of environment deformations can be monitored. The first type consists of the remodeling of the environment during the impact. When impacting the slope, boulders might sink into the loose soil before bouncing or rolling. This freshly exposed surface does not have the same temperature as its surroundings (Figure 9.8b, e). It might be colder or warmer depending on the ambient temperature. For an impact on a hard or compact surface, impacts induce heat production revealed by an augmentation of temperature (Figure 9.8c, d, f, and g) as the rapid deformation of solid materials usually results in thermo-mechanical coupling effect.

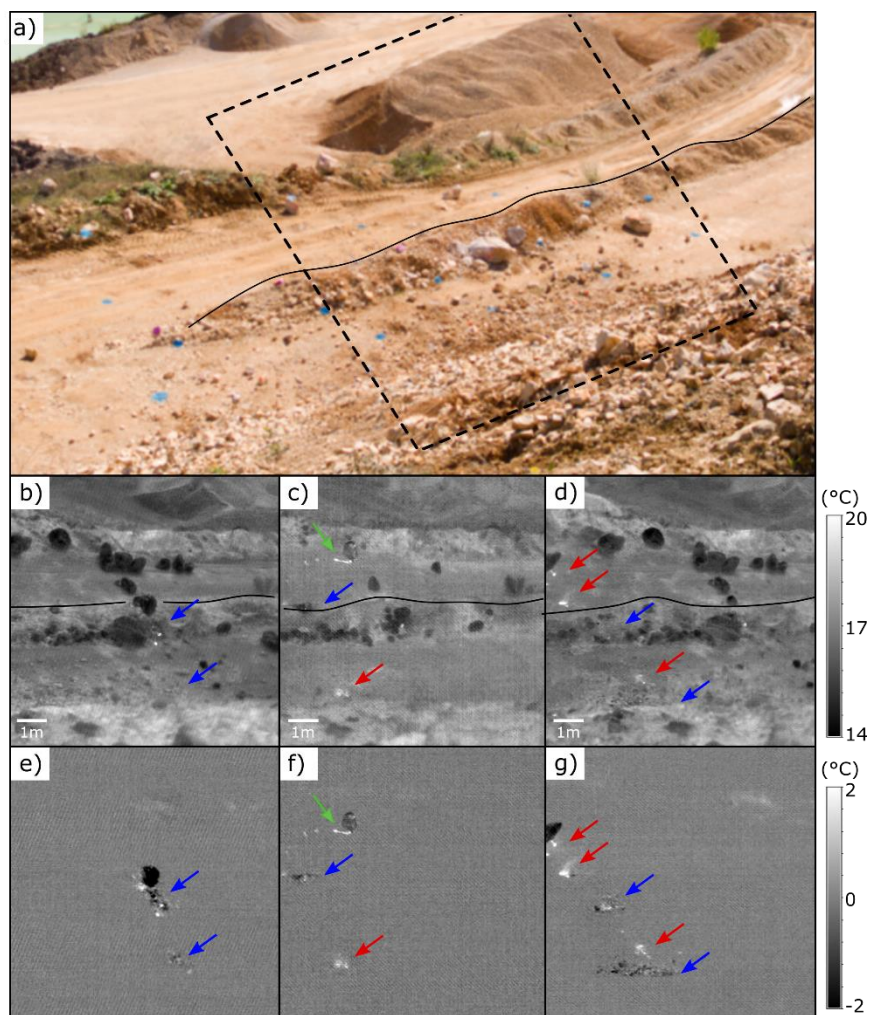


Figure 9.8. Thermography of blocks impacts. a) Photograph of the monitored area. The dashed frame represents the area covered by the thermographic images (b-g). A berm is highlighted by a black line to provide a landmark on the thermographic images of the blocks propagations b-d). e-g) represent thermographic images of the temperature changes with respect to a referent thermographic image taken before the arrival of the blocks in b-d). Blue arrows represent impacts which remodeled the slope, red arrows: impacts on hard or compacted soil leading to an increase of temperature, green arrows: blocks sliding leading to an increase of temperature.

The deformations of the soil surrounding the impact area appear clearly on the thermographic images and enable precise localization of the impacts (Figure 9.9). As each

impact of the slope is apparent, it allows us to distinguish the type of impact: bouncing (Figure 9.8d, g), rolling (Figure 9.8b, e), or sliding (Figure 9.8c, f).

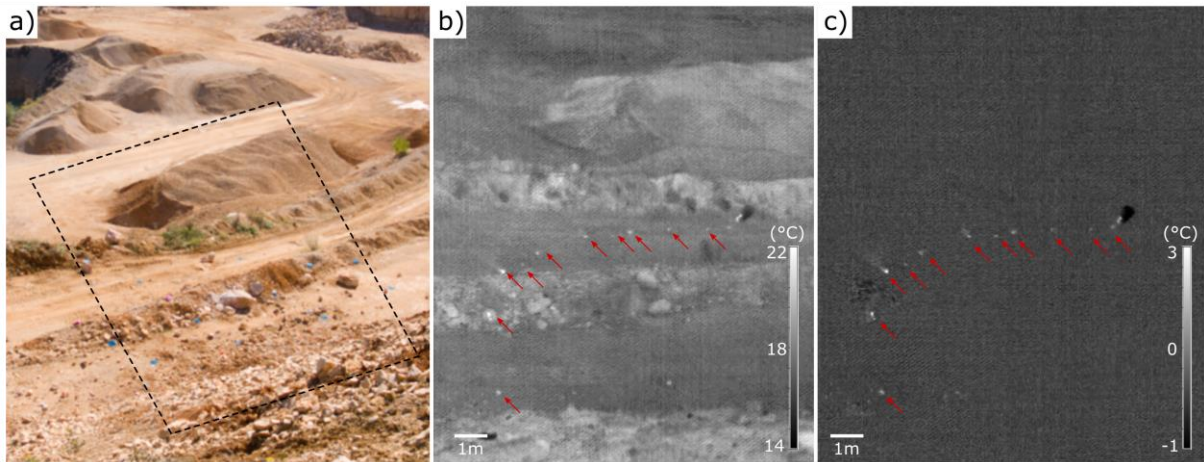


Figure 9.9. Thermography of blocks impacts. a) Photograph of the monitored area. b) Thermographic images of a block rebounds. c) Temperature changes with respect to a thermographic image of reference, taken before the arrival of the blocks in b).

Thermal inertia of the slope enables to identify the cicatrice left by the detachment of a compartment (Figure 9.10). Likewise, the thermal print left by the blocks' impacts remain observable for the period of time ranging from a dozen of seconds to several minutes (Figure 9.11, Figure 9.12).

## 9.5 Preliminary conclusions

Rockfall detection using an IR camera is possible and may be more efficient than classic detection techniques using digital camera due to the thermal inertia of the environment and its ability to function day and night. If a qualitative characterization of block impacts is possible (impact of soft/hard surface, rebound type, location, etc.) a quantitative characterization remains challenging.

The preliminary results on thermographic monitoring show that it is possible to correlate impacts thermographic prints to the impacts' kinetic energy. However, its application for rockfall characterization is much more complex. As stated before, impacts on soft or loose surface will not induce the same result than impacts on hard or well-compacted surface. Similarly weathered rock or sound rock will not lead to the same thermic prints.

The small-scale block release experiment gave us control on many parameters. Materials emissivity were known and constant through the experiment. Radiation emitted by the surroundings did not impact our measure as we aimed to characterize the augmentation of temperature and not the absolute temperature. Transmittance of the atmosphere could be neglected due to the short distance between the target and the



camera (1m). View angle and distance between target and camera remained constant. All these parameters have an influence on the measures and need to be taken into account in order to properly characterize rock impacts.

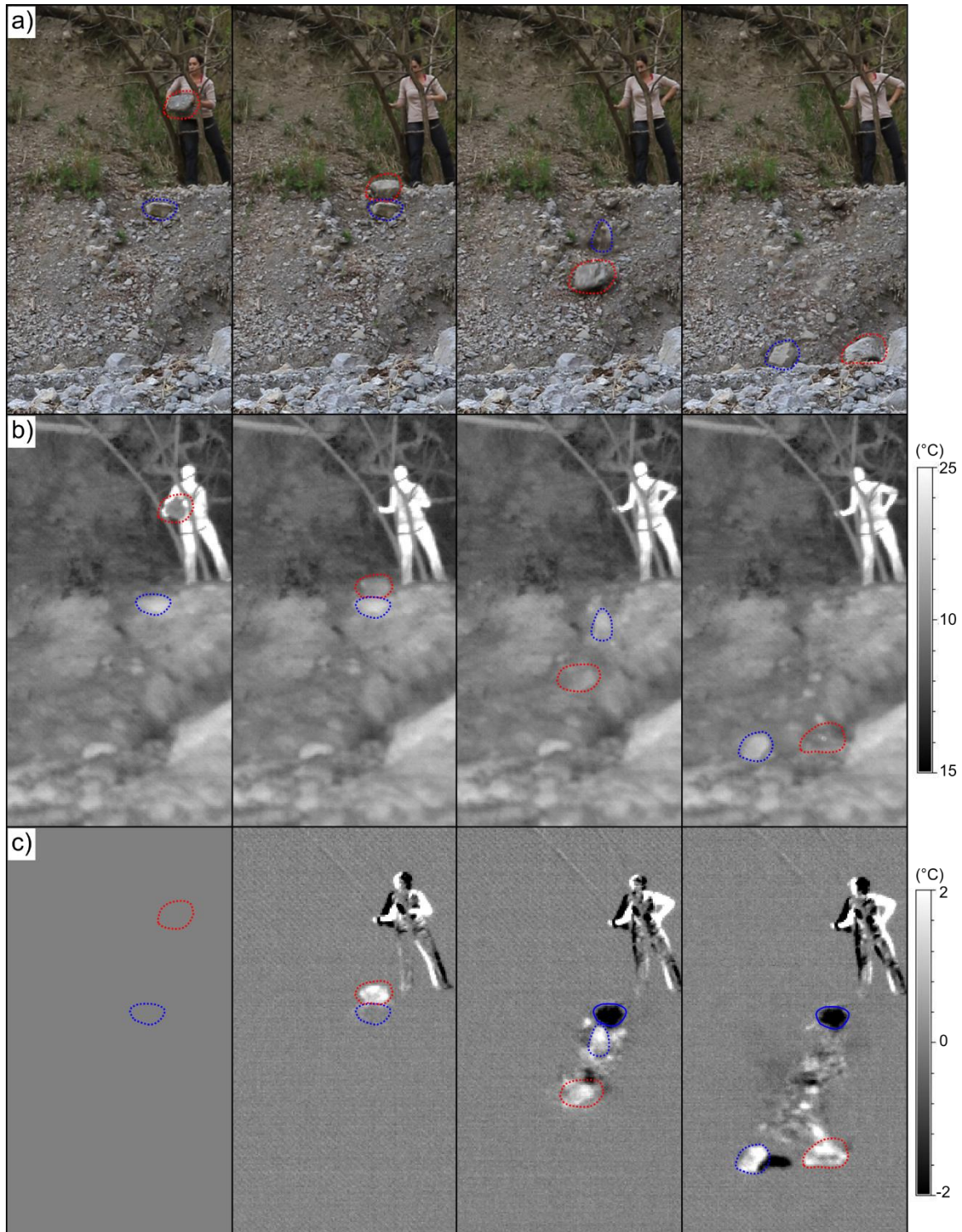


Figure 9.10. Block (red dotted circle) dropped on a loose slope. When impacting the slope, the block dislodged another block already in place (blue dotted circle). The thermic print of the cicatrice left by the removed block (blue circle) can be seen on the thermographic images. a) Photographs of the block release. b) Thermographic images of a the block propagation, c) temperature changes with respect to a thermographic image of reference taken before the arrival of the block.

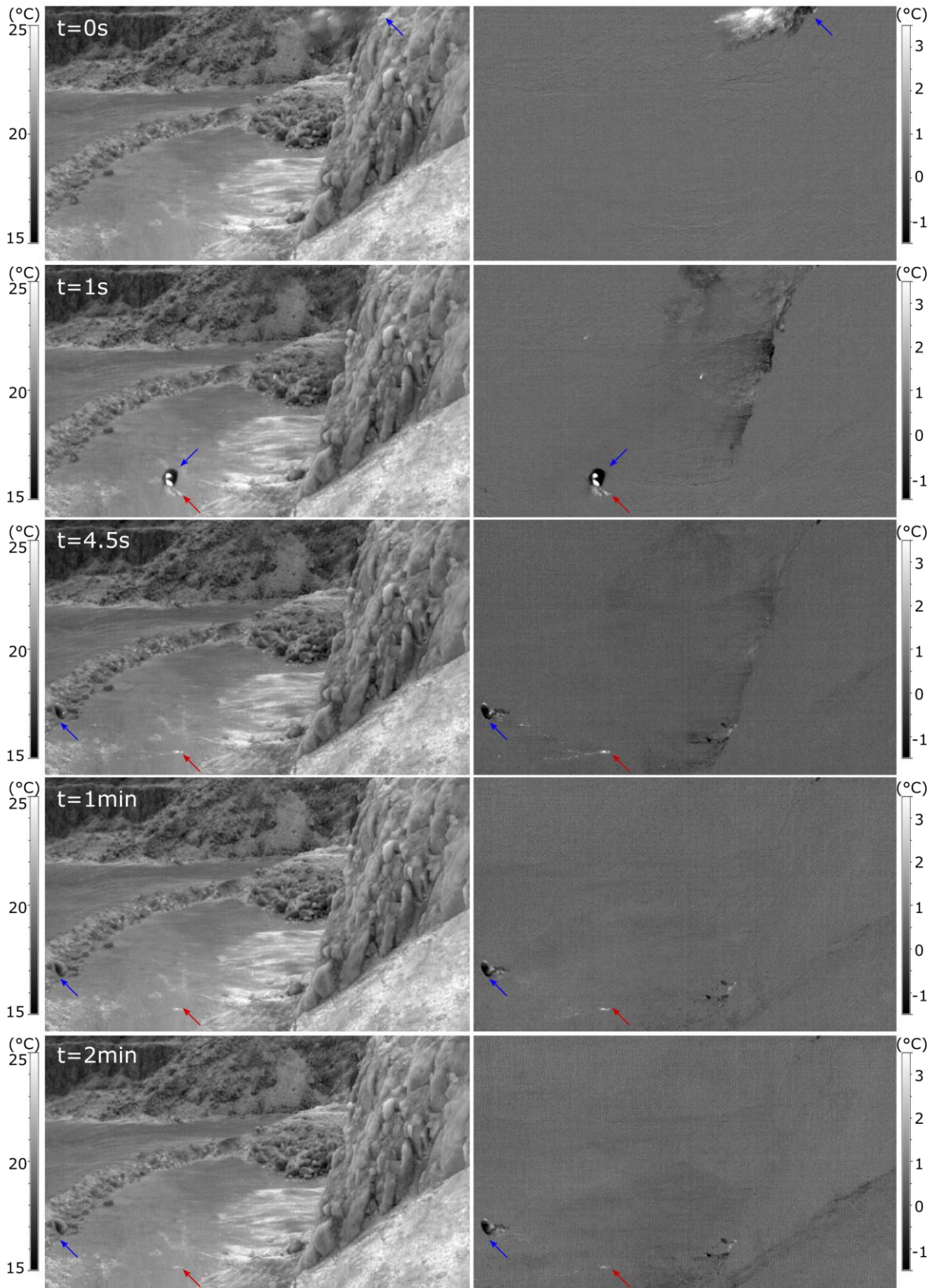


Figure 9.11. Evolution of thermography of block impact on a hard/compact surface. The thermic print left by this impact can be observed for more than 2 minutes. Left: thermographic images of a block propagation, right: temperature changes with respect to a thermographic image of reference taken before the arrival of the blocks. Blue arrows: locations of the block. Red arrows: impacts of the block.



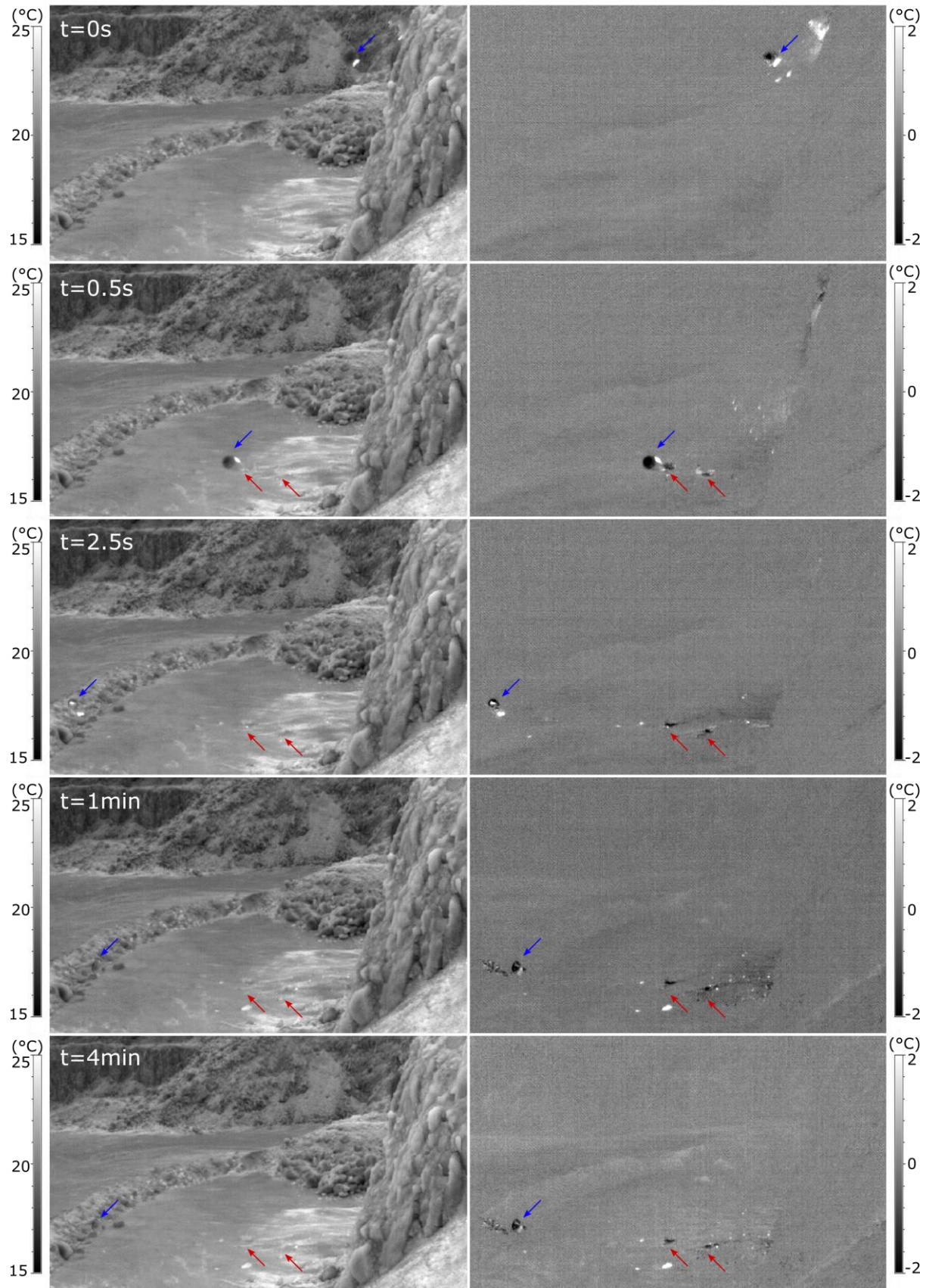


Figure 9.12. Evolution of thermography of block impact on a soft/loose surface. The thermic print left by this impact can be observed for more than 4 minutes. Left: thermographic images of a block propagation, right: temperature changes with respect to a thermographic image of reference taken before the arrival of the blocks. Blue arrows: locations of the block. Red arrows: impacts of the block.

## 10 Development outlook

Lots of work remain to be done in the field of rockfall monitoring using seismology.

Analysis of seismic signals allows to identify several phases: detachment, free fall followed by an impact, rebounds, and granular flow. As the propagation mode strongly differs among rockfalls in our dataset, we were not able to find seismic signal features allowing a satisfying estimation of rockfall dynamics (energy, volume, etc.) for our whole dataset. Using different relations for different propagation types provides more accurate volume estimates than when mixing all events.

In Chapter 8, we focus on events experiencing a granular-flow type of propagation and found a relation between seismic energy and rockfall volumes for a dataset of 10 events. This dataset needs to be broadened in order to refine this relation. Hibert et al. (2011) found that seismic and potential energies of a rockfall occurring within Dolomieu crater were linked. Using analytic simulations, we could infer potential energy of our dataset in order to check whether it could improve our relations.

In Chapter 6, we found that both duration and seismic energy of the detachment phase increase with rockfall volume. However, this relation is not well constrained. Several factors may influence the detachment seismic signal, such as the surface of the rupture area, the detachment mode (slide, free-fall or topple), its duration, fragmentation of the compartment during the detachment, etc. Due to the limited number of studied events, we were not able to analyze the influence of these factors. It would be interesting to expand this database with a larger number of events and for various geological settings.

We have shown through the observation of natural hazard and controlled block release experimentation, that seismic energy increases with blocks kinetic energy (Hibert et al., 2017; Chapters 6 and 7). All these datasets allowed us to analyze a large range of kinetic energy. This work has to be further expanded to validate these observations for different geological settings. The ratio between blocks' kinetic energy and seismic energy remains unclear. Several laboratory experiments (Farin et al., 2015; Bachelet et al., 2018; Chapter 7) showed that variations of  $R_s/p$  could be associated with the size of the impactor and with properties of the impacted medium (e.g. roughness and bed thickness, tilt angle). Thus, the value of  $R_s/p$  can be influenced by site properties and may be scale-dependent as we observe in our datasets.

To implement the methods developed during this work several steps require to be automatized. In this study, rockfall detection was carried out by a semi-automatic procedure (Helmstetter and Garambois, 2010). This procedure would require to be fully automatized even though it imply a greater percentage of event identification error. In a similar way, rockfall types (mass-flow, free-fall, rebound, etc.) need to be inferred automatically from their seismic signals properties (ratio mean/max amplitude, rise time, frequency, number of amplitude peaks, etc.). Begin and end times were manually picked as well as the detachment and first impact phases. Using a fully automatic procedure may be possible using artificial intelligence methods (Hibert et al., 2014; Provost et al., 2018). Most automatic methods (artificial neural networks, random forest, hidden Markov models, support vector machines) require a training set. By coupling different methods of detection (TLS, photogrammetry, seismology), we are confident that all events in our dataset have been correctly classified and located. Therefore, our dataset could be useful in order to develop or to test such an automatic method for rockfall detection, localization, and characterization.

Numerical modeling of rockfall events could provide insight on the seismic signals sources. Deparis et al. (2008) used a 2D dynamic finite-element code Plast2 (Baillet et al., 2005; Baillet and Sassi, 2006) to simulate detachment, frictional contact, fall, and impact. They studied the influence of elasticity and plasticity ground parameters on the synthetic signals and studied the relation between event volume and frequency content. In our case, such modeling could provide insights on the detachment phase and the physical properties of the block compartment, such as the surface of the rupture area, the detachment mode (slide, free-fall or topple), fragmentation of the compartment during the detachment, scar roughness, etc. It could also allow us to study the influence of the size of the impactor and properties of the impacted medium (e.g. roughness and bed thickness, tilt angle) for a block impact.

Monitoring combining seismology and motion detection could be implemented. A camera recording could be triggered when a rockfall event is detected using seismology. This combined monitoring could provide accurate information on the rockfall spatiotemporal occurrence and dynamics. Combined monitoring would also provide a good calibration set for rockfall seismic signals and would enable to improve seismic monitoring.

In the field of rockfall monitoring using DEMs, automated survey processes (Williams et al., 2018; Kromer et al., 2019) enabled a continuous data collection with a time-lapse ranging from one day to 1h. Such studies are very promising. Again, combined monitoring with seismic monitoring would also provide a good calibration set for rockfall seismic signals.

## Conclusions

Amongst mass wasting events, rockfalls are the most unpredictable and the most frequent hazard in the alpine region. In a context of growing urbanization in mountainous regions, rockfall events represent a major threat, both in human and material terms. Land-use planning and mitigation measures require an appropriate analysis of rockfall hazard. Defining failure locations, return periods, rockfall energy, etc. are of primary importance to support decision making and to enable appropriate remediation actions. To protect human lives or infrastructures without impeding economic activities, it is necessary to improve our knowledge about rock-fall processes and to improve rockfall monitoring methods.

In this study, several approaches have been developed to detect and monitor instabilities or rockfalls. We associated several methods such as topography measurement, seismological monitoring or thermography to better understand rockfall dynamics and how to better characterize them. This work was mainly carried out in the Chartreuse massif (Isère, French Alps), and in particular on two cliffs, Mount Saint-Eynard and Mount Granier. To widen our observations on rockfall events, several controlled block releases were realized in laboratory and on-site.

Using photogrammetry, we acquired diachronic Digital Elevation Models (DEMs) of the cliffs. Such monitoring enables us to obtain rockfall inventories and to analyze occurrence frequency. We explored the implications of different methodologies (distance calculation methods, detection thresholds, etc.) for the creation of rockfall inventories. Rockfalls number and volumes can be significantly under- or over-estimated according to the methodology adopted. This result clearly demonstrates the need for caution when interpreting rockfall inventories. Nevertheless, DEMs provide overall accurate information on rockfall locations and volumes. Events geometry and failure configuration can be determined. However, due to significant time lags between surveys, these methods cannot constrain a precise time of occurrence. This limit prevents the retrieval of information on rockfall triggering mechanisms. Similarly, the dynamics of events (multiple failures from the same area or individual stages of an event, i.e., detachment, impact, propagation) cannot be determined.

In addition to photogrammetric and LiDAR monitoring, Mount Saint-Eynard and Mount Granier were also monitored by a local seismic network. It allowed us to detect rockfall events that would not have been detected otherwise, due to their location or

time of occurrence. Seismic monitoring provide accurate time of occurrence of rockfall events. It helped us to reconstruct precise timelines of rockfall sequences, including the rockfall series of 2016 occurred at Mount Granier. This rockfall serie was characterized by a rockslide of 75 000 m<sup>3</sup> detached from the NW pillar of Mount Granier in January and about 60 000 m<sup>3</sup> of cumulated rockfall events occurred between April and May on its NE pillar. Overall, we were able to identify the seismic signal of more than thirty events detected using DEMs with volumes ranging from 1m<sup>3</sup> to several thousand of cubic meters.

Coupling these methods at Mount Granier and Mount Saint-Eynard yielded numerous information on natural rockfalls onto complex topography. Analysis of seismic signals allowed us to identify several phases: detachment, free fall followed by an impact, rebounds, and granular flow. As the propagation mode strongly differs among rockfalls in our dataset, we were not able to find seismic signal features allowing a satisfying estimation of rockfall dynamics (energy, volume, etc.) for our whole data set. By selecting events with the same propagation type, we were able to provide a more accurate characterization of rockfalls properties than when mixing different types of events.

By focusing on events experiencing a mass-flow type of propagation, we found a relation between the seismic energy and the rockfall volume for a dataset of 10 events. For free-fall type events, we focused on the beginning of the seismic signal: the detachment and the first impact. We found a significant correlation between the seismic energy of the detachment phase and the rockfall volume. By measuring the time delay between detachment and impact phases we were able to infer the free-fall heights. We also found that the seismic energy of an impact was well correlated with rockfalls potential energy. Rockfall volumes can thus be calculated by using the estimated potential energies and free fall heights. Two controlled block experiments were carried out to validate our observations on rockfall events. These experiments offered an opportunity to test how rockfall characteristics influence their induced seismic signals. It also allowed us to extrapolate results toward smaller scales. The scaling between seismic energy and kinetic energy for these experiments agrees well with the natural rockfalls.

Finally, we carried out experiments to characterize block impacts using an infrared camera. We studied how an IR camera could contribute to rockfall monitoring. In addition to the detection of the movement of the boulders, it is possible to detect their interactions with the slope for each impact. Impacts produce small environment deformations, which can be observed through the change of the environment temperature. When impacting the slope, boulders might sink into the loose soil before bouncing or rolling. This freshly exposed surface does not have the same temperature as its surroundings. For an impact on a hard or compact surface, impacts induce heat production revealed by an augmentation of temperature. This temperature variation increase with the kinetic energy of the blocks. However, if a qualitative characterization of block impacts is possible (impact of soft/hard surface, rebound type, location, etc.) a quantitative characterization remains challenging.





## References

- Abellán, A., Calvet, J., Vilaplana, J.M., Blanchard, J., 2010. Detection and spatial prediction of rockfalls by means of terrestrial laser scanner monitoring. *Geomorphology* 119, 162–171. <https://doi.org/10.1016/j.geomorph.2010.03.016>
- Adams, J., Chandler, J., 2002. Evaluation of Lidar and Medium Scale Photogrammetry for Detecting Soft-Cliff Coastal Change. *Photogramm. Rec.* 17, 405–418.
- Agliardi, F., Crosta, G.B., Frattini, P., 2009. Integrating rockfall risk assessment and countermeasure design by 3D modelling techniques. *Nat. Hazards Earth Syst. Sci.* 9, 1059–1073. <https://doi.org/10.5194/nhess-9-1059-2009>
- Aki, K., Richards, P.G., 1980. *Quantitative Seismology*, vol. 1424. Freeman, San Francisco, Calif.
- Allstadt, K., Malone, S.D., 2014. Swarms of repeating stick-slip icequakes triggered by snow loading at Mount Rainier volcano. *J. Geophys. Res. Earth Surf.* 119, 1180–1203. <https://doi.org/10.1002/2014JF003086>
- Amitrano, D., 2005. Seismic precursory patterns before a cliff collapse and critical point phenomena. *Geophys. Res. Lett.* 32, L08314. <https://doi.org/10.1029/2004GL022270>
- Asteriou, P., Saroglou, H., Tsiambaos, G., 2012. Geotechnical and kinematic parameters affecting the coefficients of restitution for rock fall analysis. *Int. J. Rock Mech. Min. Sci.* 54, 103–113. <https://doi.org/10.1016/j.ijrmms.2012.05.029>
- Bachelet, V., Mangeney, A., de Rosny, J., Toussaint, R., Farin, M., 2018. Elastic wave generated by granular impact on rough and erodible surfaces. *J. Appl. Phys.* 123, 044901. <https://doi.org/10.1063/1.5012979>
- Barla, G., Antolini, F., Gigli, G., 2016. 3D Laser scanner and thermography for tunnel discontinuity mapping. *Geomech. Tunn.* 9, 29–36. <https://doi.org/10.1002/geot.201500050>
- Barlow, J., Lim, M., Rosser, N., Petley, D., Brain, M., Norman, E., Geer, M., 2012. Modeling cliff erosion using negative power law scaling of rockfalls. *Geomorphology* 139–140, 416–424. <https://doi.org/10.1016/j.geomorph.2011.11.006>
- Baroň, I., Bečkovský, D., Míča, L., 2014. Application of infrared thermography for mapping open fractures in deep-seated rockslides and unstable cliffs. *Landslides* 11, 15–27. <https://doi.org/10.1007/s10346-012-0367-z>
- Battaglia, J., Aki, K., 2003. Location of seismic events and eruptive fissures on the Piton de la Fournaise volcano using seismic amplitudes. *J. Geophys. Res.* 108, 2364. <https://doi.org/10.1029/2002JB002193>
- Benjamin, J., Rosser, N.J., Brain, M.J., 2016. Rockfall detection and volumetric characterisation using LiDAR. Presented at the Landslides and Engineered Slopes. Experience, Theory and Practice: Proceedings of the 12th International Symposium on Landslides (Napoli, Italy, 12-19 June 2016), CRC Press, p. 7.
- Berrocal, J., Espinosa, A., Galdos, J., 1978. Seismological and geological aspects of the Mantaro landslide in Peru. *Nature* 275, p.533.



- Besl, P.J., McKay, N.D., 1992. A method for registration of 3-D shapes. *IEEE T Pattern Anal* 14, 239–256.
- Borcherdt, R.D., 1970. Effects of local geology on ground motion near San Francisco Bay. *Bull. Seismol. Soc. Am.* 60, 29–61.
- Bottelin, P., Jongmans, D., Baillet, L., Lebourg, T., Hantz, D., Levy, C., Le Roux, O., Cadet, H., Lorier, L., Rouiller, J.-D., Turpin, J., Darras, L., 2013. Spectral Analysis of Prone-to-fall Rock Compartments using Ambient Vibrations. *J. Environ. Eng. Geophys.* 18, 205–217. <https://doi.org/10.2113/JEEG18.4.205>
- Bottelin, P., Jongmans, D., Daudon, D., Mathy, A., Helmstetter, A., Bonilla-Sierra, V., Cadet, H., Amitrano, D., Richefeu, V., Lorier, L., Baillet, L., Villard, P., Donzé, F., 2014. Seismic and mechanical studies of the artificially triggered rockfall at Mount Néron (French Alps, December 2011). *Nat. Hazards Earth Syst. Sci.* 14, 3175–3193. <https://doi.org/10.5194/nhess-14-3175-2014>
- Bourrier, F., Dorren, L., Hungr, O., 2013. The use of ballistic trajectory and granular flow models in predicting rockfall propagation: ROCKFALL PROPAGATION. *Earth Surf. Process. Landf.* 38, 435–440. <https://doi.org/10.1002/esp.3372>
- Bourrier, F., Dorren, L., Nicot, F., Berger, F., Darve, F., 2009. Toward objective rockfall trajectory simulation using a stochastic impact model. *Geomorphology* 110, 68–79. <https://doi.org/10.1016/j.geomorph.2009.03.017>
- Bozzolo, D., Pamini, R., 1986. Simulation of rock falls down a valley side. *Acta Mech.* 63, 113–130. <https://doi.org/10.1007/BF01182543>
- Brunetti, M.T., Guzzetti, F., Rossi, M., 2009. Probability distributions of landslide volumes. *Nonlinear Process. Geophys.* 16, 179–188.
- Burtin, A., Hovius, N., Milodowski, D.T., Chen, Y.-G., Wu, Y.-M., Lin, C.-W., Chen, H., Emberson, R., Leu, P.-L., 2013. Continuous catchment-scale monitoring of geomorphic processes with a 2-D seismological array: SEISMIC SURVEY OF GEOMORPHIC PROCESSES. *J. Geophys. Res. Earth Surf.* 118, 1956–1974. <https://doi.org/10.1002/jgrf.20137>
- Chanut, M., Barthelet, V., Kasperski, J., 2011. Contribution de l'imagerie de face pour l'analyse des mouvements de terrain: application au versant de Séchilienne. Presented at the Journées Aléas Gravitaires, Strasbourg, p. 6.
- Chau, K.T., Wong, R.H.C., Wu, J.J., 2002. Coefficient of restitution and rotational motions of rockfall impacts. *Int. J. Rock Mech. Min. Sci.* 39, 69–77. [https://doi.org/10.1016/S1365-1609\(02\)00016-3](https://doi.org/10.1016/S1365-1609(02)00016-3)
- Chowdhury, R., Flentje, P., Bhattacharya, G., 2009. limit equilibrium methods II general slip surfaces and beyond critical equilibrium, in: *Geotechnical Slope Analysis*. pp. 223–321.
- Clauset, A., Shalizi, C.R., Newman, M.E.J., 2009. Power-law distributions in empirical data. *SIAM Rev.* 51, 661–703. <https://doi.org/10.1137/070710111>
- Coe, J.A., Harp, E.L., 2007. Influence of tectonic folding on rockfall susceptibility, American Fork Canyon, Utah, USA. *Nat. Hazards Earth Syst. Sci.* 7, 1–14. <https://doi.org/10.5194/nhess-7-1-2007>
- Collins, B.D., Stock, G.M., 2016. Rockfall triggering by cyclic thermal stressing of exfoliation fractures. *Nat. Geosci.* 9, 395–400. <https://doi.org/10.1038/ngeo2686>
- Consortium of task A3, C2ROP project, 2018. Benchmark of trajectory analysis models. Presented at the 4th International Symposium Rock Slope Stability, 13-15 November 2018, Chamébray.
- Corominas, J., Copons, R., Moya, J., Vilaplana, J.M., Altimir, J., Amigó, J., 2005. Quantitative assessment of the residual risk in a rockfall protected area. *Landslides* 2, 343–357. <https://doi.org/10.1007/s10346-005-0022-z>

- Corominas, J., Mavrouli, O., Ruiz-Carulla, R., 2017. Rockfall Occurrence and Fragmentation, in: Sassa, K., Mikoš, M., Yin, Y. (Eds.), *Advancing Culture of Living with Landslides*. Springer International Publishing, Cham, pp. 75–97. [https://doi.org/10.1007/978-3-319-59469-9\\_4](https://doi.org/10.1007/978-3-319-59469-9_4)
- Coviello, V., Arattano, M., Comiti, F., Macconi, P., & Marchi, L. 2019. Seismic characterization of debris flows: insights into energy radiation and implications for warning. *Journal of Geophysical Research: Earth Surface*, 124(6), 1440-1463
- CRED, 2019. Natural disaster.
- Cruden, D.M., Varnes, D., 1996. Landslide types and processes. *Landslides Investig. Mitig. Chapter 3-Landslide types and processes*. Transportation research board special report, 36.
- Dai, F.C., Lee, C.F., Ngai, Y.Y., 2002. Landslide risk assessment and management: an overview. *Eng. Geol.* 23.
- D'Amato, J., 2015. Apport d'une base de données d'éboulements rocheux obtenue par scanner laser dans la caractérisation des conditions de rupture et processus associés.pdf. Université Joseph-Fourier-Grenoble I, Grenoble.
- D'Amato, J., Hantz, D., Guerin, A., Jaboyedoff, M., Baillet, L., Mariscal, A., 2016. Influence of meteorological factors on rockfall occurrence in a middle mountain limestone cliff. *Nat. Hazards Earth Syst. Sci.* 16, 719–735. <https://doi.org/10.5194/nhess-16-719-2016>
- Dammeier, F., Moore, J.R., Haslinger, F., Loew, S., 2011. Characterization of alpine rockslides using statistical analysis of seismic signals. *J. Geophys. Res.* 116. <https://doi.org/10.1029/2011JF002037>
- Day, S.S., Gran, K.B., Belmont, P., Wawrzyniec, T., 2013. Measuring bluff erosion part 1: terrestrial laser scanning methods for change detection: MEASURING BLUFF EROSION PART 1. *Earth Surf. Process. Landf.* 38, 1055–1067. <https://doi.org/10.1002/esp.3353>
- Deline, P., Alberto, W., Broccolato, M., Hungr, O., Noetzi, J., Ravanel, L., Tamburini, A., 2011. The December 2008 Crammont rock avalanche, Mont Blanc massif area, Italy. *Nat. Hazards Earth Syst. Sci.* 11, 3307–3318. <https://doi.org/10.5194/nhess-11-3307-2011>
- Deparis, J., Jongmans, D., Cotton, F., Baillet, L., Thouvenot, F., Hantz, D., 2008. Analysis of Rock-Fall and Rock-Fall Avalanche Seismograms in the French Alps. *Bull. Seismol. Soc. Am.* 98, 1781–1796. <https://doi.org/10.1785/0120070082>
- Dewez, T.J.B., Rohmer, J., Regard, V., Cnudde, C., 2013. Probabilistic coastal cliff collapse hazard from repeated terrestrial laser surveys: case study from Mesnil Val (Normandy, northern France). *J. Coast. Res.* 65, 702–707. <https://doi.org/10.2112/SI65-119.1>
- Díaz, J., Ruíz, M., Crescentini, L., Amoroso, A., Gallart, J., 2014. Seismic monitoring of an Alpine mountain river: Seismic monitoring of alpine river. *J. Geophys. Res. Solid Earth* 119, 3276–3289. <https://doi.org/10.1002/2014JB010955>
- Dietze, M., Mohadjer, S., Turowski, J.M., Ehlers, T.A., Hovius, N., 2017a. Seismic monitoring of small alpine rockfalls – validity, precision and limitations. *Earth Surf. Dyn.* 5, 653–668. <https://doi.org/10.5194/esurf-5-653-2017>
- Dietze, M., Turowski, J.M., Cook, K.L., Hovius, N., 2017b. Spatiotemporal patterns, triggers and anatomies of seismically detected rockfalls. *Earth Surf. Dyn.* 5, 757–779. <https://doi.org/10.5194/esurf-5-757-2017>
- Dorren, L.K.A., 2003. A review of rockfall mechanics and modelling approaches. *Prog. Phys. Geogr. Earth Environ.* 27, 69–87. <https://doi.org/10.1191/0309133303pp359ra>
- Dussauge-Peisser, C., Helmstetter, A., Grasso, J.-R., Hantz, D., Desvarreux, P., Jeannin, M., Giraud, A., 2002. Probabilistic approach to rock fall hazard assessment: potential of historical data analysis. *Nat. Hazards Earth Syst. Sci.* 2, 15–26.

- Ebeling, C.W., Stein, S., 2011. Seismological Identification and Characterization of a Large Hurricane. *Bull. Seismol. Soc. Am.* 101, 399–403. <https://doi.org/10.1785/0120100175>
- Eissler, H.K., Kanamori, H., 1987. A single-force model for the 1975 Kalapana, Hawaii, Earthquake. *J. Geophys. Res.* 92, 4827. <https://doi.org/10.1029/JB092iB06p04827>
- Evans, S.G., Hungr, O., 1993. The assessment of rockfall hazard at the base of talus slopes. *Can. Geotech. J.* 30(4), 17.
- Fantini, A., Fiorucci, M., Martino, S., 2017. Rock Falls Impacting Railway Tracks: Detection Analysis through an Artificial Intelligence Camera Prototype. *Wirel. Commun. Mob. Comput.* 2017, 1–11. <https://doi.org/10.1155/2017/9386928>
- Farin, M., Mangeney, A., Toussaint, R., Rosny, J. de, Shapiro, N., Dewez, T., Hibert, C., Mathon, C., Sedan, O., Berger, F., 2015. Characterization of rockfalls from seismic signal: Insights from laboratory experiments: CHARACTERIZATION OF ROCKFALLS FROM SEISMIC SIGNAL. *J. Geophys. Res. Solid Earth* 120, 7102–7137. <https://doi.org/10.1002/2015JB012331>
- Farvacque, M., Lopez-Saez, J., Corona, C., Toe, D., Bourrier, F., Eckert, N., 2019. Quantitative risk assessment in a rockfall-prone area: the case study of the Crolles municipality (Massif de la Chartreuse, French Alps). *Géomorphologie Relief Process. Environ.* 25, 7–19.
- Firpo, G., Salvini, R., Francioni, M., Ranjith, P.G., 2011. Use of Digital Terrestrial Photogrammetry in rocky slope stability analysis by Distinct Elements Numerical Methods. *Int. J. Rock Mech. Min. Sci.* 48, 1045–1054. <https://doi.org/10.1016/j.ijrmms.2011.07.007>
- Frayssines, M., 2005. Contribution à l'évaluation de l'aléa éboulement rocheux (rupture) (Géologie appliquée). Université Joseph-Fourrier, Grenoble I.
- Frayssines, M., Hantz, D., 2006. Failure mechanisms and triggering factors in calcareous cliffs of the Subalpine Ranges (French Alps). *Eng. Geol.* 86, 256–270. <https://doi.org/10.1016/j.enggeo.2006.05.009>
- Frodella, W., Morelli, S., Gigli, G., Casagli, N., 2014. Contribution of infrared thermography to the slope instability characterization, in: *Proceedings of World Landslide Forum.* pp. 2–6.
- Fuchs, F., Lenhardt, W., Bokelmann, G., the AlpArray Working Group, 2018. Seismic detection of rockslides at regional scale: examples from the Eastern Alps and feasibility of kurtosis-based event location. *Earth Surf. Dyn.* 6, 955–970. <https://doi.org/10.5194/esurf-6-955-2018>
- Garland, P.P., Rogers, R.J., 2009. An experimental study of contact forces during oblique elastic impact. *J. Appl. Mech.* 763.
- Gibbons, S.J., Ringdal, F., 2006. The detection of low magnitude seismic events using array-based waveform correlation. *Geophys. J. Int.* 165, 149–166. <https://doi.org/10.1111/j.1365-246X.2006.02865.x>
- Gidon, M.: Les décrochements et leur place dans la structuration du massif de la Chartreuse (Alpes occidentales françaises), *Rev. Geogr. Alp.*, 66, 39–55, 1990.
- Girardeau-Montaut, D., Roux, M., Marc, R., Thibault, G., 2005. Change detection on points cloud data acquired with a ground laser scanner. *Int. Arch. Photogramm. Remote Sens. Spat. Inf. Sci.* 36, 6.
- Goguel, J., Pachoud, A., 1972. Géologie et dynamique de l'éroulement du Mont Granier, dans le Massif de la Chartreuse, en novembre 1248. *Bull. BRGM* 29–38.
- Groupement d'intérêt scientifique sur les sols (France), 2011. L'état des sols de France. GIS Sol, S.I.

- Gruber, S., Haeberli, W., 2007. Permafrost in steep bedrock slopes and its temperature-related destabilization following climate change. *J. Geophys. Res.* 112, F02S18. <https://doi.org/10.1029/2006JF000547>
- Guerin, A., Jaboyedoff, M., Collins, B.D., Derron, M.-H., Stock, G.M., Matasci, B., Boesiger, M., Lefeuvre, C., Podladchikov, Y.Y., 2019. Detection of rock bridges by infrared thermal imaging and modeling. *Sci. Rep.* 9, 13138. <https://doi.org/10.1038/s41598-019-49336-1>
- Guerin, A., Rossetti, J.-P., Hantz, D., Jaboyedoff, M., 2013. Estimating rock fall frequency in a limestone cliff using LIDAR measurements, in: *First International Conference on Landslides Risk*. p. p–293.
- Gutenberg, B., Richter, C.F., 1949. *Seismicity of the earth and associated phenomena*, Princeton University Press. ed. Princeton, New Jersey.
- Guzzetti, F., 2000. Landslide fatalities and the evaluation of landslide risk in Italy. *Eng. Geol.* 58, 89–107. [https://doi.org/10.1016/S0013-7952\(00\)00047-8](https://doi.org/10.1016/S0013-7952(00)00047-8)
- Guzzetti, F., Mondini, A.C., Cardinali, M., Fiorucci, F., Santangelo, M., Chang, K.-T., 2012. Landslide inventory maps: New tools for an old problem. *Earth-Sci. Rev.* 112, 42–66. <https://doi.org/10.1016/j.earscirev.2012.02.001>
- Guzzetti, F., Reichenbach, P., Ghigi, S., 2004. Rockfall Hazard and Risk Assessment Along a Transportation Corridor in the Nera Valley, Central Italy. *Environ. Manage.* 34, 191–208. <https://doi.org/10.1007/s00267-003-0021-6>
- Guzzetti, F., Reichenbach, P., Wieczorek, G.F., 2003. Rockfall hazard and risk assessment in the Yosemite Valley, California, USA. *Nat. Hazards Earth Syst. Sci.* 3, 491–503. <https://doi.org/10.5194/nhess-3-491-2003>
- Hantz, D., 2011. Quantitative assessment of diffuse rock fall hazard along a cliff foot. *Nat. Hazards Earth Syst. Sci.* 11, 1303–1309. <https://doi.org/10.5194/nhess-11-1303-2011>
- Hantz, D., Vengeon, J.M., Dussauge-Peisser, C., 2003. An historical, geomechanical and probabilistic approach to rock-fall hazard assessment. *Nat. Hazards Earth Syst. Sci.* 3, 693–701.
- Helmstetter, A., Garambois, S., 2010. Seismic monitoring of Séchillienne rockslide (French Alps): Analysis of seismic signals and their correlation with rainfalls. *J. Geophys. Res.* 115, F03016. <https://doi.org/10.1029/2009JF001532>
- Hibert, C., Malet, J.-P., Bourrier, F., Provost, F., Berger, F., Bornemann, P., Tardif, P., Mermin, E., 2017. Single-block rockfall dynamics inferred from seismic signal analysis. *Earth Surf. Dyn. Discuss.* 1–15. <https://doi.org/10.5194/esurf-2016-64>
- Hibert, C., Mangeney, A., Grandjean, G., Baillard, C., Rivet, D., Shapiro, N.M., Satriano, C., Maggi, A., Boissier, P., Ferrazzini, V., Crawford, W., 2014. Automated identification, location, and volume estimation of rockfalls at Piton de la Fournaise volcano. *J. Geophys. Res. Earth Surf.* 119, 1082–1105. <https://doi.org/10.1002/2013JF002970>
- Hibert, C., Mangeney, A., Grandjean, G., Shapiro, N.M., 2011. Slope instabilities in Dolomieu crater, Réunion Island: From seismic signals to rockfall characteristics. *J. Geophys. Res.* 116. <https://doi.org/10.1029/2011JF002038>
- Hobléa, F., Häuselmann, P., & Kubik, P. (2011). Cosmogenic nuclide dating of cave deposits of Mount Granier (Hauts de Chartreuse Nature Reserve, France): morphogenic and palaeogeographical implications. *Géomorphologie: relief, processus, environnement*, 17(4), 395-406.
- Hobléa, F., Amitrano, D., Astrade, L., Barnave, S., Buffle, A., Cavalier, E., Cayla, N., Deline, P., Gallach, X., Guerin, A., Hantz, D., Helmstetter, A., Laïly, B., Langlais, M., Lejeune, S., Le Roy, G., Malet, E., Ravanel, L., Saint-Bézar, B., 2018. Multi-method diachronic approach of the rockfalls and landslides at Mont Granier (1933 m a.s.l., Chartreuse Massif, French Alps). Presented at the EGU General Assembly 2018, Vienna, Austria.

- Hooper, A., Zebker, H., Segall, P., Kampes, B., 2004. A new method for measuring deformation on volcanoes and other natural terrains using InSAR persistent scatterers: A NEW PERSISTENT SCATTERERS METHOD. *Geophys. Res. Lett.* 31. <https://doi.org/10.1029/2004GL021737>
- Hovius, N., Stark, C.P., Allen, P.A., 1997. Sediment flux from a mountain belt derived by landslide mapping. *Geology* 25, 4.
- Hungr, O., Evans, S.G., 1988. Engineering evaluation of fragmental rockfall hazards. *Proc 5th Int Sympo Landslide* 685–690.
- Hungr, O., Evans, S.G., Hazzard, J., 1999. Magnitude and frequency of rock falls and rock slides along the main transportation corridors of southwestern British Columbia. *Can. Geotech. J.* 36, 224–238. <https://doi.org/10.1139/t98-106>
- Hungr, O., Evans, S.G., Hutchinson, I.N., 2001. A review of the classification of Landslides of the flow type. *Environ. Eng. Geosci.* 221–238.
- Hussainova, I., Schade, K.P., Tisler, S., 2006. Dynamic coefficients in impact mechanics. *Proc. Est. Acad. Sci.* 121 26–39.
- Janeras, M., Jara, J.-A., Royán, M.J., Vilaplana, J.-M., Aguasca, A., Fàbregas, X., Gili, J.A., Buxó, P., 2017. Multi-technique approach to rockfall monitoring in the Montserrat massif (Catalonia, NE Spain). *Eng. Geol.* 219, 4–20. <https://doi.org/10.1016/j.enggeo.2016.12.010>
- Kanai, K., Yamabe, K., Habasaki, A., 1984. Study of the attenuation of seismic waves, in *Proceedings of the Eighth World Conference on Earthquake Engineering*, vol. 2. Prentice-Hall, San Francisco, Calif, pp. 273–280.
- Kanamori, H., Anderson, D.L., 1975. Theoretical basis of some empirical relations in seismology. *Bull. Seismol. Soc. Am.* 1073–1095.
- Kanamori, H., Given, J.W., 1982. Analysis of long-period seismic waves excited by the May 18, 1980, eruption of Mount St. Helens-A terrestrial monopole? *J. Geophys. Res. Solid Earth* 87, 5422–5432. <https://doi.org/10.1029/JB087iB07p05422>
- Keefer, D.K., 1984. Landslides caused by earthquakes. *Geol. Soc. Am. Bull.* 95(4), 406–421.
- Krautblatter, M., Hauck, C., 2007. Electrical resistivity tomography monitoring of permafrost in solid rock walls. *J. Geophys. Res.* 112, F02S20. <https://doi.org/10.1029/2006JF000546>
- Kromer, R., Abellán, A., Hutchinson, D., Lato, M., Edwards, T., Jaboyedoff, M., 2015. A 4D Filtering and Calibration Technique for Small-Scale Point Cloud Change Detection with a Terrestrial Laser Scanner. *Remote Sens.* 7, 13029–13052. <https://doi.org/10.3390/rs71013029>
- Kromer, R., Walton, G., Gray, B., Lato, M., Group, R., 2019. Development and Optimization of an Automated Fixed-Location Time Lapse Photogrammetric Rock Slope Monitoring System. *Remote Sens.* 11, 1890. <https://doi.org/10.3390/rs11161890>
- Kromer, R.A., Hutchinson, D.J., Lato, M.J., Gauthier, D., Edwards, T., 2015. Identifying rock slope failure precursors using LiDAR for transportation corridor hazard management. *Eng. Geol.* 195, 93–103. <https://doi.org/10.1016/j.enggeo.2015.05.012>
- Kuhn, D., Prüfer, S., 2014. Coastal cliff monitoring and analysis of mass wasting processes with the application of terrestrial laser scanning: A case study of Rügen, Germany. *Geomorphology* 213, 153–165. <https://doi.org/10.1016/j.geomorph.2014.01.005>
- Lacroix, P., Helmstetter, A., 2011. Location of Seismic Signals Associated with Microearthquakes and Rockfalls on the Sechilienne Landslide, French Alps. *Bull. Seismol. Soc. Am.* 101, 341–353. <https://doi.org/10.1785/0120100110>
- Lague, D., Brodu, N., Leroux, J., 2013. Accurate 3D comparison of complex topography with terrestrial laser scanner: Application to the Rangitikei canyon (N-Z). *ISPRS J. Photogramm. Remote Sens.* 82, 10–26. <https://doi.org/10.1016/j.isprsjprs.2013.04.009>

- Larose, E., Carrière, S., Voisin, C., Bottelin, P., Baillet, L., Guéguen, P., Walter, F., Jongmans, D., Guillier, B., Garambois, S., Gimbert, F., Massey, C., 2015. Environmental seismology: What can we learn on earth surface processes with ambient noise? *J. Appl. Geophys.* 116, 62–74. <https://doi.org/10.1016/j.jappgeo.2015.02.001>
- Lato, M., Hutchinson, J., Diederichs, M., Ball, D., Harrap, R., 2009. Engineering monitoring of rockfall hazards along transportation corridors: using mobile terrestrial LiDAR. *Nat Hazards Earth Syst Sci* 9, 935–946.
- Le Breton, M., Baillet, L., Larose, E., Rey, E., Benech, P., Jongmans, D., Guyoton, F., Jaboyedoff, M., 2019. Passive radio-frequency identification ranging, a dense and weather-robust technique for landslide displacement monitoring. *Eng. Geol.* 250, 1–10. <https://doi.org/10.1016/j.enggeo.2018.12.027>
- Le Roy, G., Helmstetter, A., Guyoton, F., Le Roux-Mallouf, R., 2019. Seismic analysis of the detachment and impact phases of a rockfall and application for estimating rockfall volume and free-fall height. *J. Geophys. Res. Earth Surf.* 124. <https://doi.org/10.1029/2019JF004999>
- Lebourg, T., Binet, S., Tric, E., Jomard, H., El Bedoui, S., 2005. Geophysical survey to estimate the 3D sliding surface and the 4D evolution of the water pressure on part of a deep seated landslide. *Terra Nova* 17, 399–406. <https://doi.org/10.1111/j.1365-3121.2005.00623.x>
- Lévy, C., Baillet, L., Jongmans, D., Mourot, P., Hantz, D., 2010. Dynamic response of the Chamousset rock column (Western Alps, France). *J. Geophys. Res.* 115, F04043. <https://doi.org/10.1029/2009JF001606>
- Lévy, C., Helmstetter, A., Amitrano, D., Le Roy, G., Guyoton, F., 2018. Rayleigh waves in seismic signals of rockfalls. Presented at the 4th RSS Rock Slope Stability Symposium, Chambéry, France.
- Lévy, C., Mangeney, A., Bonilla, F., Hibert, C., Calder, E.S., Smith, P.J., 2015. Friction weakening in granular flows deduced from seismic records at the Soufrière Hills Volcano, Montserrat. *J. Geophys. Res. Solid Earth* 120, 7536–7557.
- Lim, M., Rosser, N.J., Allison, R.J., Petley, D.N., 2010. Erosional processes in the hard rock coastal cliffs at Staithes, North Yorkshire. *Geomorphology* 114, 12–21. <https://doi.org/10.1016/j.geomorph.2009.02.011>
- Loye, A., Pedrazzini, A., Theule, J.I., Jaboyedoff, M., Liébault, F., Metzger, R., 2012. Influence of bedrock structures on the spatial pattern of erosional landforms in small alpine catchments. *Earth Surf. Process. Landf.* 37, 1407–1423.
- Manconi, A., Picozzi, M., Coviello, V., De Santis, F., Elia, L., 2016. Real-time detection, location, and characterization of rockslides using broadband regional seismic networks: SEISMIC DETECTION OF ROCKSLIDES. *Geophys. Res. Lett.* 43, 6960–6967. <https://doi.org/10.1002/2016GL069572>
- Marques, F.M.S.F., 2006. Rates, patterns, timing and magnitude-frequency of cliff retreat phenomena. *Z. Für Geomorphol. New Folge Suppl.* Vol. 144, 231–257.
- Matasci, B., Jaboyedoff, M., Loye, A., Pedrazzini, A., Derron, M.-H., Pedrozzi, G., 2015. Impacts of fracturing patterns on the rockfall susceptibility and erosion rate of stratified limestone. *Geomorphology* 241, 83–97. <https://doi.org/10.1016/j.geomorph.2015.03.037>
- Matsuoka, N., 2019. A multi-method monitoring of timing, magnitude and origin of rockfall activity in the Japanese Alps. *Geomorphology* 336, 65–76. <https://doi.org/10.1016/j.geomorph.2019.03.023>
- McHugh, E.L., 2004. Video Motion Detection for Real-Time Hazard Warnings in Surface Mines. Presented at the SME annual meeting. Society for Mining, Metallurgy, and Exploration, Denver, p. 10.
- METL-MEDDE/DGPR, 2012. Les mouvements de terrain.

- Meza-Fajardo, K.C., Papageorgiou, A.S., Semblat, J.F., 2015. Identification and extraction of surface waves from three-component seismograms based on the normalized inner product. *Bull. Seismol. Soc. Am.* 105, 210–229.
- Mills, J.P., Buckley, S.J., Mitchell, H.L., Clarke, P.J., Edwards, S.J., 2005. A geomatics data integration technique for coastal change monitoring. *Earth Surf. Process. Landf.* 30, 651–664. <https://doi.org/10.1002/esp.1165>
- Mineo, S., Pappalardo, G., Rapisarda, F., Cubito, A., Di Maria, G., 2015. Integrated geostructural, seismic and infrared thermography surveys for the study of an unstable rock slope in the Peloritani Chain (NE Sicily). *Eng. Geol.* 195, 225–235. <https://doi.org/10.1016/j.enggeo.2015.06.010>
- Ministère de l'écologie, du développement durable, et de l'énergie, N., 2014. Versants rocheux: Phénomènes, aléas, risques et méthodes de gestion. Guide Pratique.
- Minkina, W., Klecha, D., 2016. Atmospheric transmission coefficient modelling in the infrared for thermovision measurements. *J. Sens. Sens. Syst.* 5, 17–23. <https://doi.org/10.5194/jsss-5-17-2016>
- Monserrat, O., Crosetto, M., 2008. Deformation measurement using terrestrial laser scanning data and least squares 3D surface matching. *ISPRS J. Photogramm. Remote Sens.* 63, 142–154. <https://doi.org/10.1016/j.isprsjprs.2007.07.008>
- Monserrat, O., Crosetto, M., Luzi, G., 2014. A review of ground-based SAR interferometry for deformation measurement. *ISPRS J. Photogramm. Remote Sens.* 93, 40–48. <https://doi.org/10.1016/j.isprsjprs.2014.04.001>
- Moore, J.R., Gischig, V., Burjanek, J., Loew, S., Fah, D., 2011. Site Effects in Unstable Rock Slopes: Dynamic Behavior of the Randa Instability (Switzerland). *Bull. Seismol. Soc. Am.* 101, 3110–3116. <https://doi.org/10.1785/0120110127>
- Morrissey, M.M., Savage, W.Z., Wiczorek, G.F., 1999. Air blasts generated by rockfall impacts: Analysis of the 1996 Happy Isles event in Yosemite National Park. *J. Geophys. Res. Solid Earth* 104, 23189–23198. <https://doi.org/10.1029/1999JB900189>
- Mueller, S.B., Varley, N.R., Kueppers, U., Lesage, P., Reyes Davila, G. á., Dingwell, D.B., 2013. Quantification of magma ascent rate through rockfall monitoring at the growing/collapsing lava dome of Volcán de Colima, Mexico. *Solid Earth* 4, 201–213. <https://doi.org/10.5194/se-4-201-2013>
- Nicoud, G., Dzikowski, M., Paillet, A., Ghoreychi, R., Emeric, P., Chignoli, 1999, 1999. Données nouvelles sur la nature et l'extension du glissement historique du Granier (Savoie, France). *Actes Colloq. Myans Doc. 2ème Sér. Tome 1* 35–54.
- OMIV, n.d. . Presented at the National French Landslide Observatory Facility and RESIF Datacenter (2006): French Multidisciplinary Observatory of Versant Instabilities. RESIF - Réseau Sismologique et géodésique Français. <https://doi.org/doi:10.15778/RESIF.MT>
- Oppikofer, T., Jaboyedoff, M., Blikra, L., Derron, M.-H., Metzger, R., 2009. Characterization and monitoring of the Aaknes rockslide using terrestrial laser scanning. *Nat. Hazards Earth Syst. Sci.* 9, 1003–1019.
- Panet, M., 1976. Propriétés mécaniques des roches, in: *La Mécanique Des Roches Appliquée Aux Ouvrages Du Génie Civil*. ENPC, Paris.
- Pappalardo, G., Mineo, S., Zampelli, S.P., Cubito, A., Calcaterra, D., 2016. InfraRed Thermography proposed for the estimation of the Cooling Rate Index in the remote survey of rock masses. *Int. J. Rock Mech. Min. Sci.* 83, 182–196. <https://doi.org/10.1016/j.ijrmms.2016.01.010>
- Popescu, M.E., 2002. Landslide causal factors and landslide remedial options. 3rd Int. Conf. Landslides Slope Stab. Saf. Infra-Struct. 61–81.

- Prendes-Gero, M., Suárez-Domínguez, F., González-Nicieza, C., Álvarez-Fernández, M., 2013. Infrared thermography methodology applied to detect localized rockfalls in self-supporting underground mines, in: ISRM International Symposium-EUROCK 2013. International Society for Rock Mechanics and Rock Engineering. CRC Press, pp. 825–829. <https://doi.org/10.1201/b15683-141>
- Provost, F., Malet, J.-P., Hibert, C., Helmstetter, A., Radiguet, M., Amitrano, D., Langet, N., Larose, E., Abancó, C., Hürlimann, M., Lebourg, T., Levy, C., Le Roy, G., Ulrich, P., Vidal, M., Vial, B., 2018. Towards a standard typology of endogenous landslide seismic sources. *Earth Surf. Dyn.* 6, 1059–1088. <https://doi.org/10.5194/esurf-6-1059-2018>
- Raveland, L., Amitrano, D., Deline, P., Gallach, X., Helmstetter, A., Hobléa, F., ... & Ployon, E. 2016, The small rock avalanche of January 9, 2016 from the calcareous NW pillar of the iconic Mont Granier (1933 m asl, French Alps). In EGU General Assembly Conference Abstracts (Vol. 18).
- Real, C.R., Teng, T.L., 1973. Local Richter magnitude and total signal duration in southern California. *Bull. Seismol. Soc. Am.* 1809–1827.
- Riedel, B., Walther, A., 2008. InSAR processing for the recognition of landslides. *Adv. Geosci.* 14, 189–194. <https://doi.org/10.5194/adgeo-14-189-2008>
- Ritchie, A.M., 1963. Evaluation of Rockfall and Its Control. Washington, DC: Highway Research Board, National Research Council Highway Research Record, 16.
- Rosser, N., Lim, M., Petley, D., Dunning, S., Allison, R., 2006. Patterns of precursory rockfall prior to slope failure. *J. Geophys. Res.* 112. <https://doi.org/10.1029/2006JF000642>
- Rousseau, N., 1999. Les signaux sismiques associés aux éboulements sur l'île de la Réunion (océan indien) - étude de deux sites : la cascade de Mahavel et la cavité de la soufrière. University Paris 7, France.
- Royán, M.J., Abellán, A., Jaboyedoff, M., Vilaplana, J.M., Calvet, J., 2014. Spatio-temporal analysis of rockfall pre-failure deformation using Terrestrial LiDAR. *Landslides* 11, 697–709. <https://doi.org/10.1007/s10346-013-0442-0>
- Saló, L., Corominas, J., Lantada, N., Matas, G., Prades, A., Ruiz-Carulla, R., 2018a. Seismic Energy Analysis as Generated by Impact and Fragmentation of Single-Block Experimental Rockfalls. *J. Geophys. Res. Earth Surf.* 123, 1450–1478. <https://doi.org/10.1029/2017jf004374>
- Saló, L., Corominas, J., Lantada, N., Matas, G., Prades, A., Ruiz-Carulla, R., 2018b. Seismic Energy Analysis as Generated by Impact and Fragmentation of Single-Block Experimental Rockfalls. *J. Geophys. Res. Earth Surf.* 123, 1450–1478. <https://doi.org/10.1029/2017JF004374>
- Schürch, P., Densmore, A.L., Rosser, N.J., Lim, M., McArdell, B.W., 2001. Earth Surface Processes and Landforms, in: Detection of Surface Change in Complex Topography Using Terrestrial Laser Scanning: Application to the Illgraben Debris-flow Channel. pp. 1847–1859.
- Shi, W., Wu, Y., Wu, L., 2007. Quantitative analysis of the projectile impact on rock using infrared thermography. *Int. J. Impact Eng.* 34, 990–1002. <https://doi.org/10.1016/j.ijimpeng.2006.03.002>
- Spampinato, L., Calvari, S., Oppenheimer, C., Boschi, E., 2011. Volcano surveillance using infrared cameras. *Earth-Sci. Rev.* 106, 63–91. <https://doi.org/10.1016/j.earscirev.2011.01.003>
- Stark, C.P., Hovius, N., 2001. The characterization of landslide size distributions. *Geophys. Res. Lett.* 28, 1091–1094. <https://doi.org/10.1029/2000GL008527>
- Stock, G.M., Collins, B.D., Santaniello, D.J., Zimmer, V.L., Wieczorek, G.F., Snyder, J.B., 2013. Historical rock falls in Yosemite National Park (1857-2011). *US Dep. Inter. US Geol. Surv.* 17.



- Straub, D., Schubert, M., 2008. Modeling and managing uncertainties in rock-fall hazards. *Georisk Assess. Manag. Risk Eng. Syst. Geohazards* 2, 1–15. <https://doi.org/10.1080/17499510701835696>
- Suwa, H., Mizuno, T., Suzuki, S., Yamamoto, Y., Ito, K., 2008. Sequential processes in a landslide hazard at a slate quarry in Okayama, Japan. *Nat. Hazards* 45, 321–331. <https://doi.org/10.1007/s11069-007-9163-9>
- Tanyaş, H., Westen, C.J., Allstadt, K.E., Jibson, R.W., 2019. Factors controlling landslide frequency–area distributions. *Earth Surf. Process. Landf.* 44, 900–917. <https://doi.org/10.1002/esp.4543>
- Terzaghi, K., 1950. Mechanisms of landslides. *Appl. Geol. Eng. Pract. Berkeley Vol. Geol. Soc. Am. Wash. DC* 83–123.
- Teza, G., Marcato, G., Pasuto, A., Galgaro, A., 2015. Integration of laser scanning and thermal imaging in monitoring optimization and assessment of rockfall hazard: a case history in the Carnic Alps (Northeastern Italy). *Nat. Hazards* 76, 1535–1549. <https://doi.org/10.1007/s11069-014-1545-1>
- Teza, G., Pesci, A., Genevois, R., Galgaro, A., 2007. Characterization of landslide ground surface kinematics from terrestrial laser scanning and strain field computation. *Geomorphology* 97, 424–437. <https://doi.org/10.1016/j.geomorph.2007.09.003>
- Usamentiaga, R., Venegas, P., Guerediaga, J., Vega, L., Molleda, J., Bulnes, F., 2014. Infrared Thermography for Temperature Measurement and Non-Destructive Testing. *Sensors* 14, 12305–12348. <https://doi.org/10.3390/s140712305>
- Valentin, J., Capron, A., Jongmans, D., Baillet, L., Bottelin, P., Donze, F., Larose, E., Mangeney, A., 2017. The dynamic response of prone-to-fall columns to ambient vibrations: comparison between measurements and numerical modelling. *Geophys. J. Int.* 208, 1058–1076. <https://doi.org/10.1093/gji/ggw440>
- Varnes, D., 1978. Slope movement types and processes. *Spec. Rep.* 176 11–33.
- Vilajosana, I., Surinach, E., Abellán, A., Khazaradze, G., Garcia, D., Llosa, J., 2008. Rockfall induced seismic signals: case study in Montserrat, Catalonia. *Nat. Hazards Earth Syst. Sci.* 8, 805–812.
- Vogt, D., Brink, V.Z., Brink, S., Price, M., Benon, K., 2010. New technology for improving entry examination, thereby managing the rockfall risk in south african gold and platinum mines. Presented at the CSIR, Center for Mining Innovation, Auckland Park, Johannesburg, South Africa, 2010.
- Voight, B., 1989. A Relation to Describe Rate-Dependent Material Failure. *Sci. New Ser.* 243, 200–203.
- Volkwein, A., Schellenberg, K., Labiouse, V., Agliardi, F., Berger, F., Bourrier, F., Dorren, L.K.A., Gerber, W., Jaboyedoff, M., 2011. Rockfall characterisation and structural protection – a review. *Nat. Hazards Earth Syst. Sci.* 11, 2617–2651. <https://doi.org/10.5194/nhess-11-2617-2011>
- Walter, M., Arnhardt, C., Joswig, M., 2012. Seismic monitoring of rockfalls, slide quakes, and fissure development at the Super-Sauze mudslide, French Alps. *Eng. Geol.* 128, 12–22. <https://doi.org/10.1016/j.enggeo.2011.11.002>
- Weichert, D., Horner, R.B., Evans, S.G., 1994. Seismic signatures of landslides: The 1990 Brenda Mine collapse and the 1965 hope rockslides. *Bull. Seismol. Soc. Am.* 84, pp.1523-1532.
- Westoby, M.J., Brasington, J., Glasser, N.F., Hambrey, M.J., Reynolds, J.M., 2012. ‘Structure-from-Motion’ photogrammetry: A low-cost, effective tool for geoscience applications. *Geomorphology* 179, 300–314. <https://doi.org/10.1016/j.geomorph.2012.08.021>

- Wheaton, J.M., Brasington, J., Darby, S.E., Sear, D.A., 2009. Accounting for uncertainty in DEMs from repeat topographic surveys: improved sediment budgets. *Earth Surf. Process. Landf.* n/a-n/a. <https://doi.org/10.1002/esp.1886>
- Wieczorek, G.F., 1996. Landslide triggering mechanisms. *Landslides: investigation and mitigation. Transportation Research Board Special Report, (247)*.
- Wieczorek, G.F., Snyder, J.B., 2009. Monitoring slope movements, in: *Geol. Monit.* pp. 245–271.
- Wieczorek, G.F., Snyder, J.B., Waitt, R.B., Morrissey, M.M., Uhrhammer, R.A., Harp, E.L., Norris, R.D., Bursik, M.I., Finewood, L.G., 2000. Unusual July 10, 1996, rock fall at Happy Isles, Yosemite National Park, California. *Geol. Soc. Am. Bull.* 112, 75–85.
- Williams, J.G., Rosser, N.J., Hardy, R.J., Brain, M.J., Afana, A.A., 2018. Optimising 4-D surface change detection: an approach for capturing rockfall magnitude–frequency. *Earth Surf. Dyn.* 6, 101–119. <https://doi.org/10.5194/esurf-6-101-2018>
- Wu, L., Wu, Y., Shi, W., Zhong, S., Ge, D., 2005. Comparisons of thermal radiation characteristics between rocks and PMMA subjected to free-fall impacts, in: Peacock, G.R., Burleigh, D.D., Miles, J.J. (Eds.), . p. 264. <https://doi.org/10.1117/12.602149>
- Yan, Z., Chai, H., 2017. A method for intelligent safety monitoring and hazard warning of highway dangerous rock, in: *Applied Mechanics and Civil Engineering VI.* pp. 31–36.
- Yin, Y., Wang, F., Sun, P., 2009. Landslide hazards triggered by the 2008 Wenchuan earthquake, Sichuan, China. *Landslides* 6, 139–152. <https://doi.org/10.1007/s10346-009-0148-5>
- Young, A.P., 2015. Recent deep-seated coastal landsliding at San Onofre State Beach, California. *Geomorphology* 228, 200–212. <https://doi.org/10.1016/j.geomorph.2014.08.005>
- Zeckra, M., Hovius, N., Burtin, A., Hammer, C., 2015. Automated Detection and Classification of Rockfall Induced Seismic Signals with Hidden-Markov-Models. *AGU Fall Meet. Abstr.*
- Zimmer, V.L., Collins, B.D., Stock, G.M., Sitar, N., 2012. Rock fall dynamics and deposition: an integrated analysis of the 2009 Ahwiyah Point rock fall, Yosemite National Park, USA. *Earth Surf. Process. Landf.* 37, 680–691. <https://doi.org/10.1002/esp.3206>



Supplementary material



# Supplementary A

*This supporting material provides further information on the methodology carried out during photogrammetric surveys of Mount Granier and Mount Saint-Eynard cliffs.*

## A.1 Equipment

Table A.1 : Surveys equipment

Camera	Canon 7D Mark II
Sensor	22.4 x 15 mm CMOS
Lens	24-105 mm, f/4L IS USM
Picture size	5472x3648

## A.2 Survey design

We have carried out two terrestrial imaging survey. The two surveys were acquired and processed identically. Photographs panoramas were taken from 14 locations, with a 60% overlap between consecutive images. In this way, data sets of 400-500 photographs were obtained. Acquisition locations were selected based on various criteria. Compromise had to be done between short distances to the cliffs and acquisition locations allowing views over the overall height of the cliff. Local topography and the highly urbanized slopes at the foot of the cliff have played an important role in the selection of these acquisition locations.

Two lines of acquisition locations were adopted. The first line of photographs acquisition presents distance to the cliff ranging from 0.6 and 1.2 km. Shorter distances to the cliffs were limited by the cliff's topography and vegetation. Due to the presence of spur and recesses in the cliff, 9 panoramas acquisitions were adopted with distances between acquisitions on average 450 m over a total distance of 3500 m. The second line of photographs acquisition (5 locations) was adopted in order to provide better viewpoints of the overall cliff (distance to the cliff ranging from 1.7 and 2.2 km). Panoramas obtained this way presents overlaps of at least 60%. Photographs were taken in either sunny or fairly hazy sky condition with even illumination conditions over the cliff and over the entire photographs dataset.

### A.3 SfM processing

Software Agisoft Photoscan Pro version 1.2.6 and Metashape Pro version 1.5.1 were used to process the data. Images were aligned with ‘Very High’ accuracy; the MVS reconstruction was set to ‘High’ quality and ‘Mild’ depth filtering.

In this way, we obtained clouds characterized by densities ranging from 50 to 70 points/m<sup>2</sup>, depending on the area, and mean point spacing of 0.12cm.

Table A.2: Surveys characteristics

Tie Points	138 228
RMS reprojection error	1.2 pix
Mean key point size	4.3 pix
Average tie points multiplicity	8.1

### A.4 Point clouds processing

Point clouds were georeferenced using a georeferenced point cloud of the site obtained by airborne laser scanning in 2011. The co-registration (or alignment) of the 3D point clouds is achieved first by a manual alignment, which consists of identifying common points in the different point clouds (at least 6 points). Following this rough matching, we then applied an automated iterative procedure with a point-to-surface Iterative Closest Point (ICP) algorithm (Besl and McKay, 1992; Teza et al., 2007), in order to minimize the co-registration errors.

Raw point clouds were cleaned to remove vegetation noise and keep only the rock surface. However, due to the presence of vegetation or grassy patch of ledges spread over the cliff surface, we were not able to remove all the vegetation patches.

### A.5 Split data tests

This test aims to produce two datasets, using the same survey design on two different dates. We compare stable zones in order to determine the errors likely to be present in the surface model (James et al, 2019).

Two point clouds (November 2016 and July 2018) were used for this test. Using photographs and previous monitoring, we defined areas affected by rockfall occurrence. In order to compare stable zones, most areas corresponding to rockfall or vegetation were removed. Over more than 30 000 000 points, 95.45% ( $2\sigma$ ) are distant of less than 11 cm and 99.73% ( $3\sigma$ ) are distant by less than 25 cm. Areas corresponding to large distance (25 cm) mainly correspond to either the remaining vegetated areas or to recesses areas. In

order to reduce the influence of such areas, most of them were removed. The choice of large rockfall detection thresholds (from 30 cm) allowed us to clear away most of this noise.





# Supplementary B

*This supporting material provides further information on the number of events considered in the chapter 6 and on the sensitivity analysis of the model parameters. First, we present the number of events detected by the various catalogs used in this study. We then study the influence of the parameters used in this study on the calculated seismic energy and rockfall volumes.*

## B.1 Rockfalls catalogs

Rockfall monitoring at Mount Saint-Eynard has been carried out since 2013 by several methods: TLS and photogrammetric surveys, continuous photographic survey (1 photograph every 10 minutes), seismic monitoring. These methods cover different areas, have different detection thresholds and temporal resolutions. In this study, we only select well-constrained events that have been detected by all methods. The two following tables present the number of events detected by each method in this study.

Table A. 1. Mount Saint-Eynard events detected using TLS data

Catalog	Sub-categories	Number of events	
TLS	total	508	
	volume > 0.5 m <sup>3</sup>	total	51
		dated <sup>(1)</sup>	31
	volume > 2m <sup>3</sup>	total	15
		dated <sup>(1)</sup>	12

<sup>(1)</sup> Events which were dated using continuous photographic monitoring. If several events detected by TLS occurred within a pair of photographs, it is impossible to associate unambiguously events detected by TLS and by the seismic network. In order to avoid any mismatch, these events were ruled out.

Table A. 2 Mount Saint-Eynard events detected using the seismic network.

Catalog	Sub-categories			Number of events	
Seismic network	Total			926	
	Rockfalls	Total			87
		Inside Area			41
		Inside area, detected by at least two stations	Total		34
			Associated with TLS	Total	15
				Free-fall	13
	Free-fall > Dff <sup>(1)</sup>	10			

<sup>(1)</sup> Events for which the duration of free fall is larger than the duration of the detachment seismic signal.

## B.2 Sensitivity analysis of parameters

To calculate the seismic energy, we assume a point-source (Eissler and Kanamori, 1987; Kanamori and Given, 1982) and we consider the medium as isotropic and homogeneous. We also consider that surface waves dominate the seismic signal (Dammeier et al., 2011; Hibert et al., 2014; Lévy et al., 2015; Hibert et al., 2017; Saló et al., 2018a). Signals were band-pass filtered between 2 and 50 Hz for the entire analysis.

The following relation was used:

$$E_s = 2\pi r p h c \int_{t_0}^{t_1} u_{env}(t)^2 e^{\alpha r} dt \quad (\text{A.1})$$

where  $t_0$  and  $t_1$  are the manually picked onset and end times of the seismic signal,  $r$  is the distance between the event and the recording station,  $h$  is the thickness of the layer through which surface waves propagate,  $p$  is the ground density,  $c$  is the phase velocity of the seismic waves,  $u_{env}(t)$  is the envelope of the ground velocity,  $\alpha$  is a damping factor that accounts for anelastic attenuation of the waves (Aki and Richards, 1980).

In these relations, several factors are sources of uncertainty.

### B.2.1 Distance error

A location error leads to uncertainties on the distance between the event and the seismic stations. In order to determine the resulting uncertainties on the estimated rockfall volume, we have studied how the seismic energy varies as a function of a location error. We have created a set of randomly distributed event locations around a reference point. For each location, the seismic energy was calculated. This analysis allowed us to determine a seismic energy uncertainty related to a location uncertainty.

This uncertainty on the seismic energy is influenced by the location of the event and by the number of seismic stations that have recorded the event. The uncertainty on the seismic energy  $E_s$  for an event located in the middle of the network will be smaller than

for an event located on the edges of the network. Similarly, the uncertainty for an event detected by four stations will be smaller than for an event detected by two stations.

In this analysis, we assume a velocity of surface waves in limestone of 1810 m/s, a density of 2500 kg.m<sup>-3</sup>. The centroid frequency of the impact seismic signals averages at 10 Hz. The thickness was taken as one wavelength of Rayleigh waves,  $h=181$  m for a frequency of 10 Hz.

In our study, the detachment location is well constrained from DEM data (error of about 1 m), leading negligible uncertainties on the rockfall volume. But location errors of the impacts can be much larger as it depends on the uncertainty of free-fall. We assume in this study, a location error of maximum 20 m around the location determined using DEM data.

The following analysis investigates what would be the influence of a large location error (50 m) on the estimated rockfall volume.

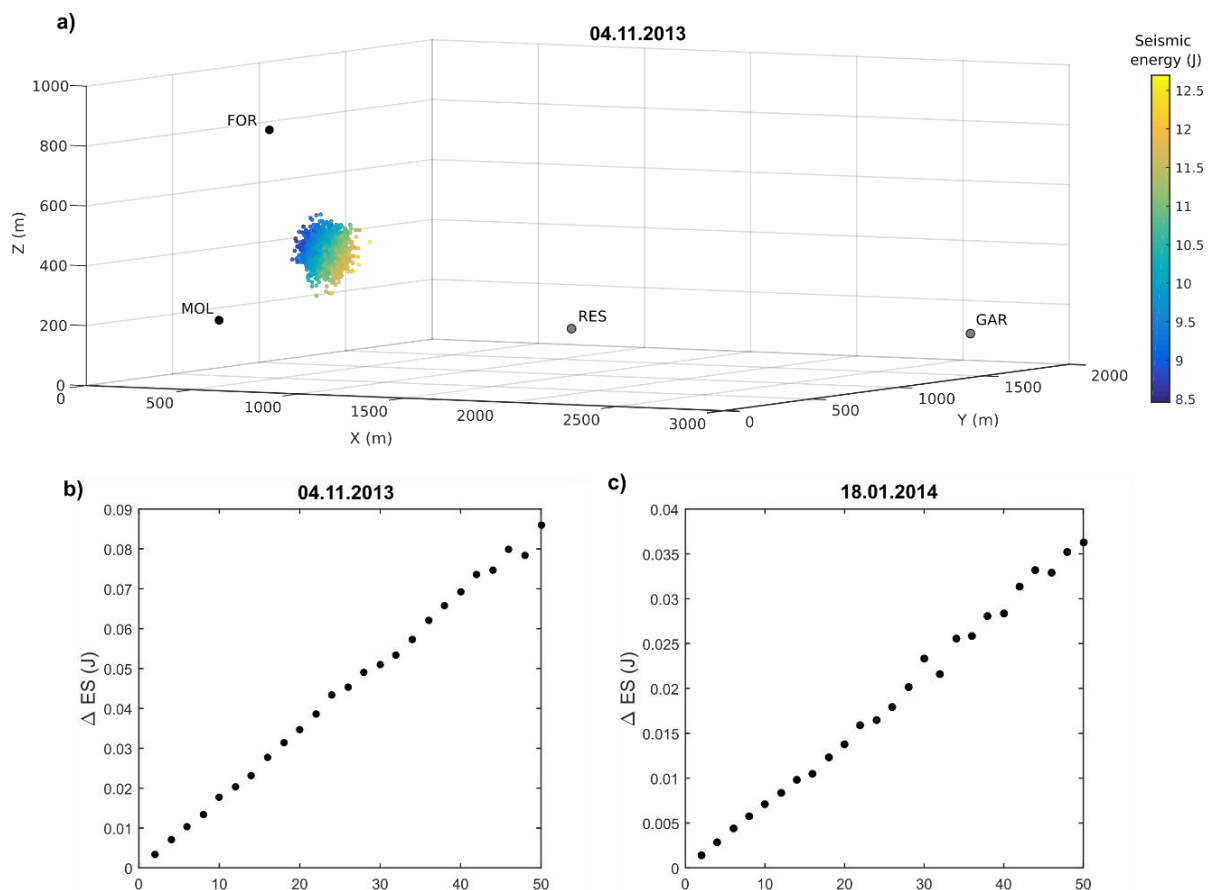


Figure A.1 . a) variation of the estimated seismic energy (J) for the 04.11.2013 event as a function of the estimated source location, assuming random locations up to 200 m away from the true location. b) relative error on the seismic energy  $\Delta Es/Es$  as a function of the distance  $r$  around the location determined using DEM data for the 04.11.2013 event and c) 18.01.2014 event.

Table A.3. Error on the estimated seismic energy for a location error of 20 m around the location determined by TLS.

Site	Event	Nb station	$\Delta E_s$ (%)
Saint-Eynard	04.11.2013 – 19:35:36	2	3.47
	16.11.2013 – 22:11:37	2	5.82
	25.11.2013 – 06:44:54	2	3.80
	06.12.2013 – 04:25:05	4	0.68
	30.12.2013 – 23:27:19	2	3.40
	15.08.2014 – 01:08:33	4	1.85
	18.01.2015 – 08:20:13	4	1.37
	22.01.2015 – 21:01:31	2	5.73
	15.02.2015 – 20:54:28	3	1.15
	25.11.2015 – 03:54:39	3	1.74
Granier	17.01.2017 – 21:38:12 (A <sub>1</sub> )	1	3.07
	17.01.2017 – 23:20:29 (A <sub>2</sub> )	1	3.07
	18.01.2017 – 01:12:30 (A <sub>3</sub> )	1	3.07
	18.01.2017 – 01:12:32 (A <sub>4</sub> )	1	3.07
	01.02.2017 – 12:14:38 (B)	1	3.07

### B.2.2 Seismic wave velocity error

In this study, the seismic wave velocity has been estimated between 1700 and 1900 m/s. This range of velocity is consistent with the velocity of surfaces waves for subsurface geology composed of sound limestone and scree deposits (Saló et al, 2018).

In Equation (A.1), the seismic energy is proportional to the wave velocity. Wave velocity also impacts the calculation of the thickness of the layer through which surface waves propagate as  $h=c/f$ , with  $f$  the centroid frequency (10 Hz).

### B.2.3 Frequency-dependence of the attenuation factor

A variation of frequency induces a variation of the damping factor that accounts for anelastic attenuation  $\alpha$  and a variation of the thickness of the layer through which surface waves propagate.

$$\log_e \left[ \frac{a_i \epsilon_j}{a_j \epsilon_i} \left( \frac{\Delta_i}{\Delta_j} \right)^n \right] = -\alpha(r_j - r_i) \quad (\text{A.2})$$

with  $a_i$  and  $a_j$  the maximum amplitudes at two stations.  $n = 0.5$  for surface waves,  $r_i$  and  $r_j$  the corresponding epicentral distances, and  $\epsilon_i$  and  $\epsilon_j$  constants accounting for site

effects of each sensor. We filter the signals in different frequency bands before computing the maximum amplitudes, using centroid frequencies varying between 2 and 25 Hz and a width of 2 Hz.

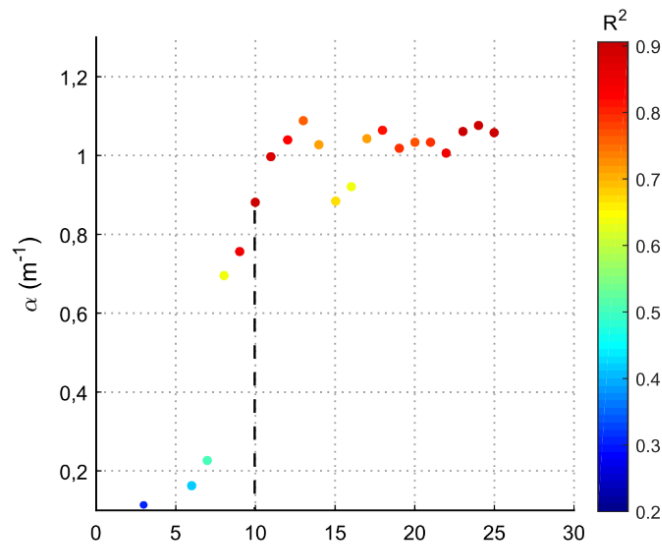


Figure A.2. Damping factor  $\alpha$  as a function of the centroid frequency. The color scale represents the correlation coefficient between the two sides of equation (A.2).

Table A.4. Frequency centroid of the detachment and impact phases seismic signals detected at stations FOR (Saint-Eynard) and GRA (Granier).

Site	Event	Volume $V_{DEM}$ ( $m^3$ )	Frequency of detachment phase (Hz)	Frequency of impact phase (Hz)
Saint-Eynard	04.11.2013 – 19:35:36	$1.4 \pm 0.1$	9.09	7.16
	16.11.2013 – 22:11:37	$13.6 \pm 0.1$	6.82	8.65
	25.11.2013 – 06:44:54	$3.2 \pm 0.1$	8.9	9
	06.12.2013 – 04:25:05	$6.1 \pm 0.1$	13.95	9.17
	30.12.2013 – 23:27:19	$5.1 \pm 0.1$	10.16	10.1
	15.08.2014 – 01:08:33	$5.3 \pm 0.2$	8.08	7.33
	18.01.2015 – 08:20:13	$100.4 \pm 0.2$	9.5	13.13
	22.01.2015 – 21:01:31	$1.9 \pm 0.1$	14.14	13.04
	15.02.2015 – 20:54:28	$8.0 \pm 0.1$	9.47	8.08
	25.11.2015 – 03:54:39	$94.0 \pm 5$	6.88	9.46
Granier	17.01.2017 – 21:38:12 (A <sub>1</sub> )		5.7	4
	17.01.2017 – 23:20:29 (A <sub>2</sub> )		15.7	11.7
	18.01.2017 – 01:12:30 (A <sub>3</sub> )	$4600 \pm 50$	7.52	9.31
	18.01.2017 – 01:12:32 (A <sub>4</sub> )		(a) 4.15 / (b) 4.64	5.11
	01.02.2017 – 12:14:38 (B)	$11.5 \pm 0.5$	11.04	5.5

A change of frequency has little impact on the correlation between the calculated and measured volume of Mount Saint-Eynard rockfalls ( $R^2=0.976$  to  $R^2=0.996$ ). The exponent of the power-law between  $E_p$  and  $E_s$  decreases with the frequency from 1.56 for

a frequency of 20 Hz down to 1.50 for a frequency of 5 Hz. For a lower frequency (e.g. 5 Hz), this change in exponent allows a better agreement with Mount Granier and Yosemite's events (figure A.3.b). The power-law exponent between  $E_p$  and  $E_s$  is almost independent of seismic wave velocity. However, when increasing the seismic wave velocity, the  $E_s/E_p$  ratio decrease

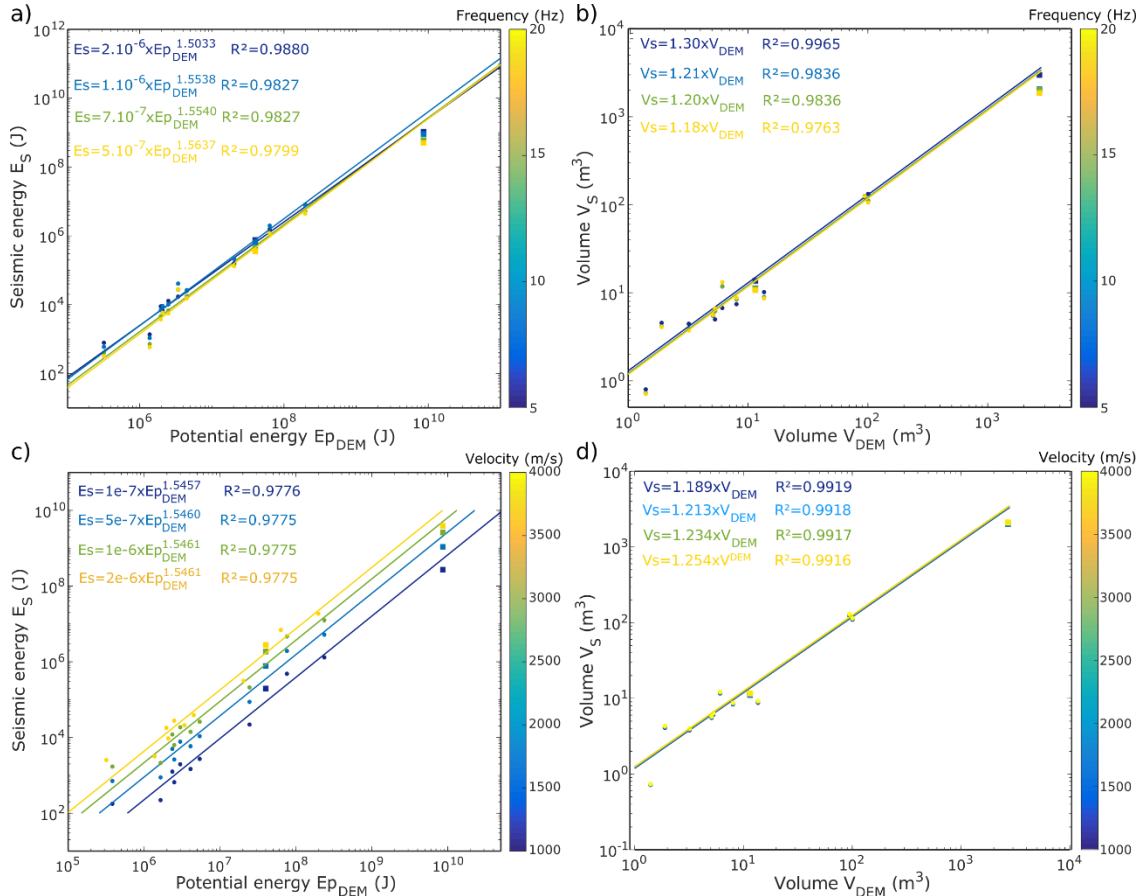


Figure A.3. a) and c) Seismic energy of the impact phase as a function of potential energy. Seismic energy is calculated from equation (1) using a) frequencies of 5, 10, 15 and 20 Hz and c) velocities of 1000, 2000, 3000 and 4000 m.s<sup>-1</sup>. b) and d) Rockfall volumes calculated as a function of measured volumes. The calculated volumes are obtained using the power-law relations between  $E_s$  and  $E_p$  presented in the plots a) and c). Power laws are fitted for each value of frequency or velocity and the correlation coefficients are indicated on each plot.

## B.2.4 Body waves hypothesis

Below are the results of our study if we assume body waves. To calculate the seismic energy for body waves, we assume the following equation:

$$E_s = 4\pi r^2 \rho c \int_{t_0}^{t_1} u_{env}(t)^2 e^{\alpha r} dt \quad (\text{A.3})$$

The correlation coefficient between potential and seismic energies obtained with body waves (in blue) are slightly lower than the ones obtained with surface waves (in red) ( $R^2=0.99$  for surface waves,  $R^2=0.90$  for body waves). There is also more discrepancy

between Mount Saint-Eynard and Mount Granier data if we assume body waves. These points comfort us in our assumption of surface wave.